Orbital Dynamics and Habitability of Exoplanets

Russell J. Deitrick

A dissertation
submitted in partial fulfillment of the
requirements for the degree of

Doctor of Philosophy

University of Washington

2017

Reading Committee:

Rory Barnes, Chair

Victoria Meadows

Thomas Quinn

Cecilia Bitz

Program Authorized to Offer Degree:
Astronomy

University of Washington

Abstract

Orbital Dynamics and Habitability of Exoplanets

Russell J. Deitrick

Chair of the Supervisory Committee:
Professor Rory Barnes
Department of Astronomy

With the discoveries of thousands of extra-solar planets, a handful of which are terrestrial in size and located within the "habitable zone" of their host stars, the discovery of another instance of life in the universe seems increasingly within our grasp. Yet, a number of difficulties remain—with current and developing technologies, the full characterization of a terrestrial atmosphere and, hence, the detection of biosignatures will be extraordinarily difficult and expensive. Furthermore, observations will be ambiguous, as recent developments have shown that there is no "smoking gun" for the presence of life. Ultimately, the interpretation of observations will depend heavily upon our understanding of life's fundamental properties and the physical context of a planet's observed properties.

This thesis is devoted to a development of the latter quantity, physical context, focusing on a topic oft-neglected in theoretical works of habitability: orbital dynamics. I show a number of ways in which orbital dynamics can affect the habitability of exoplanets. This work highlights the crucial role of stability, mutual inclinations, and resonances, demonstrating how these properties influence atmospheric states.

Studies of exoplanetary systems tend to assume that the planets are coplanar, however, the large mutual inclination of the planets orbiting υ Andromedae suggests that coplanarity is not always a valid assumption. In my study of this system, I show that the large inclination between planets c and d and their large eccentricities lead to dramatic orbital variations.

Though there is almost certainly no habitable planet orbiting υ And, the existence of this system demonstrates that we should expect other such dynamically "hot" planetary systems, some of which may contain potentially habitable planets.

Minute variations in a planet's orbit can lead to changes in the global temperature, and indeed, these variations seem to be intimately connected to Earth's Pleistocene ice ages. Mutual inclinations lead not only to larger variations in a planet's obliquity, but also uncover secular spin-orbit resonances, which lead to yet more dramatic behavior. I modeled the obliquity evolution of planets in this highly non-linear dynamical regime. Connecting the dynamical models to an simple climate model with ice sheets, I modeled the effects of such dynamical evolution on an Earth-like planet's climate. As expected, such "exo-Milankovitch cycles" can be rapid and dramatic, often leading to complete collapse into a snowball state.

By demonstrating a handful of the many ways dynamics can influence habitability, this research provides context to observations of exoplanets and connects to one of the key goals of astrobiology, to "Determine the potential for habitable planets beyond the Solar System, and characterize those that are observable" (Des Marais et al., 2008). It provides tools and techniques that may be used to help prioritize exoplanet targets for characterization missions when very little information is known other than orbital properties. It also demonstrates how orbital evolution affects observable quantities like albedo, and will assist in the interpretation of spectra.

TABLE OF CONTENTS

LIST OF FIGURES

ACKNOWLEDGMENTS

Thanks first and foremost to my family, Athena and Eloise, for taking care of me throughout my degree, always being there for me, and providing me with so much joy.

Thanks to Rory Barnes for mentorship; for keeping me on course, for teaching me how to write, how to code, how to have the self-confidence I needed, and for seeing the big picture when I was unable. Also, for being a friend and teaching me the importance of beer.

Thanks to Vikki Meadows for funding my research throughout my degree, for the unending patience and priceless feedback. Without her unwavering vision, this brand of interdisciplinary research would not be possible.

Thanks to Tom Quinn, for teaching me everything I know about Hamiltonians, for teaching me how to use a computer to solve problems, and for diagnosing all my poorly written code.

Thanks to Cecilia Bitz, for teaching me everything I know about climate and climate modeling, for patiently listening to my rambling thoughts, and for steering me back on course when I'd gone astray.

Thanks to my long-time office mate Rodrigo Luger, for always taking to the time to talk through problems with me and being absolutely determined to find solutions. And thanks, of course, for the great espresso.

Thanks to all the other graduate students in Astronomy and Astrobiology for being good friends, providing help and feedback, and generating stimulating conversations. In particular, David Fleming, Jake Lustig-Yaeger, Giada Arney, Eddie Schwieterman, Aomawa Shields, Sarah Loebman, Michael Tremmel, Nell Byler, and John Ruan.

Thanks to my long-distance collaborators, Barbara McArthur, Benjamin Charnay, and

John Armstrong, for the help and encouragement, and taking the time to work with me and to respond to my confusing questions.

Thanks to Caitlyn Wilhelm, Diego Valdivia McDonald, Ann-Margaret Stompro, and Marijn Anton Burger for teaching me how to be a mentor.

DEDICATION

To my closest friend and partner in life, Athena Dova.

Chapter 1

INTRODUCTION

"I have never listened to anyone who criticized my taste in space travel, sideshows or gorillas. When this occurs, I pack up my dinosaurs and leave the room." [Ray Bradbury]

1.1 Exoplanets

The discovery of the first planet orbiting a main sequence star (Mayor & Queloz, 1995) revolutionized both astronomy and planetary science—and gave the two fields some new common ground. It also helped to create a new field of study: astrobiology, the study of life and its place in the universe. Suddenly, the possibility of finding life elsewhere seemed tantalizingly within reach.

Just over 20 years later, we now know of thousands of extra-solar planets ("exoplanets"), most of which were discovered in "one fell swoop" by NASA's monumentally successful *Kepler* satellite (Borucki et al., 2010; Batalha et al., 2010). Technology has advanced dramatically and missions on the horizon, such as the James Webb Space Telescope (Gardner et al., 2006) and the proposed Large Ultra-Violet Optical InfraRed telescope (LUVOIR; Dalcanton et al., 2015; Bolcar et al., 2015) will provide us with unprecedented observing power. Yet a number of challenges remain in the search for habitable planets and life beyond Earth. These include technological challenges: we need better detectors, bigger aperatures, more efficient data-reduction pipelines (Fujii et al., 2017); but there are also theoretical challenges: how will we recognize a habitable planet, let alone a life-bearing world, considering we know of only a single example (Catling et al., 2017; Meadows, 2017; Meadows et al., 2017; Schwieterman et al., 2017)?

This thesis contributes to this latter challenge. I attempt to chip-away at this theoretical obstruction through an understanding of planetary system architecture: where are the planets, how big are they, and how do they move around? Further, how does architecture influence a planet's potential to have a hospitable climate for life?

Orbital dynamics, or the evolution of a planet's orbit, can affect the surface habitability of planet in several ways that I examine in this thesis. When a planet is on a non-circular orbit (its eccentricity is nonzero), the distance between it and its host star varies over an orbital period, resulting in a variation in the total amount of stellar energy absorbed (Berger, 1978; Laskar et al., 1993a). Perturbations from other planets in the system cause the eccentricity to vary (Murray & Dermott, 1999), resulting in potential variations to the climate. I discuss these concepts in more detail in Sections 1.5 and 1.6.

Another result of orbital dynamics is obliquity evolution. Obliquity, or axial tilt, governs the distribution of stellar energy across a planet's latitudes (Berger, 1978). When obliquity is low, the poles of the planet receive very little starlight. When it is high, the poles receive intense starlight for part of the year, and no starlight at all for part of it. This influences where and when ice can form on a planet's surface. Variations in obliquity, like variations in eccentricity, can lead to changes in the overall climate, and as I show in Chapter 4, can lead to runaway glaciation events that completely freeze the planet's surface.

This work is deeply rooted in two theories that each have a substantial body of literature: the theory of the habitable zone (HZ; Huang, 1959; Kasting et al., 1993) and the theory of Milankovitch cycles (Hays et al., 1976). In Chapter 4, in particular, I explore the possibility of snowball events occurring within the HZ, as a consequence of orbital and obliquity evolution. In other words, I argue that planets within the HZ are not necessarily habitable, at least not at the surface. Because the HZ concept is fundamental to this work, I review the basic theory of the HZ in Section 1.2. Milankovitch theory, *i.e*, the theory that Earth's orbital and obliquity evolution drove the ice ages of the few million years, is also fundamental to this work because I employ many of the tools used in that theory (*e.g.* frequency analysis, energy balance models, etc.) and I utilize much of the knowledge gained in its development.

I review the basics of Milankovitch theory in Section 1.5.

Orbital models are the backbone of this thesis because of potential impact of orbital variations on climate through eccentricity and obliquity. It is thus worth reviewing the theory of orbital evolution and some of the models developed from that theory. I do so in Section 1.3. In my work, I employ three orbital models of varying levels of complexity and accuracy—each has its own utility. Two of the models make use of the "disturbing function" (Murray & Dermott, 1999), which allows for both fast computation and a deeper understanding of the physics, at the cost of accuracy. There are mathematical details of the orbital theory that may appear to be unnecessarily fussy and there is quite a bit of archaic terminology. I have done my best to reduce the unnecessary details and explain jargon in qualitative ways.

Ultimately, the purpose of this work is provide a self-consistent model of the effect of orbital evolution on the habitability of exoplanets. Though a number of studies have examined this topic previously (as I discuss in Section 1.6), there are a number of shortcomings within those works. Often, some of the components of the orbital/obliquity are ignored, leading to an incomplete analysis (Spiegel et al., 2010; Way & Georgakarakos, 2017). Other times, processes in the climate model are handled inappropriately (Spiegel et al., 2010; Armstrong et al., 2014; Forgan, 2016). In this work, I have created the first, fully coupled model for the evolving orbits, obliquities, and climates of potentially habitable exoplanets, including the effects of oceans and ice sheets. This model is computationally inexpensive, which allows it to be run over broad regions of parameter space. This will help prioritize targets for characterization studies by allowing us to quantify the probability that individual targets have atmospheres that are strongly influenced by orbital variations.

In this chapter, I focus on the background that motivates the following chapters. The organization of this chapter is as follows: first, I discuss the concept of the habitable zone, followed by a foray into the theory of orbital dynamics. I then discuss the Milankovitch theory for Earth, and then as it applies to exoplanets. Finally, I provide an outline of the rest of the work.

1.2 The habitable zone

By now the concept of the habitable zone (Huang, 1959; Hart, 1979) is familiar to virtually everyone in astronomy and planetary sciences, and even to many members of the public. The HZ, as we discuss here, is the region around a star in which a planet with a roughly Earth-like atmosphere (i.e., dominated by N_2, CO_2, and water) can maintain liquid water on its surface for a significant length of time (billion of years, say). Though initially this concept was discussed only for the sun and sun-like stars, this was expanded to include stellar types F-M by Kasting et al. (1993). Their study used a one-dimensional radiation-convective model to determine the possible climates of Earth-like planets orbiting stars of types F, G, K, and M at different orbital distances to determine where the surface temperature was in the correct range for stable liquid water ($0° - 100°$ C at 1 bar of atmospheric pressure). Although this definition of the HZ does not include the possibility of subsurface life, such as life that might exist on Mars or Europa, it is the preferred definition for exoplanets because we have little hope of detecting subsurface life across interstellar distances. A key aspect of the HZ is stability of climate provided by the carbon-silicate weathering cycle, which should allow the atmospheric abundance of CO_2, a major greenhouse gas, to change with surface temperature (Walker et al., 1981). It is this weathering cycle that allowed Kasting et al. (1993) to extend the HZ to be much wider than it was previously considered. Many studies have since used one-dimensional radiative-convective models to expand on and refine this work (Selsis et al., 2007; Kopparapu et al., 2013, 2014).

In radiative-convective models, the limits of the HZ are set by the so-called "moist-greenhouse" (inner edge) and the "maximum greenhouse" (outer edge). At the inner edge of the HZ, the temperature of the surface must still be low enough for liquid water to be stable, however, the upper atmosphere of the planet may be warm enough that water vapor is no longer trapped in the troposphere. In this scenario, water vapor is then lost through photolytic breakdown into H_2 and O and the hydrogen is subsequently lost to space. The moist greenhouse limit is then the semi-major axis of the planet's orbit or the stellar flux

at which a planet like Earth will lose all of its water after ~ 4.5 Gyr (Kasting et al., 1993). The outer edge of the HZ is set by the maximum amount of greenhouse warming a planet can get out of CO_2. Increasing the CO_2 pressure warms the planet and allows it to remain habitable at lower stellar fluxes. Once CO_2 pressure reaches above ~ 8 bars, however, the increased planetary albedo from Rayleigh scattering overwhelms the greenhouse effect, and the planet begins to cool (Kopparapu et al., 2013). The outer edge of the HZ can then be found by setting the CO_2 pressure to this maximum and lowering the stellar flux until the planet freezes (Kasting et al., 1993).

One potential limitation of the radiative-convective models used for the previously mentioned HZ studies is that they are one-dimensional in the vertical direction. Any properties, including insolation and surface temperature, which vary with latitude and longitude are thus averaged in this scheme, and any dependence that the HZ may have on such properties is lost. Numerous studies have sought to evaluate the dependence of HZ limits on properties at different latitudes and/or longitudes using one-dimensional latitudinal energy balance models (EBMs) and fully three-dimensional global climate or general circulation models (GCMs). There are advantages and disadvantages to each type of model. 1D EBMs (Budyko, 1969; Sellers, 1969) are computationally fast and so allow for easy exploration of parameter space as well as the ability to capture very long term (Myr or so) behavior. On the other hand, they cannot very realistically capture a number of different processes, such as heat diffusion and circulation, and so numerous parameterizations must be used and must be tuned to Earth-like conditions (North, 1975; North & Coakley, 1979; Spiegel et al., 2008; Armstrong et al., 2014). 3D GCMs (*e.g.* Yang et al., 2013, 2014; Wolf & Toon, 2014; Kopparapu et al., 2016) are much more able to capture the myriad of climate processes, including properties that depend on latitude, altitude, *and* longitude. They are, however, so complex that simulations are generally limited to short run times (centuries to a few millenia), and so cannot usually capture most geological time-scale processes. Here, and in Sections 1.5 and 1.6, I review some of the results from both types of models, as they apply to my work.

In the present decade, a number of studies have modeled the limits of the HZ using 3D

GCMs. Abe et al. (2011) showed that dry planets (i.e., low relative humidity compared to Earth) can remain habitable closer to the host star due to the reduce water vapor greenhouse. Leconte et al. (2013); Yang et al. (2013); Wolf & Toon (2014); Yang et al. (2014) and Kopparapu et al. (2016) highlighted the importance of clouds and rotation rate (which strongly affects cloud coverage), pushing the inner edge of the HZ closer to the star than predicted by 1D models (for example, Kopparapu et al., 2013).

1.3 Orbital dynamics

The subject of orbital dynamics is one of the oldest in all of science, arguably extending back to the ancient Greeks and the first attempts to understand the motion of "wanderers"—stars that did not keep their position in the night sky, which we now know to be other planets, orbiting the same sun as ours. Whether you blame Copernicus—who correctly placed the planets on orbits around the sun (Copernicus, 1543)—or Kepler—who described the motion of the planets mathematically (Kepler, 1609, 1619)—or Galileo—who described the relativity of motion (Galilei, 1632, 1710) and made the first observations of the planets with a telescope (Galilei, 1610)—for the birth of a new science devoted to the study of planets, it was Isaac Newton that gave us orbital *dynamics*, with the realization that all objects that have mass also have a gravitational field (Newton, 1687).

Thus the study of "celestial mechanics" was born. For all the accuracy of Kepler's geometric description of orbits, it was missing a key element: gravitational perturbations between planets. Unfortunately, though Kepler provided a solution to the two-body problem (Kepler, 1609, 1619; Murray & Dermott, 1999), a solution to the three- or more-body problem proved much more elusive. Great strides were made, however, using the "disturbing function", which allowed perturbations to be decomposed into sinusoidal variations of increasing order (Le Verrier, 1855). Astronomers spent many decades calculating orbital variations of the solar system planets to ever increasing accuracy (Boquet, 1889; Newcomb, 1895; Brown & Shook, 1933; Brouwer & Clemence, 1961).

The advent of computers provided ultimately the simplest and most robust solution to

the problem. Now, gravitational forces could be resolved individually, step-by-step, for the entire solar system. Models that resolve these forces became known as "N-Body models" (Holmberg, 1941; von Hoerner, 1960; Aarseth, 1963; Applegate et al., 1986; Wisdom & Holman, 1991). Still, analysis using the disturbing function is useful, as I will explain.

There are three solutions to the many-body problem that I will discuss in this thesis: the second-order Laplace-Lagrange solution (Lagrange, 1811; Laplace et al., 1829; Murray & Dermott, 1999), the fourth-order secular disturbing function solution (Murray & Dermott, 1999), and the N-Body solution (Wisdom & Holman, 1991). Both the second-order Laplace-Lagrange solution (LL2) and the fourth-order secular solution (RD4) make use of the disturbing function. This sounds complicated, and in practice it is, but the idea is relatively simple: write down an equation for the gravitational forces (or accelerations) affecting each orbiting body and separate them by whether the force is coming from the host star or another orbiting body. The terms associated with the star give rise to the Kepler solution; the terms associated with the other orbiters constitute the disturbing function (Murray & Dermott, 1999).

One simple way of writing this is in terms of potentials:

$$\ddot{\mathbf{r}}_i = \nabla_i (U_i + \mathcal{R}_i), \tag{1.1}$$

where $\ddot{\mathbf{r}}_i$ represents the acceleration of the ith planet, ∇_i is the gradient operator, U_i is the gravitational potential between the ith planet and the host star, and $\mathcal{R}_i$ is the disturbing function: the gravitational potential between the ith planet and each of the other planets. The exact definition of the disturbing function, for N planets, is

$$\mathcal{R}_i = \sum_{j \neq i}^{N} \left[\frac{G m_j}{|\mathbf{r}_j - \mathbf{r}_i|} - G m_j \frac{\mathbf{r}_i \cdot \mathbf{r}_j}{r_j^3} \right], \tag{1.2}$$

where G is Newton's gravitational constant, m_j is the mass of the jth planet ($j \neq i$), and $\mathbf{r}_i$ and $\mathbf{r}_j$ are the positions of the planets relative to the host star.

As mentioned above, if $\mathcal{R}_i$ is ignored, the problem reduces to a two-body problem, and

the solution (for the position of the planet) is

$$r = \frac{a(1-e^2)}{1+e\cos f}, \tag{1.3}$$

where r is the radial position of the planet, a is the semi-major axis (half the long axis of an ellipse), e is the eccentricity, and f, the "true anomaly", is the angle between the planet's position at some instant and the location of its periastron (the point of closest approach to the host star). This solution gives rise to the six "osculating" orbital elements: a, e, i, ϖ, Ω, and λ. The inclination, i, is simply the angle between the planet's orbital plane and some plane of reference. The longitude of ascending node, Ω, is the "azimuthal" angle at which the planet crosses from below to above this plane of reference . The longitude of periastron, ϖ, is a dog-leg angle, measured from some line of reference to the ascending node, then to periastron ($\varpi = \Omega + \omega$, see Figure 3.1). The last angle, λ, is called the mean longitude, and is related to the planet's angular position, f, but advances linearly in time. This variable does not represent any angle in the system's geometry, and is actually better understood as a variable of time, even though it has units of angle.

To relate the mean longitude to the true anomaly, we must first introduce two new quantities, the mean anomaly, M, and the eccentric anomaly, E. These are related through Kepler's Equation:

$$M = E - e\sin E. \tag{1.4}$$

The eccentric anomaly is the angle of the planet's position (*i.e*, the true anomaly, f) projected onto a circle that is centered on the center of the planet's elliptical orbit (see Figure 1.1). The other parameter, the mean anomaly, has no geometric interpretation. It is, like the mean longitude λ, representative of time, though it has units of angle: when $M = 0°$, the planet is at its pericenter; when $M = 90°$, the planet is one-fourth of the way through its year; when $M = 180°$, the planet is half-way through its year; and so on. The transcendental equation above (1.4) must be solved for E to give the position of the planet, r, as a function of time (notice that Equation 1.3 does *not* contain time as an explicit variable)—a surprising fact that illustrates how difficult it is to solve even the *two*-body problem. Continuing on, the

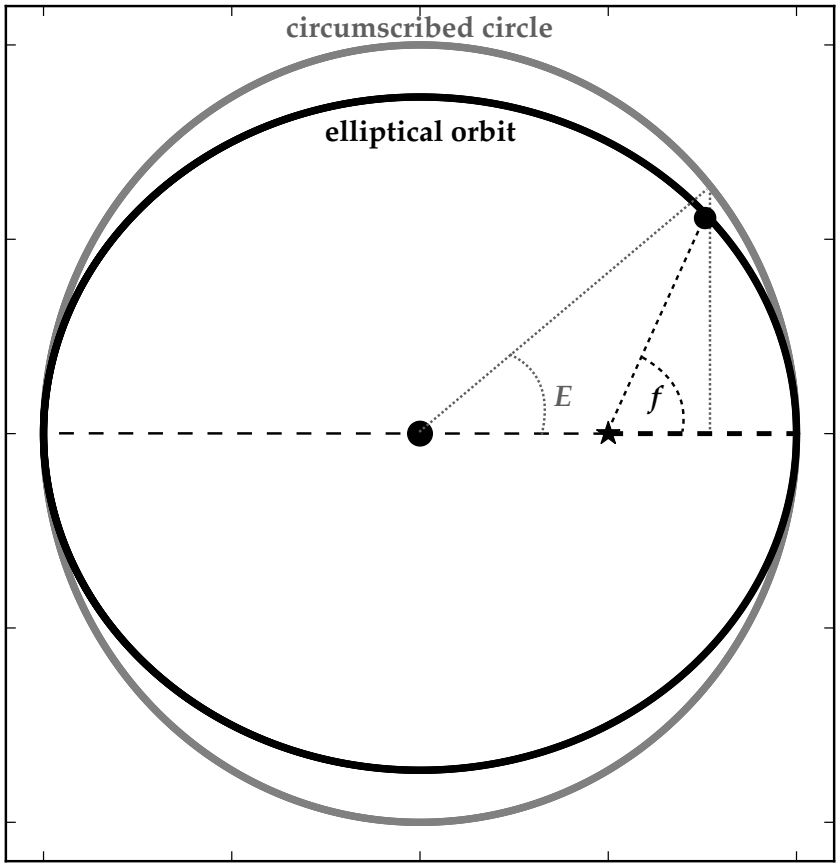

Figure 1.1: Eccentric anomaly, E, and its relationship to the true anomaly, f. The true anomaly is the angular position of the planet with respect to its pericenter. The eccentric anomaly is the projection of this position onto a circumscribed circle, perpendicular to the major axis of the ellipse.

mean anomaly is related to the mean longitude by the definition

$$\lambda \equiv M + \varpi, \tag{1.5}$$

and, finally, the eccentric anomaly is related to the true anomaly by

$$\cos f = \frac{\cos E - e}{1 - e \cos E}. \tag{1.6}$$

In the many-body problem, these six variables (a, e, i, ϖ, Ω, and λ) represent the geometry of the planet's orbit *at a single instance in time*, and vary due to perturbations from the other planets ("osculate" means "to kiss"—the planet "kisses" that orbit at a single moment in time[1]). The disturbing function (Equation 1.2) can be written in terms of the osculating elements by utilizing a series solution to Kepler's equation (Equation 1.4):

$$E = M + 2 \sum_{s=1}^{\infty} \frac{1}{s} J_s(s\,e) \sin s\,M, \tag{1.7}$$

where J_s is a Bessel function of the first kind (Abramowitz & Stegun, 1972). This gives E as a function of M and ultimately allows us to write the positions of the planets ($\mathbf{r}_i$) in terms of λ. After some fairly strenuous algebra, this results in an infinite series for $\mathcal{R}_i$ where a, e, and i appear in the coefficients of cosine terms containing ϖ, Ω, and λ. The series was written out explicitly, to fourth order in all six variables, in Murray & Dermott (1999) and Ellis & Murray (2000). It is this series that I have used in Chapters 3 and 4.

Use of the disturbing function is not simple: it requires taking derivatives of all terms with respect to all six variables and integrating Lagrange's planetary equations (see Chapter 3). If the planetary system being modeled is well away from mean-motion resonances, the averaging principle applies: over the course of many orbits, perturbations from the other planets will tend to occur at random positions in f (or λ), and will thus tend to average out to zero. Hence, the λ dependence in $\mathcal{R}_i$ can be ignored, and the disturbing function is greatly simplified. This is called the "secular" (orbit-averaged) disturbing function. The fourth-order secular disturbing function contains a mere 16 cosine terms (see Section 3.2.2).

[1]Don't expect any romance in this thesis.

Further, the semi-major axis does not change in the secular solution. That, coupled with the elimination of λ, leaves us with four differential equations for e, i, ϖ, and Ω. In Chapter 3, I write out these equations explicitly, with a variable change to eliminate singularities.

The lowest order solution involving the disturbing function is the LL2 solution, and it is an *explicit* solution in time (*i.e.* the orbital elements are given as a simple function of time). Keeping only the second-order secular terms of the disturbing function, and only linear dependence of Lagrange's planetary equations, the problem can be fully linearized. The system of four coupled, linear ODEs can then be solved using eigenvalues (this process is long and involved—I will not reproduce it here, but see Chapter 7 of Murray & Dermott (1999)).

Much work has been done to correct the LL2 solution for near-mean motion resonances[2], such as the "great inequality", a near 5:2 resonance between Jupiter and Saturn (Lovett, 1895; Brouwer & van Woerkom, 1950). Most of the works discussed in Section 1.5 used some combination of techniques involving the disturbing function (LL2 with corrections and higher-order integrations) to determine the insolation history of Earth. I utilize both the LL2 solution and a fourth order solution (which I call RD4[3]).

As I mentioned earlier, computers can provide us with an alternative solution to the many-body problem: the N-Body model. There are a number of techniques used in N-Body models, but all are based on the simple idea of resolving forces between all pairs of bodies in the system in Cartesian coordinates. These models have proven to be much more accurate than the secular solution, though more computationally expensive. In my work, I use a hierarchy of models (LL2, RD4, and N-Body) to explore parameter space, check for accuracy, and gain physical intuition about which objects and frequencies are responsible for certain behaviors. Figure 1.2 shows a comparison of the three orbital solutions, for Earth's

---

[2]A mean-motion resonance occurs when the orbital periods of two objects occur in small integer ratios, *e.g.*, the Neptune orbits the sun three times for every two times Pluto orbits, hence the two bodies are in a 3:2 mean-motion resonance

[3]The letters "RD" refer to the *direct* terms of the disturbing function, $\mathcal{R}$, resulting from the first term on the right-hand side of Equation 1.2. Fortuitously, they are also my initials.

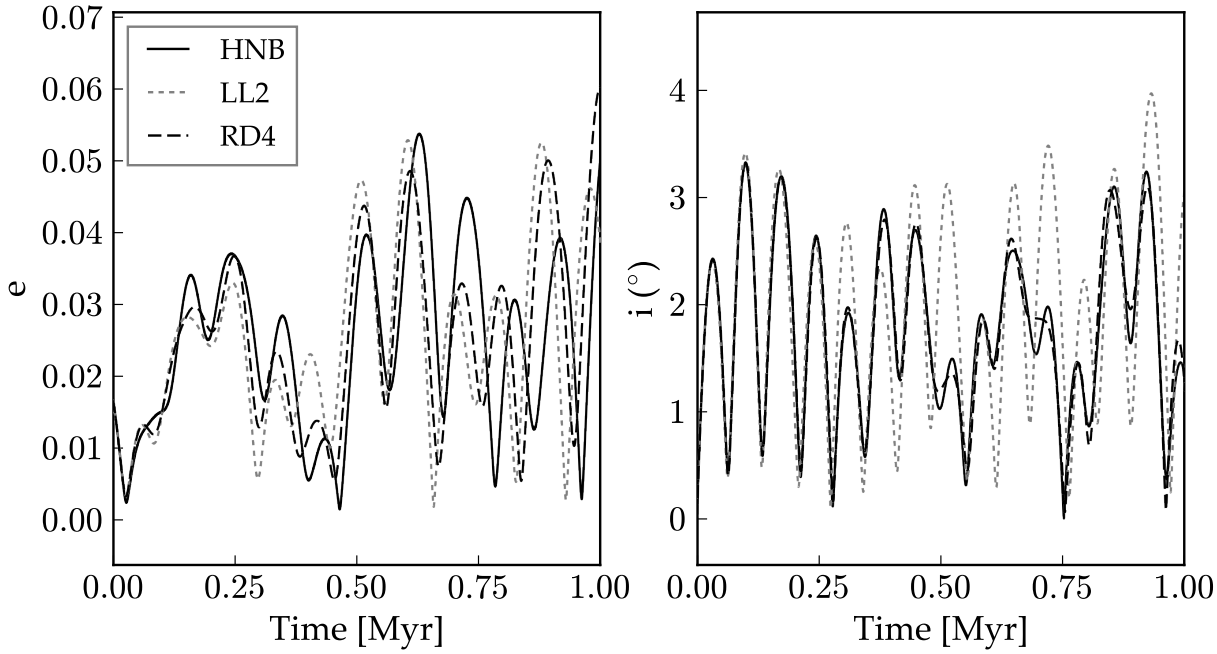

Figure 1.2: Evolution of Earth's eccentricity (left) and inclination (right; relative to the J2000 ecliptic), using three different methods of solving this nine-body problem (eight planets and the sun). The solid black line is the solution from `HNBody`, the gray dotted line is from the Laplace-Lagrange solution (LL2), and the black dashed line is from my 4th-order disturbing function solution (RD4). The `HNBody` solution is the most rigorous of the three solutions; RD4 compares better with the `HNBody` solution than does LL2, especially for the inclination.

eccentricity and inclination over the next Myr. The RD4 scheme does slightly better at approximating the eccentricity evolution than the LL2 solution; it does much better with the inclination (assuming that the N-body method provides the most accurate solution). The N-Body model used here is `HNBody` (Rauch & Hamilton, 2002).

1.4 Obliquity

Obliquity, or axial tilt, is simply the angle between a planet's spin axis and a perpendicular to its orbital plane (see Figure 1.3). This angle is a key player in planetary climate—in fact,

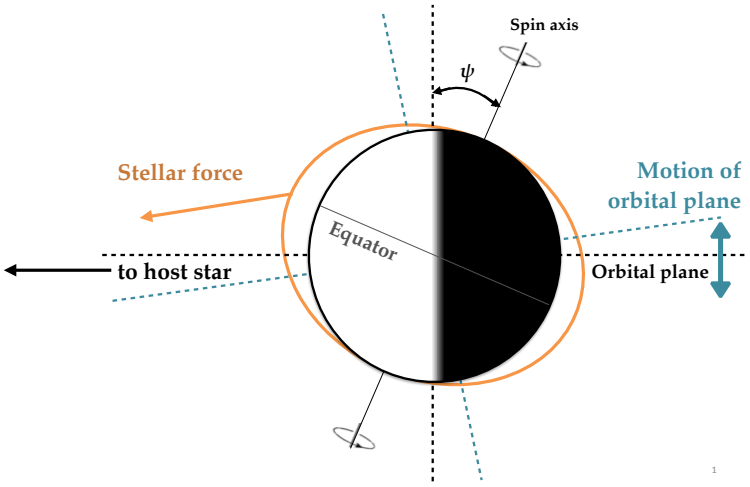

Figure 1.3: Drivers of obliquity. Geometrically, the obliquity, ψ, is the angle between a planet's spin axis and a line perpendicular to its orbital plane. In the Kinoshita model (used in Chapters 3 and 4) obliquity variations can be driven by torques on the equatorial bulge from the host star and large moons, and/or changes in the plane of the planet's orbit (its inclination). The obliquity varies with inclination because as the orbital plane moves, the rotational angular momentum is conserved, so the planet's spin axis remains fixed in absolute space. This directly changes the obliquity angle, ψ, and the spin axis's orientation relative to the ascending node, Ω. The stellar force indicated here causes a torque that is out-of-the-page, which leads to axial precession.

it gives us our seasons here on Earth.

Figure 1.4 illustrates how obliquity controls the seasons. As Earth moves through its orbit, its spin axis remains pointed in the same direction in absolute space. When the south pole is angled slightly toward the sun, the southern hemisphere receives more sunlight than the northern and it is southern summer. Six months later, the south pole is now angled away from the sun, and the southern hemisphere receives less sunlight overall—winter has come.

Of course, the spin axis only appears to remain fixed over short time scales—in reality, it moves, albeit very slowly. There are two essential components to its motion: precession and

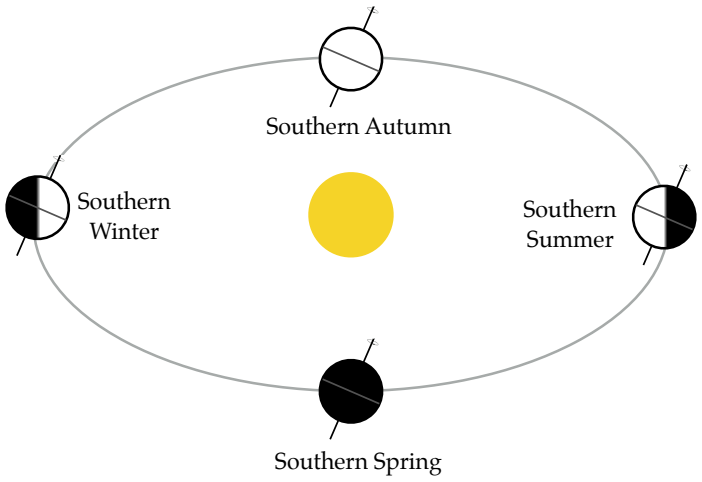

Figure 1.4: The origin of seasons on Earth. Over an orbital time-scale, the spin axis of the planet remains fixed in space. During southern summer (right), the southern hemisphere is angled so that it receives more direct sunlight than the northern. Six months later, the situation is reversed. At the time of the equinoxes (spring and autumn), the hemispheres receive equal amounts of radiation and the equator is at its warmest.

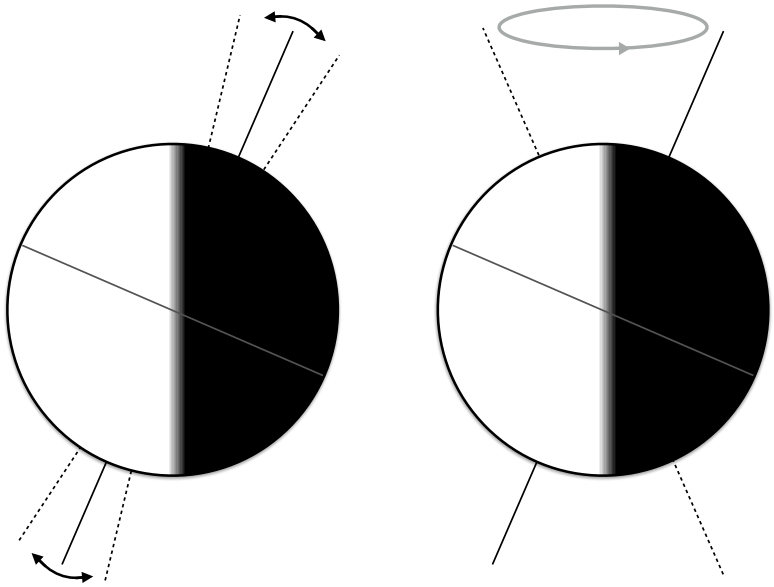

Figure 1.5: The two types of motion of the spin axis in the Kinoshita model. Like the axis of a spinning top, the axis of Earth (or other astronomical body) can "wobble" (nutation; left) and precess in a slow circle (right) in 3-dimensions.

nutation (see Figure 1.5). Precession is the circular motion of the spin axis, moving about some other axis (usually the perpendicular to the orbit), while the obliquity does not change (right panel of Figure 1.5). Nutation is the "wobble"—the direct change in the obliquity angle (left panel).

The spin axis of a planet (or satellite) can move in space as a result of a number of forces: torques on the planet's equatorial bulge, changes in inclination due to gravitational perturbations, tidal forces, and large impactors. The model that I use in this work for obliquity evolution was derived in Kinoshita (1975) and Kinoshita (1977) and has been utilized in Laskar (1986); Laskar et al. (1993a); Armstrong et al. (2004, 2014) and a number of other works (see Chapter 3). This model resolves only torques on the equatorial bulge and variations due to the changes in inclination (refer again to Figure 1.3). This is appropriate

for HZ planets orbiting sun-like stars (*i.e.*, stellar types KGF), which do not experience strong tidal damping. A key component of the Kinoshita model is, for Earth, the lunar torque. For this work, I have not include the effects of large satellites for exoplanets, because the frequency of occurrence of such is not known and because of the difficulties in modeling satellite orbits. This is one area that deserves attention in the future.

1.5 Milankovitch cycles on Earth

The connection between Earth's ice ages and its orbital/obliquity evolution was first suggested by Joseph Alphonse Adhémar in 1842. This theory was continued by James Croll in the second half of the nineteenth century, but it wasn't until the twentieth century, when Milutin Milanković performed the first highly accurate calculations of Earth's insolation history and subsequently collaborated with climate scientist Wladimir Köppen, that the theory achieved much success. Hence the theory became commonly known as "Milankovitch theory" and the insolation variations were dubbed "Milankovitch cycles".

Milanković and Köppen identified what is still believed to be the primary connection between orbital variations and the ice ages: summer-time insolation at high latitude. During summer, if high latitude insolation is strong enough to raise temperatures high enough, for a long enough period of time, to melt all snow and ice, then from year to year, ice sheets on land will shrink. Conversely, if the insolation is weaker and temperatures are cooler in summer, then ice will tend to grow from year to year, leading to larger ice sheets. This summer-time insolation is plotted in Figure 1.6.

After Milanković, calculations of Earth's orbital and insolation history continued to improve (some examples are: Brouwer & van Woerkom, 1950; Sharaf & Boudnikova, 1967; Bretagnon, 1974; Berger, 1978; Berger & Loutre, 1991). The development of the dynamical theory of the Earth-Moon-Sun system by Kinoshita (1975, 1977) facilitated perhaps the most accurate determination of the Earth's orbital and obliquity evolution by Laskar (1986); Laskar et al. (1993a). Let us also not forget the first N-Body integration of the solar system over Myr time scales, presented in Quinn et al. (1991), which showed convincingly that this

kind of numerical integration could provide highly accurate solutions to planetary problems.

How can we know Earth's climate history well enough to compare to its orbital history? A reconstruction of the timeline can be extracted from marine floor sediments (Hays et al., 1976). Ocean life takes up oxygen in the making of calcium carbonate shells. Isotopes of oxygen appear in the ocean in varying abundances, depending on the temperature of the water and on the amount of ice on land, because water bearing the lighter isotopes evaporates preferentially (Emiliani, 1954; Duplessy et al., 1970; Shackleton & Opdyke, 1973). By studying the fractionation of oxygen (specifically, the ^{18}O isotope), in sediment layers, the ocean temperatures and ice sheet volume can be determined.

There are a number of difficulties surrounding this calculation. Chief amongst these is the sedimentation rate, which governs the relationship between time and the thickness of sediment layers. Without knowing the sedimentation rate (and how it varies), it is difficult to determine the exact timing of events in the sediment cores. It is known that continental runoff affects the rate of soil sedimentation and flushes detritus onto the seafloor—for this reason, scientists use cores taken far from land masses to study climate history and its connection to orbital and obliquity variations (Hays et al., 1976). It is not well understood whether the sedimentation rate varies significantly over the time periods involved, but global magnetic pole reversals provide some ground truth (Lisiecki & Raymo, 2007; Lisiecki, 2010). When sediment cores extend deep enough into the rock (and in time), the points of geomagnetic reversal can be seen in ferromagnetic grains within the sediment. Since the ages of these reversals are known through other mechanisms, they provide "control points" to the reconstructed time line of the seafloor core (see Figure 1.6).

The aforementioned study by Hays et al. (1976) was the first to reconstruct the time line of seafloor cores and develop a link between variations in the ^{18}O isotope and the orbital variations. Those authors analyzed the frequencies of the ^{18}O isotope changes and discovered that they match Earth's obliquity, axial precession, and eccentricity frequencies. Hays et al. (1976) was such a successful study that it became common practice to use the orbital and obliquity cycles to set the timeline of cores. In fact, this "orbital tuning" can be seen within

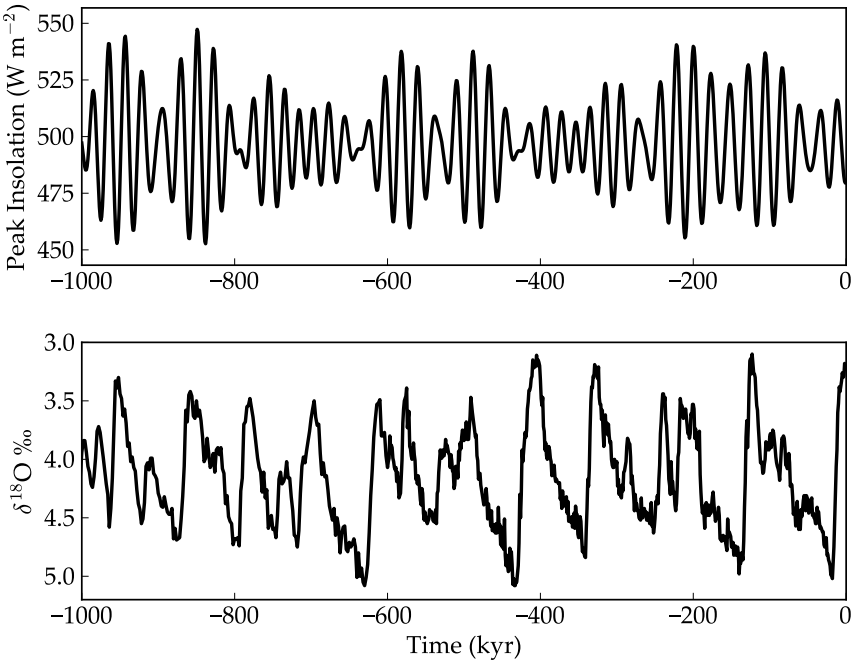

Figure 1.6: The peak summer time insolation at 65° N on Earth over the last million years (top panel) and the $^{1}8$O isotope fractionation in a marine sediment core (lower panel). The insolation was calculated from my orbital and obliquity models. The δ^{18}O signature is from the LR05 stack (Lisiecki & Raymo, 2005). The y-axis is inverted so that cold periods appear as troughs and warm periods as peaks.

the Hays et al. (1976) study itself—in the data these authors used, there appears to be a break in continuity in the rock samples. Assuming that some event must have offset the rock layering in some way, the authors of that study merely shifted the data in time so that it lined up nicely with the orbital data.

Despite these difficulties, further rock samples from the sea floor have been taken, with varying assumptions to try to eliminate bias due to orbital tuning (Lisiecki, 2010). These paint a story more-or-less consistent with the Hays et al. (1976) study—the changes in the ^{18}O isotope in seafloor cores follow the changes in Earth's orbit and obliquity.

At the same time, climate models of varying degrees of complexity respond to the insola-

tion variations determined by astronomers (Huybers & Tziperman, 2008; Abe-Ouchi et al., 2013), growing and melting ice sheets at the expected times, despite the relatively small amplitudes of those variations. How this climate response happens remains somewhat of a mystery, in part because the eccentricity and obliquity variations of Earth are very small. Several theories have proven tentatively successful at explaining this apparent discrepancy (Short et al., 1991; Clemens & Tiedemann, 1997; Clark & Pollard, 1998; Roe, 2006; Tziperman et al., 2006; Huybers & Tziperman, 2008), but others have argued that such climate cycles would appear in the absence of such astronomical variations (see Wunsch, 2004).

Do Milankovitch cycles affect habitability? We know that, certainly, during ice ages the surface of Earth was less hospitable to multi-celled lifeforms like animals and plants—the surface was colder and drier, on average. The surface did, however, remain habitable during these times, in the sense that liquid water was always available somewhere on the surface of the planet. Compared to the snowball states of the much more distant past (Harland, 1964; Kirschvink, 1992), the Pliocene and Pleistocene ice ages were rather mild. To understand how Milankovitch cycles are likely to affect habitability more broadly (for exoplanets, that is), we must consider the very different orbital and rotation states that exoplanets are likely to have.

1.6 Exo-Milankovitch cycles

The importance of the Moon on Earth's obliquity was pointed out by Ward (1974), in a study of the insolation history and climate change on Mars. Laskar et al. (1993a,b) showed that, without the Moon, Earth's obliquity would indeed oscillate by a much larger amount ($\sim 20^\circ$ over ~ 1 Myr, rather than $\sim 2.5^\circ$ *with* the Moon). As the small oscillation Earth experiences over ~ 40 kyr seems to influence the ice ages, it was logical to expect that this much larger oscillation would be catastrophic.

There is a surprisingly long history of the modeling of Earth with high obliquity (Hunt, 1982; Williams, 1988; Oglesby & Ogg, 2000; Chandler & Sohl, 2000; Jenkins, 2000). These studies all used 3D GCMs with various goals in mind. Some, like Oglesby & Ogg (2000) and

Jenkins (2000), found that high obliquity Earth could form permanent ice at the equator ("ice-belts"), but the planet remained habitable in all cases.

A very influential study, that explored a range of obliquities and included carbon cycling, was Williams & Kasting (1997). These authors used a 1D EBM with a parameterized carbon cycle to account for effects obliquity can have on weathering rates and thus changes in atmospheric CO_2 pressures. This paper did not attempt to define the limits of the HZ; rather, it directly addressed the problem that was proposed by Laskar et al. (1993b), that Earth might be uninhabitable without the Moon to stabilize its obliquity. Williams & Kasting (1997) concluded that the Earth could remain habitable with a wide range of obliquities ($23.5° - 90°$), but suggested that large regions at the poles would be frozen for extended periods of time at obliquity $= 90°$.

Further studies have since investigated the effects of obliquity on climate, using 1D EBMs and 3D GCMs (Williams & Pollard, 2003; Spiegel et al., 2009; Ferreira et al., 2014; Rose et al., 2017). The general trends suggest that high obliquity tends to slightly extend the HZ for Earth-like planets by inhibiting permanent glaciation, and that such planets may form "ice-belts" (*i.e.*, year-round ice sheets and/or sea ice at the equator, rather than at the poles), though ice-belts are much more prone to instability—complete loss of ice or planet-wide glaciation—than ice caps.

A number of studies have separately investigated the effects of eccentricity (Williams & Pollard, 2002; Dressing et al., 2010; Bolmont et al., 2016). It was initially feared that planets with eccentricities $\gtrsim 0.3$ would pass beyond the boundaries of the HZ and thus become uninhabitable—such fears are based on the misconception that the HZ is truly a circular annulus, as it is often depicted in press releases, rather than a range of stellar fluxes. The reality is that eccentricity *does* affect habitability, but the story is much more complicated.

Figure 1.7 shows an orbit with $e = 0.3$. At periastron, ϖ, the planet is closest to the host star, but because of Kepler's second law (which represents conservation of angular momentum), the planet is also moving fastest. Comparing an elliptical orbit to a circular one, the planet receives more sunlight at periastron on the eccentric orbit, but it spends

more time at apastron ($\varpi + 180°$). Intuitively, the effects might seem to cancel out, so that a planet with an eccentric orbit receives about the same amount of stellar energy as one on a circular orbit, but this is not the case.

Laskar et al. (1993a) demonstrates how this arises. If one considers the daily mean insolation received by the planet,

$$W_{dm} = \frac{S_\star}{4\rho^2}, \tag{1.8}$$

where $S_\star$ is the solar/stellar constant in W m^{-2} and ρ is the distance between the planet and host star (averaged over the planet's day and divided by the semi-major axis, so that $\rho = r/a$), then one can derive the average annual insolation by the integral

$$W_{am} = \frac{1}{2\pi}\int_0^{2\pi} W_{dm} dM, \tag{1.9}$$

where M is the mean anomaly (see Section 1.3). Performing the integral requires a form of Kepler's second law relating the true anomaly, f, to M:

$$\frac{df}{dM} = \frac{1}{\rho^2}\sqrt{1-e^2}. \tag{1.10}$$

If we substitute Equation (1.8) and the above equation into our integral, we have:

$$W_{am} = \frac{1}{2\pi}\int_0^{2\pi} \frac{S_\star}{4\rho^2}\frac{\rho^2}{\sqrt{1-e^2}} df. \tag{1.11}$$

The ρ^2 cancels and the integral is then trivial to perform. The result is then

$$W_{am} = \frac{S_\star}{4}(1-e^2)^{-1/2}. \tag{1.12}$$

Equation (1.12) shows us that the total annual insolation *increases* with eccentricity. Apparently, the added sunlight received at periastron more than compensates for the decreased sunlight *and* the additional time spent at apoastron. Eccentric orbiters receive more energy over the year than circular ones.

This picture is further complicated by seasonality. Even though, on average, an eccentric planet might receive the right amount of energy to be habitable, it may get so hot at periastron that a moist or runaway greenhouse is triggered, and it may get so cold at apoastron

that a snowball state is triggered. Though concerns remain, initial results seem to indicate that the moist and runaway greenhouse effects are not an issue (Williams & Pollard, 2002; Bolmont et al., 2016). There is however, the possibility of entering snowball states at $e \gtrsim 0.6$ at apoastron, if the planet's orbital period is sufficiently long, as it is for F and G star planets (Bolmont et al., 2016).

A handful of studies have investigated orbital and obliquity variations for exoplanets ("Exo-Milankovitch" cycles) with climate models of varying complexity (Spiegel et al., 2010; Armstrong et al., 2014; Forgan, 2016; Way & Georgakarakos, 2017). There are several shortcomings of each of these studies. Spiegel et al. (2010) did not model the obliquity variations of their test planet (just the eccentricity variations), their climate model did not include ice sheets, and they averaged the properties of land and ocean rather than treating them as separate components. Thus, that study achieved a qualitative picture of the behavior of climate under eccentricity variations, but did not fold in the additional complications of a changing obliquity or the thermal inertia of ice sheets and ocean. Armstrong et al. (2014) included obliquity variations, but the climate model was, for several reasons, extremely insensitive to snowball states. I discuss this in more detail in Chapter 4. Forgan (2016) only looked at orbital variations of circumbinary planets and the climate model used had the same flaws as that of Spiegel et al. (2010). The last study, Way & Georgakarakos (2017), was the most robust of the lot, however, because the authors used a full, computationally intensive 3D GCM, only a handful of orbital configurations could be explored. My work in Chapters 3 and 4 builds upon these works and clarifies many of the ideas contained in them. It is more comprehensive than those previous works because I include the effects of obliquity variations, ice sheets, and oceans, and because the model is computationally inexpensive, I am able to explore a broad range of initial conditions.

1.7 Outline of this Thesis

In Chapter 2, I discuss my work on the orbital dynamics and stability of the multi-jovian system υ Andromedae. This system became famous as the first multi-planet system detected

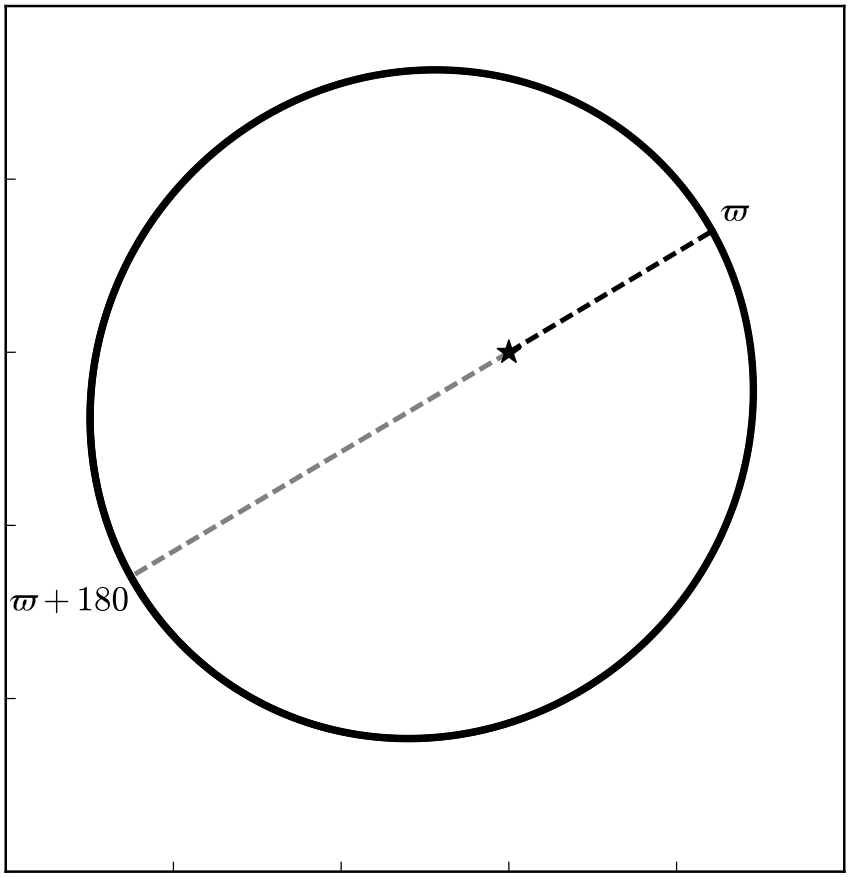

Figure 1.7: A planetary orbit with an eccentricity of 0.3. The planet is closest to the host star at periastron ϖ and furthest from the host star at apoastron $\varpi + 180$. Kepler's 2nd law says, rather esoterically, that a chord drawn between the planet and star sweeps out equal areas in two equal intervals of time. The consequence of this is that the planet moves faster at periastron and slower at apoastron, a conclusion that can also be reached through conservation of angular momentum.

around a main sequence star (Butler et al., 1999), and is still noteworthy as the only system with astrometric detections of multiple planets. In my study, I ran a number of N-Body simulations based on the observations to try and constrain the mass and inclination of the inner-most planet, which is too close to the host star to have a detectable astrometric signal. Because of the high eccentricities, masses, and mutual inclinations, the system appears to be perched on the edge of instability—perhaps because of a recent scattering event (Barnes et al., 2011). By requiring that the system must be stable over 100 Myr, I found that there is a small region of parameter space in which the orbital plane of planet b must lie. This, in turn, provides a constraint on planet b's mass. Though this system almost certainly contains no habitable planet (or moon), there are a number of important lessons learned from it. First, planetary systems can be highly-inclined and eccentric. If terrestrial planets exist in similar systems, the resulting variations in eccentricity and obliquity of those planets will likely be very large. Second, astrometry provides a powerful tool to understand planetary systems and υ And provides a roadmap for current and future astrometry missions.

Chapter 3 covers the development of an extremely quick orbital model and the application of this model to several test systems. I coupled the Kinoshita obliquity model directly to the orbital model. With these tools, I was able to identify several phenomena which have implications for habitability. First, secular spin-orbit resonance, in which the planet's axial precession frequency matches that of its orbital evolution. This type of resonance can be low-order, depending only on the semi-major axis and rotation rate, or higher-order, depending also on the eccentricity and inclination. The second phenomenon I studied was that of Cassini states, in which the obliquity of the planet remains fixed at some non-zero value, because of a combination of perturbative forces and some kind of dissipation.

In Chapter 4, I apply a simple climate model with ice sheets to a number of the cases in Chapter 3. The ice sheets couple directly to the large obliquity and eccentricity variations, resulting in severe ice ages. I found that exo-Milankovitch cycles often trigger the snowball instability on planets that would have stable ice caps with a static orbit. This is a result of the changing obliquity, which causes the latitude of the ice edge to become unstable, and

the changing eccentricity, which alters the total amount of stellar flux the planet receives. I apply an analytical theory for the ice stability, finding that this explains the climate behavior nicely in some cases, but less so in others. I also demonstrate how the ice sheets introduce hysteresis in the climate system because of their thermal inertia—a fact that makes the planets more susceptible to the snowball instability.

Finally, in Chapter 5, I summarize my work thus far, place it into broader context, and discuss open questions and future work on this subject.

Chapter 2

THE 3-DIMENSIONAL ARCHITECTURE OF THE υ ANDROMEDAE PLANETARY SYSTEM

The υ Andromedae system is the first non-transiting exoplanetary system to have the relative inclination of two planets' orbital planes directly measured, and therefore offers our first window into the 3-dimensional configurations of other planetary systems. I present, for the first time, full 3-dimensional, dynamically stable configurations for the 3 planets of the system consistent with all observational constraints. While the outer 2 planets, c and d, are inclined by $\sim 30°$, the inner planet's orbital plane has not been detected. We use N-body simulations to search for stable 3-planet configurations that are consistent with the combined radial velocity and astrometric solution. We find that only 10 trials out of 1000 are robustly stable on 100 Myr timescales, or $\sim$ 8 billion orbits of planet b. Planet b's orbit must lie near the invariable plane of planets c and d, but can be either prograde or retrograde. These solutions predict b's mass is in the range 2 - 9 M_{Jup} and has an inclination angle from the sky plane of less than 25°. Combined with brightness variations in the combined star/planet light curve ("phase curve"), our results imply that planet b's radius is $\sim 1.8\ R_{Jup}$, relatively large for a planet of its age. However, the eccentricity of b in several of our stable solutions reaches > 0.1, generating upwards of 10^{19} watts in the interior of the planet via tidal dissipation, possibly inflating the radius to an amount consistent with phase curve observations.

Material in this chapter was previously published with co-authors Rory Barnes, Barbara McArthur, Thomas R. Quinn, Rodrigo Luger, Adrienne Antonsen, and G. Fritz Benedict in the Astrophysical Journal (Deitrick et al., 2015).

2.1 Introduction

2.1.1 Observations

The υ Andromedae (υ And) planetary system was the first discovered multi-exoplanet system around a main sequence star and is still one of the most studied multi-planet systems. υ And b was discovered using the radial velocity (RV) technique by Butler et al. (1997) at Lick observatory. Two years later, combined data from Lick and the Advanced Fiber-Optic Echelle spectrometer (AFOE) at Whipple Observatory revealed the presence of two additional planets, υ And c and d (Butler et al., 1999). Follow-up by François et al. (1999) confirmed that the existence of planets was the best explanation for the RV variations. Even at the time of Butler et al. (1999), the semi-major axes of the planets (0.059, 0.83, and 2.5 au), the minimum masses (0.71, 2.11, and 4.61 M_{Jup}), and eccentricities (0.034, 0.18, and 0.41) made it clear that this system was very unlike our solar system, and it has presented a challenge to planet formation models that explain the solar system. Stepinski et al. (2000) confirmed the presence of these three RV signatures in the existing data using two different fitting algorithms, but stressed that the eccentricity of planet c was poorly constrained by the existing data.

Thus far, astrometry is one of the few techniques that can be used to break the $m \sin i$ degeneracy in the RV method for non-transiting planets (the other is a relatively new technique that uses high-resolution spectra to directly observe the radial velocity of the planet; for example, see Brogi et al., 2012; Rodler et al., 2012). Astrometry is the process of measuring a star's movement on the plane of the sky, and hence provides 2-dimensional information that is orthogonal to RV. Because this measurement is made relative to other objects in the sky, it is extremely difficult to obtain the high precision necessary to detect planets. For small, close-in planets, the necessary precision is in the micro-arcsecond (μas) range (Quirrenbach, 2010), since astrometry is more sensitive to planets with relatively large mass, low inclination and large semi-major axis. Nonetheless, Mazeh et al. (1999) reported a small, positive detection in the *Hipparcos* (HIP) data of an astrometric signal at the period of planet

d, and derived an inclination of 156° and a mass of 10.1 M_{Jup}. However, Pourbaix (2001) demonstrated that astrometric fits to the HIP data for 42 stars, including υ And, were not significantly improved by the inclusion of a planetary orbit, and that the inclinations for planets c and d could be statistically rejected. Reffert & Quirrenbach (2011) re-analyzed the HIP data and placed an upper mass limit on both planets c and d of $8.3M_{Jup}$ and $14.2M_{Jup}$, but did not claim true masses.

υ And became the first multi-planet system to have a positive astrometry detection above 3σ when McArthur et al. (2010) detected the orbits of planets c and d using *Hubble Space Telescope* (*HST*). Their orbital fit included all previously obtained RVs (including re-reduced Lick data), and added RVs from the Hobby-Eberly Telescope at McDonald Observatory. The combined astrometry+RV fit did not converge when planet b was included, indicating that planet b presents no astrometric signal. Indeed, using their Equation 8, which relates the RV and astrometry, planet b would be expected to have a signal of $\alpha \sim 40$ μas at an inclination of $\sim 3°$, well below *HST*'s detection limit of 0.25 mas. This non-detection puts a weak upper mass limit on planet b of $\sim\ 78M_{Jup}$, as the planet would be astrometrically detectable by *HST* at inclinations below $\sim 0.5°$.

McArthur et al. (2010) reported that planets c and d have inclinations of $7.868° \pm 1.003°$ and $23.758° \pm 1.316°$, respectively, relative to the plane of the sky, with corresponding masses of $14.0^{+2.3}_{-5.3}M_{Jup}$ and $10.3^{+0.7}_{-3.3}M_{Jup}$. The mutual inclination between the two planets is $29.9° \pm 1°$. This value is quite unlike any mutual inclination found amongst the planets of our solar system. Subsequent dynamical studies suggest that this may be the result of a three-body planet-planet scattering scenario in which one planet is ejected from the system (Barnes et al., 2011; Libert & Tsiganis, 2011).

By looking at the infrared excess in the stellar spectrum attributed to planet b, Harrington et al. (2006) attempted to chart the phase offset, *i.e.*, the angle between the hottest point on the surface and the sub-stellar point. Assuming a radius of < 1.4 R_{Jup}, the observed amplitude of flux variation demanded that the planet's inclination must be $> 30°$ from the plane of the sky. Unfortunately, this study was based on only five epochs of data over a

single orbit, and thus does not provide tight constraints. The infrared phase curve of υ And b was revisited with seven additional short epochs and one continuous $\sim$ 28 hour observation by Crossfield et al. (2010). The picture presented in Crossfield et al. (2010) was consistent with Harrington et al. (2006), but they allowed larger radii in their model, finding that the inclination must be $> 28°$ for a 1.3 R_{Jup} planet and $> 14°$ for a 1.8 R_{Jup}.

There is marginal evidence for a fourth planet orbiting υ And. McArthur et al. (2010) found an improvement in their fit when a linear trend indicative of a longer period planet was included. Later, Curiel et al. (2011) found a signal at 3848.9 days using the Lick (Fischer et al., 2003; Wright et al., 2009) and ELODIE radial velocities (Naef et al., 2004). These authors have taken this to be a fourth planet in the system, as suggested by McArthur et al. (2010). The McArthur et al. (2010) analysis used re-reduced Lick data (received by personal communication from Debra Fischer) for their combined RV and astrometry orbital fit. As explained in McArthur et al. (2014), these data include updated γ values (constant velocity offsets in the RVs) that removed this signal from the Lick data. Later, Tuomi et al. (2011) analyzed the older published RV data sets (Fischer et al., 2003; Wright et al., 2009) and also found a period for this fourth planet (that was an artifact of the missing γ) of 2860 days, but noted that the data sets seemed inconsistent. Tuomi et al. (2011) performed fits and calculated the Bayesian inadequacy criterion for the individual data sets. They found that the Wright et al. (2009) Lick data produced a significantly different period for "planet e" (3860 days) and the Bayesian inadequacy criterion indicates that this data set has a > 0.999 probability of being inconsistent with the other data sets. While a longer period planet, indicated by a small slope in the radial velocities, may exist in this system, the 4th planet signal reported by Curiel et al. (2011) was a product of the earlier reduction of the Lick data, which did not account for an instrument systematic that caused a shift in the values of γ. For this reason, we do not include this planet in our study.

The rotation and obliquity of υ And A are also of interest in this study (see section 2.3.1). Measurements of $v \sin i = 9.6 \pm 0.5$ km s^{-1} (Valenti & Fischer, 2005) and stellar radius $R_\star = 1.64^{+0.04}_{-0.05}$ $R_\odot$ (Takeda et al., 2007) limit the rotation period to be $\lesssim$ 8 days

for physical values of i, however the only measured period consistent with these data is 7.3 days (Simpson et al., 2010). This period suggests an obliquity $i \sim 60°$ (measured from the sky plane), but the signal at this period is very weak and it is impossible to distinguish this obliquity from $i \sim 120°$ (spinning in the opposite sense).

2.1.2 Theory

Numerous dynamical studies of υ Andromedae have been performed, both numerical and analytical. Early studies focused on the stability of the system using N-body models and analytic theory, prior to the astrometric detection of planets c and d (McArthur et al., 2010). These studies showed that the stability of the system is highly sensitive to the eccentricities of the planets (d in particular) (Laughlin & Adams, 1999; Barnes & Quinn, 2001, 2004), the relative inclinations of the planets (Rivera & Lissauer, 2000; Stepinski et al., 2000; Chiang et al., 2001; Lissauer & Rivera, 2001; Ford et al., 2005; Michtchenko et al., 2006), their true masses (since only minimum masses were known prior to McArthur et al., 2010) (Rivera & Lissauer, 2000; Stepinski et al., 2000; Ito & Miyama, 2001), the effect of general relativity on planet b's eccentricity (Nagasawa & Lin, 2005; Adams & Laughlin, 2006; Migaszewski & Goździewski, 2009), and the accuracy of the RV data (Lissauer, 1999; Stepinski et al., 2000; Goździewski et al., 2001), and also found that there were stable regions only between planets b and c and exterior to planet d (Rivera & Lissauer, 2000; Lissauer & Rivera, 2001; Barnes & Raymond, 2004; Rivera & Haghighipour, 2007). The dynamical study of McArthur et al. (2010) found stable configurations for all three planets on a timescale of 10^5 years, and constrained the inclination of planet b to $i < 60°$ or $i > 135°$. It has also been demonstrated that analytical or semi-analytical theory does not adequately describe the dynamics of the system (Veras & Armitage, 2007), unless taken to very high order in the eccentricities (Libert & Henrard, 2007), though these studies assumed coplanarity since the inclinations of the planets were not known at the time.

Other studies dealt with the evolution and formation of certain features of the system, in particular the apparent alignment of the pericenters (or "apsidal alignment", $\Delta\varpi$, noted

by Rivera & Lissauer (2000); Chiang et al. (2001)) and large eccentricities of planets c and d. Some have investigated whether the present day system could have been produced by interactions with a dissipating disk (Chiang & Murray, 2002; Nagasawa et al., 2003), by planet-planet scattering (Nagasawa et al., 2003; Ford et al., 2005; Barnes & Greenberg, 2007a; Ford & Rasio, 2008; Barnes et al., 2011), by interactions with the stellar companion, υ And B (Barnes et al., 2011), by secular or resonant orbital evolution (Jiang & Ip, 2001; Malhotra, 2002; Ford & Rasio, 2008; Libert & Tsiganis, 2011), or by accelerations acting on the host star (Namouni, 2005). Michtchenko & Malhotra (2004) found that $\Delta\varpi$ can be in a state of circulation, libration or a "non-linear secular resonance", all within the observational uncertainty. In short, the dynamical evolution of the system appears to be highly sensitive to the initial conditions, and planet-planet scattering appears to be the most promising explanation for its current state.

In particular, McArthur et al. (2010) noted that the true masses of planets c and d naturally resolve a difficulty in explaining the system's formation. When only the minimum masses of the two planets were known, it was generally assumed in dynamical analysis that planet d was the larger ($m \sin i_c = 1.8898\ M_{Jup}$ and $m \sin i_d = 4.1754\ M_{Jup}$), however, mechanisms that can excite the eccentricities of the planets, such as resonance crossing (Chiang et al., 2002) or close encounters (Ford et al., 2001), tend to result in the smaller mass planet having the larger eccentricity. Some authors noted that because planet d is observed to have the larger eccentricity ($e_c = 0.245 \pm 0.006, e_d = 0.316 \pm 0.006$ (McArthur et al., 2010)), the formation of the system may have required the presence of a gas disk or the ejection of an additional low-mass planet (Chiang et al., 2002; Rivera & Lissauer, 2000; Ford et al., 2005; Barnes & Greenberg, 2007b).

Finally, Burrows et al. (2008) produced theoretical pressure-temperature profiles and spectra for several close-in giant planets, including υ And b, and compared these results with the phase curve in Harrington et al. (2006). Unfortunately, the phase curve data were too sparse to make any conclusions about the size or structure of the atmosphere or the planet's inclination, only that a range of radii and inclinations is consistent with the data,

and that a temperature inversion in the atmosphere is also consistent. The authors suggested that more frequent observations and multi-wavelength data may break the degeneracies in their model.

2.1.3 This Work

Observations account for the inclinations and true masses of planets c and d, but the inclination and true mass of planet b remain undetermined. Early dynamical studies found stable regions of parameter space for the coplanar, three planet system, however, stable configurations have not previously been identified for three planets over long timescales since the large mutual inclination between planets c and d was discovered by astrometry. Additionally, it is unclear whether the phase curve observations (Harrington et al., 2006; Crossfield et al., 2010) are consistent with the RV+astrometry observations (McArthur et al., 2010). Here we explore all the above issues using dynamical models.

This work is a sweep through parameter space for stable configurations for all three planets, following up on the dynamical analysis in McArthur et al. (2010). An acceptable configuration in this study is one that 1) satisfies the RV+astrometry fit (McArthur et al., 2010), 2) is dynamically stable, and 3) is consistent with the IR phase curve measurements (Crossfield et al., 2010). Our results satisfy all three criteria, however, reconciliation with the phase curve measurements requires planet b to have an inflated radius and motivates us to include tidal heating in this study.

Section 2.2 describes the methods that we use to explore parameter space, model the dynamics, and estimate tidal heating in planet b. Section 2.3 describes the results we obtain for stability and system evolution. Section 2.4 focuses on tidal heating and reconciliation with Crossfield et al. (2010). In Section 2.5, we discuss our results in the context if previous studies, and summarize our conclusions in Section 2.6.

2.2 Methods

2.2.1 Updated Orbits and Parameter Space

As in McArthur et al. (2010), all RV data sets are re-examined using the published errors (which are large for the AFOE data, in particular). The Lick data set has been re-reduced since the original publications, resulting in new γ offsets. This updated set, published recently in Fischer et al. (2014), was used in McArthur et al. (2010) (received by personal correspondance with D. Fischer), and similarly we use it here. The RV fit is performed on each data set individually and compared with the other data sets for consistency, and large outliers are examined and removed, when necessary.

Trials are generated by drawing randomly from within the uncertainties of the χ^2 best fit to the RV and astrometric data. Table 2.1 shows the parameter space explored. The astrometric constraints on the semi-major axes of planets c and d are ignored as the RV derived periods provide much stricter constraints on these quantities. Trials are not generated taking into account interdependencies of the various parameters, however, because of the small size of the uncertainties all trials should be faithful to the data. Nevertheless, we include χ^2 values for our stable cases to confirm consistency. This work is not meant to represent a complete analysis of all possible configurations. We are merely establishing the existence of stable cases within the observational constraints.

The nominal eccentricity of planet d is 0.316, however, we find that very few trials are stable above $e_d \sim 0.3$ (see Figure 2.2), so we apply a much looser constraint to the lower bound of planet d's eccentricity, drawing from a uniform distribution across the domain $0.246 < e_d < 0.322$, rather than a Gaussian distribution.

2.2.2 N-Body

For the stability analysis, we use `HNBody` (Rauch & Hamilton, 2002), which contains a symplectic integrator for central-body-like systems, i.e., systems in which the total mass is dominated by a single object. This symplectic scheme alternates between Keplerian motion and

Table 2.1: **Parameter space:** parameters are drawn from Gaussian distribution with center (standard deviation) except where noted.

	υ And b	υ And c	υ And d
e	0.01186 (0.006)	0.2445 (0.1)	0.316 (0.07/0.006)*
i (°)	90 (90)†	11.347 (3.0)	25.609 (3.0)
ω (°)	44.519 (24.0)	247.629 (2.2)	252.991 (1.32)
Ω (°)	180 (180)†	248.181 (8.5)	11.425 (3.31)
P (days)	4.61711 (0.00018)	240.937 (0.06)	1281.439 (2.0)
T (days)	2450034.058 (0.3)	2449922.548 (1.5)	2450059.072 (4.32)
K (m/s)	70.519 (0.368)	53.4980 (0.55)	67.70 (0.55)

*drawn from a uniform distribution with lower/upper bounds shown

†uniform distribution

Newtonian perturbations at each timestep (see Wisdom & Holman, 1991). During one half-step (the "kick" step), all gravitational interactions are calculated and the momenta are updated accordingly. During the other half-step (the "drift" step), the system is advanced along Keplerian (2-body) motion, using Gauss's f and g equations (see Danby, 1988). The entire integration is done in Cartesian coordinates. Unlike `Mercury` (Chambers, 1999), post-Newtonian (general relativisitic) corrections are included as an optional parameter in `HNBody`, and we utilize them here.

While `HNBody` is fast and its results compare well with results from `Mercury`, its definitions of the osculating elements used at input and output differ slightly from `Mercury`'s. The mass factor used in the definitions of semi-major axis and eccentricity (for astrocentric or barycentric elements) does not include the planet's mass; in other words, the planet is treated as a zero mass particle during input and output conversions between Cartesian coordinates and osculating elements. Because of this choice, the use of osculating elements during input can result in incorrect periods and Cartesian velocities. For most planetary systems, which have poorer constraints on the periods and semi-major axes of the planets, this aspect makes little difference, but for υ Andromedae the periods are known with the high precision that comes with > 15 years of RVs, and so all of our input and output from `HNBody` is done in Cartesian positions and velocities, to ensure proper orbital frequencies.

A second important conversion must be done to account for a difference in units. `HNBody` and `Mercury` enforce the relationship $GM_{\odot}D^2/au^3 = k^2$, where k is the Gaussian gravitational constant (defined to be 0.01720209895 $\mathrm{au}^{3/2}$ $M_{\odot}^{-1/2}$ D^{-1}), D is the length of the day, and au is the astronomical unit, based on the IAU defitions prior to 2012. The current accepted IAU units fix the au to be exactly 149,597,870,700 m and the constant k is no longer taken to be a constant value. This redefinition was done for ease of use and to allow for reconciliation with the length-contraction and time-dilation of Einstein's relativity. Because these N-body models were developed prior to this redefinition, k was used as a fundamental constant, as that allowed for better accuracy in Solar System integrations when the au was uncertain. We believe these integrators still accurately represent the dynamics of

planetary systems, since these models do not attempt to account for length-contraction and time-dilation and in any case these effects will be very small. Note that `HNBody` does account for relativistic precession, which is important for the motion of planet b, as mentioned in Section 2.1.2.

The units utilized by the integrator are then au, days, and solar masses. For observations of exoplanets, SI units are more sensible, but the values of G, $M_\odot$, and au need not obey the above constraint. Hence the simulated orbital periods will not be equal to the measured orbital periods unless we first convert from SI units, which do not obey this constraint, to IAU units, which do. We accomplish this by choosing a value for the au which satisfies $GM_\odot D^2/au^3 = k^2$, given the G, $M_\odot$, and D used in the model of the observations. We then check that this definition of the au correctly reproduces the orbital periods of the planets when calculated using k and Kepler's third law,

$$T^2 = \frac{4\pi^2}{k^2(M_\star + m_p)} a^3, \tag{2.1}$$

where T is the planet's period in days, $M_\star$ and m_p are the masses of the star and planet in solar masses, and a is the planet's semi-major axis in au. Finally, to verify that `HNBody` "sees" the correct periods, we run 2-body integrations for each planet at high time resolution and performed fast-Fourier transforms (FFTs) on the planets' velocities, confirming that this approach is the most accurate.

For the reasons described above, we take the orbital elements from the RV+astrometry, convert to Cartesian coordinates for dynamical modelling, then convert back to orbital elements for stability analysis. For analysis of the orbital evolution, we convert from Cartesian "line-of-sight" coordinates to Cartesian invariable plane (the plane perpendicular to the total angular momentum of the system) coordinates prior to the conversion back to orbital elements. The invariable plane of the system is inclined by $\sim 15^\circ$ from the sky, so inclinations measured from this plane are similar to those measured from the sky-plane. See the next section for a potential pitfall in modelling astrometrically measured orbits.

The initial parameter space includes inclinations of planet b from 0° to 180°, which is

to say that any inclination is consistent with the observations. Extremely low inclination, $i_b < 1^\circ$ or $i_b > 179^\circ$, places the mass of planet b in the brown dwarf range. Inclinations $\gtrsim 90^\circ$ are retrograde orbits with respect to the orbits of the outer two planets (note that the outer system's invariable plane is inclined only $\sim 10^\circ$ from the sky plane). The observations allow for such configurations, and we cannot rule them out based on dynamical stability.

2.2.3 Comment About Coordinates

There is a difference in the conventions used by dynamicists and observers to relate the longitude of ascending node, Ω, to the Cartesian coordinate system. Dynamicists and dynamical models typically use the convention that Ω is measured from the $+X$-axis toward the $+Y$-axis (see Murray & Dermott, 1999)), while observers typically measure Ω from the $+Y$-axis (which typically corresponds to North, as in Van de Kamp, 1967) toward the $+X$-axis (typically East).

Because of this, if dynamicist's conventions are used to calculate the Cartesian coordinates of a planet's position based on the orbital elements (and these were intended for use by an observer), these coordinates would not correspond to the actual position of the planet on the sky, relative to its host star. Rather, the X and Y positions would be swapped. The reason for this can be easily understood by comparing the equations for X and Y from Van de Kamp (1967) and those from Murray & Dermott (1999).

Van de Kamp (1967) has:

$$X_{obs} = B\frac{x}{a} + G\frac{y}{a} \tag{2.2}$$

$$Y_{obs} = A\frac{x}{a} + F\frac{y}{a}, \tag{2.3}$$

where x and y are the positions of the planet in its own orbital plane, X_{obs} and Y_{obs} are the positions of the planet on the sky, using observer's conventions, and A, B, F, and G (the

Thiele-Innes constants) are:

$$A = a(\cos\omega\cos\Omega - \sin\omega\sin\Omega\cos i) \tag{2.4}$$

$$B = a(\cos\omega\sin\Omega + \sin\omega\cos\Omega\cos i) \tag{2.5}$$

$$F = a(-\sin\omega\cos\Omega - \cos\omega\sin\Omega\cos i) \tag{2.6}$$

$$G = a(-\sin\omega\sin\Omega + \cos\omega\cos\Omega\cos i).. \tag{2.7}$$

On the other hand, Murray & Dermott (1999) have:

$$\begin{aligned} X_{dyn} = \; & x(\cos\Omega\cos\omega - \sin\Omega\sin\omega\cos i) \\ & - y(\cos\Omega\sin\omega + \sin\Omega\cos\omega\cos i) \end{aligned} \tag{2.8}$$

$$\begin{aligned} Y_{dyn} = \; & x(\sin\Omega\cos\omega + \cos\Omega\sin\omega\cos i) \\ & - y(\sin\Omega\sin\omega + \cos\Omega\cos\omega\cos i), \end{aligned} \tag{2.9}$$

where X_{dyn} and Y_{dyn} are the positions of the planet on the sky, using dynamicist's conventions. Equations 2.8 and 2.9 can be rewritten,

$$X_{dyn} = A\frac{x}{a} + F\frac{y}{a} \tag{2.10}$$

$$Y_{dyn} = B\frac{x}{a} + G\frac{y}{a}. \tag{2.11}$$

Comparing Equations 2.10 and 2.11 with 2.2 and 2.3, we can see that $X_{dyn} = Y_{obs}$ and $Y_{dyn} = X_{obs}$. This means that in a dynamical model, the orbit will be a mirror image of the true observed orbit, if the observed orbital elements are taken at face value (see Figure 2.1). This point is subtle, but can lead to spurious results if an observer uses the Cartesian coordinates from an orbital simulation to plan future observations. If all observations and simulations are performed using orbital elements with their respective conventions, then all results should be consistent.

This consistency is possible because the reflection has no impact on the dynamics of the system, because all planets' orbits will be reflected about the same plane, so all relative positions and velocities are preserved, and the energy (which is a function of the semi-major

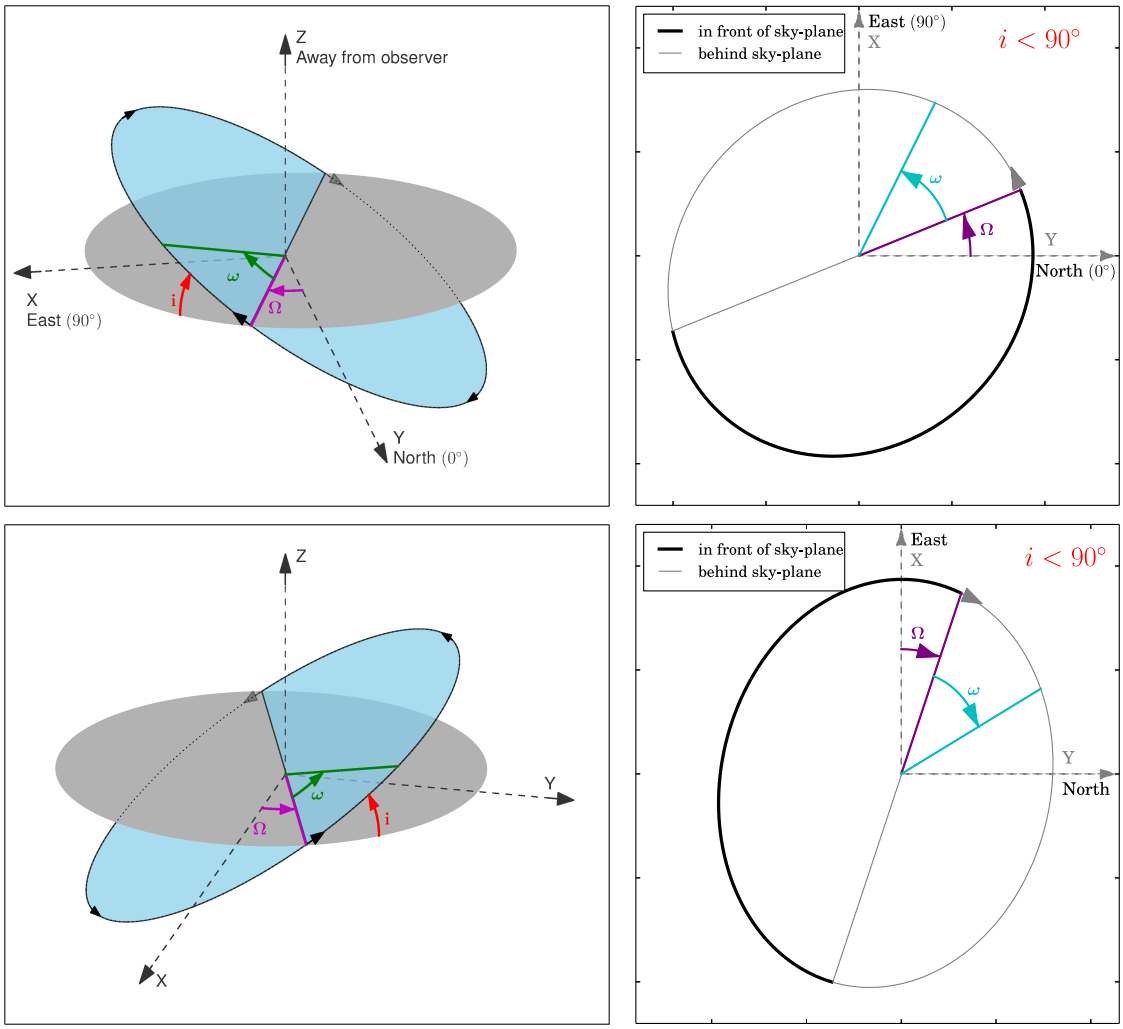

Figure 2.1: A comparison of the orbits produced in calculating Cartesian coordinates using "observer" conventions and "dynamicist" conventions. Upper left: 3D projection of the observer's orbit, from Van de Kamp (1967). Ω is measured from the $Y-$axis (North) toward the $X-$axis (East). Upper right: The observer's orbit, projected on the sky. Ω is measured counterclockwise from the $Y-$axis (North). Lower left: 3D projection of the dynamicist's orbit. Ω is measured from the $X-$axis toward the $Y-$axis, which causes the X and Y coordinates of the planet to be swapped compared to the (true) observer's orbit. Lower right: The dynamicist's orbit, projected on the sky. Again, the X and Y coordinates of the planet in its orbit will be swapped compared to the observer's orbit.

axes) and angular momentum (a function of semi-major axis, eccentricity, and inclination) are the same in the mirror image system as in the true system. Thus, as long as communication of planetary properties between observers and dynamicists is restricted to Keplerian orbital elements, there should be no difficulty in correctly modeling an observed system or in making predictions of planetary positions for future observations.

One should bear in mind the difference in Cartesian coordinates, however, when combining observational and dynamical techniques, and pass only orbital elements between models or take into account the X/Y swap if necessary.

2.2.4 Tidal Theory

We use a constant phase-lag (CPL) model (Darwin, 1880) to estimate the amount of tidal energy that could be dissipated in the interior of υ And b. This model is described in detail in appendix E of Barnes et al. (2013) (see also Ferraz-Mello et al., 2008). In short, the model treats the tidal distortion of the planet as a superposition of spherical harmonics with different frequencies, which sum to create a tidal bulge that lags the rotation by a constant phase. The strength of tidal effects is contained in the parameter Q, called the tidal quality factor, estimated to be $\gtrsim 10^4$ for the planet Jupiter (Goldreich & Soter, 1966; Yoder & Peale, 1981; Aksnes & Franklin, 2001). For close in Jovians like υ And b, Ogilvie & Lin (2004) suggest Q could be as high as 5×10^7, hence we model a range of Q values from $10^4 - 10^8$.

The CPL model, commonly used in the planetary science community, is only an approximate representation of tidal evolution (for an in-depth discussion of the limitations of the model, see Efroimsky & Makarov, 2013). However, at the eccentricities we explore here ($e \lesssim 0.15$), results from this model are qualitively similar to other tidal models. The CPL model has the advantage of fast computation and is accurate enough for our purpose here, which is merely to establish the possibility of tidal heating in the interior of planet b. Given the uncertainty in the model and in the properties of the planet, our results should not be taken to be a precise calculation of the planet's tidal conditions.

2.3 Orbital Dynamics

In this section, we present our results regarding the dynamics of the system. In Section 2.3.1, we examine the stability of the system. In Section 2.3.2, we compare the orbital evolution in our favored cases.

2.3.1 Stability

We run our initial set of 1,000 trials for 1 Myr and flag as unstable those trials in which one or more planets were lost. The resulting stability maps are shown in Figure 2.2. Here we show the most relevant parameters, *i.e.*, those with the largest uncertainty (Ω_b and i_b) and those which have a large effect on stability (e_c and e_d). The coordinate system used here is the RV+astrometry ("line-of-sight") coordinate system, in which i is measured from the plane of the sky and Ω is measured counterclockwise from North.

We note regions of greater stability concentrate around inclinations for planet b of $\lesssim 40^\circ$ and $\gtrsim 140^\circ$ and ascending nodes of $\sim 0^\circ$. A chasm of instability lies across inclinations of $\sim 60^\circ$ to $\sim 140^\circ$.

Next we examine the eccentricity and inclination evolutions for all trials in which three planets survived 1 Myr. Many of these "stable" cases exhibit chaotic evolution, with planet b even reaching eccentricities of ~ 0.9. We assume trials with chaotic evolution are in the process of destabilizing and should be discarded. This leaves us with ~ 30 trials which we then ran for 100 Myrs. Trials in which all planets survive 100 Myr integrations with no chaotic evolution or systematic regime changes are considered robustly stable. These 10 cases are plotted as x's in Figure 2.2.

υ Andromedae is estimated to be ~ 3 Gyrs old (Takeda et al., 2007); our ideal goal would thus be to demonstrate stability over this timespan; however, because a very small timestep is necessary to resolve the 4.6 day orbit of planet b, simulations of the system on spans of Gyrs are computationally prohibitive. Hence, we limit ourselves to a domain of 100 Myrs (1/30th of the system's lifetime), and note that this length of time corresponds to ~ 8 billion

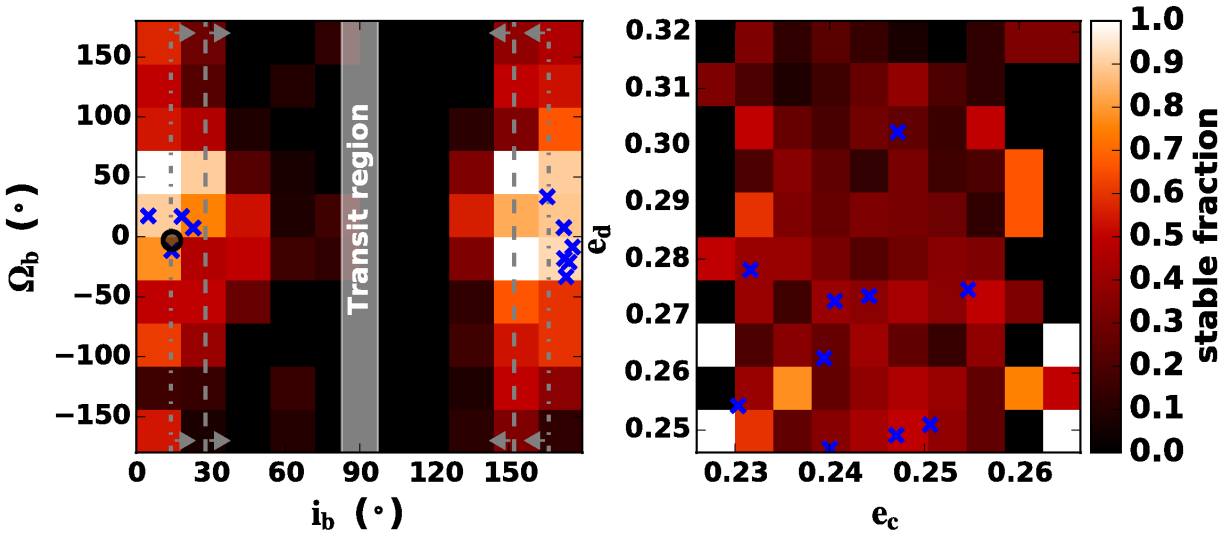

Figure 2.2: Stable fraction ($f_s = N_s/N$, where N_s is the number of trials that survived 1 Myr in each bin and N is the total number of trials in each bin), for different parameters. Left: Longitude of ascending node (Ω_b) vs. inclination (i_b) of planet b. The x's represent our robustly stable cases that survived for 100 Myr with no signs of chaos. The black circle represents the average fundamental plane of a system with planets c and d only. Shown also are the inclinations predicted by Crossfield et al. (2010) (dashed line: $R_p > 1.3R_{Jup}$; dotted line: $R_p > 1.8R_{Jup}$) and the region for which the planet would transit the host star. Higher stability occurs at $i_b \lesssim 40°$ and $i_b \gtrsim 140°$. Right: Eccentricity of planet d vs. eccentricity of planet c. Stability is most dependent on e_d, which must remain $\lesssim 0.3$ for the system to remain stable. Stability seems uncorrelated with e_c (the bright colored bins on the far left and far right contain only 1-2 trials each, and are therefore not necessarily regions of high stability).

orbits of planet b and that no previous study has been able to show stability for all three planets on this timescale.

The χ^2 results for our stable cases are shown in Table 2.2. Here, χ^2 represents the goodness of fit of each configuration to the data, and would ideally be equal to the number of degrees of freedom (DOF) in the model of the data. Configuration **PRO1** is chosen as our nominal case because it has the lowest χ^2 value of the prograde (orbit of planet b) cases.

For our 4 prograde, stable trials, we generate the stability maps shown in Figure 2.3. Keeping all other parameters constant, we vary the inclination and ascending node of planet b to further explore these "islands" of stability. In order to keep all our cases consistent with the observations of planet b, we adjust its mass with changes in inclination and subsequently must adjust its semi-major axis to maintain the observed period. Thus changes in inclination imply not only a different mass via the $m \sin i$ degeneracy, but also a change in semi-major axis.

In all cases we see that our solutions occupy stable regions of phase space. **PRO2** and **PRO3** appear to be perched on the edges of two large stable regions, while **PRO1** occupies a very narrow stable "inclination stripe" at $\sim 5^\circ$ and $\sim 2 - 3^\circ$, respectively. As in Figure 2.2, inclination in Figure 2.3 is measured from the sky-plane, not the invariable plane of the system.

An additional complication to the dynamics of the system is the oblateness of the host star. Migaszewski & Goździewski (2009) showed the importance of J_2 (the leading term in the gravitational quadrupole moment) of the star in their secular analysis, though they used a stellar radius of $R = 1.26\ R_\odot$, significantly smaller than the current best measurement of $R = 1.631\ \pm\ 0.014\ R_\odot$ (Baines et al., 2008). To verify the importance of oblateness, we simulated our best prograde χ^2 case (**PRO1**), varying J_2 from 10^{-5} to 10^{-2} and $R_\star$ from $1.26\ R_\odot$ to $1.63\ R_\odot$. We find that values of $J_2 \gtrsim 10^{-3}$ cause the system to become unstable, and lower values significantly change the eccentricity evolution of planet b. Unfortunately, the J_2 value of the star is not known and there exists some disagreement regarding its radius, and thus a detailed exploration of parameter space including these two additional parameters

Table 2.2: **Stable configurations**

Trial	χ^2 (DOF = 811)
PRO1	779
PRO2	2218
PRO3	2353
PRO4	3378
RETRO1	672
RETRO2	725
RETRO3	1292
RETRO4	1524
RETRO5	1917
RETRO6	3062

Table 2.3: **Orbital parameters for stable, prograde trials**

ID, planet	m (M_J)	P (days)	a (au)	e	i (°)	ω (°)	Ω (°)	MA (°)
PRO1, b	8.02	4.61694	0.059496	0.003547	4.97	48.39	17.47	129.43
PRO1, c	8.69	240.92	0.830939	0.254632	12.62	245.89	259.40	153.03
PRO1, d	10.05	1281.08	2.532293	0.274677	24.55	253.71	10.22	83.16
PRO2, b	1.78	4.61716	0.059408	0.011769	22.99	51.14	7.28	103.53
PRO2, c	10.78	241.02	0.831580	0.247042	10.09	248.74	256.34	154.47
PRO2, d	8.86	1282.57	2.533539	0.249090	28.30	253.27	9.97	82.57
PRO3, b	2.20	4.61726	0.059415	0.003972	18.41	44.98	17.09	148.28
PRO3, c	8.92	240.91	0.830954	0.247205	12.36	247.69	243.16	155.52
PRO3, d	9.92	1281.41	2.532645	0.302355	24.78	252.60	9.59	83.20
PRO4, b	2.81	4.61693	0.059421	0.021686	14.27	49.50	348.56	150.17
PRO4, c	9.01	240.93	0.831030	0.231669	12.31	244.39	243.47	154.06
PRO4, d	9.98	1280.56	2.531579	0.278130	24.74	252.37	9.90	83.77

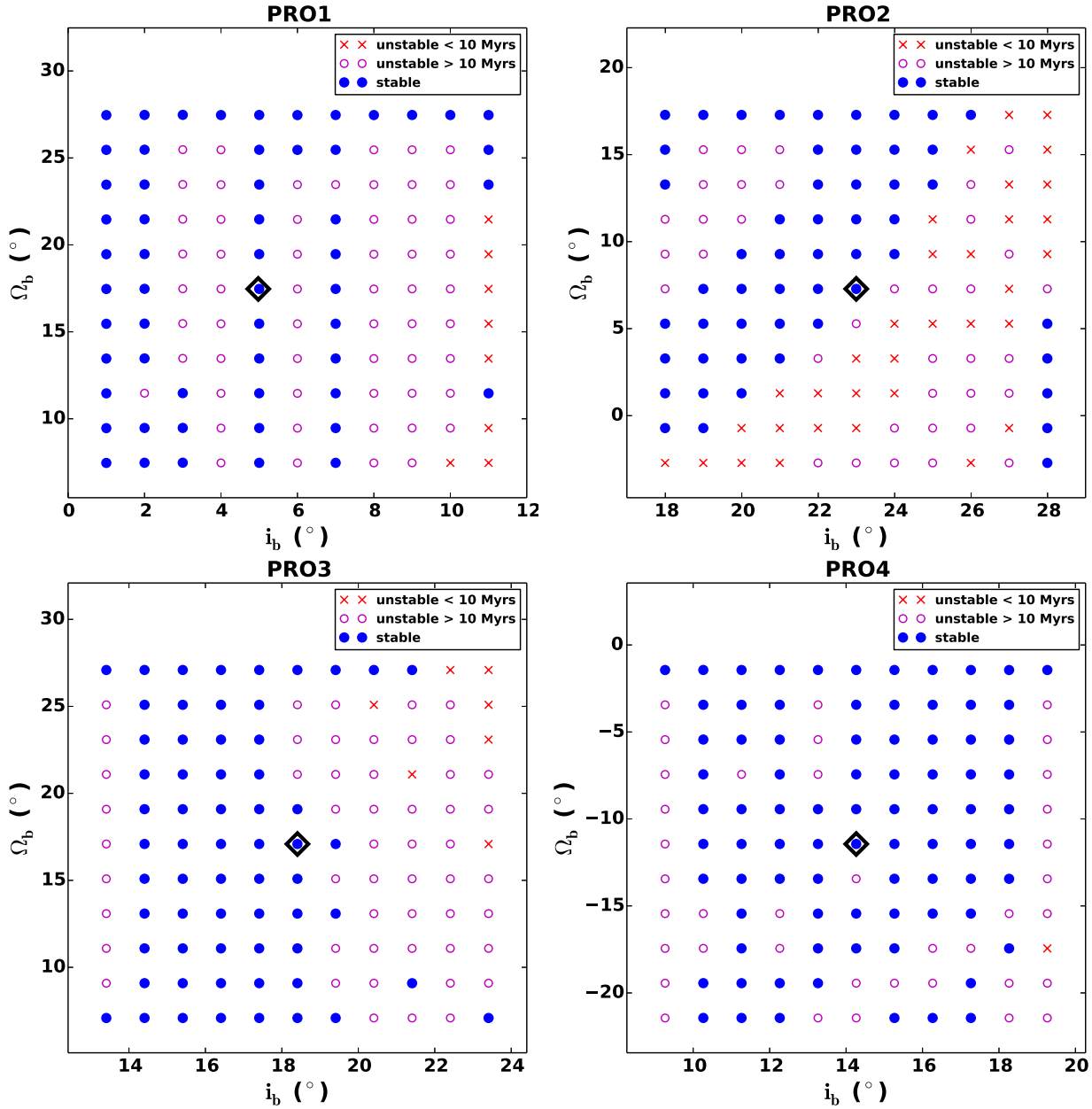

Figure 2.3: Stable regions surrounding our prograde trials, varying the orbital plane of planet b. Red x's are trials that had a planet ejected in less than 10 Myrs, pink circles displayed chaotic evolution but no ejections over 10 Myrs, and blue solid circles are those which are truly stable over 10 Myrs. The original trials are surrounded by the black diamonds.

is beyond the scope of this work. Therefore, in our primary analysis, the quadrupole moment is ignored ($J_2 = 0$).

2.3.2 System Evolution

The eccentricity and inclination evolutions for our prograde trials are shown in Figures 2.4 - 2.7. In these figures, inclination is measured from the invariable plane, that is, a plane perpendicular to the total angular momentum vector of the system. We see that for all cases, the evolution of the eccentricities and inclinations is periodic for at least 100 Myrs ($\sim$ 8 billion orbits of planet b). At a glance, one might expect for **PRO1** to lose planet b, however, as shown in Figure 2.4, the pattern seen in its eccentricity evolution is repeated reliably over many orbits, and therefore the configuration is robustly stable.

For planets c and d, Figures 2.8 and 2.9 show $\Delta\varpi = \varpi_d - \varpi_c$ (the difference of the longitudes of pericenter) and their mutual inclination Ψ_{cd} for our cases in which planet b is in prograde motion. We see that $\Delta\varpi$ undergoes circulation in cases **PRO1** and **PRO2**, and librates around anti-alignment in cases **PRO3** and **PRO4**, although it is very close to the separatrix in both. The amplitudes of libration are $\sim 240^\circ$ and $\sim 210^\circ$, for **PRO3** and **PRO4**, respectively, and RMS values about the libration center (180°) are 55° and 47°, respectively. The mutual inclination between planets c and d oscillates between $\sim 30^\circ$ and $\sim 40^\circ$ in cases **PRO2**, **PRO3**, and **PRO4**. The angle explores a slightly wider range in case **PRO1**.

2.4 Tidal Heating

The phase curve measurements (Crossfield et al., 2010) require planet b to have a radius of 1.3 R_{Jup} at an inclination of 28° (1.8 R_{Jup} at $i = 14^\circ$). This large radius could be explained by a combination of intense stellar irradiation and tidal heating in the planet's interior. To that end, we present predictions of tidal energy dissipation in several of our cases.

In reference to the planet HD 209458 b, Ibgui & Burrows (2009) found that early episodes of high eccentricity can cause tidal dissipation of $\sim 10^{19}$ watts of power, which helps to explain

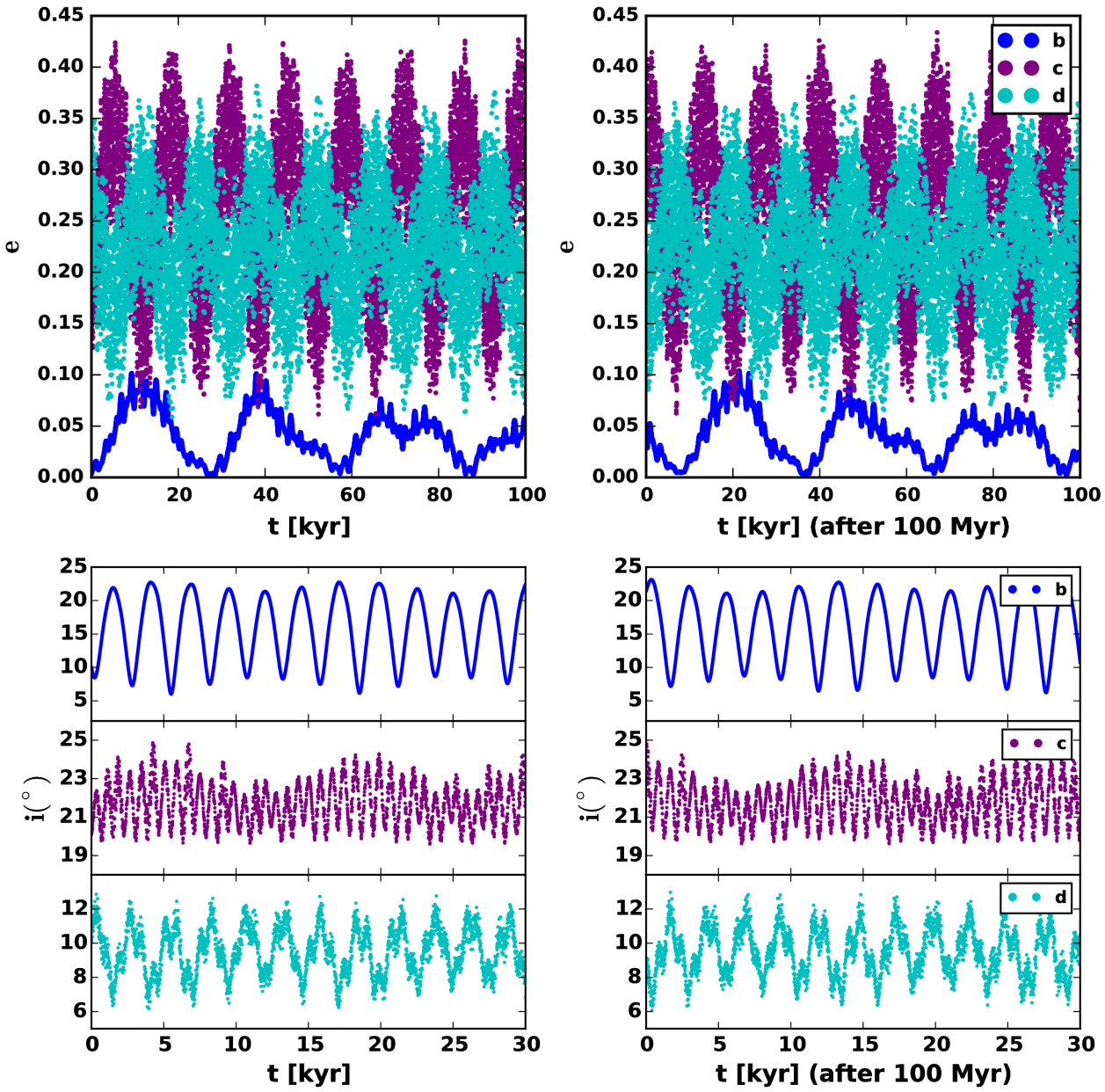

Figure 2.4: Eccentricity evolution (top panels) and inclination evolution (bottom panels) for planet b (blue), planet c (purple), and planet d (cyan) over 100,000 years, from the current epoch (left) and after a 100 Myr integration (right), in the **PRO1** system. The eccentricity evolution of planet b may appear unstable, but as seen in the right panel, the pattern is periodic over at least 100 Myr timescales. Inclinations here are measured from the invariable plane of the system, rather than the sky-plane.

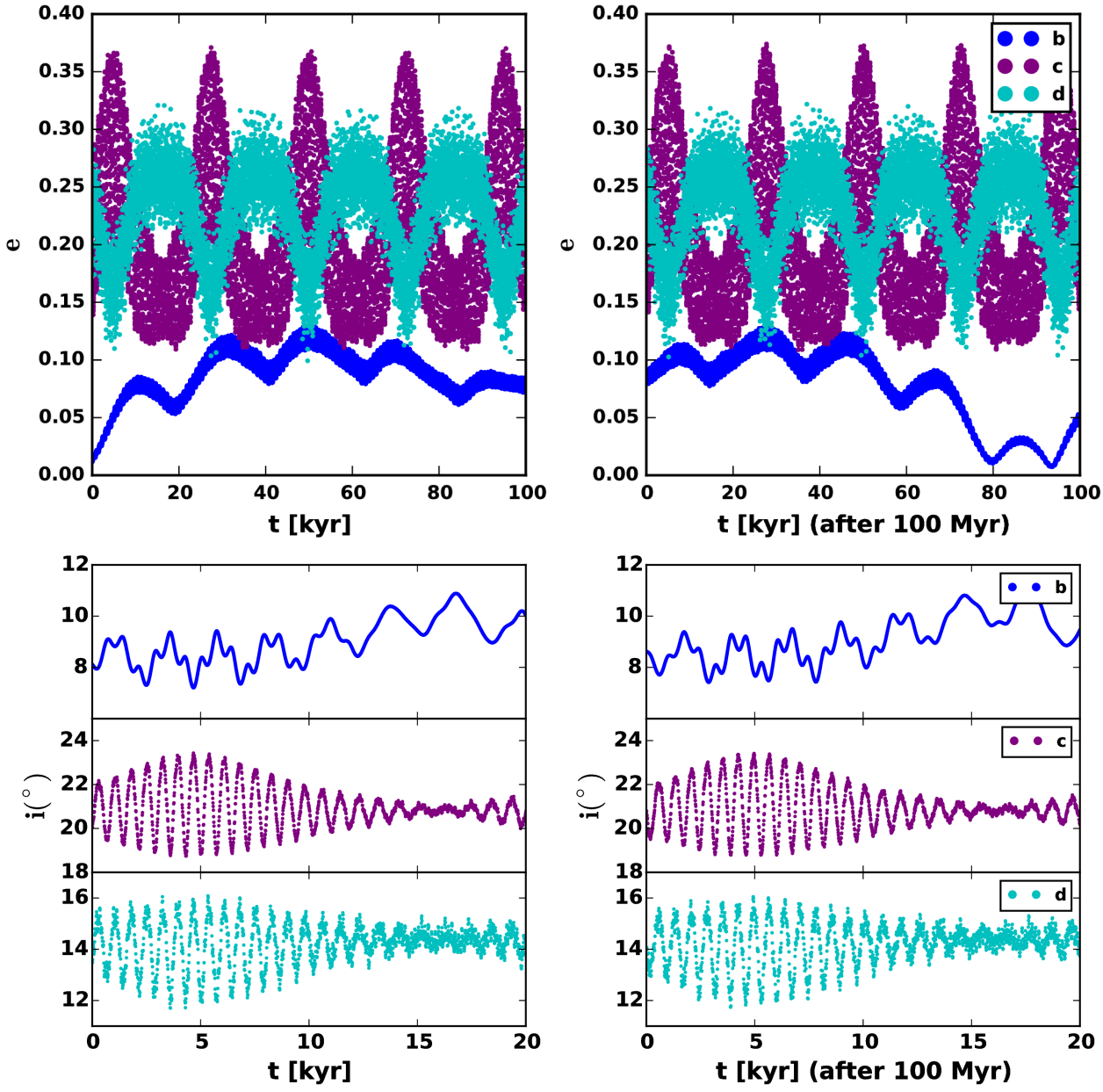

Figure 2.5: As in Figure 2.4 but for case **PRO2**.

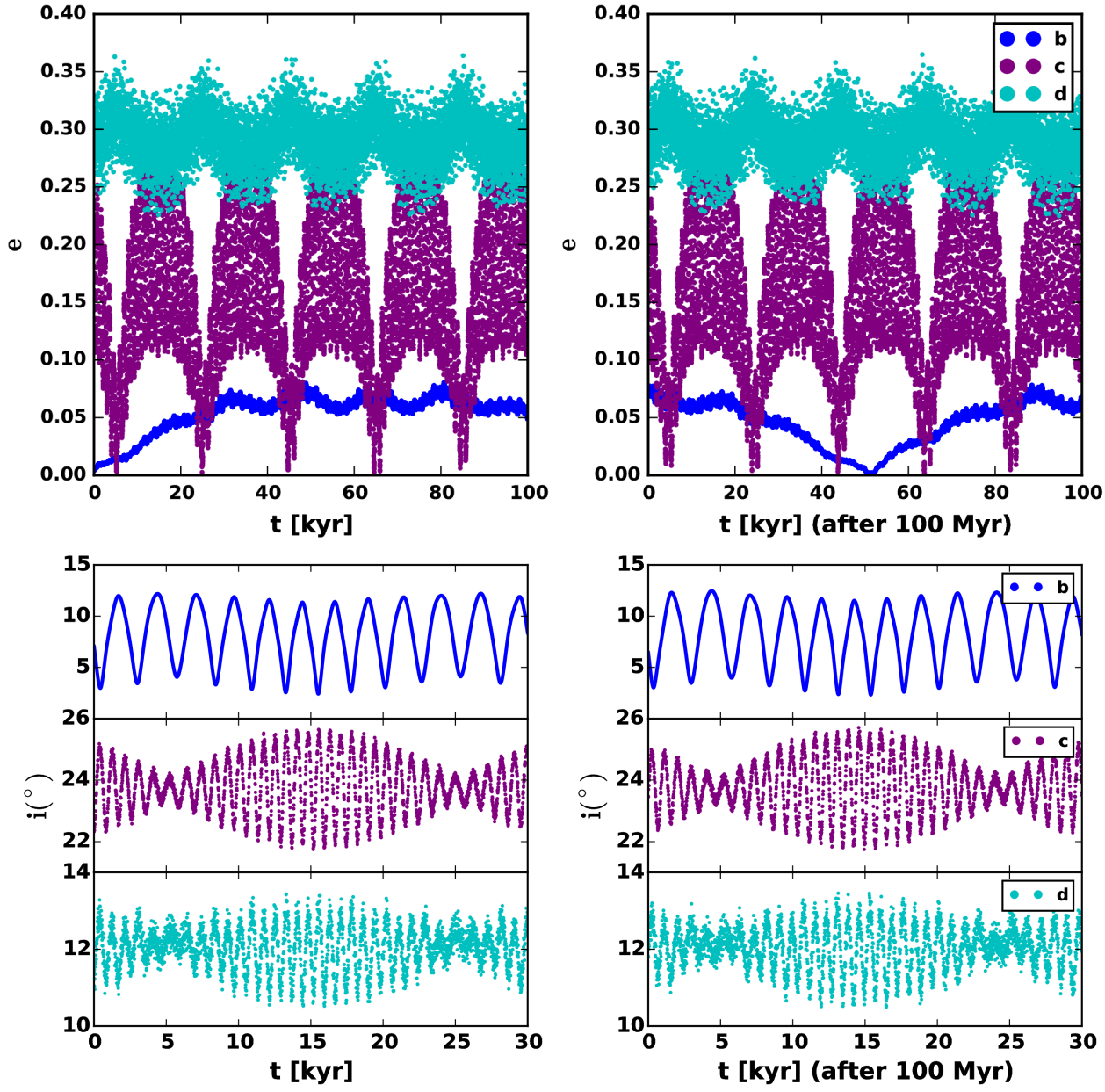

Figure 2.6: As in Figure 2.4 but for case **PRO3**.

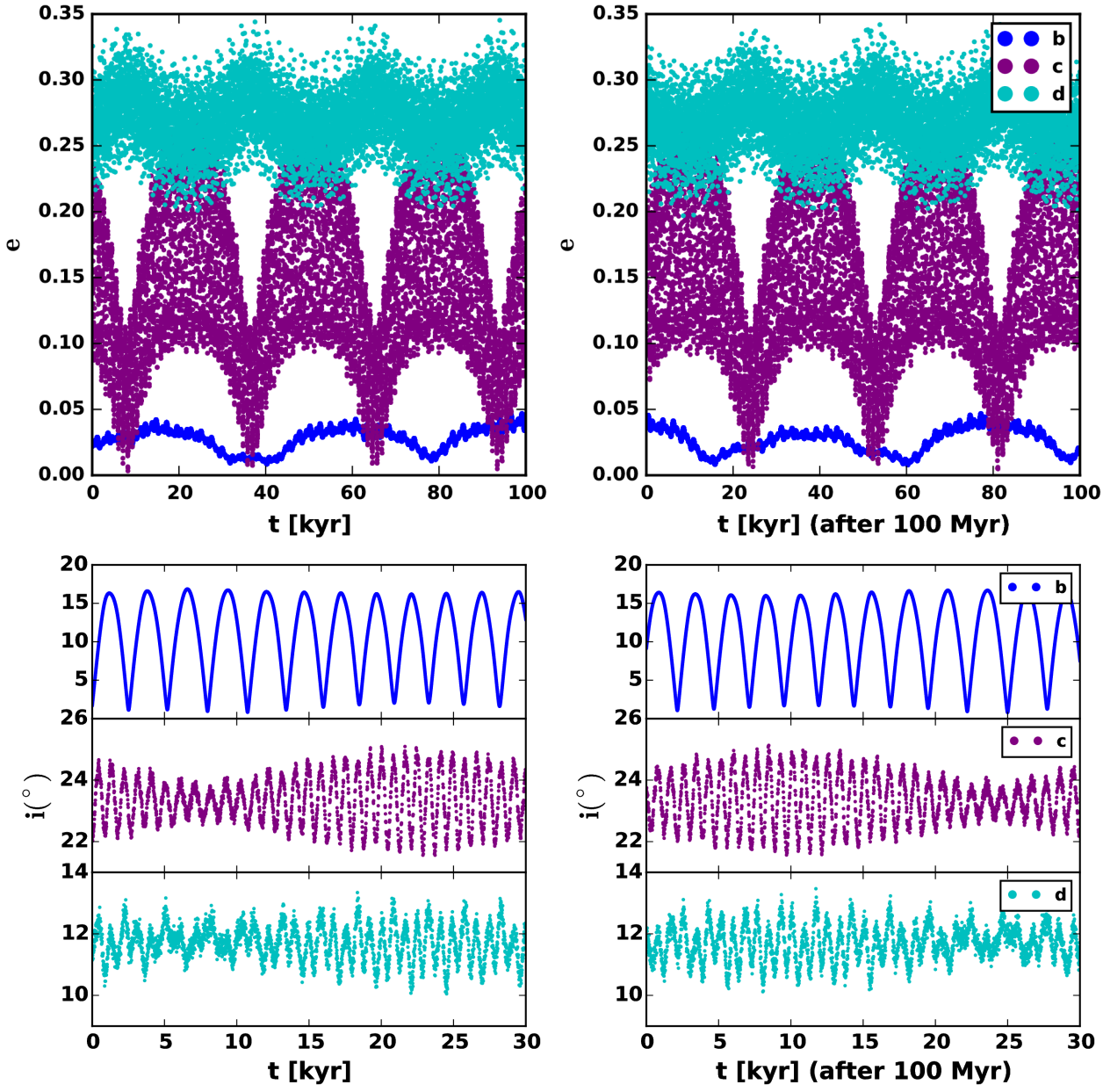

Figure 2.7: As in Figure 2.4 but for case **PRO4**.

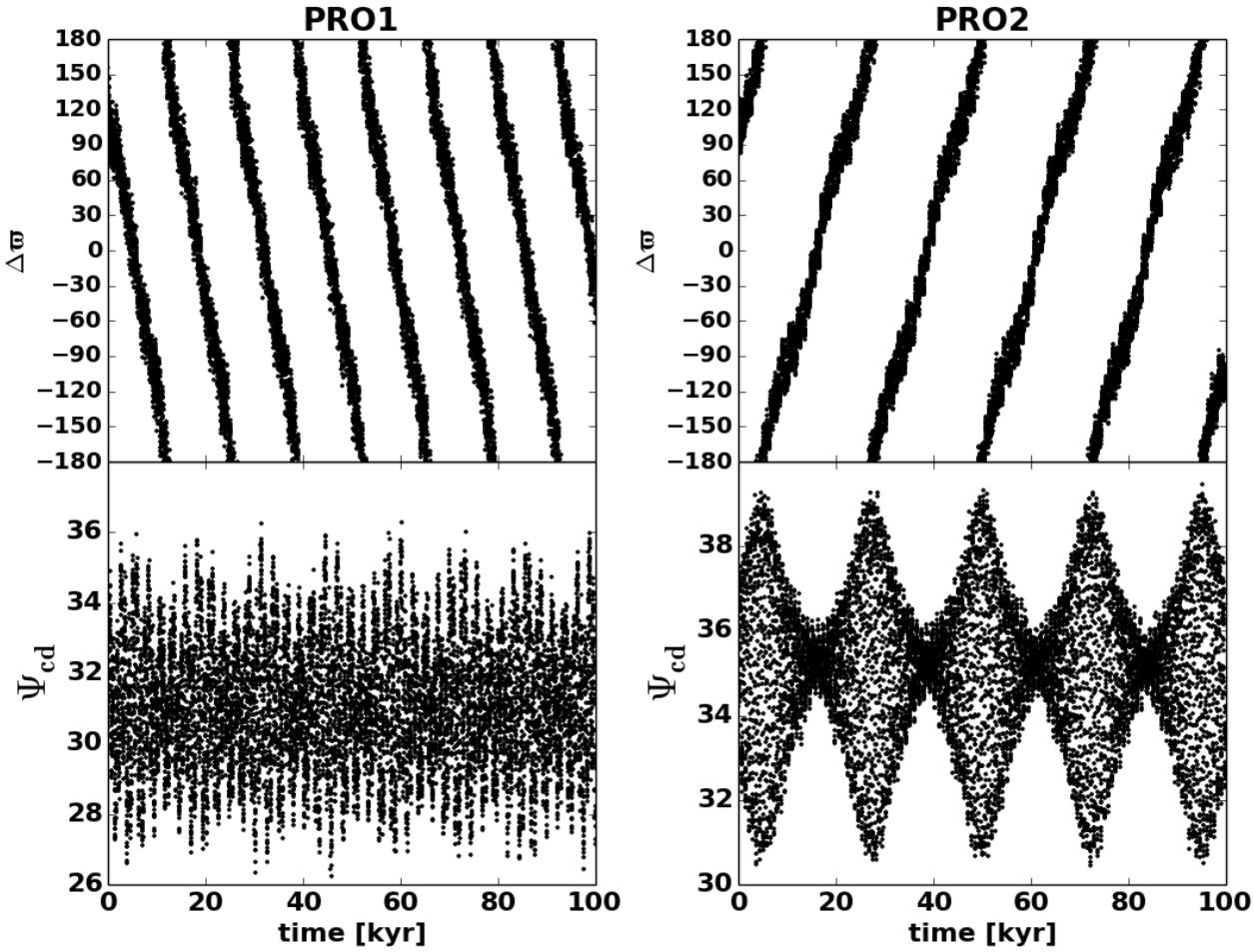

Figure 2.8: Secular behavior of planets c and d. $\Delta\varpi = \varpi_d - \varpi_c$ circulates in both cases. The mutual inclination, Ψ_{cd}, oscillates about $\sim 31^\circ$ in **PRO1** and $\sim 35^\circ$ in **PRO2** with a $\sim 10^\circ$ amplitude in both.

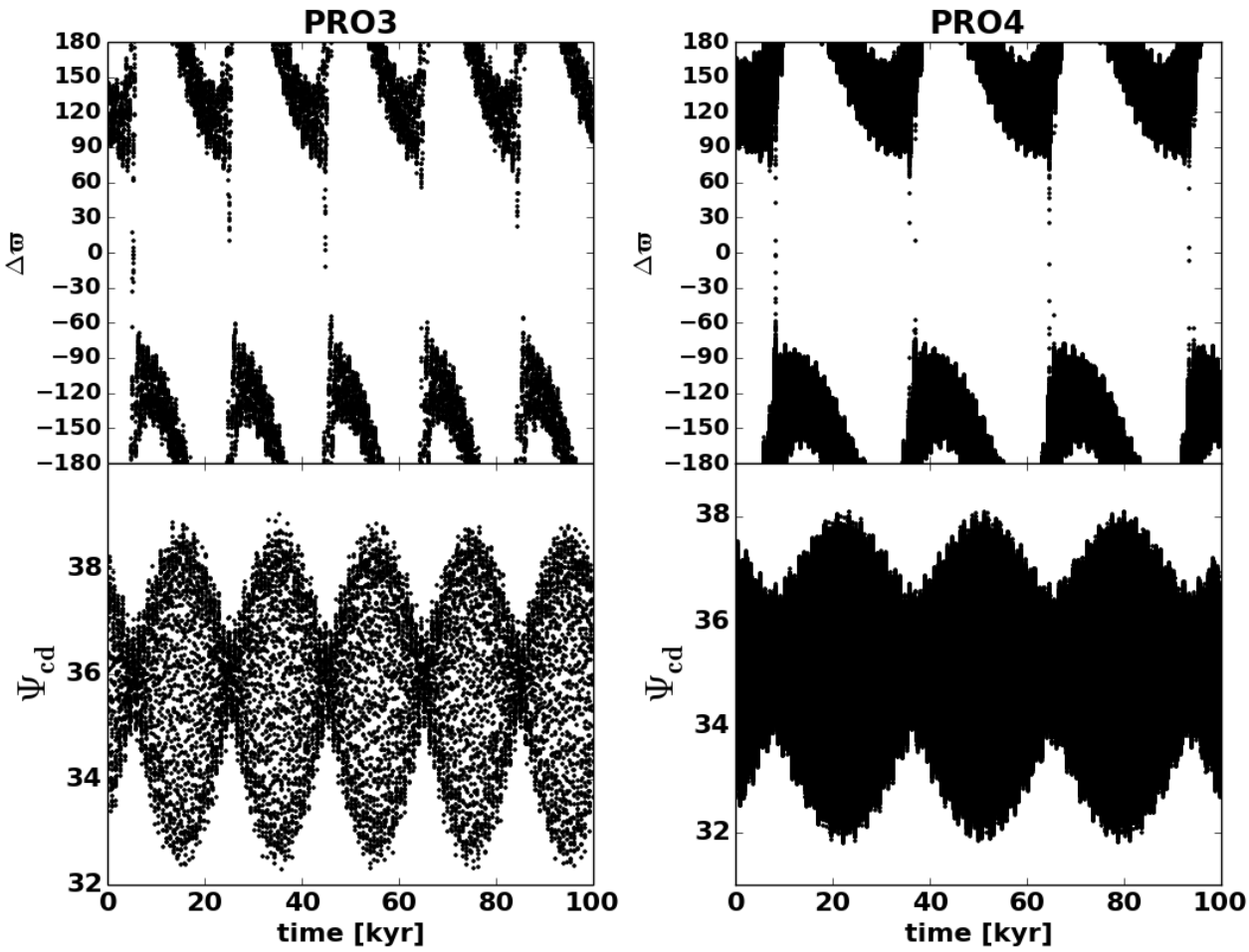

Figure 2.9: Secular behavior of planets c and d. $\Delta\varpi = \varpi_d - \varpi_c$ librates with intermittent circulation in both cases. **PRO4** is plotted with finer time resolution to show the circulation, which occurs very quickly. The mutual inclination, Ψ_{cd}, oscillates about $\sim 35°$ in both cases with a $\sim 6°$ amplitude.

the planet's radius of 1.3 R_{Jup}, though it may not be necessary, considering the stellar flux received. We find that planet b in our prograde cases experiences significant eccentricity evolution (Figures 2.4 - 2.7), which should trigger similar episodes of tidal heating. As discussed in section 2.5, this may be necessary to reconcile our results with that of Crossfield et al. (2010).

In Figure 2.10 we show tidal energy dissipated in the interior of planet b for case **PRO1**. Tidal heating for **PRO2** looks very similar. We explore a range of tidal factor Q (left panel, with planet radius $R = 1.5\ R_{Jup}$) and planet radius (right panel, with $Q = 10^6$). We find that, depending on the true radius of the planet and the equation of state of the interior, planet b could indeed have episodes of intense tidal heating. Coupled with the intense stellar radiation at ~ 0.06 au, for the case **PRO2**, this could reconcile the results of McArthur et al. (2010), Crossfield et al. (2010), and this study (see the right panel in Figure 2.10).

The results are more difficult to reconcile for the lower inclination case **PRO1**. Miller et al. (2009) showed that radius inflation for hot Jupiters is a strong function of mass. Referring to their Figure 6, with 10^{19} W $= 10^{26}$ erg s^{-1}, and the mass of planet b of $\sim 8\ M_{Jup}$ for **PRO1**, it seems unlikely that even the combination of tidal heating and stellar irradiation could inflate planet b beyond $\sim 1.5\ R_{Jup}$. Additionally, the planet in that case would need to have a radius of $> 3\ R_{Jup}$ in order to explain the phase curve. However, given the lingering uncertainty in the apparently large radii of some hot Jupiters, as well as the shortcomings of tidal theory, these configurations may still be compatible with the Crossfield et al. (2010) results.

2.5 Discussion

Only four of our stable architectures (three of them prograde) are fully consistent with Crossfield et al. (2010), which requires that planet b in these cases be as large as 1.8 R_{Jup}, and would place it amongst the largest known exoplanets. Still, this size is reasonable, as, for example, the radius of the hot Jupiter HAT-P-32 b was determined to be $R = 2.037 \pm 0.099\ R_{Jup}$—a planet orbiting a star of similar spectral type (late FV) and age (~ 3

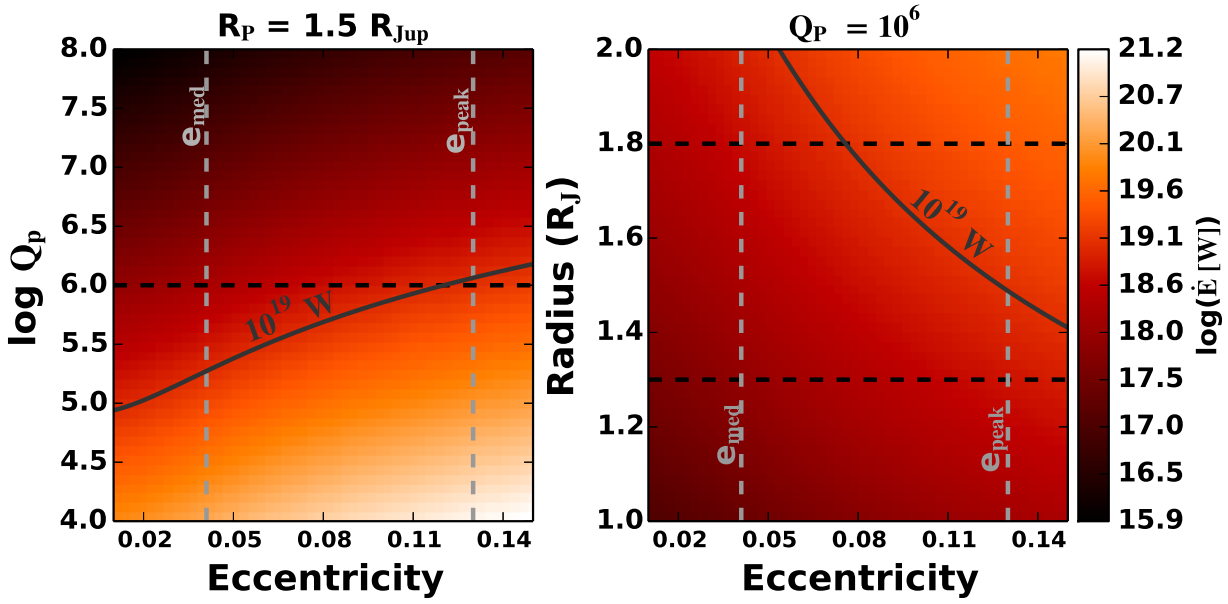

Figure 2.10: Tidal heating for υ And b in case **PRO1**. Left: the equilibrium heating rate in Watts as a function of tidal quality factor, Q_p and eccentricity. The horizontal dashed line represents $Q_p = 10^6$, the value of Q_p in the right panel. Right: the equilibrium heating rate as a function of planet radius and eccentricity. Horizontal dashed lines represent the characteristic radii suggested by Crossfield et al. (2010) to explain the infrared phase curve. At $i_b = 14°$, the planet must be 1.8 R_{Jup} to produce the observed variational amplitude, while at $i_b = 28°$ it must be 1.3 R_{Jup}. The vertical gray dashed lines represent the median and peak eccentricity of the planet, $e_{med} = 0.041$ and $e_{peak} = 0.13$. The gray curve indicates the heating rate predicted by Ibgui & Burrows (2009) for the planet HD 209458 b in the first two billion years of its tidal evolution. We find that υ And b can have similar internal heating rates. Heating plots for **PRO2** and look very similar to those for **PRO1**.

Gyr) to υ And (Hartman et al., 2011). We have demonstated that the eccentricity evolution of planet b in several cases allows for significant tidal energy dissipation which will help to explain its very large size.

Yet the case with the lowest χ^2 value, **PRO1**, has an inclination of $\sim 5^\circ$ for planet b, which may be more difficult to reconcile with the Crossfield et al. (2010) result. From Equation 2 in Crossfield et al. (2010), we conclude that planet b in **PRO1** would have to have a radius of $\sim 3\ R_{Jup}$ to be consistent with the phase curve measurements, while its large mass may prevent inflation to even beyond $\sim 1.5\ R_{Jup}$.

There are two retrograde cases with comparable χ^2 to our nominal solution, but we cautiously favor prograde orbits for planet b over retrograde on the grounds that it is difficult to explain the formation of a multi-planet system with mutual inclinations this extreme ($\Psi \sim 180^\circ$). Transits of many hot Jupiters have permitted detection of a Rossiter-McLaughlin effect, in which the alignment of the planet's orbit, relative to the spin axis of the star, can be inferred from asymmetries during the transit in Doppler-broadening spectral lines (Triaud et al., 2010). A significant number of these orbits are misaligned with the stellar obliquity, however, as υ And A's obliquity is unknown, it is impossible to say at this time whether our so-called "retrograde" orbits are in fact misaligned with the star's rotation (or that our prograde orbit are aligned with it). Rather, it is the high mutual inclination between planet b and planets c and d that must be explained in order to justify our retrograde cases. It is noteworthy that no detected exoplanet (and host star) with $> 90^\circ$ misalignment has been found in a multiple planet system. Because of the lack of observational precedent, we are reluctant to favor our retrograde systems.

Early studies found that the pericenters of planets c and d were oscillating about alignment, such that $\Delta\varpi = \varpi_d - \varpi_c \sim 0^\circ$ (Chiang et al., 2001, 2002). Michtchenko & Malhotra (2004) found that $\Delta\varpi$ could take on a full range of behaviors from libration to circulation, based on initial conditions within the uncertainties of the observations at the time. Ford et al. (2005) found $\Delta\varpi$ near separatrix, and more recently, Barnes et al. (2011) found $\Delta\varpi$ librating about anti-alignment ($\Delta\varpi \sim 180^\circ$). Here, we have in our prograde cases a variety

of behavior for $\Delta\varpi$: precession in one case, recession in one, and libration in two.

The exact nature of the secular relationship between planets c and d appears to be highly sensitive to the orbital parameters, as we see that $\Delta\varpi$ and Ψ_{cd} take on very different modes of behavior just within the observational uncertainties. It seems that the planets are close to an apsidal separatrix.

Whereas the orbital fit (McArthur et al., 2010) suggests that planet c has larger mass than planet d, stability seems to slightly favor planet d having the larger mass (prograde cases only), though strong conclusions should not be drawn from only four examples. While this eccentricity ratio is less likely, Barnes et al. (2011) have shown that the relative inclinations are significantly more difficult to produce. However, that study also demonstrated that planet-planet scattering resulting in the ejection of an additional planet is able to produce both the eccentricities and the mutual inclination of planets c and d.

From Figure 2.3, it is clear that the system resides close to instability. This proximity to instability and the large eccentricities and mutual inclination of planets c and d suggest that the system arrived at its current configuration by a past planet-planet scattering event, as found by Barnes et al. (2011). The near-separatrix behavior of c and d additionally suggest that this event was more likely to be a collision than the ejection of a fourth planet from the system (Barnes et al., 2011).

2.6 Chapter Summary

We have presented 10 dynamically stable configurations consistent with the combined radial velocity/astrometry fit first presented in McArthur et al. (2010). In six of these cases, planet b orbits retrograde with respect to planets c and d. Because of the apparent difficulty in the formation of such a system, our analysis focuses instead on the four remaining prograde cases. The case **PRO1** represents our best estimate of the system's true configuration, because of its low χ^2 and the relative ease of explaining its formation.

In our stable prograde results, planet b's inclination spans the range of $3^\circ \lesssim i_b \lesssim 23^\circ$. The corresponding mass range is $1.78\ M_{Jup} \leq m_b \leq 8.02\ M_{Jup}$. Three of the four prograde trials

are consistent with the predicted inclination from the infrared phase curve results (Crossfield et al., 2010), but require a planet radius of $\sim 1.3 - 1.8\ R_{Jup}$.

υ Andromedae is a benchmark that may portend a new class of planetary system, *i.e.*, "dynamically hot" systems with high eccentricities and high mutual inclinations. Currently υ And is the only multi-planet system with astrometry measurements, but *Gaia* (Casertano et al., 2008) and perhaps a *NEAT*-like mission (Malbet et al., 2012) will discover if such architectures are common or rare. If υ And-like systems are common in the galaxy, we should even expect to find potentially habitable planets in dynamically complex environments.

2.7 Acknowledgments

Russell Deitrick, Rory Barnes, Tom Quinn, and Rodrigo Luger acknowledge support from the NASA Astrobiology Virtual Planetary Laboratory lead team. Russell Deitrick also acknowledges support from the University of Washington GO-MAP fellowship. Rory Barnes acknowledges support from NSF grant AST-1108882. Support for HST υ And was provided by NASA through grants GO-09971, GO-10103, and GO-11210 from the Space Telescope Science Institute, which is operated by the Association of Universities for Research in Astronomy (AURA), Inc., under NASA contract NAS5-26555. We would additionally like to thank Jonathan Fortney, Mike Line, and Eric Agol for helpful discussions.

Chapter 3

EXO-MILANKOVITCH CYCLES I: ORBITS AND ROTATION STATES

The obliquity of the Earth, which controls our seasons, varies by only $\sim$2.5° over $\sim$40,000 years, and its eccentricity varies by only $\sim$ 0.05 over 100,000 years. Nonetheless, these variations influence Earth's ice ages. For exoplanets, variations can be significantly larger. Previous studies of the habitability of moonless Earth-like exoplanets have found that high obliquities, high eccentricities, and dynamical variations can extend the outer edge of the habitable zone by preventing runaway glaciation (snowball states). We expand upon these studies by exploring the orbital dynamics with a semi-analytic model that allows us to map broad regions of parameter space. We find that in general, the largest drivers of obliquity variations are secular spin-orbit resonances. We show how the obliquity varies in several test cases, including Kepler-62 f, across a wide range of orbital and spin parameters. These obliquity variations, alongside orbital variations, will have a dramatic impact on the climates of such planets.

Material in this chapter has been submitted to the Astronomical Journal with co-authors Rory Barnes, Thomas R. Quinn, John Armstrong, Benjamin Charnay, and Caitlyn Wilhelm.

3.1 Introduction

As discussed in Chapter 1, the habitable zone (HZ) is the region around a star in which a planet with an Earth-like atmosphere can maintain liquid water on its surface for billion of years (*i.e*, long enough for life to originate and evolve). I will restate some of the important points from earlier, in particular, how orbital properties influence habitability.

The original concept of the HZ is based on one-dimensional radiative-convective mod-

els (Kasting et al., 1993; Selsis et al., 2007; Kopparapu et al., 2013; Goldblatt et al., 2013; Kopparapu et al., 2014). These take an input stellar flux, and calculate the surface temperature based on that and an assumed atmospheric composition. When the planet has a surface temperature in between the freezing and boiling points of water, it is in the HZ. A carbon-silicate cycle is a key component of habitability in such models: it is assumed that the planet will maintain an adequate amount of CO_2 in its atmosphere to maintain liquid water because of this negative feedback.

Planets are obviously not one-dimensional atmospheres with a single surface temperature, and the stellar flux received does not stay constant. This complicates the idea of the HZ, to some extent. We can see a hint of this in Earth's Milankovitch cycles: the ice ages of the Pliocene and Pleistocene appear to be influenced by variations in its orbit and obliquity (Berger, 1978; Laskar et al., 1993a; Clark & Pollard, 1998; Roe, 2006; Tziperman et al., 2006; Huybers & Tziperman, 2008). The basic mechanism by which this occurs is as follows: as the orbit and obliquity change, the insolation received at each latitude varies. When the insolation at high latitudes is weak during summer time, the ice sheets on land are able to grow from year to year. When the insolation is stronger at high latitudes, the ice sheets will tend to retreat, and because of a number of possible effects, eventually collapse. Thus it is thought that summer-time insolation is the primary driving mechanism of the ice ages.

With exoplanets, the story can be much more dramatic. The solar system is relatively dynamically "cool" compared to many exoplanet systems (see Chapter 2) and Earth's obliquity is stabilized by its large moon. A number of works have previously studied the climate's response to different eccentricities and obliquities (Williams & Kasting, 1997; Williams & Pollard, 2002, 2003; Spiegel et al., 2009; Dressing et al., 2010; Bolmont et al., 2016; Rose et al., 2017) and variations of these quantities (Armstrong et al., 2014; Forgan, 2016; Way & Georgakarakos, 2017). The present work builds upon these prior studies with a detailed examination of the parameter space of several example systems.

3.1.1 This study

The goals of this study are (1) to introduce our secular (orbit-averaged) orbital framework, which allows us to map wide regions of parameter space; (2) to demonstrate the complexity of planetary systems and the potential ways orbital evolution can influence climate, including large eccentricities and mutual inclinations, in preparation for the discovery of dynamically "hot" systems; and (3) to generate initial conditions for climate modeling in a follow up study (Chapter 4). Our formulations allow us to understand the fundamental causes of large obliquity variations, and to identify higher order secular resonances that depend on eccentricity and inclination.

Section 3.2 contains a description of our model, which we validate against an N-body model in Section 3.3. In Section 3.4, we lay out results from the model for several example systems, and discuss secular resonances and Cassini states. In Section 3.5, we offer some interpretation and broader context, and we conclude in Section 3.6.

3.2 Methods

3.2.1 Orbital model

Our model for the orbital evolution, called `DISTORB`, uses the literal, 4th order disturbing function developed in Murray & Dermott (1999) and Ellis & Murray (2000). We use only the secular terms, meaning that the rapidly varying terms that depend on the mean longitudes of the planets are ignored on the assumption that these terms will average to zero over long timescales. This is a valid assumption as long as no planets are in proximity of mean-motion resonances. There are, in fact, two orbital models in `DISTORB`: the first is simply a direct Runge-Kutta integration of the fourth-order equations of motion with variable time-stepping (RD4); the second is the Laplace-Lagrange eigenvalue solution (LL2), which reduces the accuracy in the disturbing function to second-order, but returns a solution that is explicit in time, and thus provides a solution that is perfectly stable in much less computation time. Most of the work we present here takes advantage of the fourth-order solution for its accuracy,

but we briefly discuss some results using the Laplace-Lagrange method in Sections 3.4.2 and 3.4.3.

The equations of motion are Lagrange's equations (see Murray & Dermott, 1999). In the secular approximation the equations for semi-major axis and mean longitude, and any disturbing function derivatives with respect to these variables, are ignored. Additionally, to avoid singularities in the equations for the longitudes of pericenter and ascending node, which occur at zero eccentricity and inclination, respectively, we rewrite Lagrange's equations and the disturbing function in terms of the variables (a form of Poincaré coordinates):

$$h = e \sin \varpi \tag{3.1}$$

$$k = e \cos \varpi \tag{3.2}$$

$$p = \sin \frac{i}{2} \sin \Omega \tag{3.3}$$

$$q = \sin \frac{i}{2} \cos \Omega, \tag{3.4}$$

where e is the orbital eccentricity, i is the inclination, Ω is the longitude of ascending node, and $\varpi = \omega + \Omega$ is the longitude of periastron (see Figure 3.1).

Lagrange's equations for secular theory are then:

$$\frac{dh}{dt} = \frac{\sqrt{1-e^2}}{na^2}\frac{\partial \mathcal{R}}{\partial k} + \frac{kp}{2na^2\sqrt{1-e^2}}\frac{\partial \mathcal{R}}{\partial p} + \frac{kq}{2na^2\sqrt{1-e^2}}\frac{\partial \mathcal{R}}{\partial q} \tag{3.5}$$

$$\frac{dk}{dt} = -\frac{\sqrt{1-e^2}}{na^2}\frac{\partial \mathcal{R}}{\partial h} - \frac{hp}{2na^2\sqrt{1-e^2}}\frac{\partial \mathcal{R}}{\partial p} - \frac{hq}{2na^2\sqrt{1-e^2}}\frac{\partial \mathcal{R}}{\partial q} \tag{3.6}$$

$$\frac{dp}{dt} = -\frac{kp}{2na^2\sqrt{1-e^2}}\frac{\partial \mathcal{R}}{\partial h} + \frac{hp}{2na^2\sqrt{1-e^2}}\frac{\partial \mathcal{R}}{\partial k} + \frac{1}{4na^2\sqrt{1-e^2}}\frac{\partial \mathcal{R}}{\partial q} \tag{3.7}$$

$$\frac{dq}{dt} = -\frac{kq}{2na^2\sqrt{1-e^2}}\frac{\partial \mathcal{R}}{\partial h} + \frac{hq}{2na^2\sqrt{1-e^2}}\frac{\partial \mathcal{R}}{\partial k} - \frac{1}{4na^2\sqrt{1-e^2}}\frac{\partial \mathcal{R}}{\partial p}, \tag{3.8}$$

where $\mathcal{R}$ is the disturbing function (see Appendix), and a, n, and e are the semi-major axis, mean motion, and eccentricity, respectively. See Berger & Loutre (1991) for the complete set of Lagrange's equations in h, k, p, and q, including resonant effects.

General relativity is known to affect the apsidal precession (associated with eccentricity) of planetary orbits, so we include a correction to Equations (3.5) and (3.6). Following Laskar

(1986), we have:

$$\frac{dh}{dt}\Big|_{GR} = \delta_R k \tag{3.9}$$

$$\frac{dk}{dt}\Big|_{GR} = -\delta_R h, \tag{3.10}$$

where

$$\delta_R = \frac{3n^3a^2}{c^2(1-e^2)}, \tag{3.11}$$

and c is the speed of light.

The secular approximation allows us to take large timesteps (years to hundreds of years) and thus to run thousands of simulations quickly and explore parameter space with relatively minimal computer usage compared with N-body models.

3.2.2 The disturbing function and its derivatives

Here we present, for the sake of clarity, the disturbing function as used in `DISTORB`, in the variables h, k, p, and q (see Section 3.2.1). These were originally derived by Ellis & Murray (2000); we have simply applied coordinate transformations and calculated derivatives with respect to the new coordinates. This disturbing function, in its original form, can also be seen in Murray & Dermott (1999). We will not restate the semi-major axis functions, f_1, f_2, f_3 and so on, in this paper, as they are taken directly from the appendix of Murray & Dermott (1999).

The secular disturbing function, for any pair of planets, is:

$$\mathcal{R} = \frac{\mu'}{a'}\mathcal{R}_D, \tag{3.12}$$

for the inner body and:

$$\mathcal{R}' = \frac{\mu}{a'}\mathcal{R}_D, \tag{3.13}$$

for the outer body. Here, a' is the semi-major axis of the exterior planet and the mass factors are $\mu = \kappa^2 m$ and $\mu' = \kappa^2 m'$, where m is the mass of the interior planet and m' is the mass of the exterior planet. Finally,

$$\mathcal{R}_D = \mathrm{D0.1} + \mathrm{D0.2} + \mathrm{D0.3} + \ldots, \tag{3.14}$$

where the terms D0.1, D0.2, and so on, are given in Table 3.1.

3.2.3 Obliquity model

The obliquity model, `DISTROT`, is derived from the Hamiltonian for rigid body motion introduced by Kinoshita (1975, 1977) and later used by Laskar (1986); Laskar et al. (1993a); Armstrong et al. (2004, 2014) and several others. In the absence of large satellites (such as the Moon), the equations of motion for a rigid planet are (borrowing the notation of Armstrong et al. (2014)):

$$\begin{aligned}\frac{dp_A}{dt} = R(\psi) - \cot(\psi)\ [&A(p,q)\sin p_A \\ &+ B(p,q)\cos p_A] - 2\Gamma(p,q) - p_g\end{aligned} \tag{3.15}$$

$$\frac{d\psi}{dt} = -B(p,q)\sin p_A + A(p,q)\cos p_A, \tag{3.16}$$

where,

$$R(\psi) = \frac{3\kappa^2 M_\star}{a^3\nu} E_D S_0 \cos\psi \tag{3.17}$$

$$S_0 = \frac{1}{2}(1-e^2)^{-3/2} \tag{3.18}$$

$$A(p,q) = \frac{2}{\sqrt{1-p^2-q^2}}[\dot{q} + p\Gamma(p,q)] \tag{3.19}$$

$$B(p,q) = \frac{2}{\sqrt{1-p^2-q^2}}[\dot{p} - q\Gamma(p,q)] \tag{3.20}$$

$$\Gamma(p,q) = q\dot{p} - p\dot{q}. \tag{3.21}$$

Note the sign error in Equation (8) of Armstrong et al. (2014), corrected in our Equation (3.19). Our Equation (3.17) does not contain the lunar constants present in Equation (24) of Laskar (1986). Here, ψ represents the obliquity, p and q as in Equations (3.3) and (3.4), $\dot{p}$ and $\dot{q}$ are their time derivatives (Equations (3.7) and (3.8)), κ is the Gaussian gravitational constant, $M_\star$ is the mass of the host star in solar units, ν is the rotation frequency of the planet in rad day^{-1}, and E_D is the dynamical ellipticity of the (oblate) planet:

$$E_D = \frac{C-A}{C}, \tag{3.22}$$

Table 3.1: The **Disturbing function**, to 4th order, with no mean longitude terms.

Term	
D0.1	$f_1+(h^2+k^2+h'^2+k'^2)f_2+(p^2+q^2+p'^2+q'^2)f_3+(h^2+k^2)^2f_4+(h^2+k^2)(h'^2+k'^2)f_5$ $+(h'^2+k'^2)^2f_6+[(h^2+k^2)(p^2+q^2)+(h'^2+k'^2)(p^2+q^2)+(h^2+k^2)(p'^2+q'^2)$ $+(h'^2+k'^2)(p'^2+q'^2)]f_7+[(p^2+q^2)^2+(p'^2+q'^2)^2]f_8+(p^2+q^2)(p'^2+q'^2)f_9$
D0.2	$(hh'+kk')[f_{10}+(h^2+k^2)f_{11}+(h'^2+k'^2)f_{12}+(p^2+q^2+p'^2+q'^2)f_{13}]$
D0.3	$(pp'+qq')[f_{14}+(h^2+k^2+h'^2+k'^2)f_{15}+(p^2+q^2+p'^2+q'^2)f_{16}]$
D0.4	$(h^2h'^2-k^2h'^2-h^2k'^2+k^2k'^2+4hh'kk')f_{17}$
D0.5	$(h^2p^2-h^2q^2-k^2p^2+k^2q^2+4hkpq)f_{18}$
D0.6	$[hh'(p^2-q^2)-kk'(p^2-q^2)+2pq(hk'+kh')]f_{19}$
D0.7	$(h'^2p^2-h'^2q^2-k'^2p^2+k'^2q^2+4h'k'pq)f_{20}$
D0.8	$(h^2pp'-h^2qq'-k^2pp'+k^2qq'+2hkp'q+2hkpq')f_{21}$
D0.9	$[(hh'+kk')(pp'+qq')+(hk'-kh')(pq'-qp')]f_{22}$
D0.10	$[(hh'+kk')(pp'+qq')+(hk'-kh')(qp'-pq')]f_{23}$
D0.11	$[(hh'-kk')(pp'-qq')+(hk'+kh')(pq'+qp')]f_{24}$
D0.12	$(h'^2pp'-h'^2qq'-k'^2pp'+k'^2qq'+2h'k'p'q+2h'k'pq')f_{25}$
D0.13	$(h^2p'^2-h^2q'^2-k^2p'^2+k^2q'^2+4hkp'q')f_{18}$
D0.14	$[hh'(p'^2-q'^2)-kk'(p'^2-q'^2)+2p'q'(hk'+kh')]f_{19}$
D0.15	$(h'^2p'^2-h'^2q'^2-k'^2p'^2+k'^2q'^2+4h'k'p'q')f_{20}$
D0.16	$(p^2p'^2-p^2q'^2-q^2p'^2+q^2q'^2+4pqp'q')f_{26}$

where C and A are the moments of inertia about the short and long axes, respectively. The final term in Equation (3.15), p_g, accounts for precession due to general relativity and is very small in most cases. The symbol p_A refers to the precession angle, defined as $p_A = \Lambda - \Omega$, where Λ is the angle between the vernal point Υ, the position of the sun/host star at the planet's northern spring equinox, and the location of the ascending node, Ω, measured from some reference direction Υ_0 (often taken to be the direction of the vernal point at some reference date, hence the use of the symbol Υ[1]), see Figure 3.1. The convention of defining Υ as the location of the sun at northern spring equinox is sensible for the solar system since we observe from Earth's surface, however, it is a confusing definition to use for exoplanets, for which the direction of the rotation axis is unknown. We adhere to the convention for the sake of consistency with prior literature. In the coming decades, it may become possible to determine the obliquity and orientation of an exoplanet's spin axis; in that event, care should be taken in determining the initial p_A for obliquity modeling. One can equivalently refer to Υ as the position of the planet at its northern spring equinox $\pm 180°$. The relevant quantity for determining the insolation, however, is the angle between periastron and the spring equinox, $\omega + \Lambda = \varpi + p_A$.

An additional complication for obliquity evolution is, of course, the presence of a large moon. We do not include the component of the Kinoshita (1975) model that accounts for the lunar torque because the coefficients used are specific to the Earth-Moon-Sun three body problem and were calculated from the Moon's orbital evolution (and are therefore not easily generalized). However, we can approximate the effect of the Moon by *forcing* the precession rate (Equation (3.17)) to be equal to the observed terrestrial value. We do not use this feature of the model in our exploration of exoplanets, but use it to validate our models by reproducing the Earth's obliquity evolution.

Equation (3.15) for the precession angle contains a singularity at $\psi = 0$. To avoid numerical instability, we instead recast Equations (3.15) and (3.16) in terms of the rectangular

[1]The vernal point occurred in the constellation Aries during Ptolemy's time, thus it is also called the "first point of Aries" and the "ram's horn" symbol is used.

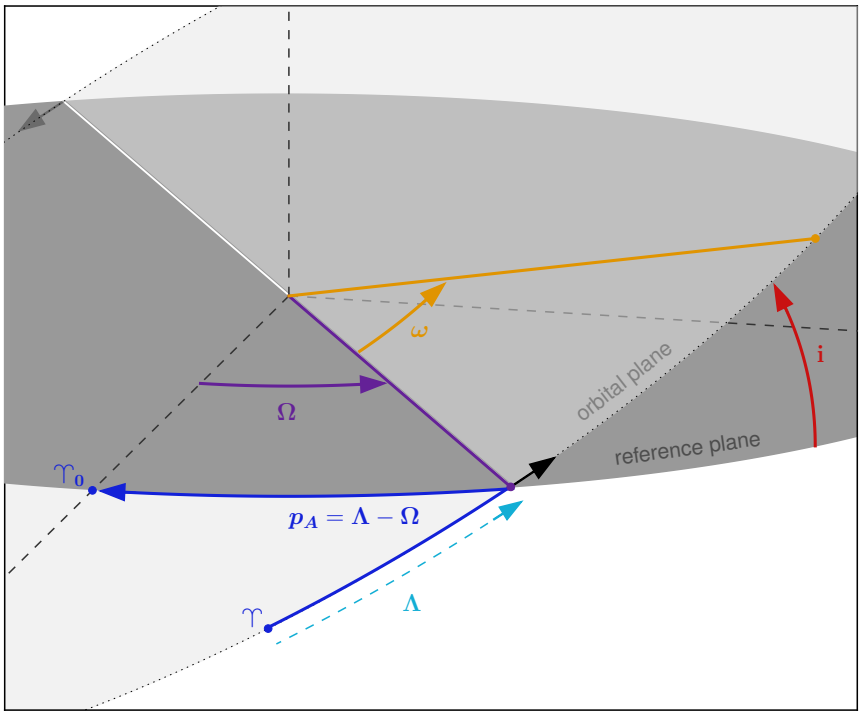

Figure 3.1: Geometry used in the obliquity model, `DISTROT`. The light gray represents the planet's orbital planet, while the darker gray represents a plane of reference. The important orbital angles are the inclination, i, the longitude of ascending node, Ω, and the argument of pericenter, ω. The *longitude* of pericenter is a "dog-leg" angle, $\varpi = \Omega + \omega$. The angle Λ is measured from the vernal point Υ at time t, to the ascending node, Ω. The precession angle is defined as $p_A = \Lambda - \Omega$ (also a dog-leg angle). The reference point for Ω is usually chosen as the vernal point at some known date for solar system, however, there is probably a more sensible choice for exoplanetary systems.

coordinates:

$$\xi = \sin\psi \sin p_A \tag{3.23}$$

$$\zeta = \sin\psi \cos p_A \tag{3.24}$$

$$\chi = \cos\psi. \tag{3.25}$$

The third coordinate, χ, is necessary to preserve sign information when the obliquity crosses 90° (see Laskar et al., 1993a). The equations of motion for these variables are then:

$$\frac{d\xi}{dt} = -B(p,q)\sqrt{1-\xi^2-\zeta^2} + \zeta[R(\psi) - 2\Gamma(p,q) - p_g] \tag{3.26}$$

$$\frac{d\zeta}{dt} = A(p,q)\sqrt{1-\xi^2-\zeta^2} - \xi[R(\psi) - 2\Gamma(p,q) - p_g] \tag{3.27}$$

$$\frac{d\chi}{dt} = \xi B(p,q) - \zeta A(p,q). \tag{3.28}$$

The dynamical ellipticity is a function of the planet's rotation rate and density structure. In hydrostatic equilibrium, the Darwin-Radau relation (Cook, 1980; Murray & Dermott, 1999) shows that the planet's gravitational quadrupole moment, J_2, scales with the rotation rate squared. Earth is very close to hydrostatic equilibrium, while Mars and the Moon are not. For the purposes of this study, we assume that planets are in hydrostatic equilibrium, and scale J_2 according to:

$$J_2 = J_{2\oplus}\left(\frac{\nu}{\nu_\oplus}\right)^2\left(\frac{R}{R_\oplus}\right)^3\left(\frac{M}{M_\oplus}\right)^{-1}, \tag{3.29}$$

where ν is the rotation rate, R is the mean planetary radius, and M is its mass, and Earth's measured values of $J_{2\oplus}$, $\nu_\oplus$, $R_\oplus$, and $M_\oplus$ are used for reference. This is identical to the method used by Brasser et al. (2014). Like that study, we assume that J_2 cannot go below the measured value of Venus from Yoder (1995), which would ordinarily occur at rotation periods $\gtrsim$ 13 days. The assumption then is that there is a limit to hydrostatic equilibrium for a partially rigid body, which is difficult to validate, but does not affect our results greatly as most of our parameter space results in J_2 well above this value.

The dynamical ellipticity can be calculated from J_2 and the *specific* polar moment of inertia of a planet, $CM^{-1}R^{-2}$, which is always between 0.2 and 0.4:

$$E_D = \frac{J_2 M R^2}{C} \tag{3.30}$$

Here we assume the $CM^{-1}R^{-2}$ value of the Earth, 0.33, (Cook, 1980). A different assumption for $CM^{-1}R^{-2}$ *will* change the exact values of our results, however, as the moment of inertia should be similar to this value for a terrestrial planet, the overall nature of our results shouldn't change dramatically.

3.2.4 Cassini state theory

The coupling of the obliquity model and the orbital model allows for the appearance of Cassini states, and indeed, we do see several of their features in our simulations. These special rotation states will have implications for obliquity evolution and climate, and so it is worth reviewing the theory here.

A planet or satellite is in a Cassini state if Cassini's laws (initially described in reference to the Moon) are satisfied. Cassini's laws, generalized and paraphrased here, are: 1. The planet or satellite is in a spin-orbit resonance, such as the synchronous rotation of the Moon, or the 3:2 resonance of Mercury. 2. The planet's or satellite's obliquity is approximately constant, with respect to an appropriate plane of reference, such as the invariable plane (the plane perpendicular to the total angular momentum) of the planetary system or the Laplace plane of the satellite (defined by the host planet's orbit and equator). 3. Three vectors, the spin angular momentum of the planet or satellite, its orbital angular momentum, and the perpendicular to the reference plane from the second law, are approximately coplanar at all times.

Though Cassini wrote these laws in reference to Earth's Moon, these were later generalized by Colombo (1966) and Peale (1969) and found to apply to Mercury and other natural satellites of the solar system. The Cassini state theory developed by these later authors is elegant and mathematically rigorous and can be used to describe the trajectory of a body's

spin axis as it evolves toward or around any of four unique Cassini states. The theory can be applied when the body is not actually within one of the Cassini states, provided that the obliquity evolution is dominated by the central torque and a single perturbing frequency (see Ward & Hamilton, 2004; Hamilton & Ward, 2004). When the theory applies, the body's spin axis will oscillate about one of the Cassini states and Cassini's third law may be satisfied, even when the first two are not. A damping force, such as tidal friction, can drive the body into its ultimate state which satisfies all three of Cassini's laws, hence the prevalence of Cassini states among the solar system satellites.

The conditions specified by the first two laws are easily identified in dynamical simulations of obliquity and orbital evolution. The third law can be identified by invoking the following relation, from Hamilton & Ward (2004):

$$\sin\Psi = \left\| \frac{(\mathbf{K}\times\mathbf{H})\times(\mathbf{s}\times\mathbf{H})}{|\mathbf{K}\times\mathbf{H}||\mathbf{s}\times\mathbf{H}|} \right\|, \tag{3.31}$$

where $\mathbf{K}$, $\mathbf{H}$, and $\mathbf{s}$ are the vectors associated with the perpendicular to the appropriate reference plane (the invariable plane or Laplace plane, for example), the angular momentum of the body's orbit, and the angular momentum of the body's rotation. Alternatively, the complimentary relation can be used:

$$\cos\Psi = \frac{(\mathbf{K}\times\mathbf{H})\cdot(\mathbf{s}\times\mathbf{H})}{|\mathbf{K}\times\mathbf{H}||\mathbf{s}\times\mathbf{H}|}. \tag{3.32}$$

In a Cassini state, Cassini's third law states that the angle Ψ will librate about 0° or 180°, and so we would expect to see $\sin\Psi \sim 0$ and $\cos\Psi \sim \pm 1$. Note that there is a 180° ambiguity in the determination of Ψ by this method, because of the degeneracy in the cross product in Equation (3.31). This makes it slightly more tricky to determine when Ψ is circulating, as it would outside of a Cassini state—essentially, 360° circulation and libration with 180° amplitude will look similar in $\sin\Psi$ and $\cos\Psi$. However, if the amplitude of libration reaches $\sim 180^\circ$, the planet is relatively far from the Cassini state, and hence we will assume that if $\sin\Psi$ and $\cos\Psi$ explore all allowed values, the planet is not in a Cassini state.

3.2.5 Initial conditions

Our first test system, which we will refer to as SYS1, is one with a warm Neptune mass planet, an Earth-mass planet in the habitable zone, and a 1.5 M_{Jup} planet exterior to the HZ. This system is loosely based on HD190360, which contains a Neptune-mass planet and the super-Jovian, and appears to have a stable habitable zone (assuming the minimum masses and that there are no additional planets between the two known planets). The initial conditions and parameter space we explore for SYS1 are shown in Table 3.2. We fix the parameters of the two known planets and vary the initial eccentricity, inclination, rotation rate, and obliquity of the Earth-mass planet. The angle p_A we explore briefly in 90° intervals. For the sake of simplicity, we assume the planets 1 and 3 are roughly coplanar.

Table 3.2: Initial conditions for **SYS1**

Planet	1	2	3
m ($M_\oplus$)	18.75	1	487.81
a (au)	0.1292	1.0031	3.973
e	0.237	0.001-0.4	0.313
i (°)	1.9894	0.001-35	0.02126
ϖ (°)	353.23	100.22	181.13
Ω (°)	347.70	88.22	227.95
P_{rot} (days)		0.1667-10	
ψ (°)		0-90	
p_A		281.78	

The second planetary system we explore is that of Kepler-62, a K type star with 5 known transiting planets (Borucki et al., 2011, 2013). The outer-most planet, f, is particularly inter-

esting for the purposes of this study because it is in the habitable zone and far enough from the star to potentially have any spin-state (as opposed to tidally-locked and zero obliquity) (Bolmont et al., 2015).

Since the eccentricities and inclinations of these planets are well constrained, we use the masses from Bolmont et al. (2015) (their stable case $\mathscr{B}$), and eccentricities and inclinations from Borucki et al. (2013), varying the obliquity, and rotation rate of planet f. The longitude of pericenter, ϖ, was randomly chosen for each planet, while the longitude of ascending node, Ω, was set to zero to keep the planets very coplanar. The orbital and spin properties are given in Table 3.3. Since Bolmont et al. (2015) showed that general relativistic corrections are important to the stability of this system, we include those here according to Equations (3.9) and (3.10).

Table 3.3: Initial conditions for Kepler-62

Planet	b	c	d	e	f
m ($M_\oplus$)	2.72	0.136	14	6.324	3.648
a (au)	0.0553	0.0929	0.12	0.427	0.718
e	0.071	0.187	0.095	0.13	0.094
i (°)	89.2	89.7	89.7	89.98	89.9
ϖ (°)	178.175	138.074	151.127	312.615	276.2767
Ω (°)	0	0	0	0	0
P_{rot} (days)					0.25-20
ψ (°)					0-90
p_A (°)					0

3.3 Model Validation

The orbital and obliquity models, `DISTORB` and `DISTROT` are validated by comparison with N-Body integrators and known results for the obliquity evolution of solar system bodies (Laskar et al., 1993a,b). The obliquity evolution of Mars and a moonless Earth are in good agreement with these studies. We also find good agreement between our model and Earth *with* a Moon when we force Earth's precession rate to equal the observed value of 50.290966 arcsec year^{-1} (Laskar et al., 1993a).

One comparison with N-body, using our first test system from Section 3.4, is shown in Figure 3.2. The N-body integration was done using the GPU code GENGA (Grimm & Stadel, 2014). For the N-body results, the obliquity evolution was done using the code used in Armstrong et al. (2014), to provide a comparison to our new code `DISTROT`.

The largest source of error between the secular models, `DISTORB` and `DISTROT`, comes from a slight offset in the frequencies, which we see as a drift in phase in Figure 3.2. This is simply because some mean motion effects, such as minor variations in the semi-major axes of the planets, are neglected in the secular model. Overall, the secular model captures the general behavior (amplitudes of the oscillations and approximate frequencies) very well. The advantage of the secular model is that it can run millions of years in seconds, compared to hours with the N-body model, allowing us to explore wide regions of parameter space. When necessary or advantageous, we also perform the integrations using the N-body formulation.

3.4 Results

We apply our model to handful of simple planetary test systems, orbiting K and G stars, which reveal a wealth of dynamical (and potentially climatic) phenomena.

3.4.1 Test System 1

We see with SYS1 that the presence of a gas giant with significant eccentricity has a dramatic effect on the eccentricity, inclination, and obliquity of an Earth-mass planet. Interestingly,

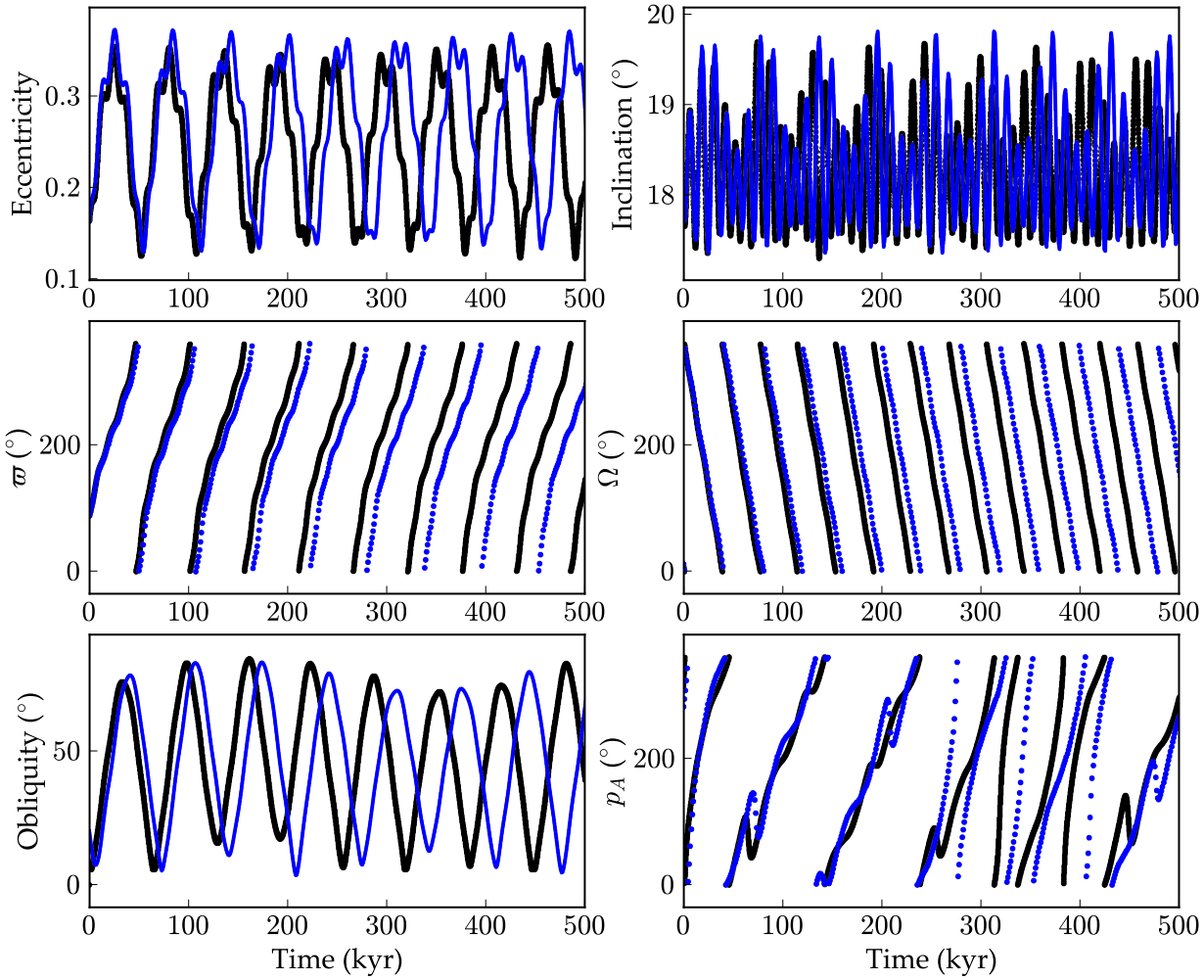

Figure 3.2: Orbital and obliquity evolution for a case in our test system 1 (Section 3.4.1), comparing our secular model (blue) to an N-body model (black). There is some drift between the two solutions. Nevertheless, the secular model does a good job reproducing the general behavior of the system, in a small fraction of the computation time.

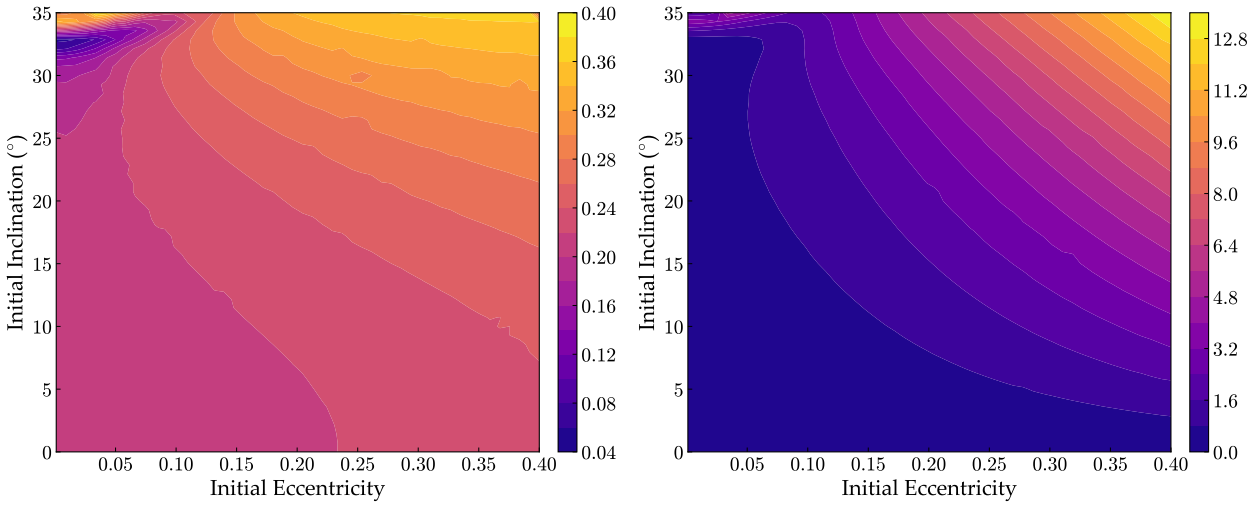

Figure 3.3: The amplitude of the eccentricity oscillation (left) and inclination oscillation (right) for the Earth-mass planet in SYS1 over our e/i parameter space (Table 3.2). In general, eccentricity and inclination vary more strongly as the initial values increase. The inclination oscillation directly affects the planet's obliquity.

the inner-most planet turns out to have a minimal effect on the dynamical evolution of the Earth-mass planet.

Figure 3.3 shows the amplitudes (maximum - minimum) of the eccentricity and inclination oscillations of the Earth-mass planet, over the range of initial eccentricities and inclinations we explored, for 2 Myr simulations. The inclination oscillations directly affect the obliquity, as we will explain below. The eccentricity affects the precession rate through Equation (3.17). In general, raising the initial eccentricity or inclination (and hence, the mutual inclination between planets 2 and 3) increases the size of these oscillations. A nonlinear feature appears at low eccentricity and high inclination, but otherwise the relationships appear as we expect from the 4th order secular theory—increasing e or i increases the oscillations in both variables.

The panels of Figures 3.4-3.6 show the maximum change in obliquity of the Earth-mass planet in several interesting regions of this parameter space. In general, the amplitude of

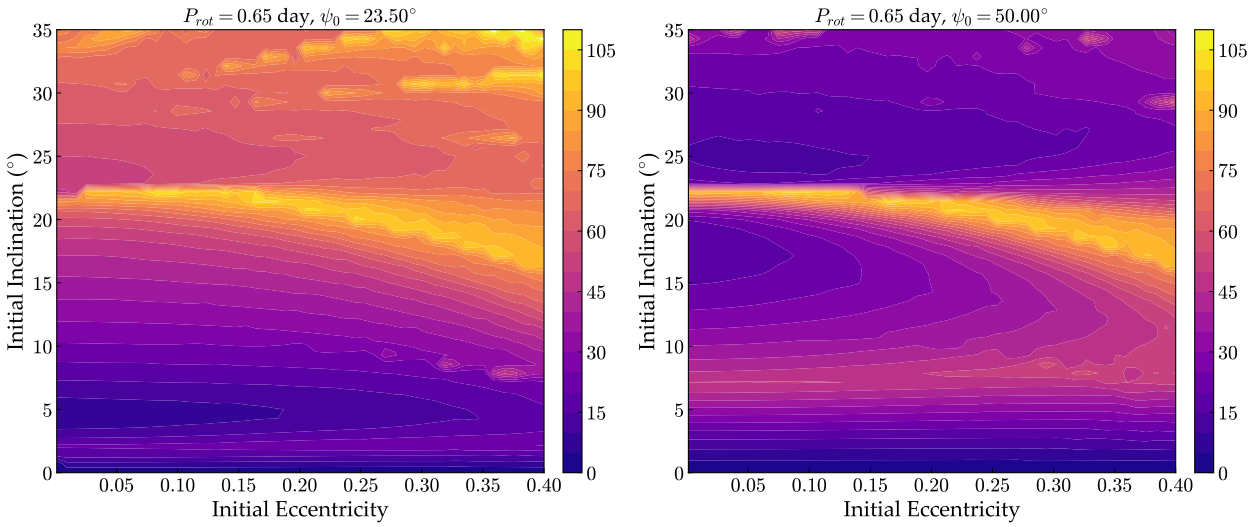

Figure 3.4: Amplitude of the obliquity oscillation for the Earth-mass planet in SYS1, over our e/i parameter space, for two initial obliquities and $P_{rot} = 0.65$ day. The left hand panel corresponds to an initial obliquity of 23.5° and the right to initial obliquity of 50°. The obliquity oscillation is largest within the curved "arc", which is the result of secular spin-orbit resonance, reaching $\sim 110°$. Minima occur at low inclinations (as expected), and within an area at low e that moves upward with initial obliquity. The latter corresponds to a nearby Cassini state (see text).

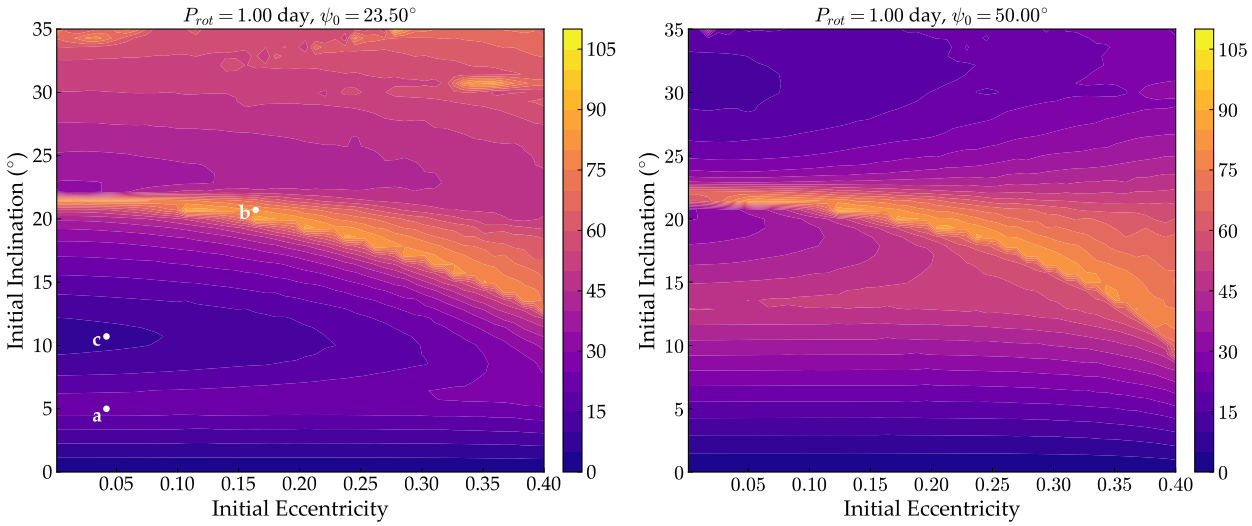

Figure 3.5: Same as Figure 3.4, but for $P_{rot} = 1$ day. The shapes and locations of the secular resonance and Cassini state have changed slightly.

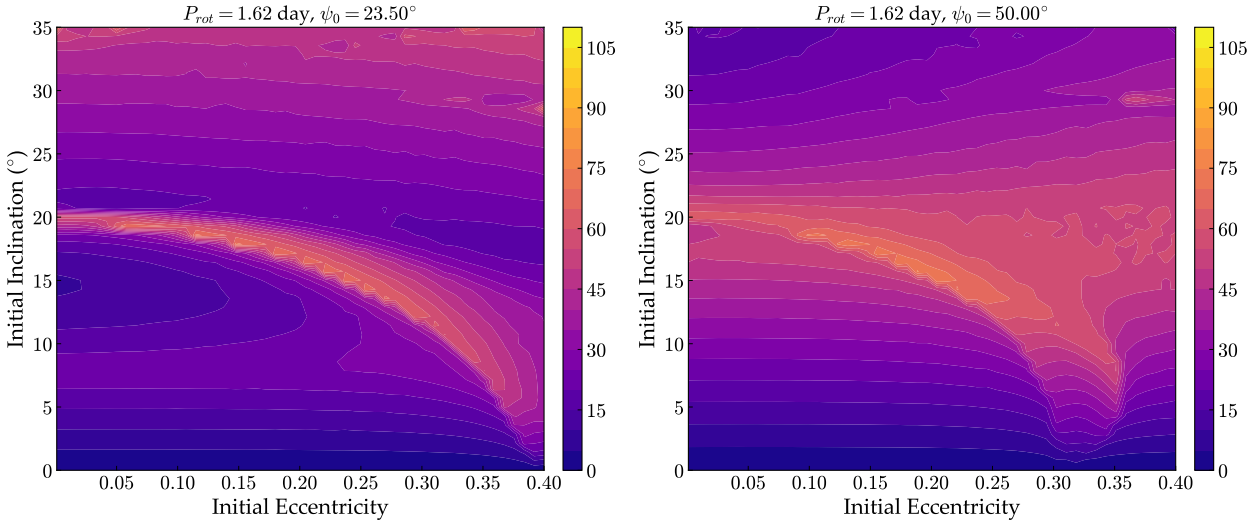

Figure 3.6: Same as Figure 3.4, but for $P_{rot} = 1.62$ day. Again, he shapes and locations of the secular resonance and Cassini state have changed slightly.

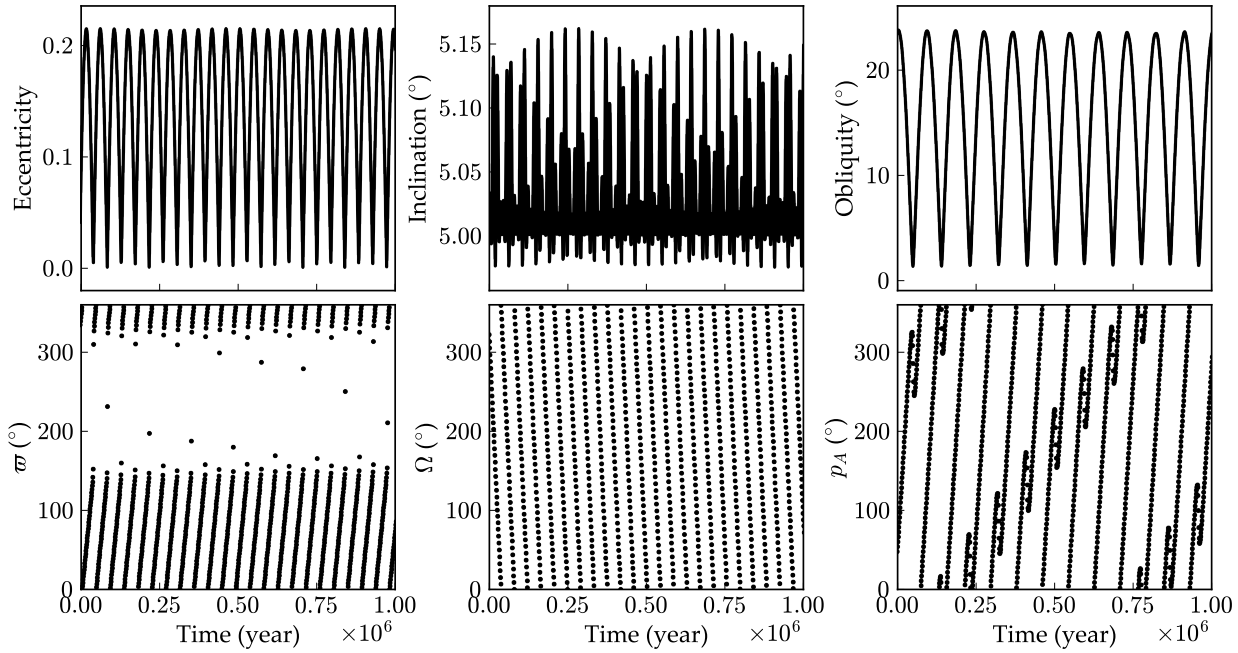

Figure 3.7: Orbital and obliquity evolution for the Earth-mass planet in SYS1, outside the secular resonance (point **a** in Fig. 3.5)

the obliquity oscillation is expected to be related to the size of the inclination variation (which increases with initial inclination) (see Ward, 1992). We do see that this amplitude increases with the initial inclination, particularly with initial obliquity of 23.5° (left-hand panels), however, there are other noteworthy regions that have substantially larger obliquity oscillations. In particular, there is a curved feature (the "arc") across the center of each plot in which the obliquity oscillates by $\sim 70°$ to $\sim 110°$, and a minimum that appears below the arc in the left hand panels (see point **c**), and appears on either side of the arc in the right hand panels. As we will show, the prominent arc is a result of a secular spin-orbit resonance (Ward, 1992), while the minimum (point **c**) is associated with a Cassini state (see Section 3.2.4).

In the absence of a large moon (like Earth's) and strong tidal forces (which will damp the obliquity of short period planets (Heller et al., 2011)), there are two components to

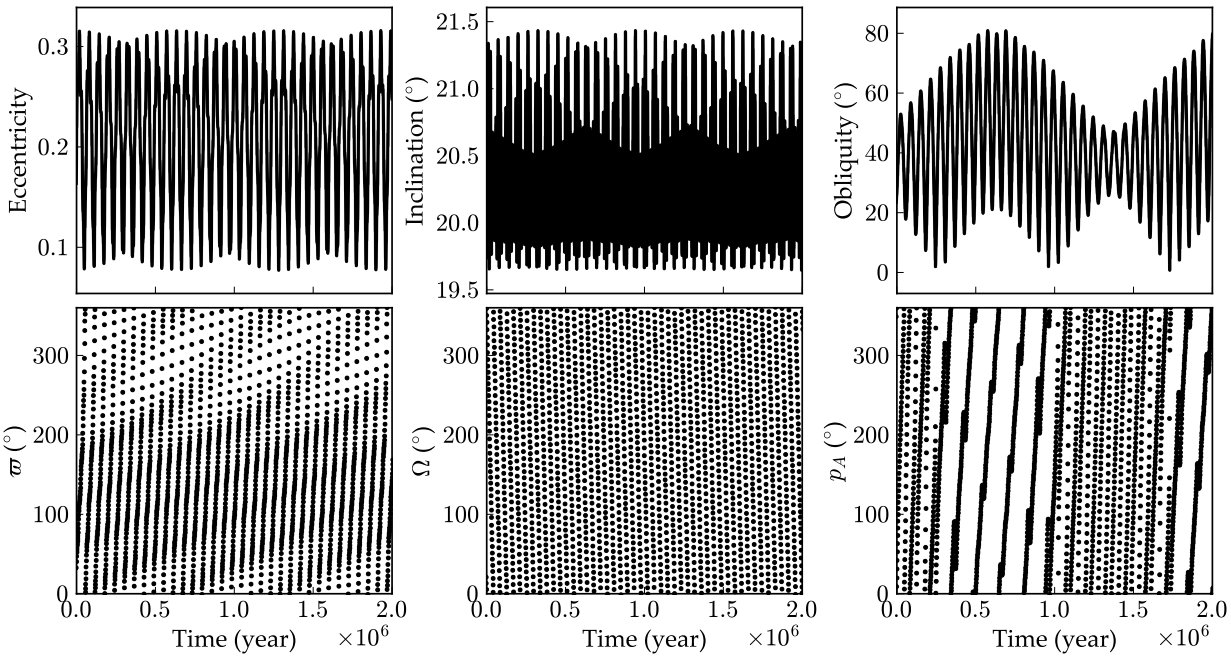

Figure 3.8: Same as Fig. 3.7, but for a configuration within the secular resonance (point **b** in Fig. 3.5)

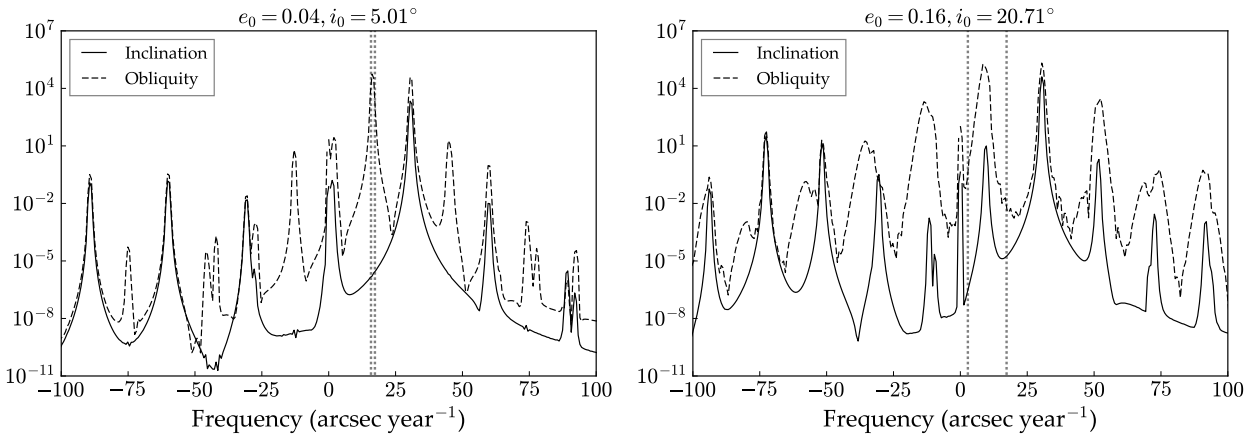

Figure 3.9: Power spectra of the obliquity and inclination evolution for the Earth-mass planet in SYS1, at points **a** (left) and **b** (right). The vertical dotted lines correspond to the minimum and maximum *natural* axial precession rates (Equation (3.17)). Outside the secular resonance, the axial precession frequency fall in between peaks in the inclination spectrum. Within the resonance, this natural precession frequency falls right on top of an inclination peak at 10 (arcsec year^{-1}).

the motion of the planet's spin axis. The first is the precession due to torques from the host star acting on the planet's equatorial bulge. This precession rate is given by Equation (3.17), though in many cases the eccentricity factor can be neglected (as in much of the literature). The functional form of Equation (3.17) gives us a general sense of the behavior of the precession with the different parameters. The precession rate increases with the mass of the host star, $M_\star$, the dynamical ellipticity of the planet, E_D, the eccentricity of its orbit, and rotation rate, ν (since $E_D \propto \nu^2$). The precession rate decreases with obliquity, ψ, and the semi-major axis, a. In the absence of perturbations on the planet's orbit, the spin axis will precess, but the obliquity angle will remain constant.

The second driver of obliquity evolution is the change in inclination as a result of gravitational interactions with other planets. This takes the form of the derivatives $\dot{p}$ and $\dot{q}$ in Equations (3.19-3.21). As the inclination varies, the spin angular momentum is conserved, directly changing the obliquity angle. The combination of the motion of the orbital plane and the axial precession gives rise to complex (and often chaotic) behavior (e.g. Laskar et al., 1993b).

A secular spin-orbit resonance occurs when the natural precession period is close to a strong period of oscillation in the inclination, and is thought to be partly responsible for the large amplitude obliquity oscillations of Mars (Ward, 1992; Laskar et al., 2004). In this case, the obliquity variation is similar to a driven harmonic oscillator, where the axial precession rate is analogous to the natural frequency of the oscillator and the inclination variation is analogous to the driving force. When the oscillator is driven at a frequency close to the natural frequency, resonance occurs. The analytical solutions in Ward (1992) and Atobe et al. (2004) illustrate why this occurs mathematically: the difference between the two frequencies appears in the denominator of the solution for the obliquity, resulting in a small divisor when the frequencies are close. However, as we discuss in Section 3.5, the 2nd order orbital theory used in some studies fails to predict the resonance we see here because it does not consider the e and i dependence of the frequencies.

Figure 3.7 shows the orbital and obliquity evolution for a case with initial eccentricity

$e = 0.0417$ and initial inclination $i = 5°$. This case is from the horizontal band in Figure 3.5 with obliquity, $\psi = 23.5°$ and rotation period of 1 day (point **a**). Figure 3.8 shows the same orbital parameters, but for initial eccentricity $e = 0.164$ and initial inclination $i = 20.71°$, which is within the arc in Figure 3.5, left middle (point **b**). Note that the orbital parameters plotted here are calculated with respect to the invariable plane of the system.

The obliquity evolution is particularly dramatic in Figure 3.8, within the secular resonance. We see that over ~ 1.5 Myrs, the planet experiences obliquities from nearly zero to 80°. Such variations, along with the somewhat large oscillations in eccentricity, would have a large influence on the climate of a planet with an atmosphere similar to Earth's.

An interesting component to this evolution is that the obliquity and eccentricity evolve with nearly the same frequency, in sync with each other. It would seem then that the variation in e is tightly coupled to the variation in i, which drives the obliquity, and hence all three evolve more-or-less in lock step.

Figure 3.9 shows power spectra for both of the cases. The vertical dashed lines represent the natural precession frequency as calculated from Equation (3.17) at the minimum and maximum obliquity over the 2 Myr simulation. The curves show the power calculated from the obliquity variables, $\zeta + \sqrt{-1}\xi$, and the inclination variables, $q + \sqrt{-1}p$. Note that we have inverted the sign of the frequencies in the inclination variables, because the resonance occurs when the frequencies in obliquity and inclination are opposite in sign. This can be seen by rewriting Equations (3.15) and (3.16) in terms of i and Ω instead of p and q (see Laskar, 1986). The longitude of ascending node, Ω, and the precession angle, p_A appear together inside sine and cosine functions as $\Omega + p_A$.

In both panels, the dominant inclination peaks appear in the obliquity power spectrum because they drive the obliquity, as explained above. We can see in the case on the left that the natural precession rate (vertical dashed lines) falls in a valley between several strong inclination peaks, indicating that this case is not in a secular spin-orbit resonance. Interestingly, the inclination forcing is slightly stronger than the natural precession rate.

In the case shown in the right hand panel of Figure 3.9, the natural precession rate falls

directly on top of one of the secondary inclination peaks. This case is a true secular spin-orbit resonance. Refering back to Figure 3.8, we can see that the obliquity response is indeed very strong as a result of the resonance, evolving from a relatively small oscillation of about $\sim 40^\circ$ to an almost 80° swing.

We also tested different starting precession angles in 90° intervals, to see what effect this parameter has. The secular resonance in this parameter space is insensitive to p_A, and appears in all orientations of the equinox ($p_A = 11.78^\circ, 101.78^\circ, 191.78^\circ, 281.78^\circ$). However, the minimum in Figure 3.5 (in which point **a** is located) disappears for $p_A \neq 281.78^\circ$. As we will discuss further in Section 3.4.3, we observe that 2 of Cassini's laws (Colombo, 1966) appear to be satisfied in and around this minimum feature (points **a** and **c**). It appears then that $p_A = 281.78^\circ$ places the planet near a Cassini state, while the other precession angles we tested are far from it.

Since we cannot reasonably show all of the parameter space here, we briefly describe how the features change. In general, low initial obliquity cases tend to have the largest obliquity oscillations, reaching amplitudes of $\Delta\psi \sim 120^\circ$. The secular resonance remains present across all initial obliquities $< 90^\circ$, and its shape and location change only slightly. The rotation rate appears to be the most important parameter for governing the appearance of the resonance, which disappears at $P_{rot} \lesssim 0.4$ days and $P_{rot} \gtrsim 4$ days.

We can see the effect of rotation in Figure 3.10, which shows the obliquity amplitude as a function of initial obliquity and rotation period, with the eccentricity and inclination fixed to values inside the arc in Figure 3.5. The secular resonance appears here as a strong vertical bar around $P_{rot} = 1$ day. At longer rotation periods and about 20° initial obliquity, we are again in proximity to a Cassini state, wherein the obliquity oscillation approaches a minimum value.

3.4.2 Test System 2: Kepler-62

Figure 3.11 shows the amplitude of the obliquity oscillation for Kepler-62 f, as a function of its initial obliquity and its rotation period. Interestingly, there is a clear secular spin-

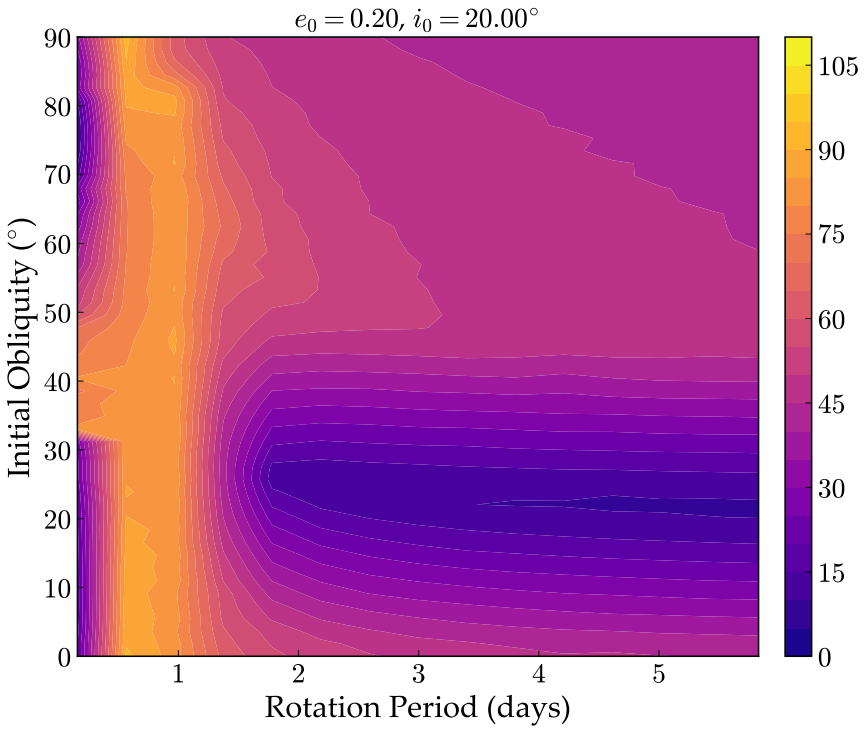

Figure 3.10: Amplitude of the obliquity oscillation for the Earth-mass planet in SYS1 as a function of initial obliquity and rotation period. The initial eccentricity and inclination are fixed, so that the orbital evolution is identical for every point within this figure. The secular resonance appears as a bright vertical band at ~ 1 day. A minimum appears at $P_{rot} \gtrsim 5$ days and obliquity $\psi_0 \sim 20°$.

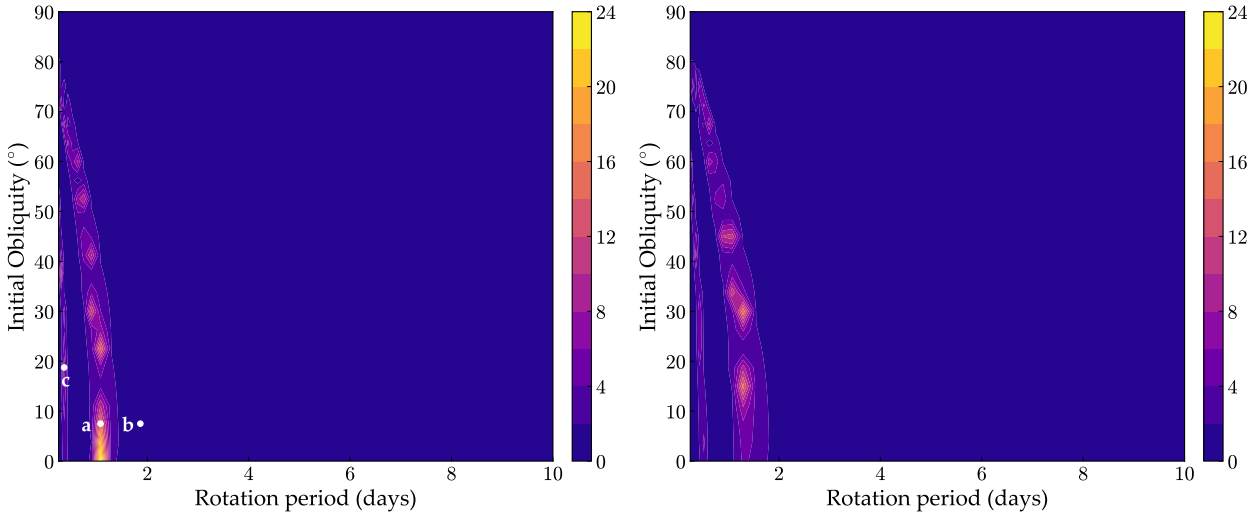

Figure 3.11: Amplitude of the obliquity oscillation for Kepler-62 f as a function of the initial obliquity and rotation period, for the stable orbital configuration from Bolmont et al. (2015). The left panel shows the solution from our secular models `DISTORB` and `DISTROT`, and the right panel shows the same solution achieved by coupling `HNBody` to `DISTROT`. Secular resonances appear at rotation periods $\lesssim$ 2 days. These are slightly shifted in the N-body solution compared to the secular solution, because of the small orbital time-scale variations in the semi-major axes of the planets.

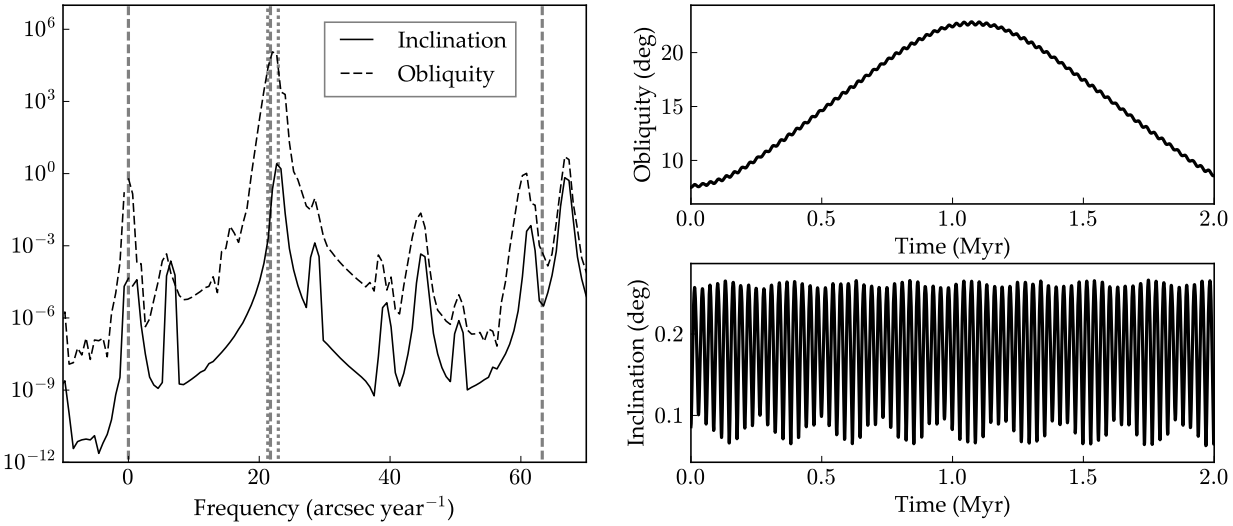

Figure 3.12: Power spectra for the obliquity and inclination evolution (left) for Kepler-62 f, in larger secular resonance in Fig 3.11 (point **a**). The vertical dotted lines are the natural axial precession frequency from Equation (3.17) and the vertical dashed lines are the inclination eigenvalues from the Laplace-Lagrange solution. As with the secular resonance in SYS1, the natural precession rate is approximately equal to one of the inclination frequencies. In this case, it corresponds to one of the eigenvalues. The left panels show the obliquity and inclination evolution over 2 Myr.

orbit resonance in this parameter space, visible as a bright arc. This appears to be almost identical to the secular spin-orbit resonance identified for the planet HD40307 g in Brasser et al. (2014) (see Section 3.4.3), suggesting that such resonances may be a common feature of packed super-Earth/mini-Neptune systems.

Figure 3.12 shows the obliquity and inclination evolution of planet f, as well as a periodogram of the obliquity and inclination frequencies, at initial obliquity of 7.5° and a rotation period of 1.077 days. The natural precession frequency is very close to one of the frequency peaks in the inclination—an indication of spin-orbit resonance. We see the obliquity slowly rise from zero to about 25° over $\sim$ 1.5 Myr. In contrast, a slightly longer rotation period

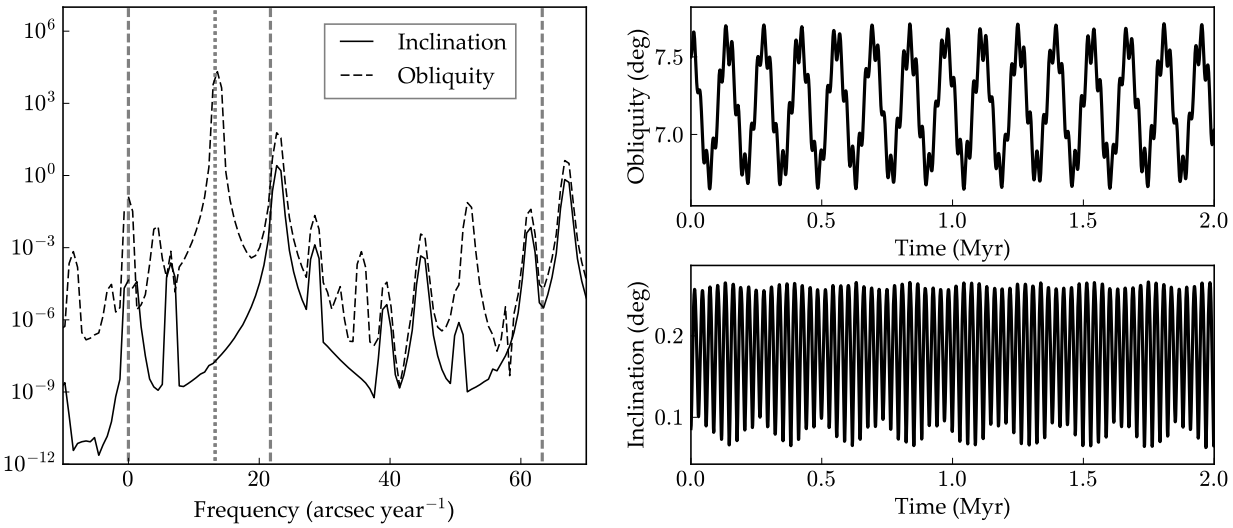

Figure 3.13: Same as Fig. 3.12, but outside the secular resonances (point **b**). The axial precession rate falls in between inclination frequency peaks.

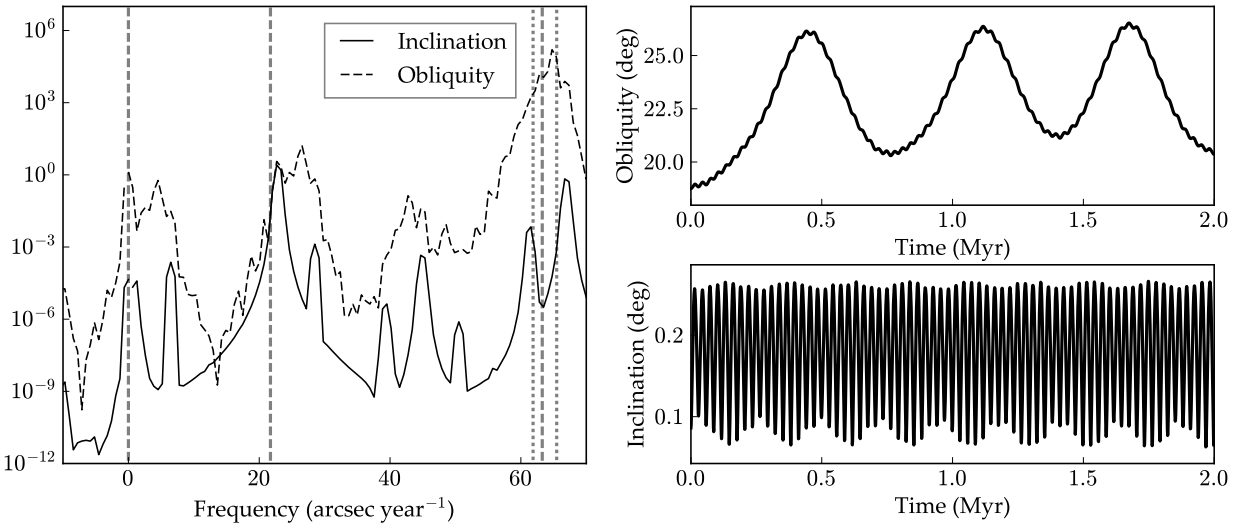

Figure 3.14: Same as Fig. 3.12, inside the smaller secular resonance in Fig. 3.11 (point **c**). The axial precession rate falls close to two peaks in the inclination evolution, which correspond to a single eigenvalue.

(1.86 days) produces the behavior in Figure 3.13. Here, the axial precession frequency is close to the same peak in inclination, but far enough that the resonant behavior and resulting obliquity oscillation are not as strong.

Following the example of Atobe et al. (2004), we can calculate the eigenvalues associated with the Lagrange-Laplace linearized solution. These eigenvalues correspond to secular frequencies in the lowest order solution to the N-body problem (see Murray & Dermott, 1999). The eigenvalues for this system are listed in Table 3.4, where g_i are associated with the eccentricity and f_i are associated with the inclination. Spin-orbit resonances will appear whenever the axial precession is close to (and opposite in sign) the inclination eigenvalues, f_i. The secular resonance above occurs because planet f's precession rate is close to $-f_4 = 21.71$ arcsec year^{-1}.

Table 3.4: Eigenvalues for Kepler-62 (secular solution)

	g_i (arcsec year^{-1})	f_i (arcsec year^{-1})
1	4923.54	-4932.41
2	659.46	-681.49
3	76.54	-1.56×10^{-5}
4	53.24	-21.71
5	16.92	-63.27

There is a second secular resonance in Figure 3.11, which appears as a fainter arc below the previously mentioned one. Again, this can be attributed to another eigenvalue: $-f_5 = 63.27$ arcsec year^{-1}). The obliquity/inclination evolution and frequencies of point **c** inside this resonance are shown in Figure 3.14.

To verify that the secular model is not missing important mean motion effects in the Kepler-62 orbits, we also run a simulation of the system in `HNBody` (Rauch & Hamilton,

Table 3.5: Eigenvalues for Kepler-62 (N-body solution)

	g_i (arcsec year^{-1})	f_i (arcsec year^{-1})
1	4877.92	-4886.79
2	630.38	-681.71
3	75.07	-1.74$\times 10^{-15}$
4	53.21	-21.70
5	16.90	-63.28

2002), which includes general relativistic corrections. We couple the output to `DISTROT` using a finite differencing scheme for the derivatives $\dot{p}$ and $\dot{q}$ in Equations (3.19 - 3.21). In the N-body solution, the eigenvalues vary slightly because the semi-major axes of the planets vary by a small amount over orbital time scales. The average eigenvalues are computed and shown in Table 3.5. The slight shift in the location of the secular resonances between the secular and N-body solution is explained by this shift in the eigenvalues. The difference in amplitudes shown in the two figures is due to the coarseness of the grid spacing—essentially, a grid point lands right on the secular resonance in the secular solution, but lands slightly farther from it in the N-body solution. We recover a maximum obliquity oscillation of $\sim 24^\circ$ if we fine tune the rotation rate in the N-body solution, so that the precession rate lies right on top of the secular resonance.

Like SYS1, we also tested different initial precession angles for planet f in 90° intervals. Like that system, we find that this parameter has virtually no effect on the appearance of the secular resonance, or on the amplitude of the obliquity oscillation.

3.4.3 Cassini States?

In their dynamical analysis of the HD 40307 system, Brasser et al. (2014) noticed the existence of a secular resonance that can amplify the obliquity oscillation of the outermost

planet, depending on the planet's initial obliquity and rotation rate, almost exactly as we find for Kepler-62 f. It is stated in that work that inside the secular resonance, the planet enters a Cassini state. This is a dynamical phenomenon that is worth reviewing and exploring here, as we also see some of the features of Cassini states.

Note that the existence of planet HD 40307 g is currently under scrutiny (Díaz et al., 2016). Even if planet g does not exist, the system as modeled by Brasser et al. (2014) is nonetheless interesting as a test case of dynamical phenomena.

We have modeled the HD 40307 system according to the initial conditions used by Brasser et al. (2014), with a starting p_A of 0°. Plotting the amplitude of the obliquity oscillation of planet g as a function of its initial rotation period and obliquity, we roughly reproduce their Figure 8 (upper left panel) in our Figure 3.15. The left panel of Figure 3.15 shows our results using Laplace-Lagrange 2nd order theory, while the right shows the same using the 4th order model. Our 2nd order solution produces a comparable amplitude obliquity oscillation in the secular resonance to that found by Brasser et al. (2014), but including 4th order terms reduces the amplitude and shifts the resonance to slightly shorter rotation periods. As Brasser et al. (2014) explain, this resonance can be easily identified in the eigenvalue solution, just as we showed for Kepler-62.

It is not clearly explained how these authors determined that planet g (in their simulations) is in a Cassini state *inside* the secular resonance, where the obliquity oscillates by the largest amount. In fact, this claim appears to be at odds with the first two of Cassini's laws. But, as Ward & Hamilton (2004) showed for Saturn, the Cassini state theory may still be applied, if the obliquity evolution is dominated by a single term of the disturbing function (or a single inclination eigenvalue), as is true in the case of strong secular resonance.

Additionally, it is interesting to note that within the secular resonance, the angle Ψ circulates very slowly. In Figure 3.16 we show the evolution of $\cos\Psi$ and $\sin\Psi$ for a point near the resonance (right panel; point **b** in Figure 3.15). $\cos\Psi$ takes about 300 kyr to move through a full cycle. This length of time is extended even further deeper within the resonance (right panel; point **a** in Figure 3.15). Thus if only $\cos\Psi$ is examined over the right window of

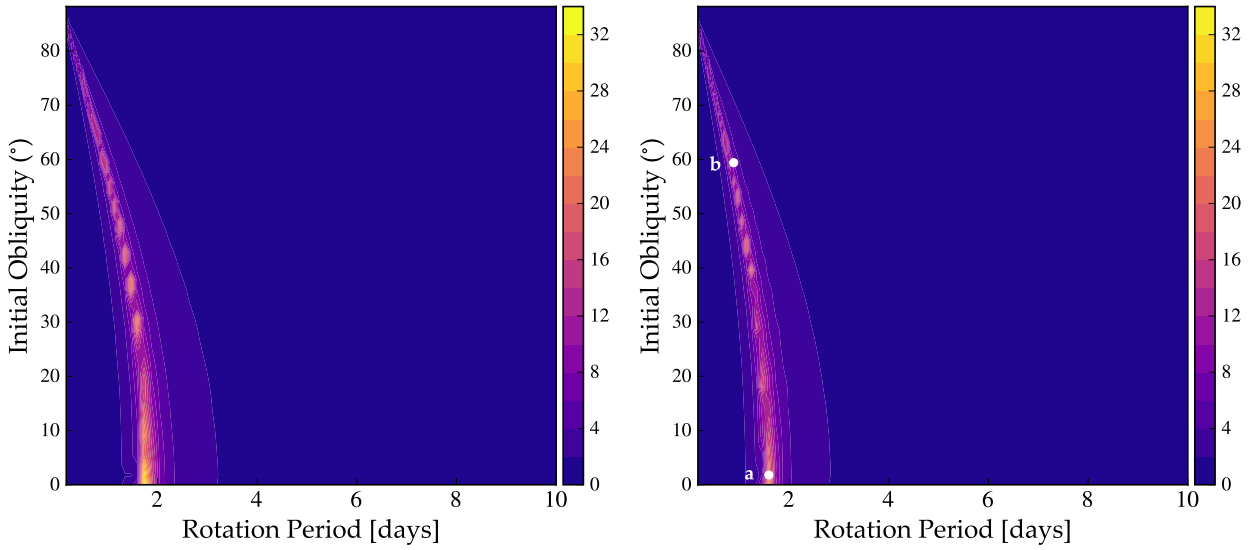

Figure 3.15: Amplitude of the obliquity oscillation for HD40307 g, as a function of initial obliquity and rotation period. Compare to Fig. 8 in Brasser et al. (2014). The left panel is the Laplace-Lagrange eigenvalue solution, the right is the 4th-order numerical solution. There is a secular resonance at rotation rates $\lesssim 2$ days, similar to the for Kepler-62 f in Fig. 3.11.

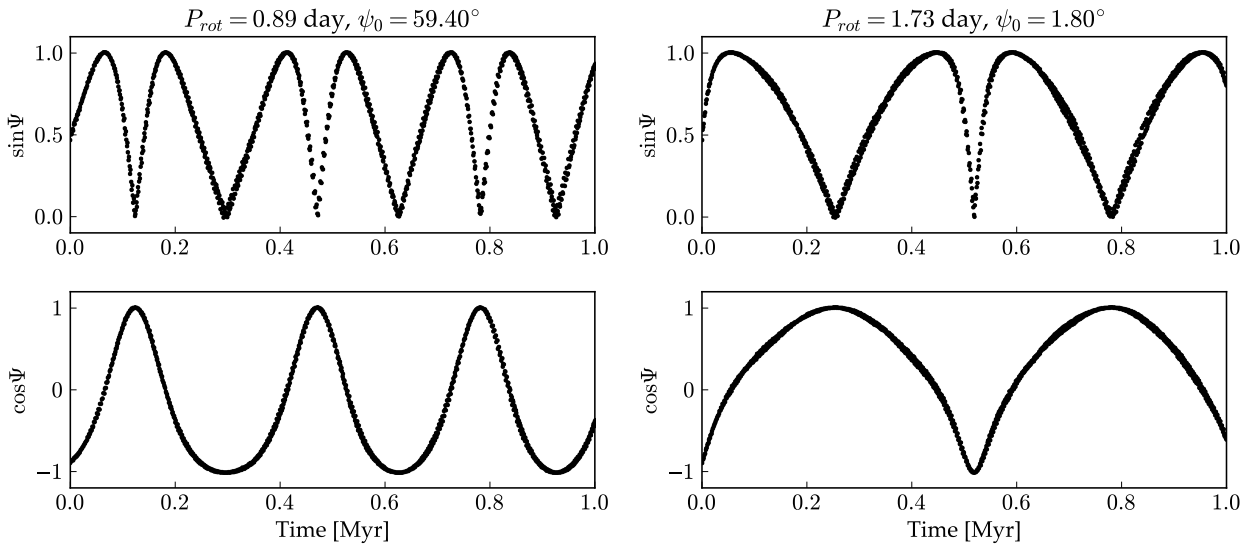

Figure 3.16: Cassini parameters, $\sin\Psi$ and $\cos\Psi$, for HD40307 g, at two different initial rotation states. The left panel corresponds to point **b** in Fig. 3.15, the right panel to point **a**. Cassini's third law says that Ψ will librate about some fixed value in a Cassini state, but in both cases here, $\sin\Psi$ and $\cos\Psi$ extends to all possible values, indicating that the planet is far from a Cassini state.

time, it might appear that the planet is indeed within or close to a Cassini state. However, looking at $\sin\Psi$ and extending the length of time analyzed to ~ 1 Myr or more, we can see clearly that the angle Ψ is circulating, not librating. Thus we argue here that planet g in this example is oscillating about, but is not within, a Cassini state when near this secular resonance. Everywhere outside the resonance, Ψ circulates much more rapidly.

And what about the secular resonance in our SYS1? The similarity between the arc feature in Figures 3.4-3.6 and that in Figures 3.11 and 3.15 is certainly striking. Of course, the HZ planet in these simulations is not tidally locked, and its obliquity evolves significantly in most configurations, so Cassini's first two laws are not satisfied. The third, however, does seem to be satisfied, at certain initial conditions away from the resonance, perhaps because of the simplicity of this system compared with the 5 and 6 planet configurations of Kepler-62 and HD 40307. Figure 3.17 shows $\cos\Psi$ and $\sin\Psi$ for a case within the obliquity amplitude minimum (left; point **c** in Figure 3.5) and a case within the secular resonance arc (right; point **b**). The case on the left satisfies 2 of Cassini's laws—the obliquity oscillation is small and Ψ librates. In the case on the right, inside the secular resonance, we see that the third law appears to be satisfied initially, but as the amplitude of the obliquity oscillation grows, the angle Ψ begins to circulate.

It appears, then, that the minimum seen in the panels of Figures 3.4-3.6 and 3.10 represents the region around a Cassini state. It is probable that with enough tidal damping (which we do not model here), the planet would fully enter the Cassini state, wherein the rotation rate would be in a small integer resonance (e.g., 1:1 or 3:2) with the orbital period, and the obliquity would become fixed, in some cases at a value well above 0°. To our knowledge, the climate of a planet in such a rotation state has not been modeled.

3.5 Discussion

In our simulations of SYS1 and Kepler-62, we see that the amplitude of the obliquity variations is largest in secular spin-orbit resonances, in which the natural precession frequency of the planet's spin axis is near to the frequency of inclination variations. The planet's rotation

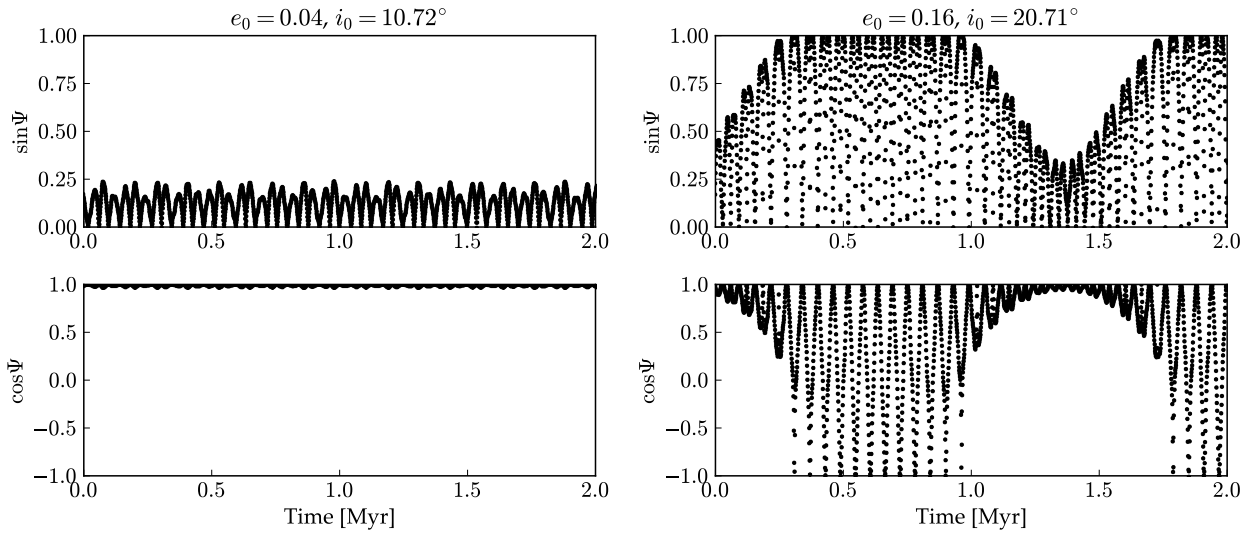

Figure 3.17: Same as Fig. 3.16, but for the Earth-mass planet in our SYS1. The left panel corresponds to point **c** in Fig. 3.5, the right to point **b**. Cassini's third law appears to be satisfied in the left panel—the angle Ψ librates about 0°. It appears at first to be in effect in the right hand panel, however, the secular resonance quickly amplifies the obliquity oscillation, pulling the planet away from the Cassini state, before returning again ~ 750 kyr later.

rate and initial obliquity play an extremely important role, especially in planar systems like Kepler-62. In our SYS1, in which eccentricity and mutual inclination are allowed be somewhat large, we see the appearance of higher order secular resonances that depend strongly on the initial e and i.

As several studies have shown before, variations in orbit and obliquity can have a discernable impact on the surface habitability of Earth-like exoplanets (Spiegel et al., 2010; Armstrong et al., 2014; Bolmont et al., 2016). These studies, along with studies of our solar system, have hinted at the complexity of these dynamical phenomena. In particular, Armstrong et al. (2014) highlighted the power of mutual inclinations between planets to influence obliquities.

While certainly a powerful influence on climate, it is still not clear how likely terrestrial (and possibly habitable) planets are to exist in mutually inclined systems. The triple Jovian system υ Andromedae certainly shows that strongly inclined systems exist, at least for high mass planets (McArthur et al., 2010). Transiting surveys such as *Kepler* have shown the prevalence of compact, coplanar super-Earth systems in the galaxy, however, with this detection method we may be missing many inclined systems. The only truly unbiased way of detecting mutually inclined systems is to use a combination of techniques, such as radial velocity and astrometry, or high-resolution spectrometry to detect molecular lines associated with planets. Thus far, these detection methods cannot reliably probe down to low mass, terrestrial bodies.

On the theory end, numerous studies have shown that instabilities resulting in the loss of one or more planets from a system can result in high inclinations and high eccentricities in the remaining planets (Ford et al., 2005; Raymond et al., 2009; Barnes et al., 2011). Even our own solar system may have had such an event in its early history. The additional complications associated with binary stars and galactic effects (Kaib et al., 2013) add further weight to the idea that many systems will have experienced such scattering events.

While we see here that mutual inclinations do play a role in the obliquity evolution (as in SYS1), we also see that secular resonances play a much more important role. The secular resonance that appears in our SYS1 does appear most strongly at modest inclinations or high eccentricity, but the secular resonance for Kepler-62 f, like that noted by Brasser et al. (2014) for a HD 40307 g, appears in a relatively planar configuration. It would appear that the rotation state and initial obliquity play a very important role in such systems. While there are a number of studies that lay out possible means of determining rotation rate and obliquity for exoplanets (Cowan et al., 2009; Fujii & Kawahara, 2012; Cowan et al., 2013; Schwartz et al., 2016), we are probably a decade or more away for doing sio for small mass planets. In the mean time, modeling studies such as this may be helpful in predicting possible climate states, which may then be verified by visible phase curve observations or spectroscopic detections.

The resonance in SYS1 is particularly curious because of its e/i dependence. The identification of secular resonances in the past has often relied upon the Lagrange-Laplace (eigenvalue/eigenvector) theory, a lowest-order linearization of the N-body problem (the work of Laskar (1985, 1990), however, identified frequencies in a higher order expansion). In that formulation, the secular frequencies are a function of the masses and semi-major axes only—the eccentricities and inclinations of the planets drop out of the linear solution. Hence we only see the appearance and shape of this resonance because we are using a 4th order expansion of the disturbing function.

Though, for simplicity, we model planets without large moons (like Earth's) here, a few words are in order. It is commonly understood that in the absence of our moon, Earth would undergo much large obliquity oscillations than it does (Laskar et al., 1993a; Lissauer et al., 2012; Li & Batygin, 2014). Before we assume that planets which have large moons are safe from large variations, we should consider how it is that Earth's moon actually stabilizes its obliquity. The moon, because of its mass and proximity, induces a torque on Earth's equatorial bulge that is stronger than the Sun's, and this torque significantly increases the planet's axial precession rate. This speed up protects Earth from large obliquity swings, because it is far from the secular frequencies of the solar system, and hence secular spin-orbit resonances are avoided. When we consider the tidal effect of the moon, that is, the slowing of Earth's rotation rate, the matter becomes more complicated. This is because the axial precession rate is a also strong function of rotation rate—in fact, it is predicted that the moon will eventually drag our planet into a secular spin-orbit resonance (Ward, 1982). Furthermore, Earth's rotation rate might be very different without the moon and its tidal tug. Thus, we argue that we should not simply assume that a large moon is beneficial (or detrimental, for that matter) to climate and habitability.

We expect secular resonances of this nature will have a substantial impact on the climate, if the atmosphere is at all similar to Earth's. Figure 3.18 shows the insolation (stellar flux) received by the Earth-mass planet in SYS1, in the secular resonance (point **b**), for three latitudes. The insolation shown here is calculated from the formulae in Berger (1978) and is

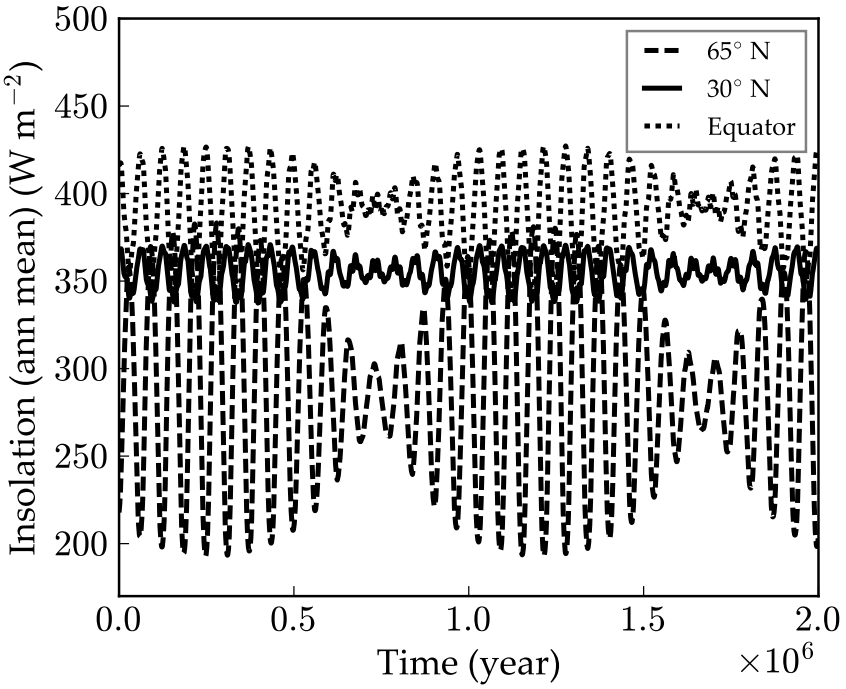

Figure 3.18: Insolation curves over time for the Earth-mass planet in SYS1, at three latitudes, for the secular resonance case. The dashed curve is 65° N, the solid is 30° N, and the dotted is the equator. The insolation is averaged over an orbital period, so the variations are entirely due to changes in obliquity and orbital parameters.

averaged over an orbit. For this calculation, the stellar constant is ~ 1346 W m^{-2}, slightly less than Earth's value. The annual insolation changes dramatically, especially for the poles, as the obliquity and eccentricity oscillate. If a planet like this has surface water, we would expect it to have severe ice age cycles, and ice sheets may not ever be stable on its surface due to the ice-albedo feedback.

3.6 Chapter Summary

I presented a secular model for the orbital and obliquity oscillations associated with planetary perturbations. The speed of the model allows us to explore broad regions of parameter space

and to rapidly identify interesting dynamical phenomena. I apply this model to several test cases of Earth-like (or potentially Earth-like) exoplanets to understand how climate and habitability might be affected by planetary companions. In the following chapter, I apply a simplified climate model to further explore this problem.

I find, in particular, that secular spin-orbit resonances are prevalent, even in systems with only a few planets or with coplanar orbits. Such resonances can potentially have a dramatic impact on climate by inducing strong obliquity variations. In the following chapter, I explore whether such obliquity variations, combined with eccentricity variations and precession, make planets more or less susceptible toward climate states that might be render the surface inhospitable to life.

I must emphasize that planetary systems are extremely complex, and that habitable zones based simply on semi-major axis may be fundamentally limited. In assessing a planet's potential to host life, it is important that companion planets be looked for and considered as possible complications, especially for planets that may have not undergone strong tidal evolution.

The previous chapter on υ Andromedae illustrated how large orbital variations can be in a real exoplanetary system. This chapter demonstrates the importance of companion planets and orbital architecture when assessing the habitability of exoplanets. Used in tandem with climate models, as I show in the next chapter, this type of analysis will provide testable predictions of atmospheric states for upcoming exoplanet characterization missions, and will aid in the interpretation of potential biosignatures.

3.7 Acknowledgements

This work was supported by the NASA Astrobiology Institute's Virtual Planetary Laboratory under Cooperative Agreement number NNA13AA93A. This work was facilitated though the use of advanced computational, storage, and networking infrastructure provided by the Hyak supercomputer system at the University of Washington. The results reported herein benefited from the authors' affiliation with the NASA's Nexus for Exoplanet System Science (NExSS)

research coordination network sponsored by NASA's Science Mission Directorate.

Chapter 4

EXO-MILANKOVITCH CYCLES II: CLIMATE RESPONSE

Here, we examine the climate response of an Earth-like planet (orbiting a G dwarf star) to large orbital and obliquity variations using an energy balance model with ice sheets. We find that ice caps in this scenario couple strongly to the orbital forcing, leading to extreme ice ages. In contrast with previous studies, we find that such exo-Milankovitch cycles tend to impair habitability by inducing snowball states within the habitable zone. This is a result of large amplitude changes in obliquity, which cause the ice edge, the lowest latitude extent of the ice caps, to become unstable and grow to the equator, and the large amplitude changes in eccentricity, which greatly alter the intensity of incoming stellar flux. We apply an analytical theory of the ice edge latitude to our results to determine the fundamental cause of the instability. The thermal inertia of the ice sheets and the spectral energy distribution of the G dwarf star increase the sensitivity of the model to triggering runaway glaciation. This work illustrates the importance of orbital evolution for habitability in dynamically rich planetary systems.

Material in this chapter is in preparation to be submitted to the Astronomical Journal with co-authors Rory Barnes, Cecilia Bitz, David Fleming, Benjamin Charnay, Victoria Meadows, Caitlyn Wilhelm, Thomas R. Quinn, and John Armstrong.

4.1 Introduction

Milankovitch cycles, or orbitally-induced climate variations, are thought to influence, if not control, Earth's ice ages (Hays et al., 1976; Imbrie & Imbrie, 1980; Raymo, 1997; Lisiecki & Raymo, 2007). This mechanism has also been proposed as an important player in the habitability of exoplanets, which may have orbital evolution very different from that of Earth.

In Chapter 1, I discussed much of the work that has been done to understand Milankovitch cycles, both for Earth and for exoplanets. Here, I review the some of that literature more concerned with the modeling of climate than the studies discussed in Chapters 1 and 3.

Milutin Milanković and Wladimir Köppen supplied a plausible explanation for the orbital forcing of Earth's ice ages: small variations in summer-time insolation at high latitudes controls whether ice sheets on the continent grow or retreat. This idea still seems to be generally accepted as at least part of the story (Hays et al., 1976; Roe, 2006; Huybers & Tziperman, 2008; Lisiecki, 2010), though the reality is somewhat more complicated because of geography, ice shelf calving, atmospheric circulation, and changes in greenhouse gases (Clark & Pollard, 1998; Abe-Ouchi et al., 2013), and some recent studies have challenged the role of orbital forcing entirely (Wunsch, 2004; Maslin, 2016).

Much of the controversy surrounding Milankovitch theory stems from the fact that Earth's orbital and obliquity variations are rather small—Earth's obliquity varies by $\sim 2.5^\circ$ and its eccentricity by ~ 0.05. For exoplanets, the role of orbital forcing may be more compelling—many exoplanets have variations that are much larger than Earth's, and there is reasonable evidence that primordial obliquities (*i.e.*, the obliquity after the formation stage) can be very different from Earth's present value (Miguel & Brunini, 2010).

Williams & Kasting (1997) explored the effect of high and low (static) obliquity on Earth-like planets with a 1D energy balance model (EBM), finding that at the present solar flux, the planet can remain habitable (with stable liquid water on its surface), at all obliquities. Williams & Pollard (2002) and Williams & Pollard (2003) further explored the effects of high eccentricity and obliquity with a 3D GCM, finding that in all cases, habitability was maintained, even during excursions beyond the habitable zone due to high eccentricity. Noteably, Williams & Pollard (2003) found that at high obliquity, planets could form permanent ice "belts" at the equator.

These concepts were again explored, over broader regions of parameter space, by Spiegel et al. (2008, 2009) and Dressing et al. (2010). These authors used a 1D EBM, and varied stellar flux in addition to eccentricity and obliquity, to explore how the edges of the habitable

zone (HZ) depend on eccentricity and obliquity. In general, it was found that high obliquity tends to extend the HZ. Likewise with eccentricity, which increases the planet's yearly average insolation.

Spiegel et al. (2010) and Armstrong et al. (2014) explored the climatic response of orbital and obliquity variations (*i.e.*, true Milankovitch cycles), again using 1D EBMs. Spiegel et al. (2010) found that variations in eccentricity can trigger the onset of snowball states (at low e) and subsequent escape from snowball state (at higher e). In other words, surface habitability may be highly variable for exoplanets. Armstrong et al. (2014) explored a number of hypothetical arrangements of planets using an N-Body model, coupled to obliquity evolution and a simple EBM. These authors found that in many cases, the dynamical evolution acts to inhibit widespread glaciation and enhances the extent of the HZ beyond the extension granted by simply having fixed high obliquity or eccentricity.

Ferreira et al. (2014) used a GCM with dynamic ocean heat-transport to investigate climate at high obliquity. As others found before, this study found that planets can remain clement at high obliquity, but unlike Williams & Pollard (2003), did not observe the formation of ice belts.

Bolmont et al. (2016) expanded on the work of Williams & Pollard (2002) and Dressing et al. (2010) with a GCM, exploring the effects of eccentricity on the HZ for different orbital periods. The different orbital periods correspond to the HZs of star of different spectral types, and though those authors adjusted the luminosity of the host star accordingly, they did not account for the difference in spectral energy distributions, which greatly affects the albedo of ice. As before, they showed that excursions beyond the HZ due to eccentricity are not a death-sentence to most planets. However, they also found that for planets orbiting in the HZ of early-type stars, high eccentricity can induce snowball states because the planet spends so long at apoastron.

Forgan (2016) studied Milankovitch cycles of circumbinary planets (*i.e.* planets orbiting two tightly bound stars). In this case, the planet's climate is driven not only by its own orbital variations, but also the constantly changing distances to each star. Such planets

experience Milankovitch behavior even in the absence of other planets, with stronger varying global temperatures on timescales of $\lesssim 1000$ years, much shorter than Earth's.

Way & Georgakarakos (2017) explored Milankovitch cycles with a 3D GCM for an Earth-like planet perturbed by a close giant planet in a handful of situations. This was the first study to use a sophisticated climate model with an evolving orbit. They found that the planet can remain habitable through large eccentricity cycles, though the planet may periodically enter a moist-greenhouse state (in which the upper atmosphere becomes moist and subsequent hydrogen loss occurs).

Finally, Rose et al. (2017) provided an analytical solution to the annually averaged EBM and used this solution to explore ice edge stability as a function of obliquity. They found that high obliquity planets can, under the right conditions, form equatorial ice belts, as opposed to ice caps, but these tend to be less stable than ice caps on low obliquity planets. Further, there are obliquities ($\sim 55^\circ$) at which no permanant ice (*i.e.* ice that persists year-round) is stable. Tests with the seasonal EBM (*i.e.*, a model that resolves seasonal variations) showed that this analytical solution is reasonably accurate for predicting the stability of ice edges, but there are conditions under which it fails.

Though the effects of different orbital/obliquity conditions and their variations have been studied by the previously discussed works, their remains no complete synthesis of orbital evolution, obliquity evolution, and climate, including the effects of ice sheets and oceans. The majority of the aforementioned works examined only static orbits and obliquities (Williams & Kasting, 1997; Williams & Pollard, 2002, 2003; Spiegel et al., 2009; Dressing et al., 2010; Ferreira et al., 2014; Bolmont et al., 2016; Rose et al., 2017). The studies that did model climate under varying orbital conditions were limited in various ways. Spiegel et al. (2010); Way & Georgakarakos (2017) allowed eccentricity to vary, but did not include obliquity variations. Armstrong et al. (2014) included obliquity variations (in addition to orbital variations), but their model contained a sign error which was, unfortunately, propagated to Forgan (2016). The climate models used by Spiegel et al. (2010) and Forgan (2016) did not include ice sheets and the thermal inertia associated with them, and so produce climates that

are too warm and too stable against the snowball instability. The climate model used in Armstrong et al. (2014) included ice sheets, but the outgoing longwave radiation prescription and the lack of latitudinal heat diffusion makes that model excessively stable against snowball states, and they did not include oceans. Spiegel et al. (2010) and Forgan (2016) included oceans only in a limited capacity: the albedo and heat capacities used are the average of land and ocean properties. This "mutes" the seasonal response of land and the thermal inertia of water. Way & Georgakarakos (2017) used a 3D GCM, easily the most robust model of the lot, but because that model is so computationally expensive, only a handful of simulations were run.

Here, I present the first fully coupled model of orbits, obliquities, and climates of Earth-like exoplanets. This model treats land and ocean as separate components and includes ice sheet growth and decay on land. Because the model is computationally inexpensive, thousands of coupled orbit-obliquity-climate simulations can be run in a reasonable time frame. This facilitates the exploration of broad regions of parameter space and will help in the prioritization of planet targets for characterization studies.

The purpose of this study is to examine the effect of obliquity and orbital evolution on potentially habitable planets. I model the orbit and obliquity of an Earth-mass planet, in the habitable zone of a G dwarf star, with an eccentric gas giant companion (see Chapter 3). I then coupled the climate model described in Section 4.2.1 to the orbit and obliquity model and analyze the ultimate climate state of the planet. In a number of interesting scenarios, I apply a fully-analytic climate model (Rose et al., 2017) to gain some deeper understanding of the results.

4.2 Methods

We use a combination of a secular orbital model (`DISTORB`), N-Body models (`HNBody` (Rauch & Hamilton, 2002) and `GENGA` (Grimm & Stadel, 2014)), a secular obliquity model (`DISTROT`), and a 1D Latitudinal EBM. For a more detailed description of `DISTORB` and `DISTROT`, and a description of how we employ the N-Body models, see Chapter 3. We describe the EBM

below.

4.2.1 Climate model

The climate model, `POISE` (Planetary Orbit-Influenced Simple EBM), is a one-dimensional energy balance model (EBM) based on North & Coakley (1979), with a number of modifications, foremost of which is the inclusion of a model of ice sheet growth, melting, and flow. The model is one-dimensional in $x = \sin\phi$, where ϕ is the latitude. In this fashion, latitude cells of size dx will not have equal width in latitude, but will be equal in area. The general energy balance equation is:

$$C(x)\frac{\partial T}{\partial t}(x,t) - D(x,t)\nabla^2 T(x,t) + I(x,T,t) = S(x,t)(1-\alpha(x,T,t)), \tag{4.1}$$

where $C(x)$ is the heat capacity of the surface at location x, T is the surface temperature, t is time, D is the coefficient of heat diffusion between latitudes (due to atmospheric circulation), $I(x,t)$ is the outgoing long-wave radiation (OLR) from the surface, i.e., the thermal infrared flux, $S(x,t)$ is the incident insolation (stellar flux), and α is the top-of-atmosphere (TOA) albedo and represents the percent of the insolation that is reflected back into space.

Though the model lacks a true longitudinal dimension, each latitude is divided into a land portion and a water portion. The land and water have distinct heat capacities and albedos, and heat is allowed to flow between the two regions. The energy balance equation can then be separated into two equations:

$$\begin{aligned} C_L\frac{\partial T_L}{\partial t} - D\frac{\partial}{\partial x}(1-x^2)\frac{\partial T_L}{\partial x} + \frac{\nu}{f_L}(T_L - T_W) + I(x,T_L,t) \\ = S(x,t)(1-\alpha(x,T_L,t)), \end{aligned} \tag{4.2}$$

$$\begin{aligned} C_W^{eff}\frac{\partial T_W}{\partial t} - D\frac{\partial}{\partial x}(1-x^2)\frac{\partial T_W}{\partial x} + \frac{\nu}{f_W}(T_W - T_L) + I(x,T_W,t) \\ = S(x,t)(1-\alpha(x,T_W,t)), \end{aligned} \tag{4.3}$$

where we have employed the co-latitudinal component of the spherical Laplacian, ∇^2 (the radial and longitudinal/azimuthal components vanish). The effective heat capacity of the

ocean is $C_W^{eff} = m_d C_W$, where m_d is introduced as an adjustable mixing depth of the ocean. The parameter ν is used to adjust the land-ocean heat transfer to reasonable values, and f_L and f_W are the fractions of each latitude cell that are land and ocean, respectively.

The insolation (or solar/stellar flux) received as a function of latitude, ϕ, and declination of the host star, δ, is calculated using the formulae of Berger (1978). Declination, δ, varies over the course of the planet's orbit for nonzero obliquity. For Earth, for example, $\delta \approx 23.5^\circ$ at the northern summer solstice, $\delta = 0^\circ$ at the equinoxes, and $\delta \approx -23.5^\circ$ at the northern winter solstice. Because δ is a function of time (or orbital position), the insolation varies, and gives rise to the seasons (again, assuming the obliquity is nonzero). For latitudes and times where there is no sunrise (e.g., polar darkness):

$$S(\phi, \delta) = 0, \tag{4.4}$$

while for latitudes and times where there is no sunset:

$$S(\phi, \delta) = \frac{S_\star}{\rho^2} \sin\phi \sin\delta, \tag{4.5}$$

and for latitudes with a normal day/night cycle:

$$S(\phi, \delta) = \frac{S_\star}{\pi\rho^2}(H_0 \sin\phi \sin\delta + \cos\phi \cos\delta \sin H_0). \tag{4.6}$$

Here, $S_\star$ is the solar/stellar constant (in W m^{-2}), ρ is the distance between the planet and host star normalized by the semi-major axis (*i.e.* $\rho = r/a$), and H_0 is the hour angle of the of the star at sunrise and sunset, and is defined as:

$$\cos H_0 = -\tan\phi \tan\delta. \tag{4.7}$$

The declination of the star with respect to the planet's celestial equator is a simple function of its obliquity ψ and its true longitude θ:

$$\sin\delta = \sin\psi \sin\theta. \tag{4.8}$$

See also Laskar et al. (1993a) for a comprehensive derivation. For these formulas to apply, the true longitude should be defined as $\theta = f + \varpi + p_A$, where f is the true anomaly (the

angular position of the planet with respect to its periastron). Essentially, then, $\varpi + p_A$ is just the longitude of periastron and θ the true longitude, if both angles were measured from the *orbital* location of the planet's current spring equinox (which moves with time). Note that in works like Berger (1978) and Laskar et al. (1993a), which studied Earth, θ is taken to be the true longitude of the *sun*, not Earth. Because the sun is opposite Earth when perihelion occurs ($\varpi_\odot = \varpi_\oplus \pm 180°$), the true longitudes are also opposite: $\theta_\odot = \theta_\oplus \pm 180°$. However, if we take p_A (and the vernal point, Υ) to refer to the *planet's* position at northern spring equinox, rather than the sun's position, the $\pm 180°$ term cancels and we can take $\theta = \theta_\oplus$ in Equation (4.8). We are free to play "fast and loose" with the definitions as long as we understand that $\delta > 0$ during northern summer and $\delta < 0$ during northern winter and ensure that the Equation (4.8) produces the desired behavior (some works, such as North & Coakley (1979), use $\cos\theta$ to calculate $\sin\delta$ instead of $\sin\theta$).

A point of clarification is in order: EBMs (at least the models employed in this study) can be either *seasonal* or *annual*. The EBM component of `POISE` is a seasonal model—the variations in the insolation throughout the year/orbit are resolved and the temperature of the surface at each latitude varies in response, according to the leading terms in Equations (4.2) and (4.3). In an annual model (we utilize one in this study to understand ice sheet stability; see Section 4.2.2), the insolation at each latitude is averaged over the year, and the energy balance equation (Eqn 4.1) is forced into "steady state" by setting $\partial T/\partial t$ equal to zero (this can be done numerically or analytically). By "steady state", we mean that the surface conditions (temperature and albedo) come to final resting values and remain there. Seasonal EBMs, on the other hand, can be in "equilibrium", in that the orbitally averaged surface conditions remain the same from year to year, but the surface condition vary *throughout* the year.

The planetary albedo is a function of surface type (land or water), temperature, and

zenith angle. For land grid cells, the albedo is:

$$\alpha = \begin{cases} \alpha_L + 0.08 P_2(\sin Z) & \text{if } M_{ice} = 0 \text{ and } T > -2^\circ \text{ C} \\ \alpha_i & \text{if } M_{ice} > 0 \text{ or } T <= -2^\circ \text{ C}, \end{cases} \tag{4.9}$$

while for water grid cells it is:

$$\alpha = \begin{cases} \alpha_W + 0.08 P_2(\sin Z) & \text{if } T > -2^\circ \text{ C} \\ \alpha_i & \text{if } T <= -2^\circ \text{ C}, \end{cases} \tag{4.10}$$

where Z is the zenith angle of the sun at noon and $P_2(x) = 1/2(3x^2 - 1)$ (the second Legendre polynomial). This last quantity is used to approximate the additional reflectivity seen at shallow incidence angles, *e.g.* at high latitudes on Earth. The zenith angle at each latitude is given by

$$Z = |\phi - \delta|. \tag{4.11}$$

The albedos, α_L, α_W, and α_i (see Table 4.1), not accounting for zenith angle effects, are chosen to match Earth data (North & Coakley, 1979) and account, over the large scale, for clouds, various surface types, and water waves. Equation (4.9) means that when there is ice on land ($M_{ice} > 0$), or the temperature is below freezing, the land takes on the albedo of ice. Though there are multiple conditionals governing the albedo of the land, in practice the temperature condition is only used when ice sheets are turned off in the model, since ice begins to accumulate at $T = 0^\circ$ C, and so is always present when $T < -2^\circ$ C. Equation (4.10) indicates a simpler relationship for the albedo over the oceans: when it is above freezing, the albedo is that of water (accounting also for zenith angle effects); when it is below freezing, the albedo is that of ice.

We take the land fraction and water fraction to be constant across all latitudes. This is roughly like having a single continent that extends from pole to pole. The effect of geography on the climate is beyond the scope of this work, which is to isolate the orbitally-induced climate variations.

North & Coakley (1979) utilized a linearization of the OLR with temperature:

$$I = A + BT, \tag{4.12}$$

where, for Earth, $A = 203.3$ W m^{-2} and $B = 2.09$ W m^{-2} °C^{-1}, and T is the surface temperature in °C. The purpose of this linearization is that it allows the coupled set of equations to be formulated as a matrix problem that can be solved using an implicit Euler scheme with the following form:

$$\mathscr{M} \cdot T_{n+1} = \frac{CT_n}{\Delta t} - A + S(1-\alpha), \tag{4.13}$$

where T_n is a vector containing the current surface temperatures, T_{n+1} is a vector representing the temperatures to be calculated, and C, A, S, and α are vectors containing the heat capacities, OLR offsets (Equation 4.12), insolation at each latitude, and TOA albedos, respectively. The matrix $\mathscr{M}$ contains all of the information on the left-hand sides of Equations 4.2 and 4.3 related to temperature. The time-step, Δt, is chosen so that conditions do not change significantly between steps, resulting in typically 60 to 80 time-steps per orbit. The new temperature values can then be calculated by taking the dot-product of $\mathscr{M}^{-1}$ with the right-hand side of Equation 4.13. The large time step allowed by this integration scheme greatly speeds the climate model, allowing us to run thousands of simulation for millions of years. Each simulation takes ~ 1 hour in real-time.

We model ice accumulation and ablation in a similar fashion to Armstrong et al. (2014). Ice accumulates on land at a constant rate, r_{snow}, when temperatures are below 0° C. Melting/ablation occurs when ice is present and temperatures are above 0° C, according to the formula:

$$\frac{dM_{ice}}{dt} = \frac{2.3\sigma(T_{freeze}^4 - (T + T_{freeze})^4)}{L_h}, \tag{4.14}$$

where M_{ice} is the surface mass density of ice, $\sigma = 5.67 \times 10^{-8}$ W m^{-2} K^{-4} is the Stefan-Boltzmann constant, L_h is latent heat of fusion of ice, 3.34×10^5 J kg^{-1} and $T_{freeze} = 273.15$ K. The factor of 2.3 that appears here, though not in Armstrong et al. (2014), is added to scale the melt rate to roughly Earth values of 3 mm °C^{-1} day^{-1} (see Braithwaite & Zhang, 2000; Lefebre et al., 2002; Huybers & Tziperman, 2008).

The ice sheets are able to flow across the surface via deformation and sliding at the base. We use the formulation from Huybers & Tziperman (2008) to model the changes in ice height

due to these effects. Bedrock depression is important in this model (despite the fact that we have only one atmospheric layer and thus cannot resolve elevation-based effects), because the flow rate is affected. The ice flow (Huybers & Tziperman, 2008) is then:

$$\frac{\partial h}{\partial t} = \frac{\partial}{\partial y}\left[\frac{2A_{ice}(\rho_i g)^n}{n+2}\left|\left(\frac{\partial(h+H)}{\partial y}\right)^{n-1}\right| \cdot \frac{\partial(h+H)}{\partial y}\ (h+H)^{n+2} + u_b h\right], \tag{4.15}$$

where h is the height of the ice, H is the height of the bedrock (always negative or zero, in this case), A_{ice} represents the deformability of the ice, ρ_i is the density of ice, g is the acceleration due to gravity, and n is the exponent in Glen's flow law (here $n = 3$). The ice height and ice surface mass density, M_{ice} are simply related via $M_{ice} = \rho_i h$. The first term inside the derivative represents the ice deformation; the second the sliding of the ice at the base. The latitudinal coordinate, y, is related to the radius of the planet and the latitude, $y = R\phi$, thus $\Delta y = R\Delta x(1-x^2)^{-1/2}$. Finally, u_b, the ice velocity across the sediment, is:

$$u_b = \frac{2D_0 a_{sed}}{(m+1)b_{sed}}\left(\frac{|a_{sed}|}{2D_0\mu_0}\right)^m \cdot \left(1 - \left[1 - \frac{b_{sed}}{|a_{sed}|}\min\left(h_s, \frac{|a_{sed}|}{b_{sed}}\right)\right]^{m+1}\right), \tag{4.16}$$

as described by Jenson et al. (1996). The constant D_0 represents a reference deformation rate for the sediment, μ_0 is the reference viscosity of the sediment, h_s is the depth of the sediment, and $m = 1.25$. The shear stress from the ice on the sediment is:

$$a_{sed} = \rho_i g h \frac{\partial(h+H)}{\partial y}, \tag{4.17}$$

and the rate of increase of shear strength with depth is:

$$b_{sed} = (\rho_s - \rho_w) g \tan\phi_s, \tag{4.18}$$

where ρ_s and ρ_w are the density of the sediment and water, respectively, and ϕ_s is the internal deformation angle of the sediment. We adopt the same numerical values as Huybers & Tziperman (2008) for all parameters related to ice and sediment (see Table 4.2), with a few exceptions. We use a value of A_{ice} (ice deformability) that is consistent with ice at 270 K (Paterson, 1994), and a value of r_{snow} (the precipitation rate) that best allows us to

reproduce Milankovitch cycles on Earth (see Section 4.3). Note also that the value of D_0 in Table A2 of Huybers & Tziperman (2008) appears to be improperly converted for the units listed (the correct value, from Jenson et al. (1996), is listed in the text, however). With Equations 4.16 and 4.17, Equation 4.15 can be treated numerically as a diffusion equation, with the form:

$$\frac{\partial h}{\partial t} = D_{ice}\frac{\partial^2(h+H)}{\partial y^2}, \tag{4.19}$$

where,

$$\begin{aligned} D_{ice} = {} & \frac{2A_{ice}(\rho_i g)^n}{n+2}\left|\left(\frac{\partial(h+H)}{\partial y}\right)^{n-1}\right| (h+H)^{n+2} \\ & + \frac{2D_0\rho_i g h^2}{(m+1)b_{sed}}\left(\frac{|a_{sed}|}{2D_0\mu_0}\right)^m \cdot \left(1-\left[1-\frac{b_{sed}}{|a_{sed}|}\min\left(h_s, \frac{|a_{sed}|}{b_{sed}}\right)\right]^{m+1}\right), \end{aligned} \tag{4.20}$$

and D_{ice} is evaluated at each time-step, at every boundary to provide mass continuity.

Because of the longer time-scales (years) associated with the ice sheets, the growth/melting and ice-flow equations are treated differently from the rest of the energy balance model. First, the energy balance model (Equation 4.1) is run for 4-5 orbital periods, and ice accumulation and ablation is tracked over this time frame, but ice-flow (Equation 4.15) is ignored. The annually-averaged ice accumulation/ablation is then calculated from this time-frame and passed to the ice-flow time-step, which can be much longer (years). The EBM is then re-run periodically to ensure that conditions vary smoothly and continuously.

To clarify, the hierarchy of models and their time-steps is as follows:

1. The EBM (shortest time-step): run for a duration of several orbital periods with time-steps on the order of days. The model is then rerun at the end of every orbital/obliquity time-step and at user-set intervals throughout the ice-flow model.

2. The ice-flow model (middle time-step): run at the end of every orbital time-step (with time-steps of a few orbital periods), immediately after the EBM finishes. The duration of the model will follow one of two scenarios:

a If the orbital/obliquity time-step is sufficiently long, the EBM is rerun at user-set intervals, then the ice-flow model continues. The ice-flow model and the EBM thus alternate back-and-forth until the end of the orbit/obliquity time-step.

b If the orbital/obliquity time-step is shorter than the user-set interval, the ice-flow model simply runs until the end of the orbital time-step.

3. The orbital/obliquity model (longest time-step). The time-steps are set by the fastest changing variable (see Chapter 3) amongst those parameters.

See also Figure 4.1. The user-set interval discussed above must be considered carefully. The assumption is that annually-averaged climate conditions like surface temperature and albedo do not change much during the time span over which the ice-flow model runs. Hence, we choose a value that ensures that the ice-flow does not run so long that it dramatically changes the albedo without updating the temperature and ice balance (growth/ablation) via the EBM.

The initial conditions for the EBM as follows. The first time the EBM is run, the planet has zero ice mass on land, the temperature on both land and water is set by the function

$$T_0 = 7.5^\circ\mathrm{C} + (20^\circ\mathrm{C})(1 - 2\sin\phi), \tag{4.21}$$

where ϕ is the latitude. This gives the planet a mean temperature of $\sim 14^\circ$ C, a temperature of $\sim 28^\circ$ C in the tropics, and $\sim -13^\circ$ at the poles. This is thus a "warm start" condition and treats the planet initially as if it were low obliquity. The initial albedo of the surface is calculated from the initial temperatures. We then perform a "spin-up" phase, running the EBM iteratively until the mean temperature between iterations changes by $< 0.1^\circ$ C, *without* running the orbit, obliquity, or ice-flow models, to bring the seasonal EBM into equilibrium at the actual stellar flux the planet receives and its actual initial obliquity. Then, every time the EBM is rerun (at the user-set interval or the end of the orbit/obliquity time-step), the initial conditions are taken from the previous EBM run (temperature distribution) and the end of the ice-flow run (albedo, ice mass).

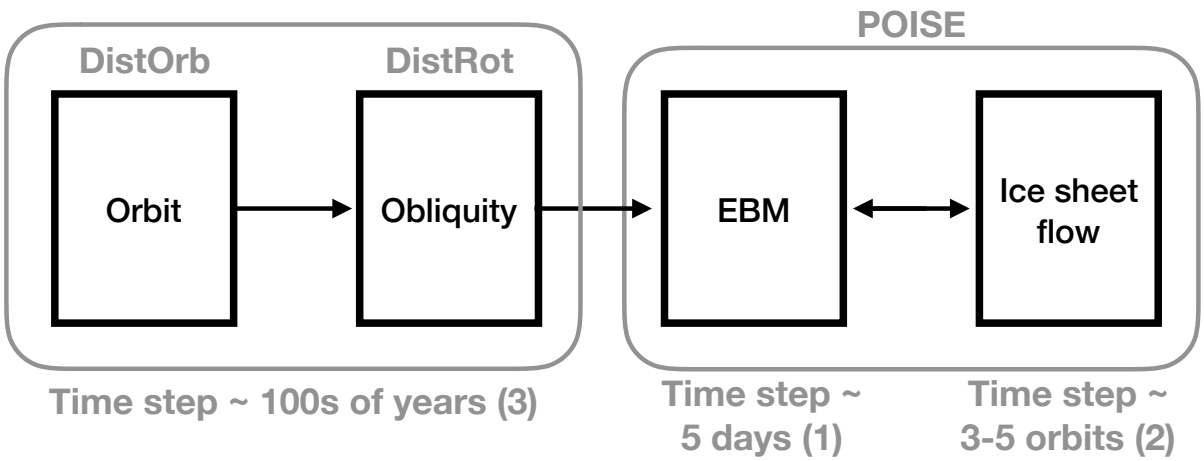

Figure 4.1: Hierarchy of `POISE` and orbit and obliquity models. The orbit and obliquity models (`DistOrb` and `DistRot`) are run for $\sim$ hundreds of years (with an adaptive time step determined by the rates of change of the orbital/obliquity parameters). `POISE` is run at the end of each orbit/obliquity time step. First, the EBM is run for several orbits, with time steps of ~ 5 days. Then the ice flow model is run with time steps of $\sim 3-5$ orbits. The ice flow model runs until the next orbit/obliquity time step, or until a user-set time, at which point the EBM is rerun for several orbits.

Table 4.1: **Parameters used in the EBM**

Variable	Value	Units	
C_L	1.55×10^7	J m^{-2} K^{-1}	land heat capacity
C_W	4.428×10^6	J m^{-2} K^{-1}	ocean heat capacity
m_d	70	m	ocean mixing depth
D	0.58	W m^{-2} K^{-1}	meridional heat diffusion coefficient
ν	0.8		coefficient of land-ocean heat flux
A	203.3	W m^{-2}	OLR coefficient
B	2.09	W m^{-2} K^{-1}	OLR coefficient
α_L	0.363		albedo of land
α_W	0.263		albedo of water
α_i	0.6		albedo of ice
f_L	0.34		fraction of latitude cell occupied by land
f_W	0.66		fraction of latitude cell occupied by water

Table 4.2: **Parameters used in the ice sheet model**

Variable	Value	Units	
T_{freeze}	273.15	K	freezing point of water
L_h	3.34×10^5	J kg^{-1}	latent heat of fusion of water
r_{snow}	2.25×10^{-5}	kg m^{-2} s^{-1}	snow/ice deposition rate
A_{ice}	2.3×10^{-24}	Pa^{-3} s^{-1}	deformability of ice
n	3		exponent of Glen's flow law
ρ_i	916.7	kg m^{-3}	density of ice
ρ_s	2390	kg m^{-3}	density of saturated sediment
ρ_w	1000	kg m^{-3}	density of liquid water
D_0	7.9×10^{-7}	s^{-1}	reference sediment deformation rate
μ_0	3×10^9	Pa s	reference sediment viscosity
m	1.25		exponent in sediment stress-strain relation
h_s	10	m	sediment depth
ϕ_s	22	degrees	internal deformation angle of sediment
T_b	5000	years	bedrock depression/ rebound timescale

4.2.2 Analytical solution for ice stability

To better understand the snowball instability, we compare our results to the analytical EBM from Rose et al. (2017). This model is *annual* EBM and is analytic in that there is an algebraic solution, rather than a numerical solution. While this model does not capture seasonal variations or the thermal inertia associated with ice sheets, it is nonetheless instructive for understanding how the snowball state is triggered.

According to the "slope-stability theorem" (Cahalan & North, 1979), the ice edge is stable as long as

$$\frac{dq}{dx_s} > 0, \tag{4.22}$$

where $x_s = \sin\phi_s$, ϕ_s is the latitude of the ice edge (land and ocean are not separate component in the analytic model), and q is the non-dimensional quantity

$$q = \frac{a_0 Q}{A + BT_{ref}}. \tag{4.23}$$

The quantity q represents the absorbed solar/stellar radiation, divided by the planet's cooling function (or outgoing longwave radiation) at some temperature. Thus it is analogous to the total heating that the planet receives, both from the host star and its own greenhouse effect. Equation (4.22) applies to low obliquity planets. If the planet has high obliquity, ice will tend to form at the equator, and the stability condition is

$$\frac{dq}{dx_s} < 0. \tag{4.24}$$

In the annual model, there is a distinct boundary between "low" and "high" obliquity, and the transition occurs at

$$\psi = \sin^{-1}\left(\sqrt{\frac{2}{3}}\right) \approx 54.74^\circ. \tag{4.25}$$

See Equation (3b) of Rose et al. (2017). This angle is the obliquity at which the average annual insolation is the same at all latitudes.

Here, Q is the global average incoming flux ($4Q$ is the solar/stellar constant, $S_\star$) and T_{ref} is the temperature threshold at which the planetary albedo switches from a value appropriate

for ice free to ice covered (T_{ref} is the freezing point, in other words). For ice free latitudes, the co-albedo, a_0, is a single value in the annual model. In our comparison using our seasonal model, we take this to be the average co-albedo of the unfrozen surfaces, $a_0 = f_L(1-\alpha_L) + f_W(1-\alpha_W)$, and we set $T_{ref} = -2^\circ$ C.

Figure 4.2 shows the ice edge solution from this analytical EBM for a low obliquity planet. At a single value of q, there can be multiple equilibrium locations for the ice edge—but only some of these "branches" are stable (those with positive or zero slopes). To understand why this occurs, consider the conditions at point a. This point represents a planet with an ice cap extending from the poles to the mid-latitudes. If a small positive perturbation Δq is added to q, the planet becomes slightly warmer. This causes the ice edge to retreat until a new equilibrium solution is found. As long as the perturbation is small, this new equilibrium ice edge occurs on the same branch as the original ice edge. If q is perturbed the other direction ($\Delta q < 0$), the planet cools, and the ice edge extends further toward the equator. As before, if the perturbation is small, the ice edge remains on the same (stable) branch. Applying the same thought experiment at points b and c, we can see that, although these represent equilibrium solutions, they are unstable. Positive Δq at point b will result in ice-free conditions; negative Δq will cause the ice to jump to mid-latitudes. Any positive Δq will cause the ice edge at point c to jump to the mid-latitudes; any negative Δq will cause it to fall into the snowball state (frozen from equator to pole). The upper unstable branch (point b) represents the "small ice cap instability" (SICI) and the lower unstable branch represents the "large ice cap instability" (LICI).

As we will show, this stability concept is useful in understanding how the snowball states occur in many of our simulations. However, because the seasonal EBM (`POISE`) is not an equilibrium model, it does deviate from the annual model at times. Hence, these ice stability diagrams do not always accurate predict the occurrence of snowball states.

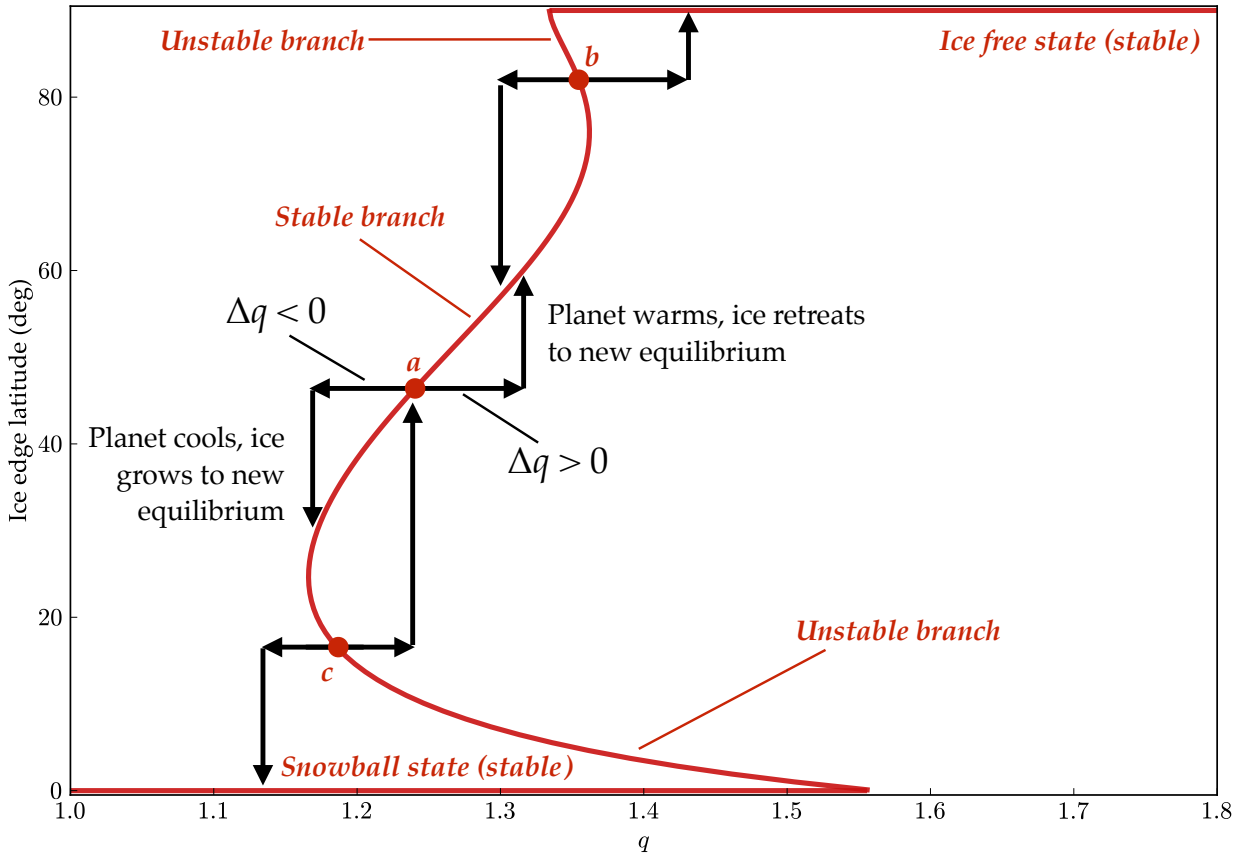

Figure 4.2: Conceptual diagram illustrating the slope-stability theorem (Cahalan & North, 1979). The red curve shows the equilibrium ice edge latitude for a planet with obliquity of 23.5°. Branches with positive or zero slope are stable; branches with negative or undefined slope are unstable.

Table 4.3: **Parameters used in statistical analysis and machine-learning algorithm**

Parameter	Description
S	Incident stellar flux (stellar constant)
e_0	Initial eccentricity
Δe	Maximum change in eccentricity
$\langle e \rangle$	Mean eccentricity
i_0	Initial inclination
Δi	Maximum change in inclination
$\langle i \rangle$	Mean inclination
ψ_0	Initial obliquity
$\Delta \psi$	Maximum change in obliquity
$\langle \psi \rangle$	Mean obliquity
δ_{snow}	Equal to 1 in snowball state, 0 otherwise
f_{ice}	Fractional area permanently (year-round) covered in ice

4.2.3 Statistics and machine learning

To further extend the predictive power and utility of the model, we calculate correlations between orbital parameters and snowball states and area of ice coverage. We then employ a machine learning algorithm to determine how often we can correctly predict the climate state of the planet considered here, given a set of orbital properties. The properties that go into this analysis are shown in Table 4.3. There are 10 model inputs (orbit/spin parameters), and 2 model outputs (δ_{snow} and f_{ice}).

We examine how the input features of our model (Table 4.3) correlate with a given simulation's final climate state (δ_{snow} and f_{ice}) in order to gain insight into how the underlying

physical processes influence the outcomes of our simulations. For example, if the mean eccentricity is shown to strongly correlate with likelihood that the planet enters a snowball state, we can infer that orbital dynamical processes could influence the climate evolution. Note that we cannot and do not seek to show causal relationships in the correlation analysis, but rather to identify the features that may impact the climate evolution.

The relationship between any feature of our model and the final state of the simulated planet climate likely has a non-linear correlation given the inherent complexities of our coupled orbital dynamics and climate model. As a means to characterize these correlations, we compute the simple Pearson correlation coefficient (R) and the maximal information coefficient (MIC; Reshef et al., 2011). Pearson's R measures the linear relationship between two variables and ranges from [-1,1] with 0 representing no linear correlation and 1 and -1 represent a perfect positive and negative linear correlation, respectively. We also compute the $p-$values associated with each correlation, which are measure of statistical significance ($p < 0.05$ is the traditional definition of significance).

The MIC characterizes non-linear relationships between variables by estimating the maximum mutual information between two variables. Broadly speaking, the mutual information between two variables characterizes the reduction in uncertainty of one variable after observing the other (see Reshef et al., 2011). For independent variables, their mutual information is 0 as observing one does not provide any insight into the other. The MIC ranges from [0,1] where MIC = 0 represents no relationship while MIC = 1 represents some noiseless functional relationship of any form.

The MIC depends on the estimate of the joint distribution of the two variables when computing the maximum mutual information and hence is sensitive to how the variables are binned. Following the suggestion of Reshef et al. (2011), we set the number of bins to be $N^{0.6}$ for N simulations. We computed the MIC using the python package `minepy` (Albanese et al., 2013) for each feature versus the final surface area coverage of ice (f_{ice}) and whether or not the simulation resulted in a snowball state (δ_{snow}).

We also define a measurement of the non-linearity associated with each parameter:

$$\zeta_{NL} = \text{MIC} - R^2. \tag{4.26}$$

As an alternative method to estimate the correlation between various features and simulation results, we turn to a machine learning approach akin to that of Tamayo et al. (2016). The purpose of this method is to look for correlations not found by either of the previous methods and to ultimately reduce the number of full simulations that need to be run. Following the procedure of that study, we use a machine learning algorithm to predict the results of our simulations as a function of the features of our model, *i.e.*, e_0, $S_\star$, etc. In our case, we use the `scikit-learn` (Pedregosa et al., 2011) implementation of the random forest algorithm (Breiman, 2001). The random forest algorithm is a particularly powerful and flexible algorithm that fits an ensemble of decision trees on numerous randomized sub-samples of the data set and averages the predictions of the decision trees to produce an accurate, low-variance prediction. The random forest algorithm has a particular advantage for our purposes in that it can compute "feature importances" as a means to estimate how the algorithm weights various inputs when producing an output. An input with a high feature importance implies that the algorithm weights that feature more heavily when making a prediction. Feature importances, ξ_i, can hence be considered as a proxy for how much that feature correlates with the predictive variable, the simulation output. The feature importances are all normalized such that they sum to 1: $\sum \xi_i = 1$.

For our purposes, we cast our machine learning problem in two forms. First, we consider the binary classification problem in which we use a random forest classifier (RFC) to predict whether or not the simulation results in a snowball planet state, δ_{snow}. Second, we consider the regression problem in which we use a random forest regressor (RFR) to predict the area fraction of the planet covered in ice, f_{ice}, a continuous quantity that ranges from 0 to 1. In both cases, we fit the machine learning algorithms with the following procedure. We divide our data set using 75% of the data for our training set in which we fit and calibrate our algorithms and the remaining 25% as the testing set used to estimate the performance of our

fitted algorithms on unseen data. We fit each algorithm, a process commonly referred to as "training", and use $k-$folds cross-validation with $k = 5$ to tune the hyperparameters of our model using only the training set. After training the algorithms, we find that both the RFC and RFR algorithms generalize exceptionally well. For example, the RFC's predictions of δ_{snow} achieve a classification accuracy of $\sim 97\%$ on the testing set. After training the models and verifying their accuracy, we extract the feature importances (ξ_i) for each algorithm as shown in Tables 4.5 and 4.6.

Note that in order prevent the random forest regressor (RFR) from predicting negative values for f_{ice}, we instead use the value $\log_{10}(f_{ice} + 1)$ as the model output.

4.2.4 Initial orbital and obliquity conditions

We model the climate of planet 2 in the dynamically evolving system, SYS1, from the previous study (Chapter 3), over a narrower range of rotational periods. The initial orbital and spin properties are shown in Table 4.4. To understand the effects of orbital evolution over a range of stellar fluxes, we leave the semi-major axis fixed at $a = 1.0031$ au and instead vary the luminosity of the star over the range $L_\star = 3.6 \times 10^{26}$ W to $L_\star = 3.95 \times 10^{26}$ W. This corresponds to an incident stellar flux range of $S = 1304.00$ W m^{-2} to $S = 1395.88$ W m^{-2}.

The planet Kepler-62 f, discussed in the previous study, requires some additional adjustments to the climate model because of its (cooler) location in the HZ and the different stellar spectrum. It is also interesting enough to warrant its own study and so we will reserve a climate analysis of this planet for a future work.

4.3 Model Validation

To validate the climate model, we adjust our input parameters to reproduce Earth-like values. We use the OLR coefficients, A and B, and heat diffusion coefficient D from North & Coakley (1979) and surface albedos for land, water, and ice that give us good agreement to the data used in that paper, see Table 4.1.

Table 4.4: Initial conditions for **SYS1**

Planet	1	2	3
m ($M_\oplus$)	18.75	1	487.81
a (au)	0.1292	1.0031	3.973
e	0.237	0.001-0.4	0.313
i (°)	1.9894	0.001-35	0.02126
ϖ (°)	353.23	100.22	181.13
Ω (°)	347.70	88.22	227.95
P_{rot} (days)		0.65,1,1.62	
ψ (°)		0-90	
p_A		281.78	

4.3.1 Comparison with Earth and LMD

Like Spiegel et al. (2009), we compare our vertical heat fluxes to the Earth Radiation Budget Experiment satellite data (Barkstrom et al., 1990). In Figure 4.3 we show the values for the flux in (blue), flux out (red), and the difference, or net heating (orange), as a function of latitude, for the Earth, using our climate model `POISE`. Our model compares well with the zonally- and monthly-averaged satellite data, though it is too simple to capture all of the variations. Our model also produces sharp jumps at high latitudes because of the sudden change in albedo at freezing temperatures. For the Earth, this sudden change is not seen because of a combination of things—geographic variations, darkening of snow and ice, clouds, etc.—that are not captured in our somewhat simplistic model.

Further, in Figures 4.4-4.7, we compare `POISE` to the Generic LMDZ 3D Global Climate Model (GCM) (Hourdin et al., 2006; Wordsworth et al., 2011; Leconte et al., 2013; Charnay

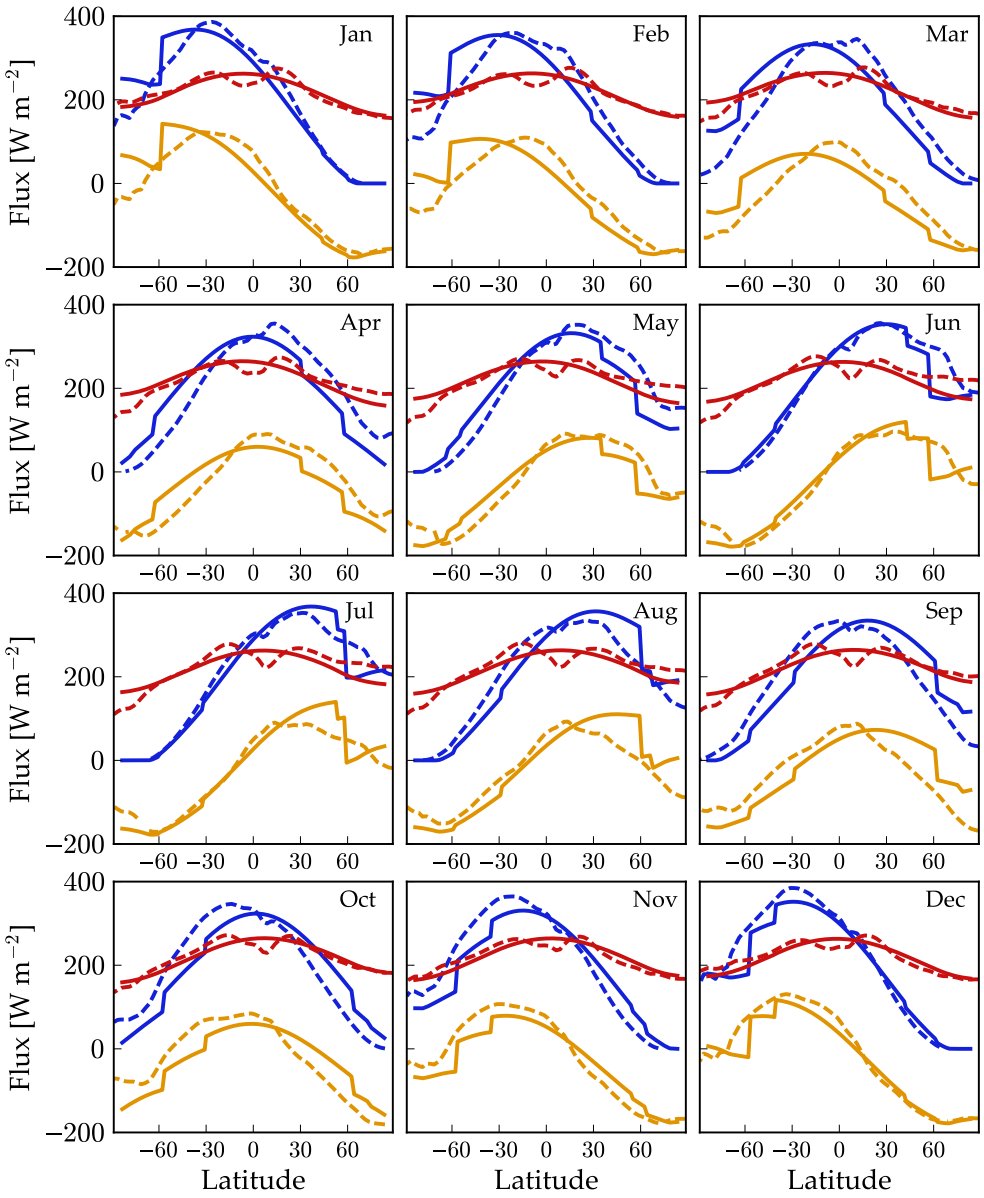

Figure 4.3: Monthly averaged vertical fluxes for the EBM (solid lines) and satellite data for Earth (dashed lines). Blue corresponds to incoming flux (equal to $(1-\alpha)S(\phi)$), red is the outgoing long-wave radiation (OLR), and orange is the difference (net heating).

et al., 2013), for rotation periods of 0.65 and 1.62 days, obliquities of 23.5° and 85°, and eccentricities of 0.1 and 0.3 (eight GCM simulations in total). These initial orbital and rotational conditions sample a broad range of the conditions we explore further with the EBM. We use present Earth geography in the LMD simulations, though in the EBM there is a fixed quantity of land at each latitude, so some difference in the models is attributable to geography.

In Figures 4.4-4.7 we plot the annually-averaged surface temperature, outgoing longwave radiation, albedo, and meridional flux as a function of latitude for the `POISE` and LMD simulations. With a climate model as simple as an EBM, we cannot hope to replicate all of the variations with latitude in these quantities that LMD does. Still, the `POISE` captures LMD's general trends in surface temperature, and heat fluxes. It captures the surface temperature better in the low obliquity cases than in the high obliquity cases, though, oddly, the meridional flux in `POISE` matches LMD more closely in the high obliquity cases.

A primary source of error in the high obliquity cases is that the EBM simply does not capture all of the physical process that occur during the extreme summers the planet experiences. During the summer, nearly an entire hemisphere experiences sunlight for months on end. This leads to extremely high temperatures and strong circulation. Ultimately, the simple parameterization of the OLR ($I = A + BT$) probably breaks down under such conditions, and convection should lead to cloud formation and a change in albedo (Yang et al., 2013).

4.3.2 Reproducing Milankovitch cycles

For the purpose of this study, we tune the ice deposition rate so that the model can reproduce the Earth's ice age cycles at $\sim 40,000$ years and $\sim 100,000$ years over a 10 million year simulation. To reproduce the effect of Earth's moon, we force the precession rate to be $50.290966''$ year^{-1} (Laskar et al., 1993a). This does not perfectly match the dynamics of the Earth-moon-sun system, but it is close enough to replicate the physics of the ice age cycles. The results of this tuning are shown in Figure 4.8 (see Huybers & Tziperman (2008), Figure

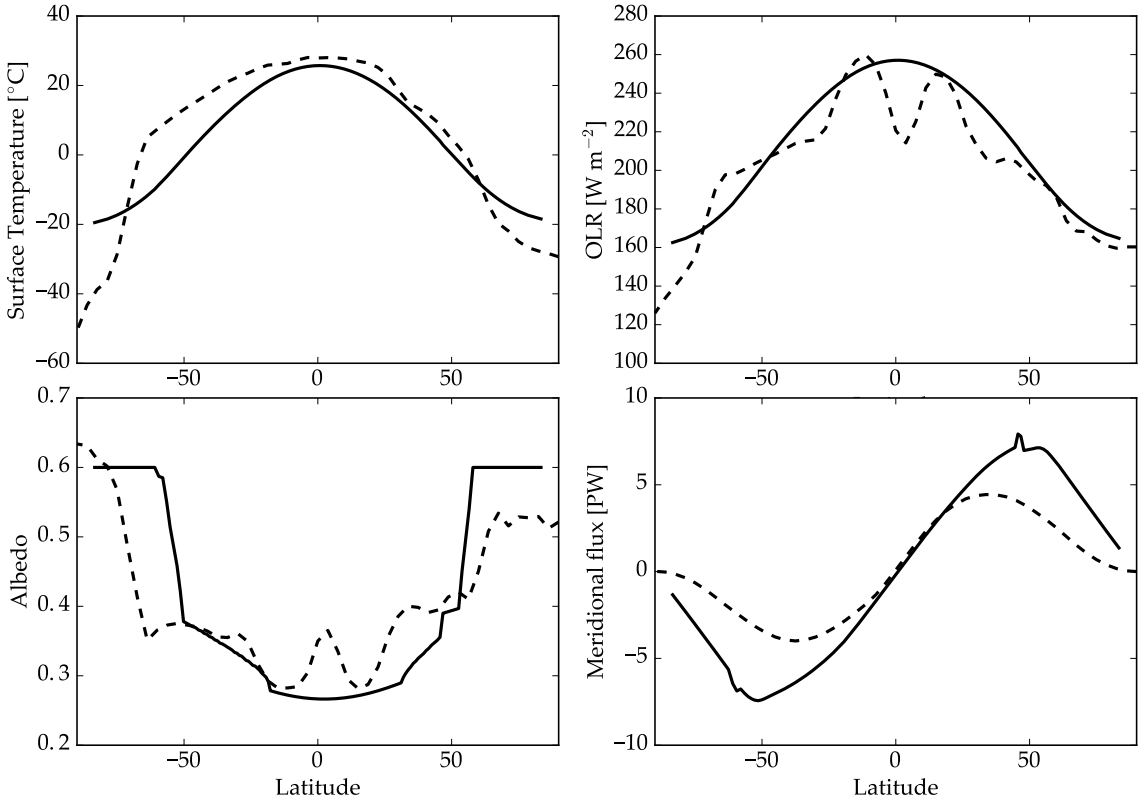

Figure 4.4: Comparison between our EBM (solid lines) and the LMDZ 3D GCM (dashed lines), for $\psi = 23.5°$, $P_{rot} = 0.65$ day, and $e = 0.1$. The surface temperature, OLR, and albedo compare reasonably well to the zonally-averaged quantities from LMDZ considering the differences in geography and missing physics (*e.g.* clouds and Hadley cells). The meridional flux in the EBM peaks at ~ 7 PW, a bit higher than Earth's ~ 6 PW, while LMDZ's peak is a tad low ~ 5 PW.

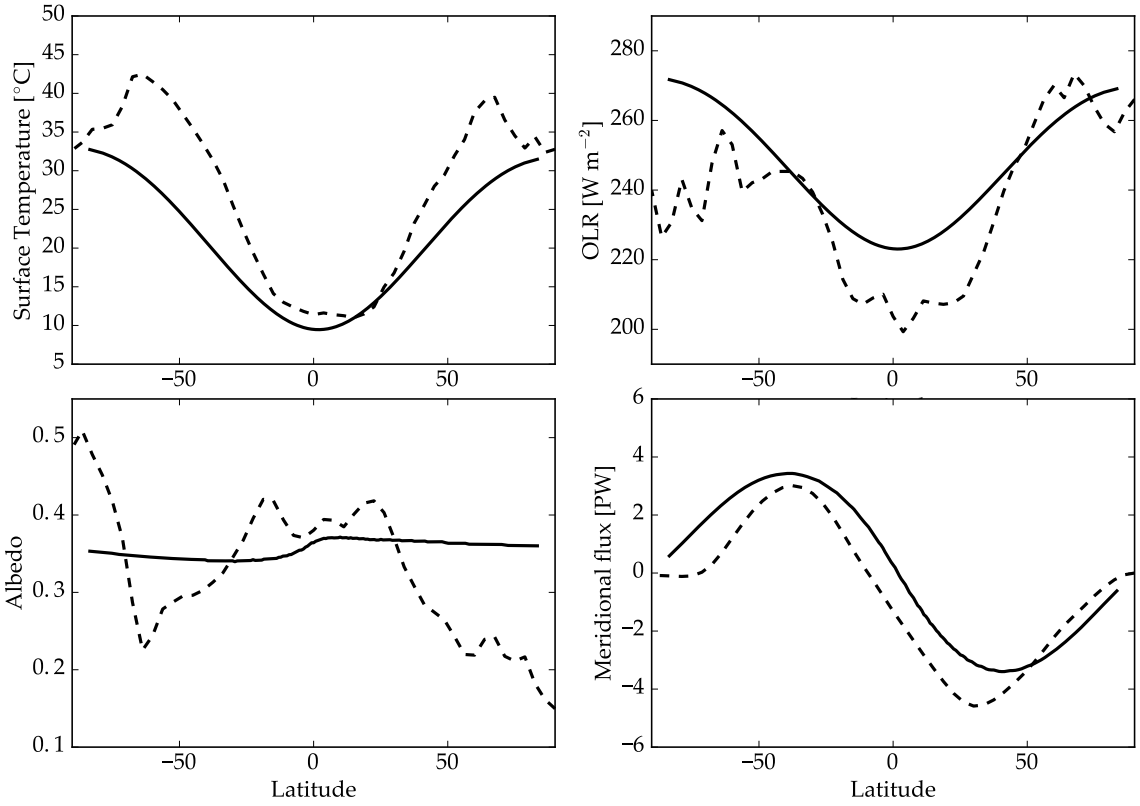

Figure 4.5: Same as Figure 4.4 but for $\psi = 85°$, $P_{rot} = 0.65$ day, and $e = 0.3$. The EBM captures the general trends but underestimates the surface temperature at mid-latitudes and overestimates the OLR at the equator and south pole. At high obliquity, the geography may play a larger role than at low obliquity, due to the extreme seasonality—land and ocean have different heat capacities and so will heat on different time-scales. This might explain much of the discrepancy between the models.

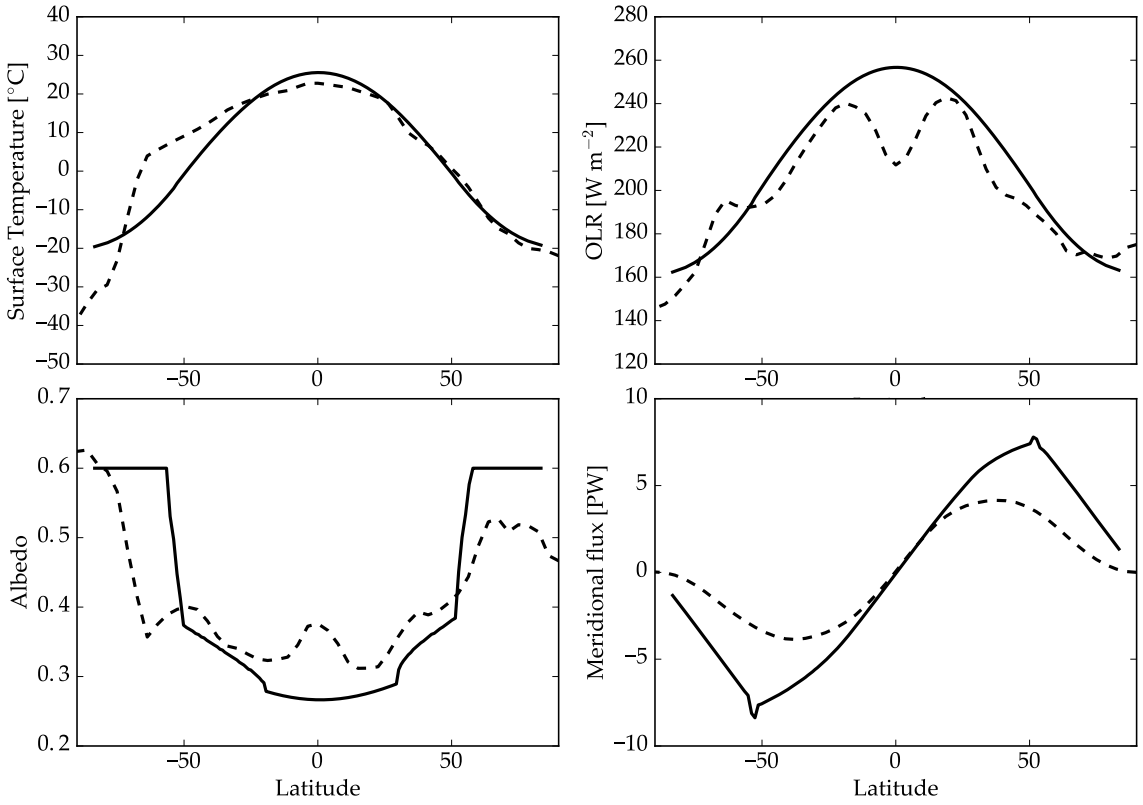

Figure 4.6: Same as Figure 4.4 but for $\psi = 23.5°$, $P_{rot} = 1.62$ day, and $e = 0.1$. Despite the slower rotation, the meridional flux is very similar to that of the $P_{rot} = 0.65$ day rotator, which suggests that parameterizations of the heat flux with rotation rate Ω ($D \propto \Omega^{-2}$) probably overestimate the latitudinal heat flow.

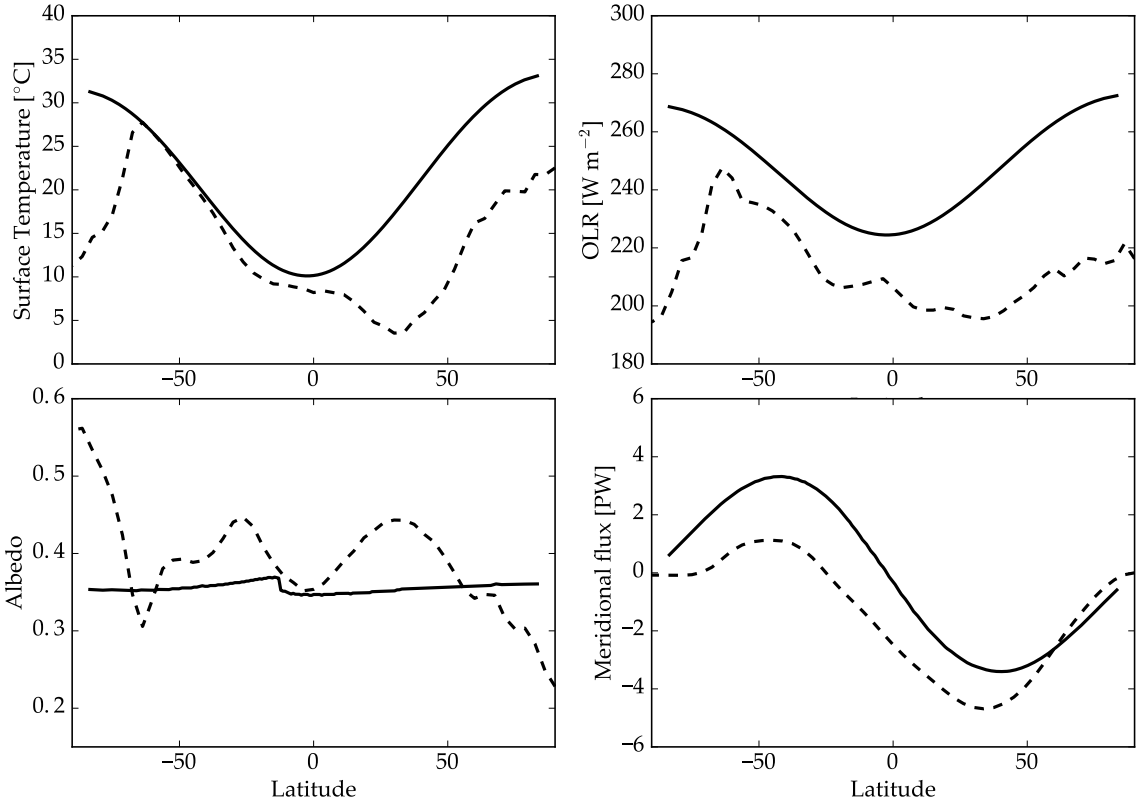

Figure 4.7: Same as Figure 4.4 but for $\psi = 85°$, $P_{rot} = 1.62$ day, and $e = 0.3$. In this case, `POISE` does worse than in the other cases at capturing the general trends in the LMDZ simulation. Though we capture the general trends, the errors are large at these initial conditions. Fortunately, the cases we explore rarely reach obliquity this high.

4, for comparison), for a 200,000 year window. The ice sheets in the northern hemisphere high latitude region grow and retreat as the obliquity, eccentricity (not shown), and climate-precession-parameter, or CPP ($e \sin(\varpi + p_A)$), vary. The ice deposition rate is less than that used by Huybers & Tziperman (2008) and so the ice accumulation per year is slightly smaller. The ice ablation occurs primarily at the ice edge (around latitude 60°) and is slightly larger than Huybers & Tziperman (2008), but is qualitatively similar.

There are a number of differences between our reproduction of Milankovitch cycles and Huybers & Tziperman (2008). Most notably, our ice sheets tend to persist for longer periods of time, taking up to three obliquity cycles to fully retreat. We also require a lower ice deposition (snowing) rate than Huybers & Tziperman (2008) in order to ensure a response from the ice sheets to the orbital forcing. We attribute these differences primarily to the difference in energy balance models used for the atmosphere, though see Section 4.3.3. For example, our model has a single-layer atmosphere with a parameterization of the OLR tuned to Earth, while Huybers & Tziperman (2008) used a multi-layer atmosphere with a simple radiative transfer scheme. Further, while the model Huybers & Tziperman (2008) contained only land, our model has both land and water which cover a fixed fraction of the surface. The primary effect of having an ocean in this model is to change the effective heat capacity of the surface. This has a large effect on the seasonal cycle, and affects the ice sheet growth and retreat. Thus, our seasonal cycle is somewhat muted compared to theirs, and our ice sheets do not grow and retreat as dramatically on orbital time scales. Ultimately, our ice ages cycles are more similar to the longer late-Pleistocene cycles than to $\sim 40,000$ year cycles of the early-Pleistocene.

Even though we cannot perfectly match the results of Huybers & Tziperman (2008), we are comfortable with these results for a number of reasons. First, both models make approximations to a number of physical processes and thus have numerous parameters that have to be tuned to reproduce the desired behavior. Second, both models are missing boundary conditions based on the continent distribution of the Earth—continental edges can limit the equator-ward advance of ice sheets or alter the speed of their flow through calving of ice

shelves. Finally, because the purpose of this study is to understand the response of ice sheets and climate to orbital variations, it is enough to merely ensure that the ice sheets respond in a way qualitatively similar to the Earth's without being overly sensitive (*i.e.*, resulting in ice free or snowball conditions with an insolation value of the solar constant, ~ 1370 W m^{-2}, and an OLR prescription similar to Earth's).

4.3.3 Note on Huybers & Tziperman (2008)

In the process of coding the ice sheet model, we ran and compared to the original MATLAB code used in Huybers & Tziperman (2008). If one takes the formulae for a_{sed} (Equation 4.17) and u_b (Equation 4.16) and plugs them into Equation (4.15), one ends up with the general form

$$\frac{dh}{dt} \propto h^2, \tag{4.27}$$

for the final term in Equation (4.15). It appears, however, that the exponent is missing for this term in the MATLAB code, at least in the version we had access to. Including this power of two increases the flow velocity at the base of the ice sheet, resulting in dramatically different behavior.

Interestingly, the error in the listing of D_0 in Table A2 of Huybers & Tziperman (2008) seems to also have propagated to the MATLAB code, so that the value used was 2.5×10^{-14} s^{-1}, not 7.9×10^{-7} s^{-1}. Oddly, for Earth conditions like those we tested in the previous section, the two errors (*i.e.*, the incorrect value of D_0 and the missing power of 2 in dh/dt), cancel to within a factor of a few. In a corrected version of the MATLAB code, we get ice sheets that are about 1/2 to 3/4 the size of those shown in Figure 4 of Huybers & Tziperman (2008). Hence, our reproduction of Milankovitch cycles is less about matching this previous work than extracting the obliquity and eccentricity frequencies from the ice volume.

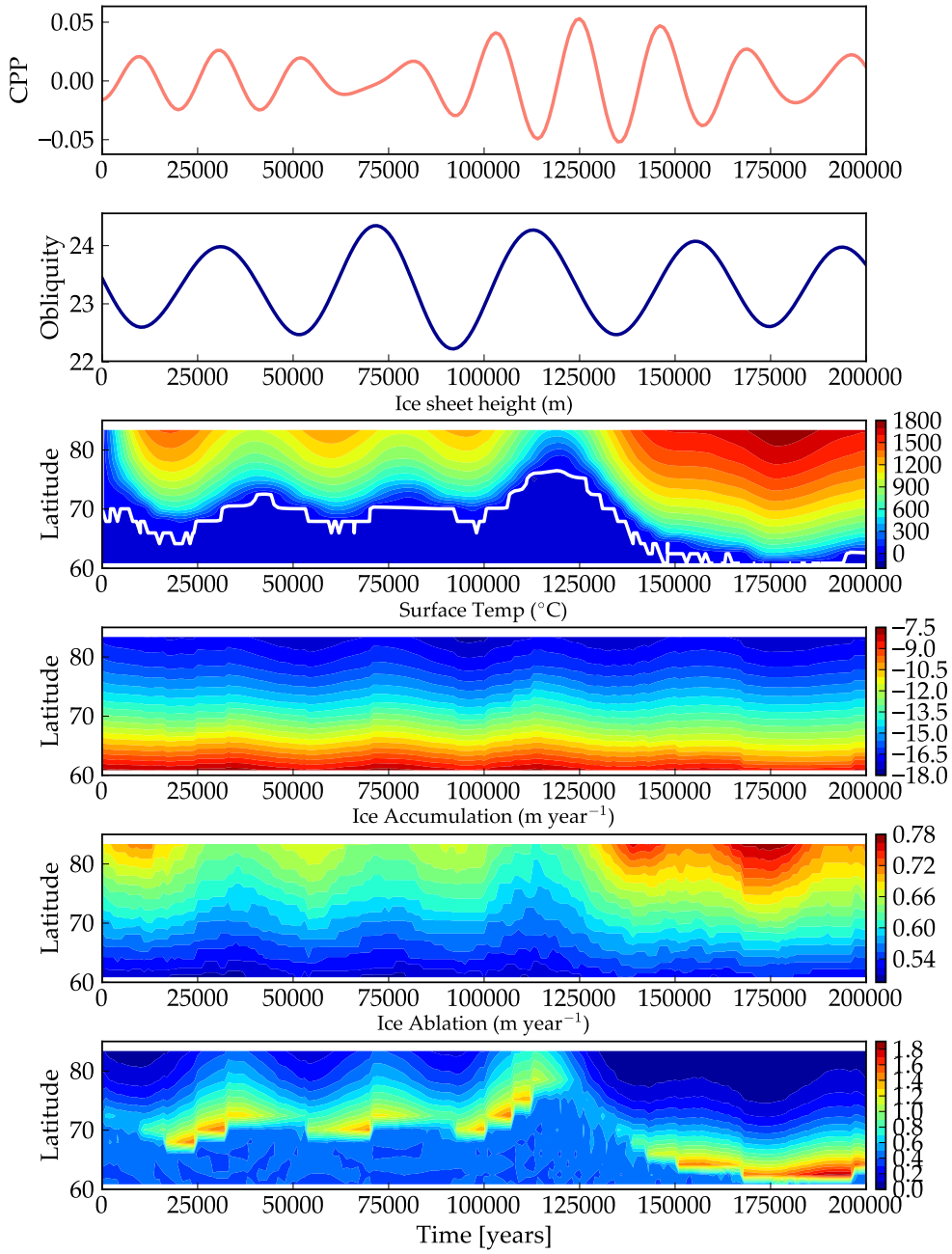

Figure 4.8: Milankovitch cycles on Earth, in the northern hemisphere. The panels are arranged to compare with Figure 4 of Huybers & Tziperman (2008). From top to bottom, we have: CPP $= e \sin(\varpi + p_A)$, obliquity, ice sheet height (m), annually averaged surface temperature (°C), annual ice accumulation rate (m yr^{-1}), and annual ice ablation rate (m yr^{-1}).

4.4 Results

4.4.1 Static cases

First, we identify the regimes in which ice sheets are able to form. The presence and distribution of permanent ice on land will depend on the stellar flux received by the planet and the planet's obliquity. In Figure 4.9 we show how ice coverage varies with incoming stellar flux at two obliquities ($\psi = 23.5°$ and $\psi = 50°$). Note that this initial ice coverage in each simulation is determined by the initial temperature distribution (Eqn. 4.21), and is very different from the final result in most cases. The ice coverage includes both land and ocean grid-points. The stellar flux is normalized by Earth's value, $S_0 = 1367.5$ W m^{-2}. No orbital evolution occurs in these simulations, however, the spin axis is allowed to precess at a rate set by the stellar torque (see Chapter 3). Two quantities are displayed in these plots: the fractional area of the planet that is permanently ice covered (*i.e.* ice covered year-round) and the total ice mass at the end of the simulation.

At the lowest stellar flux values, the planet is globally ice covered, but the ice sheet mass remains at zero. This is because, in our model, precipitation is shut off when the oceans are frozen over, and in these coldest cases, the oceans freeze over immediately, thus no ice accumulates on land. In the $\psi = 50°$ case, the coldest cases are actually not ice covered year round. Since the oceans have frozen before ice sheets can grow on land, and the thermal inertia of the land is low (compared to the oceans and the ice sheets), the temperature over land actually gets above freezing during the summer months. Thus the area coverage of < 1 is probably a side effect of our modeling choices—these cases really are in a snowball state. At higher stellar flux values, it takes hundreds to thousands of years for the planet to cool into the snowball state, thus ice sheets are allowed to grow on land. Because it takes much more energy in the model to melt a thick layer of ice (than to simply heat the land), these cases remain fully ice covered year-round.

All points within the gray-shaded region entered a snowball state in < 200 kyr, after which all ice sheets appear to be stable under static orbital/obliquity conditions. The light-

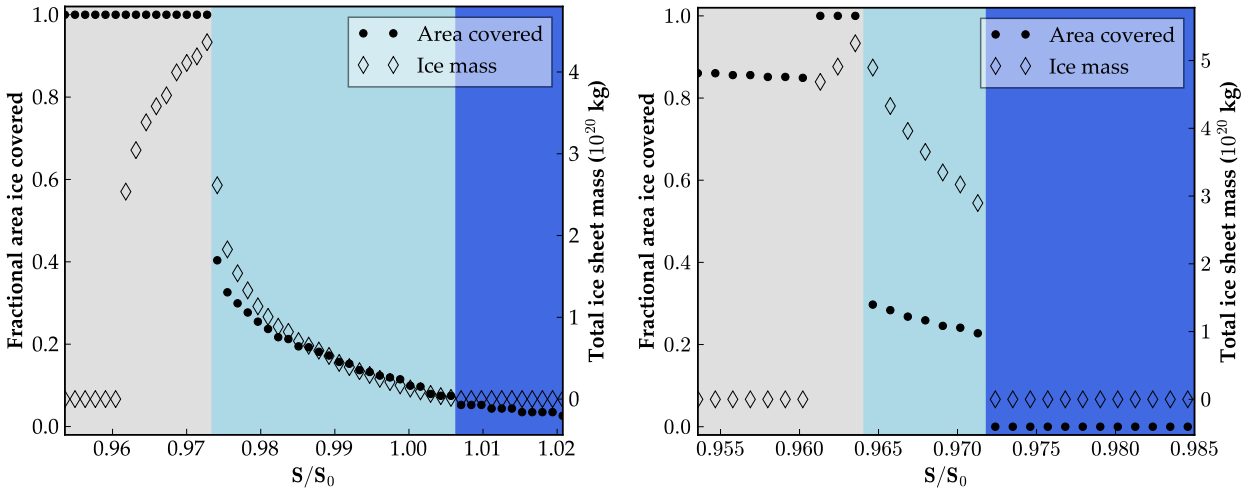

Figure 4.9: The climate states for static orbital/obliquity conditions as a function of stellar flux, S/S_0, where $S_0 = 1367.5$ W m^{-2}, for $\psi = 23.5°$ (left) and $\psi = 50°$ (right). The ice covered area includes both land and ocean grid-points. The gray shaded area represents snowball states (the ocean surface is permanently and completely ice-covered), dark-blue represent ice-free (no year-round ice) states, and light-blue is the "transition region", where the ocean is not totally ice-covered and ice sheets form on land.

blue region corresponds to our "transition region", wherein stable ice sheets form at some latitudes and persist year-round. In the dark-blue region, ice may form seasonally, but no permanent ice sheets appear. Note that in the $\psi = 23.5°$ cases, the ice covered area is not necessarily equal to zero—this is because the oceans remain frozen at the poles year round, even though no ice sheets grow from year to year.

The higher obliquity case remains clement (not in a snowball state) at lower stellar flux, and thus higher semi-major axis, than the low obliquity case. This is consistent with past results (Spiegel et al., 2009; Armstrong et al., 2014). The transition region is also narrower in this case, and the boundary between the transition region and the ice sheet free region (light- and dark-blue) is sharper. This is consistent with the results of Rose et al. (2017), which demonstrated that ice (as represented by $T < 0°$ C on land or ocean) is less stable

on higher obliquity planets. Interestingly, even though the obliquity is less than 55° (the point at which the annual insolation at the poles begins to exceed that of the equator), the ice sheets in the transition region form along the *equator*, not the poles. This is a result of the temperature dependence of ice ablation—when the atmosphere is warmer, the ice melts faster (see Equation (4.14)). Even though the equatorial latitudes receive more sunlight over the course of an orbit, the summers are much more intense at the poles. High latitude summers are then much warmer than conditions ever get at the equator. So while the snowy season at the poles may be colder and longer, the intense summers are more than enough to melt the ice accumulated during winters, whereas the melting seasons are not hot enough or long enough to fully melt the equatorial ice.

4.4.2 Dynamically evolving cases

Figures 4.10-4.15 show several slices of the parameter space for planet 2 in our test system, SYS1 (see Figures 3.4-3.6), with an incident stellar flux of $S = 1332.27$ W m^{-2}, or $S/S_0 = 0.974$. This stellar flux puts the planet right at the boundary between the snowball state and the transition zone for a planet with low eccentricity and 23.5° obliquity (Figure 4.9, left panel). This places the $\psi_0 = 50°$ simulations in the ice-free regime.

The obliquity amplitude ($\Delta\psi$) maps from the previous chapter are reproduced here for reference. The other panels in each figure show the fraction, f_{ice}, of the total area of the panel that is permanently ice-covered, where "permanent" means covered year-round as in the previous section. Thus, some cases that have $f_{ice} = 0$ do have seasonal ice formation.

The upper right panel shows the climate conditions assuming a static orbit and obliquity fixed at the initial values. The initial eccentricity thus determines the variation of f_{ice}—at low e, $f_{ice} = 1$ and the planet is in a snowball state, but as e increases, f_{ice} decreases. This is simply due the dependence of the stellar flux on the eccentricity (Equation 1.12).

In the lower left panel, the orbit and obliquity are also fixed, but they are fixed at the mean values from the 2 Myr simulation. The structure of this phase space is very different from that of the fixed initial conditions (upper right). For the cases with $\psi_0 = 23.5°$ (Figures

4.10, 4.12, and 4.14), using the mean properties tends to decrease the number of cases that are in a snowball state, however, for the $\psi_0 = 50°$ cases (Figures 4.11, 4.13, and 4.15), the mean properties produce snowball states where none existed before (at the initial values). Hence, using the mean orbital/obliquity properties in a climate simulation produces very different results from using the initial (or, perhaps, observed) properties.

Finally, the lower right panel in each figure shows the final ice coverage fraction for the full 2 Myr simulation with evolving orbits and obliquities. Now, the ice coverage increases almost universally, and snowball states are much more frequent than under static conditions. There are some configurations which had $f_{ice} = 1$ under static conditions but are not completely ice covered under evolving conditions (at low inclination and low eccentricity, for example), but in general, the evolution tends to encourage the snowball instability, except at higher e_0.

Interestingly, there are several blue "islands" (where $f_{ice} < 1$) that are completely surrounded by snowball states in the dynamically evolving cases. There is an interesting interplay between the obliquity and eccentricity that we will discuss in more detail in Section 4.4.3.

Figure 4.16 shows the climate and orbit evolution for a point in the parameter space of Figure 4.12 ($\psi = 23.5°$ and $P_{rot} = 1.62$ day). In this figure we have the surface temperature, top-of-atmosphere (TOA) albedo, ice sheet height, bedrock height, and insolation, all averaged over an orbit or "year", as a function of latitude and time. Also shown are the three parameters which affect the insolation: obliquity, eccentricity, and "climate-obliquity-precession-parameter" (COPP), which is defined as:

$$\text{COPP} = e \sin\psi \sin(\varpi + p_A), \tag{4.28}$$

where, again, $\varpi + p_A$ represents the instantaneous angle between periastron and the planet's position at its northern spring equinox. This is essentially the same as the commonly used "climate precession parameter" or CPP, but additionally takes into account the effect of obliquity variations (which are neglected in the CPP because Earth's are very small). COPP can be thought of as a measurement of the asymmetry between the northern and southern

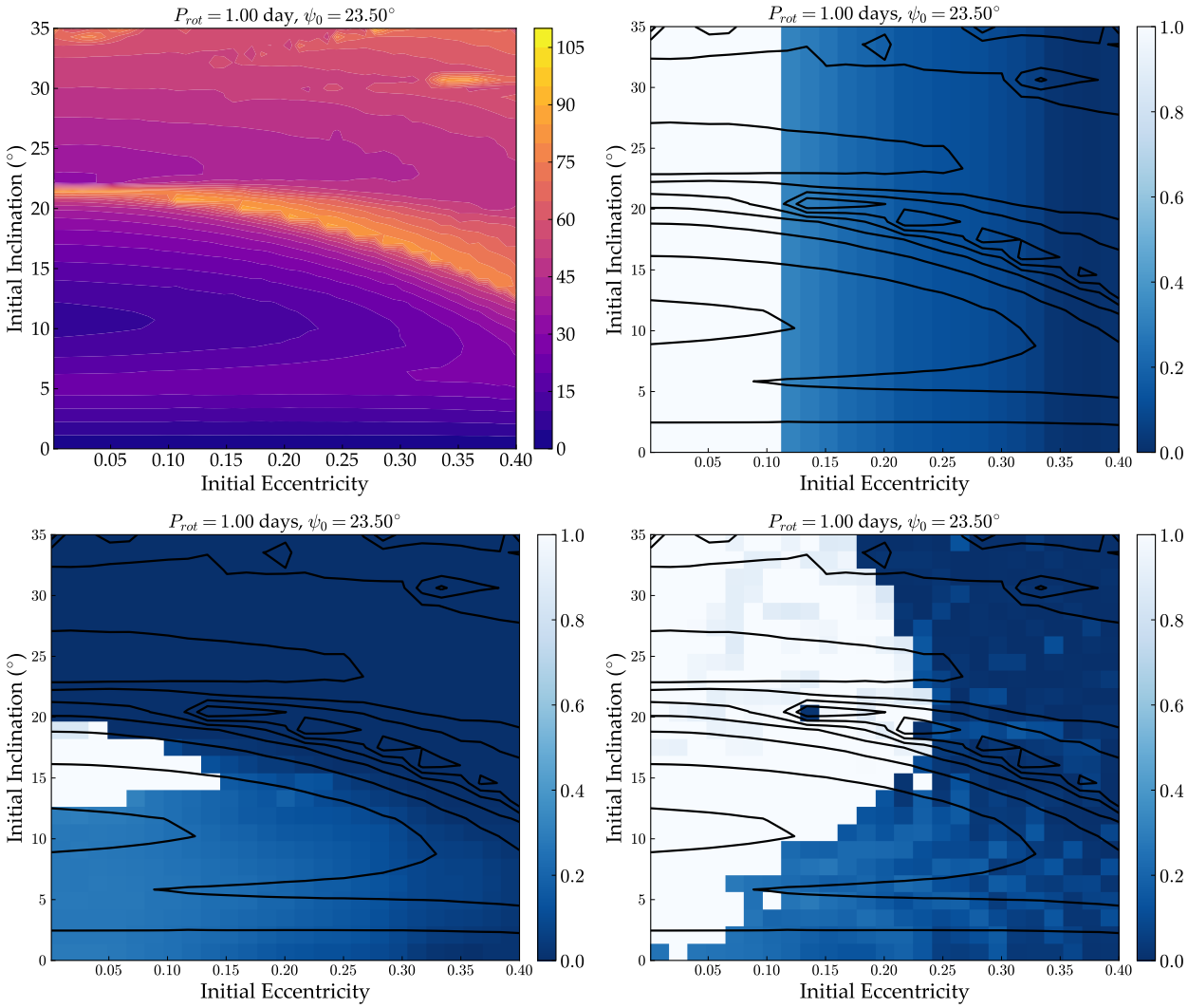

Figure 4.10: Climate states as a function of initial eccentricity and inclination, for $P_{rot} = 1$ day and initial obliquity $\psi_0 = 23.5°$, with a stellar constant of $S = 1332.27$ W m^{-2}. The upper left panel shows $\Delta\psi$, which reaches a maximum in the secular resonance (see previous chapter) and at high inclination, and is at a minimum at low inclination and near the Cassini state. The remaining panels show the fraction of the surface area that is permanently ice-covered over the final orbit (blue color-scale) and contours of $\Delta\psi$ (black lines), under three different conditions: upper right, static orbit and obliquity at the initial values; lower left, static orbit and obliquity at the mean values from the simulation; lower right, dynamically evolving orbit and obliquity.

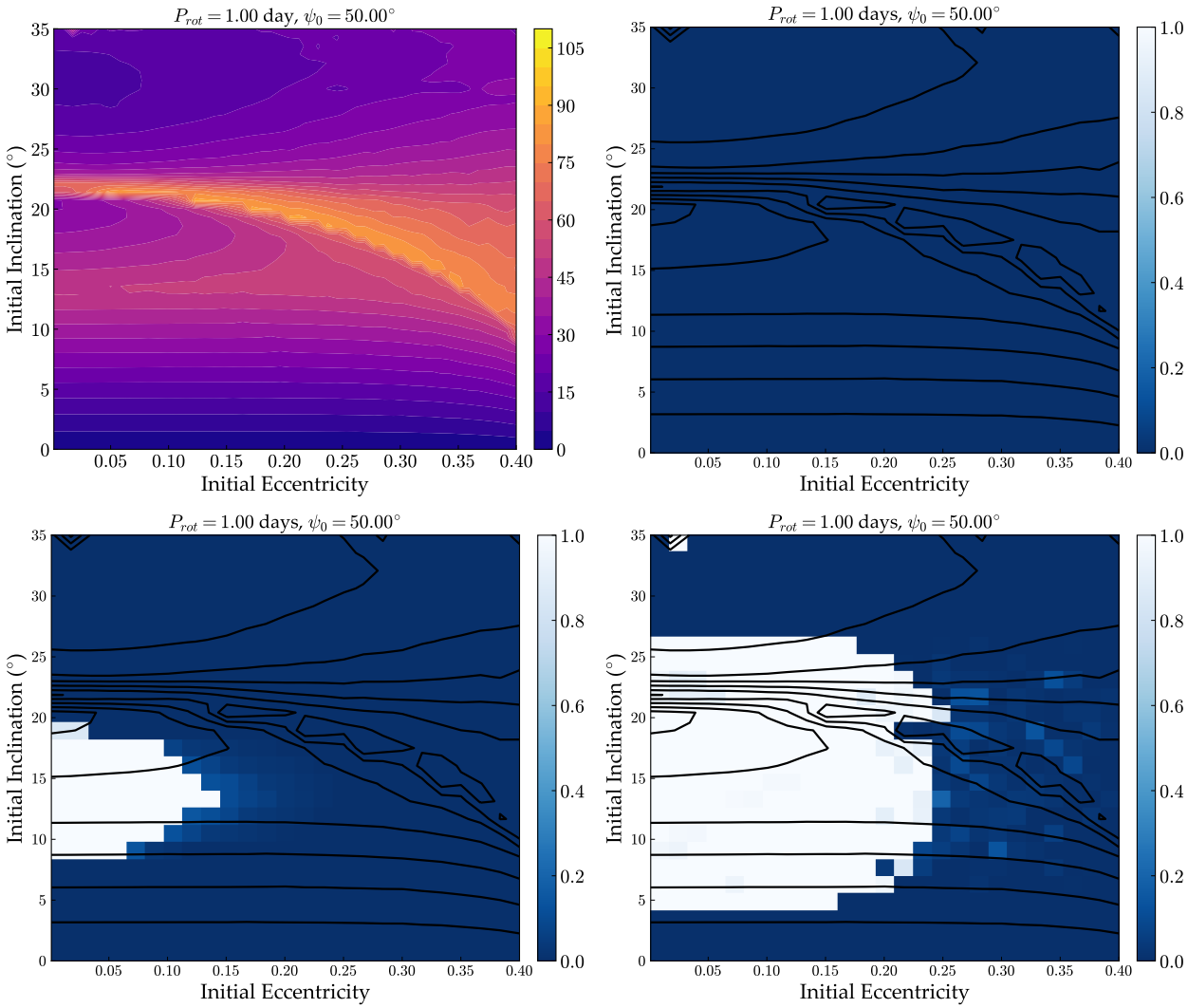

Figure 4.11: Same as Figure 4.10 but for $P_{rot} = 1$ day and initial obliquity $\psi_0 = 50°$.

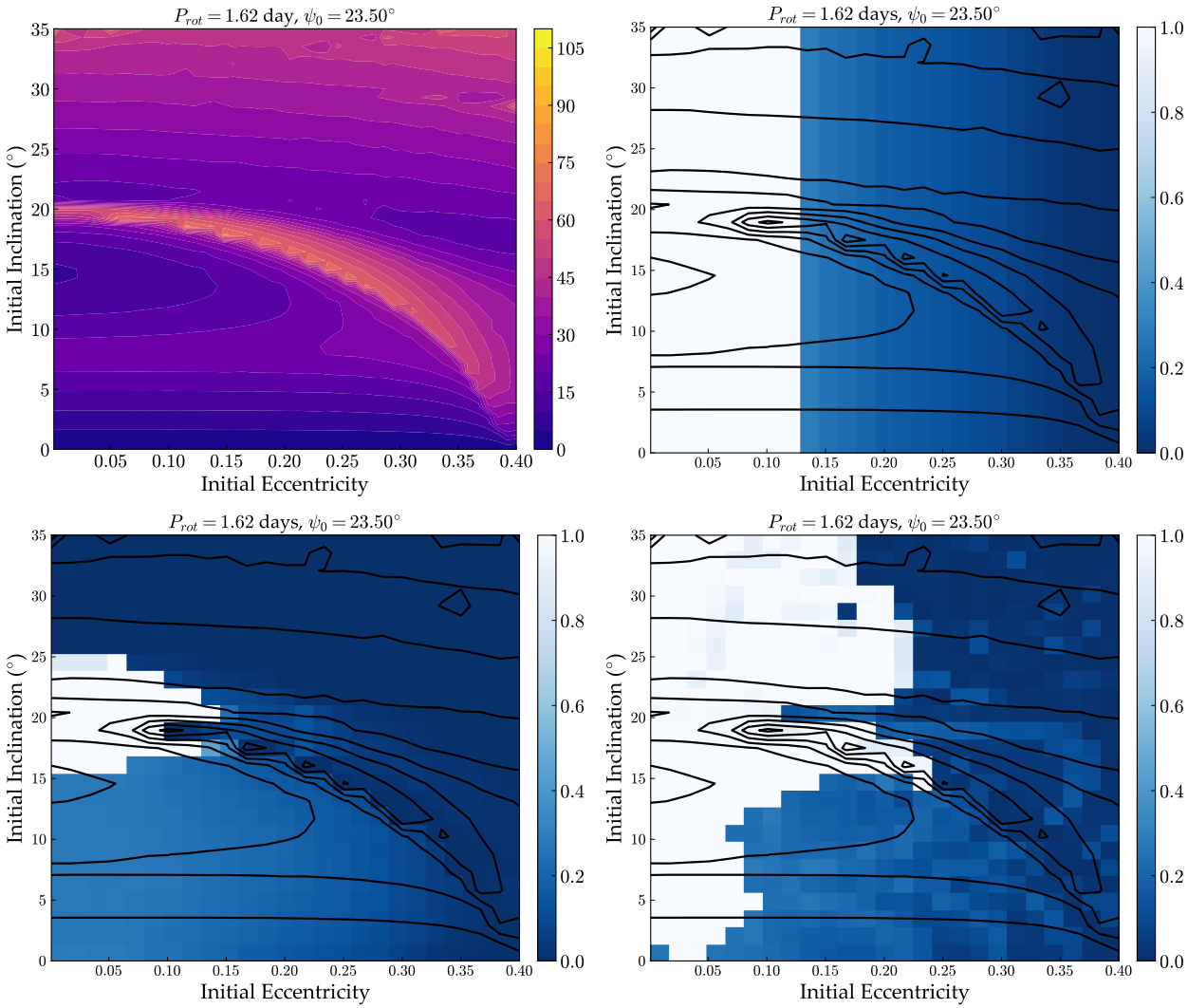

Figure 4.12: Same as Figure 4.10 but for $P_{rot} = 1.62$ day and initial obliquity $\psi_0 = 23.5°$.

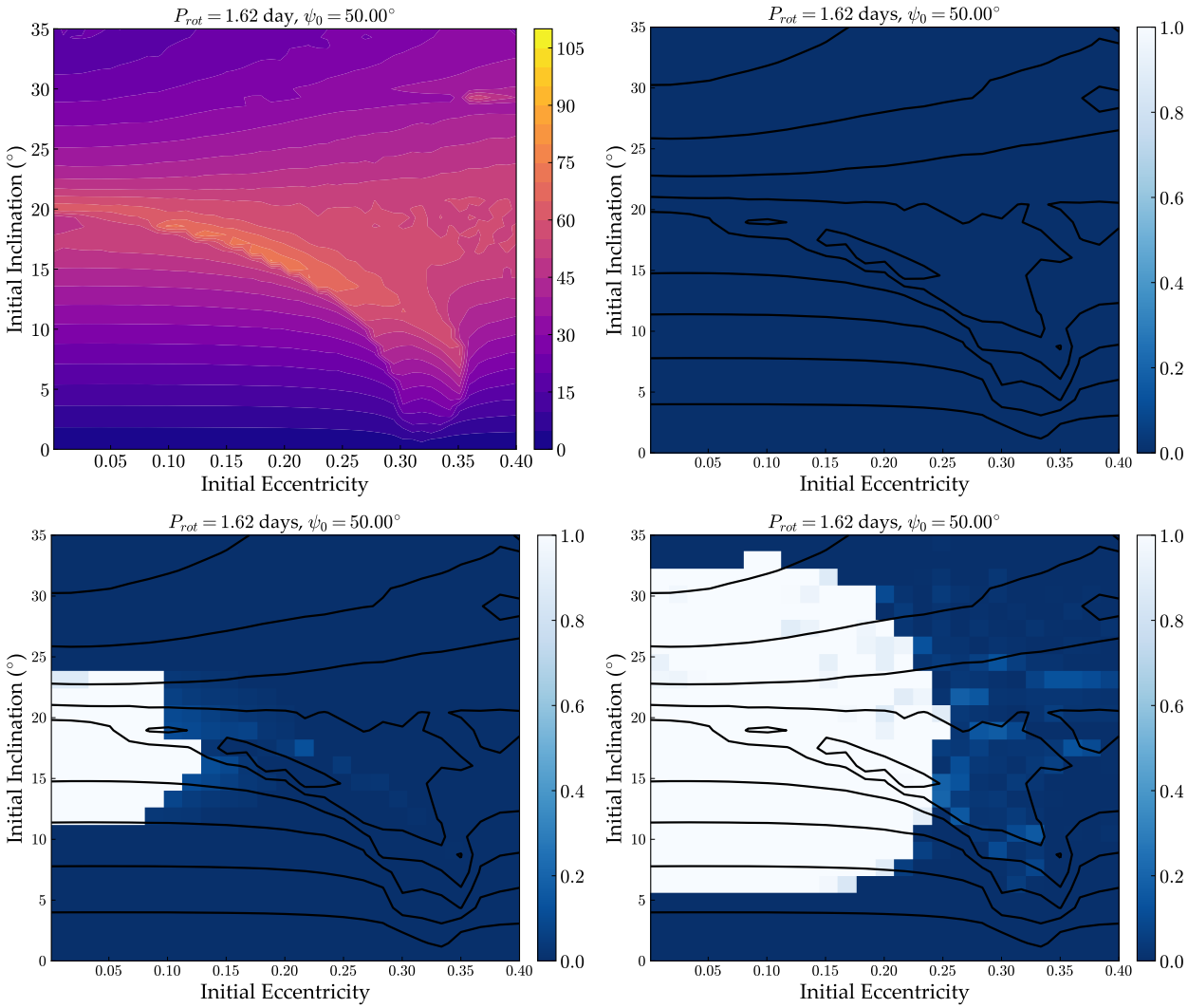

Figure 4.13: Same as Figure 4.10 but for $P_{rot} = 1.62$ day and initial obliquity $\psi_0 = 50°$.

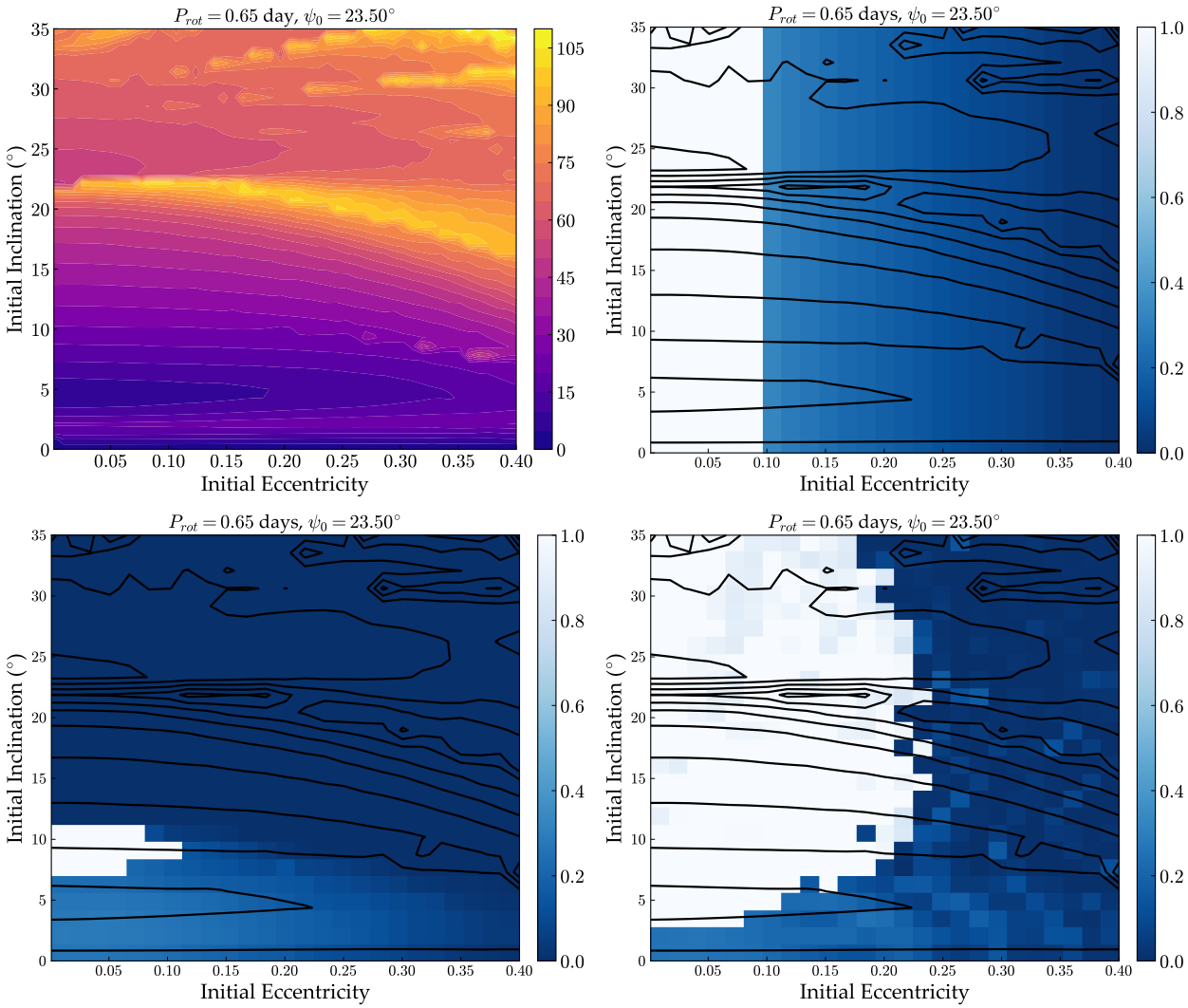

Figure 4.14: Same as Figure 4.10 but for $P_{rot} = 0.65$ day and initial obliquity $\psi_0 = 23.5°$.

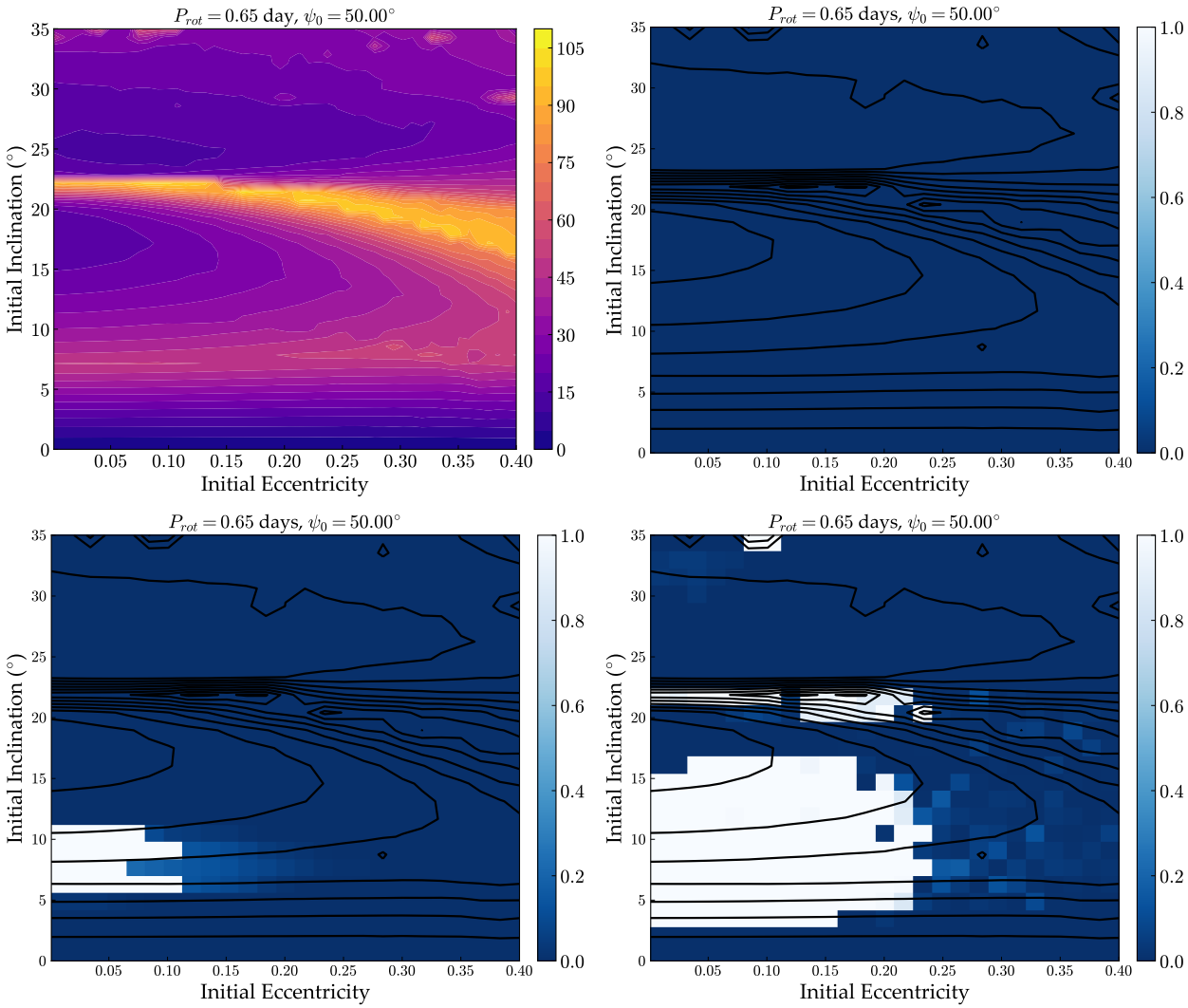

Figure 4.15: Same as Figure 4.10 but for $P_{rot} = 0.65$ day and initial obliquity $\psi_0 = 50°$.

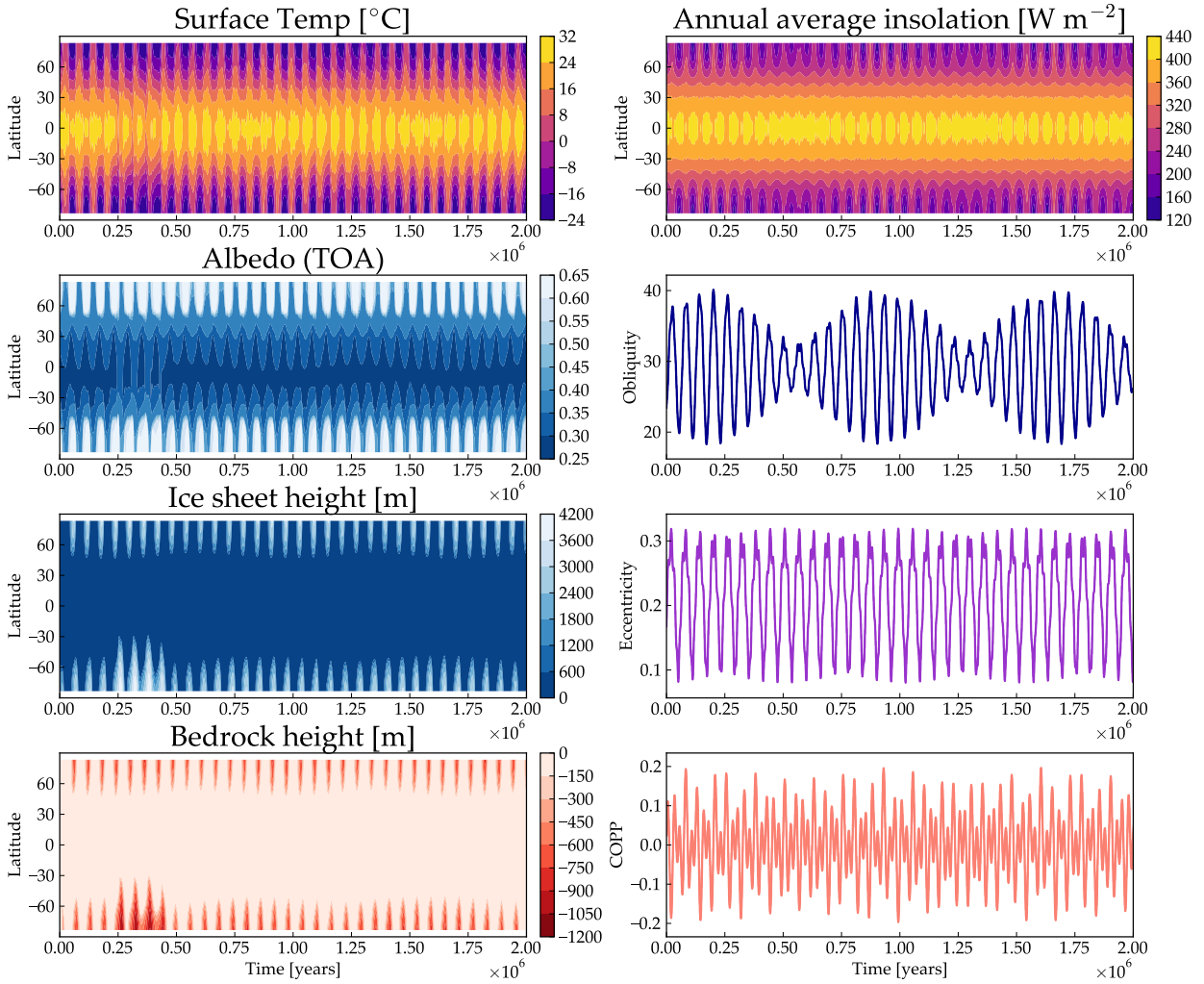

Figure 4.16: Evolution of climate and orbit for a case at initial values: $S = 1332.27$ W m^{-2}, $e_0 = 0.16725$, $i_0 = 20.412°$, $\psi_0 = 23.5°$, and $P_{rot} = 1.62$ day (inside the horizontal blue strip near the center of Figure 4.12, lower right panel). The climate-obliquity-precession-parameter is defined as COPP $= e \sin\psi \sin(\varpi + p_A)$ and represents the asymmetry between the northern and summer hemispheres (see text).

hemispheres, and so varies with the angle $\varpi + p_A$, modulated by the eccentricity and obliquity. When COPP > 0, the northern hemisphere receives more stellar flux than the southern; vice-versa for COPP < 0.

Despite this case lying very near to snowball states, the planet remains clement throughout this 2 Myr evolution. Ice sheets grow and recede at both poles rather dramatically, from almost nothing to nearly 4 km in height (in some regions) and back. This is a result of a nearly 200 W m^{-2} swing in the annual insolation over $\sim 50,000$ years, due to the combined effects of the obliquity and eccentricity variations. The envelope of the obliquity oscillation is neatly imprinted on the latitude of the ice edge, though the primary driver of growth and retreat is the change in eccentricity. The ice edge progresses into the mid-latitudes during periods when the obliquity oscillation is lowest in amplitude.

In Figure 4.17, we have the same evolution for a case immediately adjacent to that in Figure 4.16. The eccentricity and obliquity variations are very similar to the previous case, however, the obliquity peaks at a slightly higher value ($\sim 35°$, compared to $\sim 30°$ in the previous). The ice sheets grow and retreat in a similar fashion until the obliquity approaches its highest value, at which point the planet abruptly enters a snowball state. The appearance of the large ice cap instability (LICI) is somewhat counter to expectation here—as we have shown before (and numerous other studies have found), high obliquity tends to grant a planet additional warmth at low stellar flux. The analytic solution to the annual EBM from Rose et al. (2017) provides an explanation for how the instability occurs.

Figure 4.18 shows the ice edge latitude as a function of the parameter q, from the Rose et al. (2017) solution, for the two cases discussed above. The dimensionless parameter q describes the combined effects of insolation and greenhouse warming. For the calculation of q, we take a_0 to be the average albedo of the land and water ($a_0 = f_L a_L + f_W a_W$, where a_l and a_w are the co-albedos of the land and water) and T_{ref} to be our freezing point of water, $T_{ref} = -2°$ C.

The plots in Figure 4.18 show the ice edge latitude at different obliquities—the light blue line at each cases' minimum obliquity, and the red line at its highest obliquity. The gray

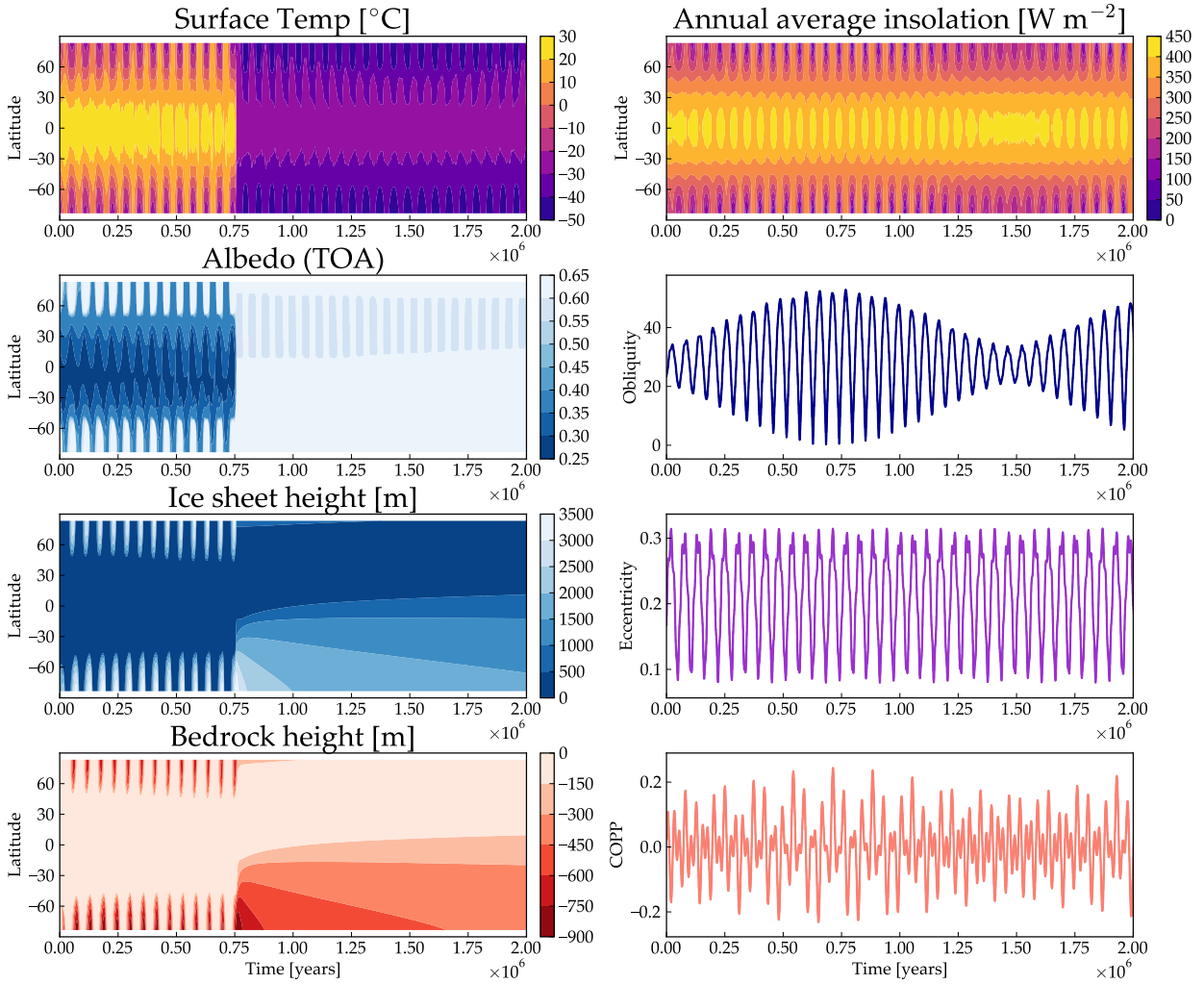

Figure 4.17: Same as Figure 4.16 but for $e_0 = 0.16725$, $i_0 = 18.955°$, $\psi_0 = 23.5°$, and $P_{rot} = 1.62$ day (slightly lower inclination than the case in that Figure). A snowball state occurs at $t \sim 750,000$ years—the temperature drops globally, the albedo approaches that of ice everywhere, and ice sheets no longer grow (precipitation is shut off artificially) and instead just gradually flatten.

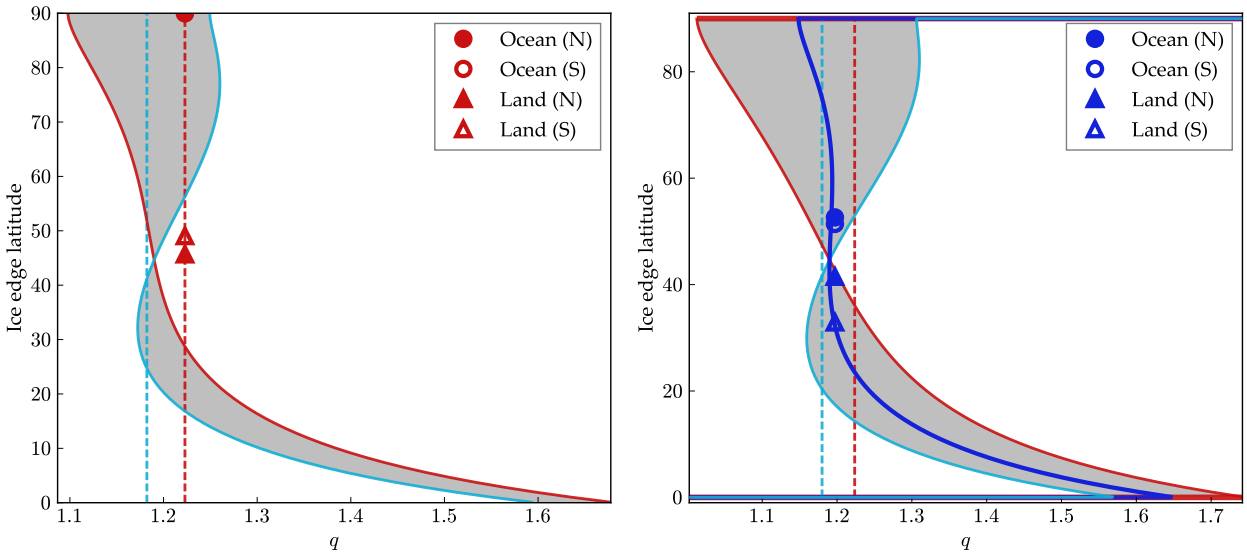

Figure 4.18: Ice edge latitude as a function of the parameter q (see Section 4.2.1) from the analytical annual energy balance model (Rose et al., 2017), for the cases shown in Figures 4.16 (left) and 4.17 (right). The solution is a function of obliquity: light blue corresponds to the minimum obliquity in the simulation, red to the maximum obliquity, and the gray-shaded area is the range explored by the planet. Vertical dashed lines indicate the value of q, which is a function of eccentricity, at the corresponding times. In the left panel, markers show the ice edge latitude for northern and southern land and ocean at the time of maximum obliquity, at the coeval value of q, which depends on the eccentricity. The right panel also shows these ice edge latitudes and the analytical solution at 500 years before the planet becomes fully glaciated (dark blue).

shaded area indicates the full range of solutions the simulation explores. When the slope of the line is positive or zero (as in the upper and lower branches), the ice edge is in a stable equilibrium (the annual solution is an equilibrium model). When the slope is negative or undefined, the ice edge is unstable—this gives rise to the small ice cap instability (SICI) at the highest latitudes, and the large ice cap instability (LICI) at the mid to low latitudes. When the ice edge is at 90°, there is no ice cap; when it is at 0°, the planet is in a snowball state.

The left-hand panel corresponds to the case that does not experience the LICI (Figure 4.16). In this case, there is always a stable branch for the ice edge at all obliquities. The points shown in the plot are the actual ice edges from our full seasonal model, for both the land and ocean in each hemisphere, at the time of the highest obliquity. The vertical dashed lines indicate the average annual value of q (which depends on the eccentricity) at each obliquity extreme. These points follow the analytic ice edge solution (which represents the climate in equilibrium) in time, and are dependent on the seasonality and the nature of the ice sheet model, and so do not fall directly on the analytical solution at most times. Nevertheless, the points stay very near to the analytical solution, and give a sense of why the instability occurs when it does. In this case, the instability never occurs because the ice edges (land and ocean in each hemisphere) remain on a stable branch of the analytical solution at mid-latitudes (or retreat to 0°).

In the right-hand panel, we see the same quantities plotted for the second case (Figure 4.17), which experiences the LICI. We can see that at the highest obliquity (red curve), there is no stable ice edge between 0° and 90°. We have additionally plotted the analytical solution ~ 500 years before the planet has fully entered the snowball state. We can see that the ice edges in each hemisphere are precariously perched upon a branch of the solution where the slope is becoming undefined. At this point, the ice must either retreat entirely or expand to the equator. Because this occurs near a minimum in global insolation (because the eccentricity is low), and the ice sheets have a lot of thermal inertia, the snowball state is more easily reached. This demonstrates the susceptibility of planets with large orbital/obliquity

variations to the snowball instability. Essentially, if planets proceed to a high obliquity and low eccentricity state with ice sheets extending to mid-latitudes, the ice edge becomes unstable and the entire planet quickly freezes.

This can be seen even in the warmest cases. In the cases shown in Figure 4.19, we increased the star's luminosity slightly, to $L_\star = 3.81 \times 10^{26}$ W, which corresponds to a stellar constant of $S = 1346.4$ W m^{-2} for the planet. The planet is completely free of permanent ice even at $e = 0$ in the unperturbed case. With perturbations, there is a narrow region in which snowball events occur when we start the planet with $\psi = 50°$. Figures 4.20 and 4.21 show how the climate evolves for one of the snowball simulations. The snowball instability occurs at ~ 1.8 Myrs, after an eccentricity minimum, as the planet is beginning to warm. At this time, the planet is not able to deglaciate before it moves toward high obliquity, when the ice edge becomes unstable.

Many of the preceding cases (*e.g.* Figures 4.16 and 4.20) show taller and greater area ice sheets in the southern hemisphere than in the northern. The reason for this is, in part, that we did not vary the initial precession angle in these simulations. The parameter, COPP, describes the asymmetry in insolation between northern and southern hemispheres. When COPP > 1, the northern hemisphere receives more flux than the southern; vice versa for COPP < 1. This asymmetry is enhanced when obliquity and eccentricity are large (COPP $= 0$ when either parameter is zero). In this case, the initial value of the angle between periastron and northern vernal equinox is $\varpi + p_A \sim 22°$, and COPP is small (COPP $= 0.0098$ at the start of the simulation in Figure 4.20). Thus, there is not a large asymmetry between hemispheres initially, and the relative ice sheet growth between hemispheres would be random if the precession rate, eccentricity, and obliquity were uncorrelated. This is not the case—the ice sheets are almost always larger in the southern hemisphere with this choice of initial precession angle. But as we discussed in Chapter 3, the parameters in this system are not uncorrelated, particularly in the proximity of the secular resonance. The obliquity and eccentricity evolve nearly in sync here.

We can better understand this by viewing the insolation at high latitude. Figure 4.22

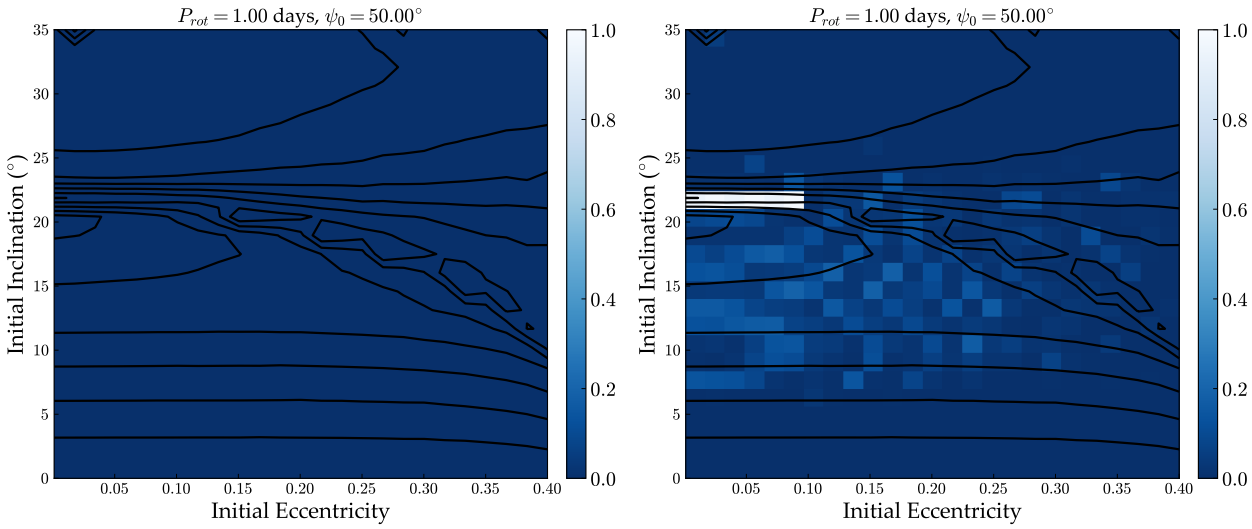

Figure 4.19: Fractional ice-covered area for $\psi_0 = 50°$, $P_{rot} = 1$ day, and stellar constant $S = 1346.40$ W m^{-2}. The left panel is the static case at the initial values; the right panel is the dynamically evolving case. The obliquity amplitude is shown in Figure 4.11 and in the black contours here. The static case with the mean orbital/obliquity values is identical to the left panel (ice-free everywhere). Including the orbital evolution causes the planet to have partial ice coverage in some areas, and triggers snowball states at $i_0 \sim 22°$.

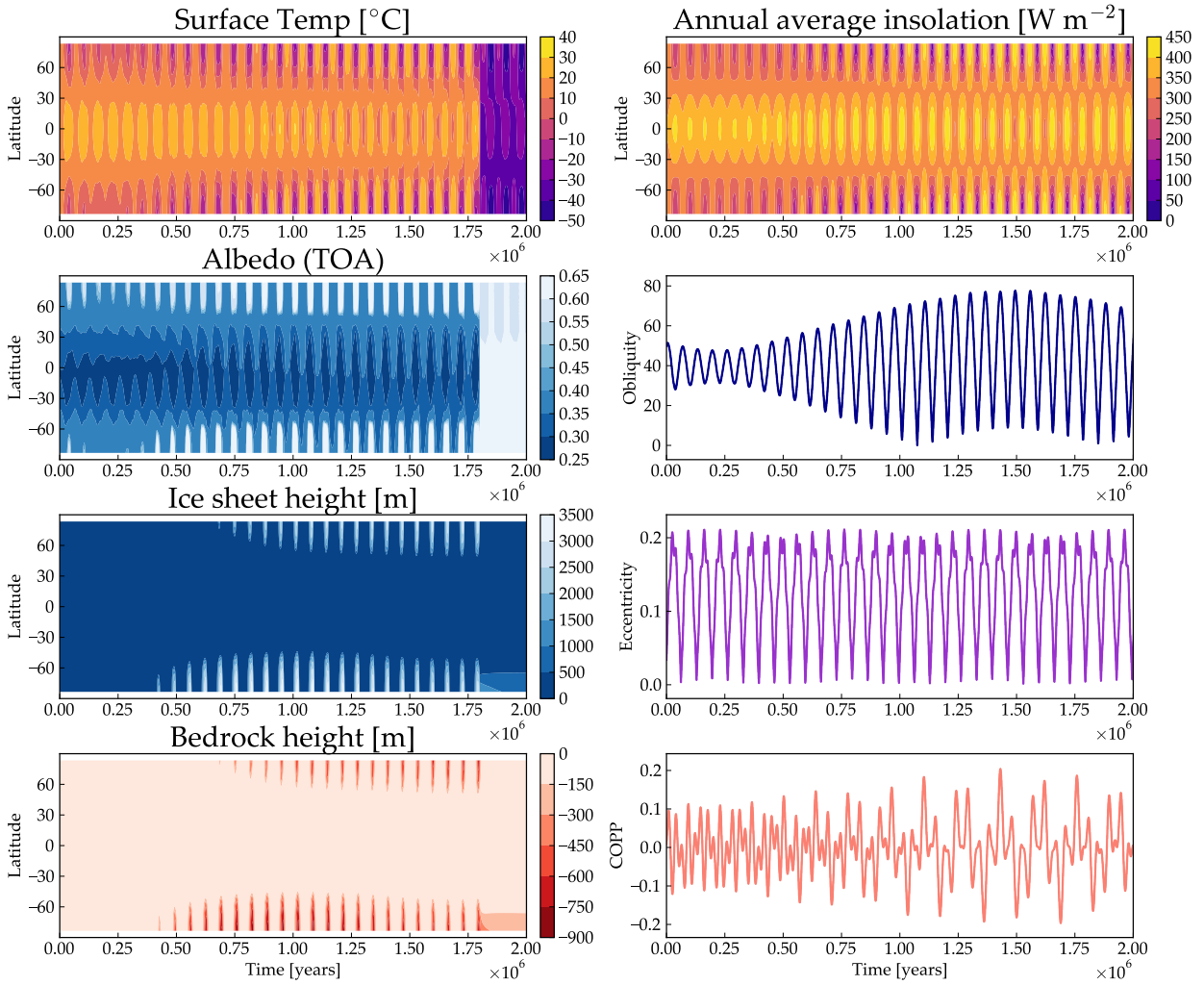

Figure 4.20: Same as Figure 4.16 but for $S = 1346.40$ W m^{-2}, $e_0 = 0.03425$, $i_0 = 21.87°$, $\psi_0 = 50°$, and $P_{rot} = 1$ day (*i.e.* a snowball case from Figure 4.19).

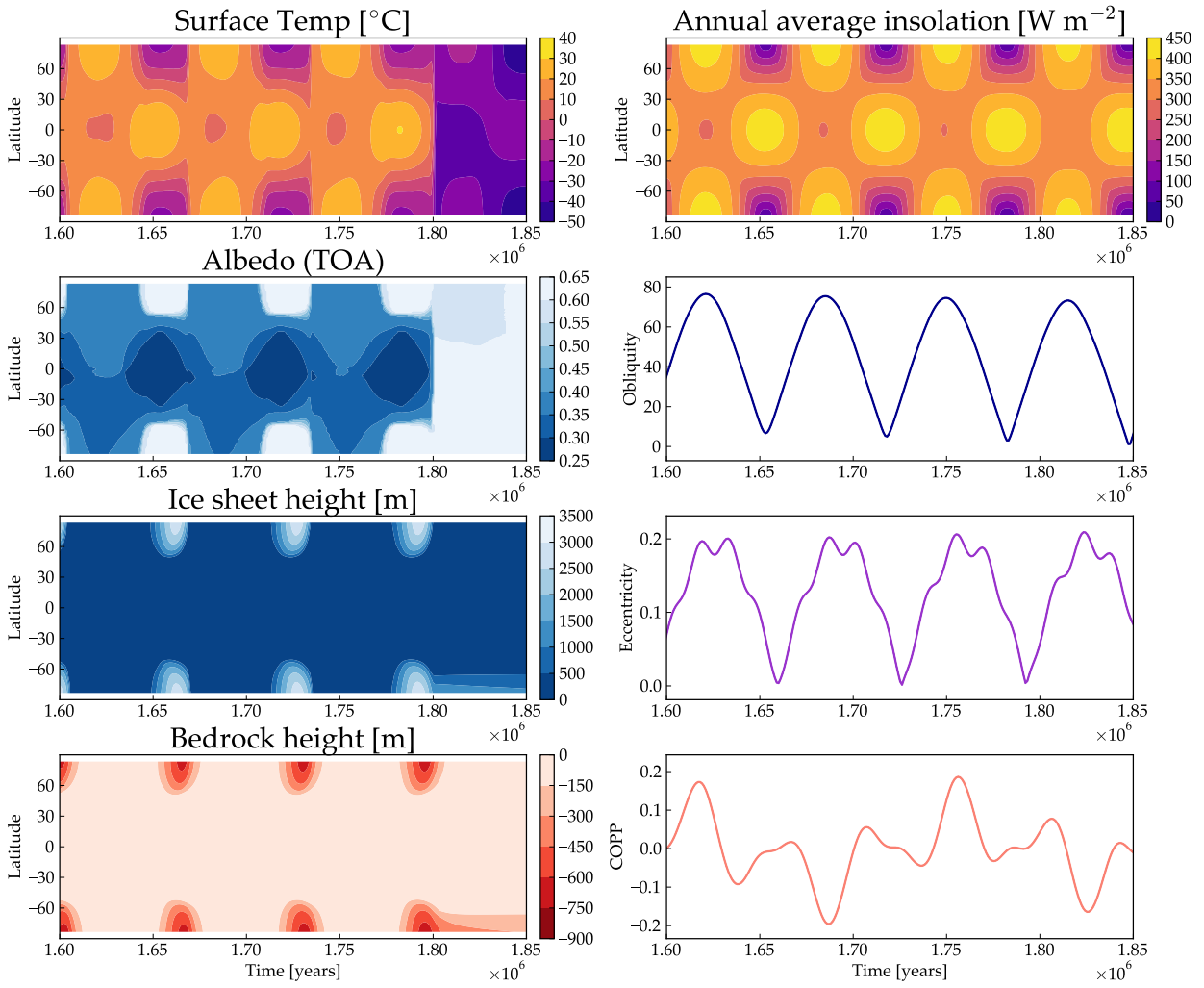

Figure 4.21: Zoom in on the last three glacial cycles before the snowball state in Figure 4.20. The obliquity and eccentricity evolve *nearly* in sync. The resulting phase shift in eccentricity and obliquity plays an important role in triggering the snowball instability.

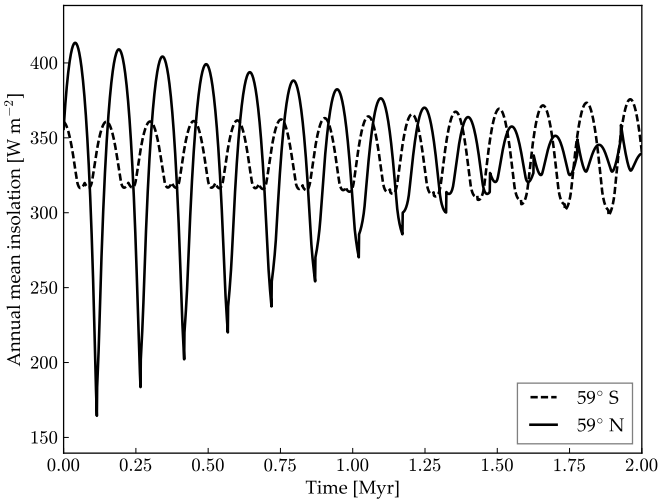

Figure 4.22: Annual average insolation at 59° north and south for a case at $S = 1346.40$ W m^{-2}, $e_0 = 0.03425$, $i_0 = 21.87°$, $\psi_0 = 50°$, and $P_{rot} = 1$ day. For most of this simulation, the southern ice sheet is larger than the northern, however, it is the northern ice sheet that ultimately triggers the snowball instability. The insolation peaks are higher for the northern hemisphere until ~ 1.25 Myr, after which the southern peaks become slightly stronger. This case is very near to the secular resonance in Figure 4.11. As a result, the ψ and e evolve nearly in sync, and the insolation asymmetry between hemispheres is maintained for an extended period of time.

shows the annually averaged insolation at $\sim 59^\circ$ latitude in both hemispheres. Though this does not show the peak summer insolation, which we have argued is critical to ice sheet growth and decay, we can still see that there is an asymmetry between the southern and northern hemisphere *cycle*—the northern hemisphere experiences much higher peaks for the first ~ 1.25 Myrs.

This initial precession angle can itself be important. Even though it does not have a strong effect on the insolation, it does affect the obliquity cycle. Figure 4.23 shows the obliquity amplitude and ice coverage for the same parameters as in Figure 4.10, with $p_A = 101.77976^\circ$ instead of $p_A = 281.77976^\circ$. Note that the secular resonance (the "arc") is still present, while the Cassini state (the obliquity amplitude minimum) is not. The ice covered area (and snowball states) occur in similar locations at high initial inclination, but at low inclination, below the secular resonance, the ice covered area extends to high initial eccentricities.

In addition to snowball states, we also observe some very high temperatures at high obliquity, high eccentricity times. For a case with $\psi_0 = 23.5^\circ$, $P_{rot} = 1$ day, $e_0 = 0.3$, and $i_0 = 17.5^\circ$, which is inside the secular resonance in Figure 4.10, the obliquity reaches $\sim 80^\circ$ while the eccentricity is ~ 0.4. Figure 4.24 shows the orbital/obliquity evolution and the resulting average, minimum, and maximum surface temperatures (over an orbital period). At the highest obliquity times, the north pole of the planet reaches 140° C. Such strong heating should probably result in strong convection, which would increase the TOA albedo (due to cloud formation) and cause increased horizontal heat flow, but our simple EBM does not model such effects. It is beyond the scope of this study to comprehensively model this scenario with a GCM, but it is worth future investigation in the future.

4.4.3 Examining ice stability

In the previous section, we saw that the ice caps often become unstable as a result of the orbital/obliquity evolution. Though we highlighted the snowball instability (or LICI), the SICI can also be observed in the rapid retreat of the ice sheets. We can use the analytical solution from Rose et al. (2017) (Section 4.2.2) to plot the ice edge latitude as a function

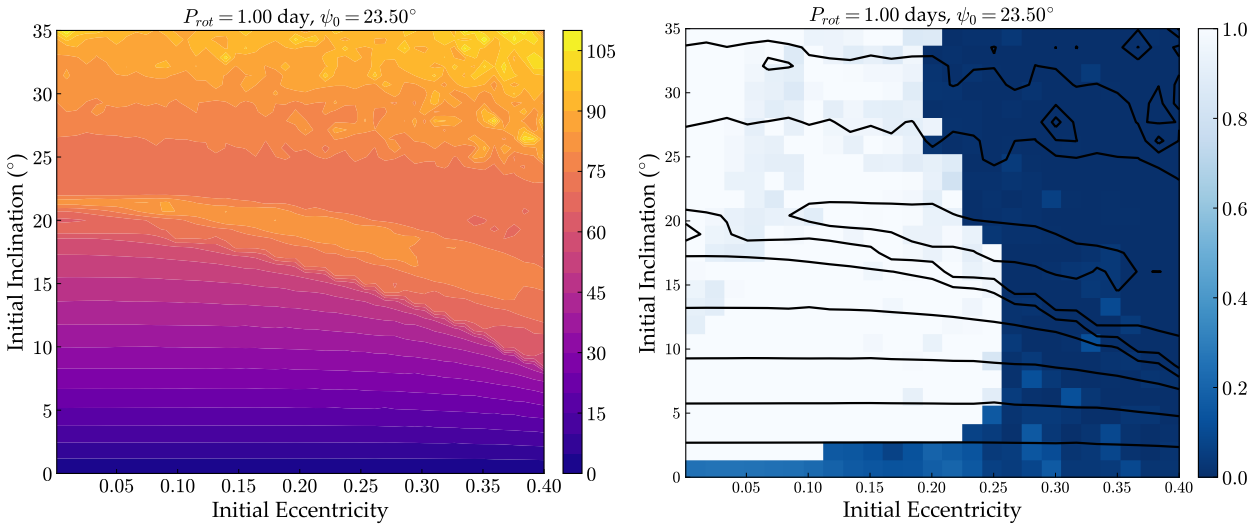

Figure 4.23: Obliquity amplitude and fractional ice coverage for $P_{rot} = 1$ day and initial obliquity $\psi_0 = 23.5°$, with a stellar constant of $S = 1332.27$ W m^{-2}—same as Figure 4.10 but with a 180° rotation in initial p_A. The Cassini state vanishes. While the climate behavior is similar to Figure 4.10 at high inclination, at lower inclination, the snowball states extend to higher eccentricity here, due to the absence of the Cassini state.

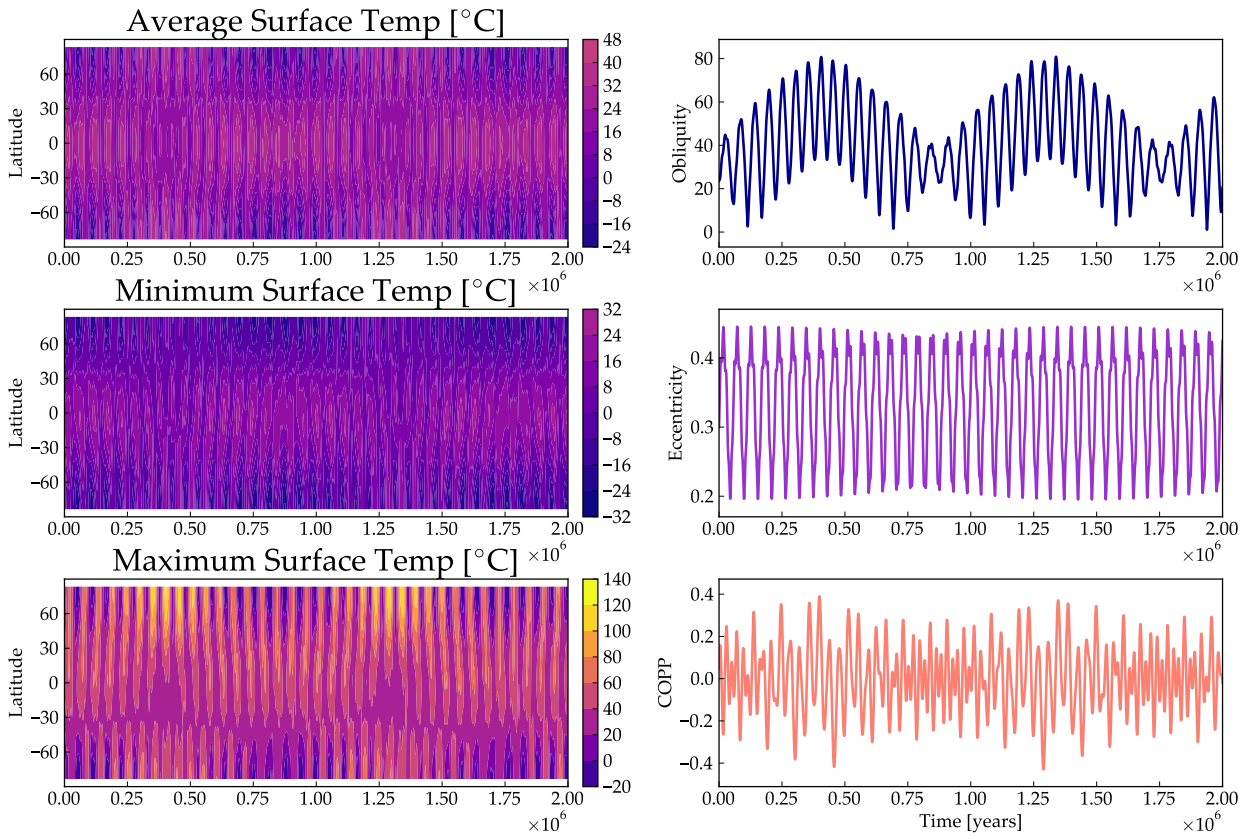

Figure 4.24: Evolution of the orbit, obliquity and surface temperature for a case with $P_{rot} = 1$ day, $\psi_0 = 23.5°$, $e_0 = 0.3$, and $i_0 = 17.5°$. The top left panel is the annually averaged surface temperature; middle left, the minimum surface temperature over an orbit; and lower left, the maximum over an orbit. The obliquity evolution is strong because of the secular spin-orbit resonance (see Chapter 3). The highest obliquity times correspond to high eccentricity times. As a result, the insolation at high latitudes is extremely high during summer and the surface temperature exceeds the boiling point of water. This effect depends also on the angle $\varpi + p_A$ (the angle between the equinox and pericenter)—this is responsible for the additional variation in maximum temperature between these warm periods.

of the dimensionless parameter, q (Figure 4.18). As we discussed, the slope of this curve indicates whether the equilibrium ice line is stable or unstable.

Figure 4.25 shows two parameters that can be used to analyze the ice edge stability: dq/dx_s and Δq, for a clement (*i.e.* non-snowball) case with $P_{rot} = 1.62$ day and $\psi_0 = 23.5°$. Both quantities are calculated at the ice edge latitude for northern and southern land and ocean, for a total of four ice edges. The "perturbation", Δq, is

$$\Delta q = q_{true} - q_{equil}, \tag{4.29}$$

where q_{true} is the "true" value of q, calculated from the stellar flux and the eccentricity at that instant in time and q_{equil} is calculated from the analytical solution, at each ice edge and the current obliquity. Thus, it is when both dq/dx_s and Δq are negative that we would expect the snowball states to occur—this corresponds to the third quadrant in the right panel of the figure. Both dq/dx_s and q_{equil} are calculated from the Python package developed in Rose et al. (2017).

As described previously, the ice caps will become unstable any time $dq/dx_s < 0$. Whether or not the caps collapse to the poles or grow to the equator depends on the direction of the perturbation, Δq (see Figure 4.2). Figure 4.25 shows a case in which the ice edges are truly stable (except in the earliest phase, when the ice sheets are growing): $dq/dx_s > 0$ over the entire simulation and the ice edges neatly avoid the third quadrant in the right panel.

The same quantities are shown in Figure 4.26 for an adjacent case which undergoes the snowball instability. In this case, dq/dx_s becomes negative several times for the sea ice in both hemispheres and Δq is negative during some of these excursions. The ice edges do not grow immediately to the poles, however. This may be due to the fact that the model is not in equilibrium, but since the sea ice is treated as a thin veneer that melts instantly when $T > -2$, the response time of the oceans to changes in insolation should be relatively short. Rose et al. (2017) shows that the seasonal model does deviate from the analytical solution; this is probably the reason the instability does not occur during those times.

Careful inspection of the upper left panel in Figure 4.26 shows that it is actually the

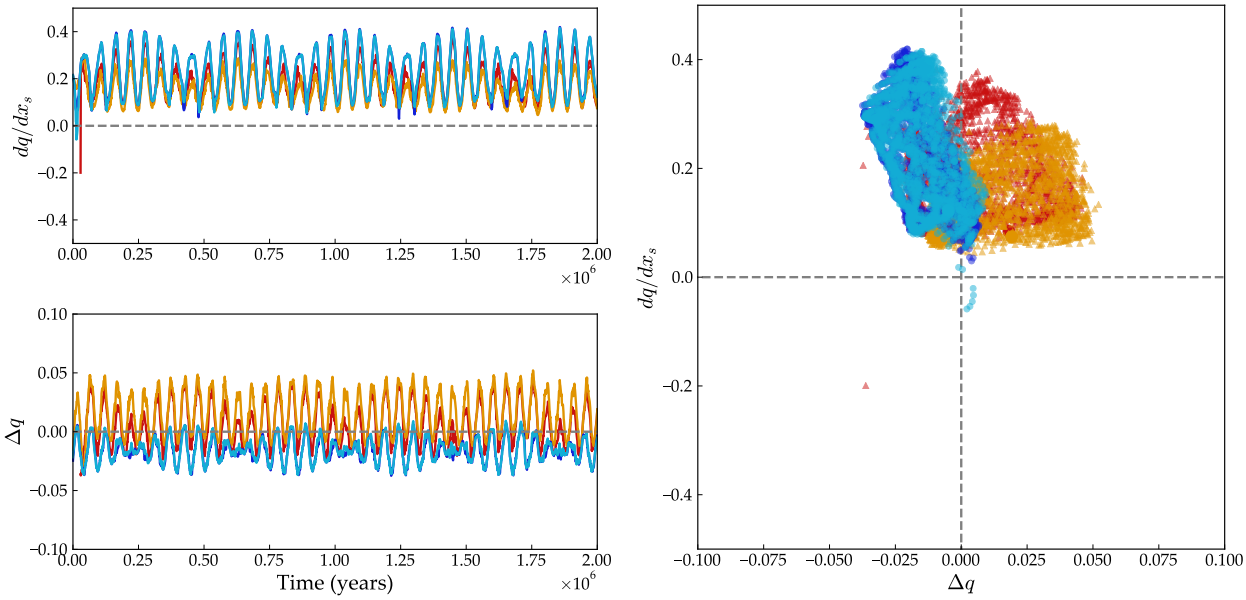

Figure 4.25: The quantities dq/dx_s and Δq, which are related to the stability of ice caps in the annual EBM (see text), for a case with $P_{rot} = 1.62$ day, $\psi_0 = 23.5°$, $e_0 = 0.167$, and $i_0 = 14.54°$. On the left, dq/dx_s and Δq are plotted as a function of time for the northern ice sheet on land (red), the southern ice sheet (orange), the northern sea ice (dark blue), and the southern sea ice (light blue). Negative values of dq/dx_s indicate the ice cap is unstable in the annual model (but not necessarily in our seasonal model). Negative values of Δq indicate that the average insolation is below that required to maintain the ice edge at its current latitude, suggesting that the ice should grow. On the right, dq/dx_s is plotted as a function of Δq, for each of the four ice edges (same colors as in the left plot). The case shown here does not experience a snowball state.

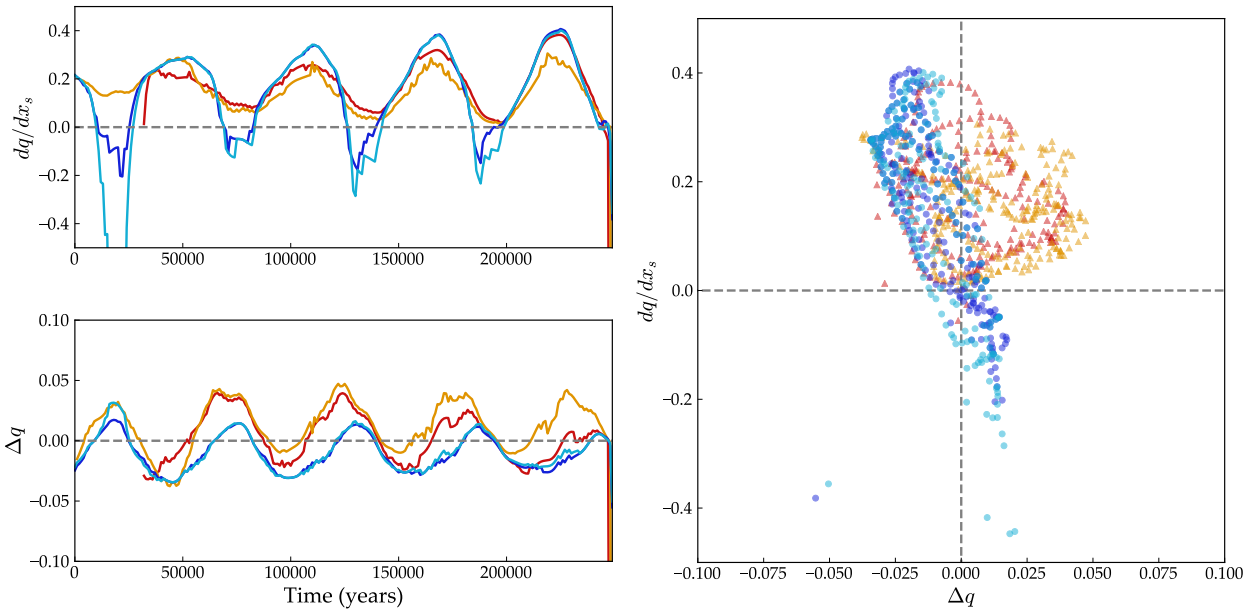

Figure 4.26: Same as Figure 4.25, but for $P_{rot} = 1.62$ day, $\psi_0 = 23.5°$, $e_0 = 0.167$, and $i_0 = 16.04°$. This case, with slightly higher inclination than that in Figure 4.25, enters a snowball state at $\sim 250,000$ years.

northern ice sheet (red curve) that leads the way into the snowball state, not the sea ice in either hemisphere. It is interesting that this happens so quickly after dq/dx_s crosses zero for this ice sheet. It is possibly a result of hysteresis: one may note that Δq at the northern ice edge was fairly large and positive during the first three eccentricity cycles. During the fourth ($\sim 220,000$ years), however, Δq barely exceeds zero before dq/dx_s becomes negative. In other words, the ice sheet received strong heating during all of the previous three eccentricity maxima, but very weak heating during the last, which left it poised to continue growing at the time of the next instability.

The analytical theory does not always provide a simple explanation, as it does for the case shown in Figure 4.25. Figure 4.27 shows another nearby case that undergoes the snowball instability (the time evolution for this case is shown in Figure 4.17). The quantity Δq is at the time of the instability, and it seems that whenever $dq/dx_s < 0$, Δq is positive. At these times the sea ice usually disappears entirely (gaps in the blue curves left panels). The instability may be a result of hysteresis again—Δq does undergo a negative period short prior to the snowball state, but this period does not appear significantly different from the cycles before it.

4.4.4 Predicting climate states with machine learning

Results from the statistical analysis and machine learning model are shown in Tables 4.5 and 4.6. The $p-$values for Pearson's R are displayed in parentheses. Correlations appear to be strongest with stellar flux, S, and the eccentricity parameters. The MIC values are similar $\sim 0.2 - 0.3$ across most of the parameters, except for ψ_0's relationship to δ_{snow}. Interestingly, Δi shows a stronger correlation, R, with δ_{snow} and f_{ice} than the obliquity parameters, despite the fact that the inclination has no direct impact on climate. The linear relationships between i_0 and $\langle i \rangle$ and the climate state are insignificant, however, the MIC shows a non-linear relationship about as strong as any other parameter. One plausible explanation is that the inclination (especially the variation in inclination) affects both the evolution of the eccentricity and the evolution of the obliquity, and thus is indirectly coupled

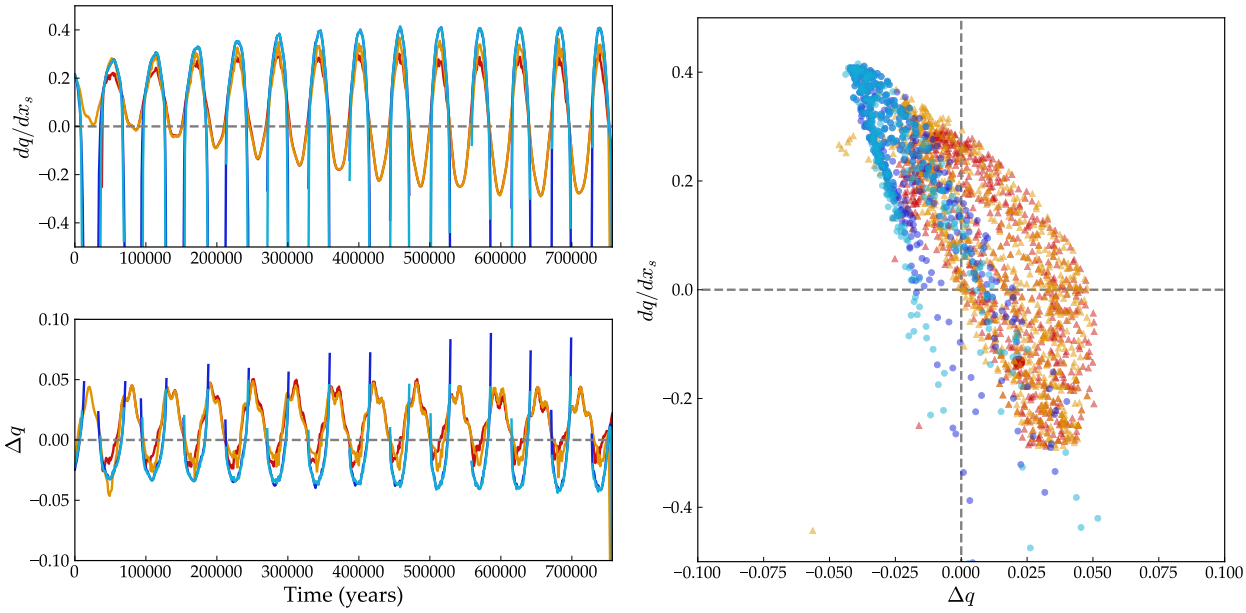

Figure 4.27: Same as Figure 4.25, but for $P_{rot} = 1.62$ day, $\psi_0 = 23.5°$, $e_0 = 0.167$, and $i_0 = 18.96°$. This case enters a snowball state at $\sim 750,000$ years. The northern and southern sea ice caps melt completely numerous times prior to the instability at ~ 760 kyr—shown as gaps in the blue curves. Eccentricity and obliquity are high during these times.

Table 4.5: **Relative importance of input parameters on δ_{snow}**

Parameter	Pearson R (p)	MIC	ζ_{NL}	ξ_i
$S_\star$	-0.517486 (0.0)	0.259659	-0.008133	0.367391
e_0	-0.469633 (0.0)	0.191850	-0.028705	0.088580
Δe	-0.281968 (0.0)	0.181865	0.102360	0.014340
$\langle e \rangle$	-0.480688 (0.0)	0.256887	0.025826	0.227943
i_0	0.026494 (0.0132)	0.256149	0.255448	0.022177
Δi	-0.318399 (0.0)	0.216146	0.114768	0.024869
$\langle i \rangle$	0.056757 (1.08×10^{-7})	0.200756	0.197534	0.047204
ψ_0	-0.026059 (0.01478)	0.000490	-0.000189	0.015797
$\Delta\psi$	0.084789 (1.95×10^{-15})	0.097013	0.089824	0.094639
$\langle \psi \rangle$	-0.031998 (0.00276)	0.124936	0.123913	0.097059

to the climate through two variables.

The stellar flux, $S_\star$ (defined here for a circular orbit), is unsurprisingly the most important parameter in determining the final climate parameters, δ_{snow} and f_{ice}, in the machine learning (ML) algorithm. The mean eccentricity, $\langle e \rangle$, tends to be the next most important parameter. This is also expected, since the mean stellar flux is related to e (Equation 1.12). The remaining variables tend to have similar, and relatively small, weighting. About half the time, one could correctly predict the climate state of our test planet knowing the stellar flux and the mean insolation. However, including all variables, the ML model can predict δ_{snow} correctly 97% of the time, and f_{ice} about 93% of the time (it is somewhat easier to sort things into discrete states). The similar weights of the remaining variables illustrates the complexity of the interplay between orbit and climate.

In Figure 4.28, we show the predicted ice area coverage for $P_{rot} = 1$ day and initial

Table 4.6: **Relative importance of input parameters on f_{ice}**

Parameter	Pearson R (p)	MIC	ζ_{NL}	ξ_i
$S_\star$	-0.502261 (0.0)	0.260615	0.008349	0.396097
e_0	-0.498351 (0.0)	0.268657	0.020303	0.085960
Δe	-0.322404 (0.0)	0.218874	0.114929	0.012151
$\langle e \rangle$	-0.515085 (0.0)	0.295807	0.030495	0.249936
i_0	-0.011158 (0.2967)	0.255632	0.255508	0.016456
Δi	-0.361029 (0.0)	0.216911	0.086569	0.021697
$\langle i \rangle$	0.020870 (0.0509)	0.199982	0.199546	0.036169
ψ_0	-0.062202 (5.77×10^{-9})	0.170839	0.166970	0.018088
$\Delta\psi$	0.059806 (2.16×10^{-8})	0.148690	0.145113	0.079007
$\langle \psi \rangle$	-0.092422 (4.61×10^{-18})	0.242192	0.233650	0.084440

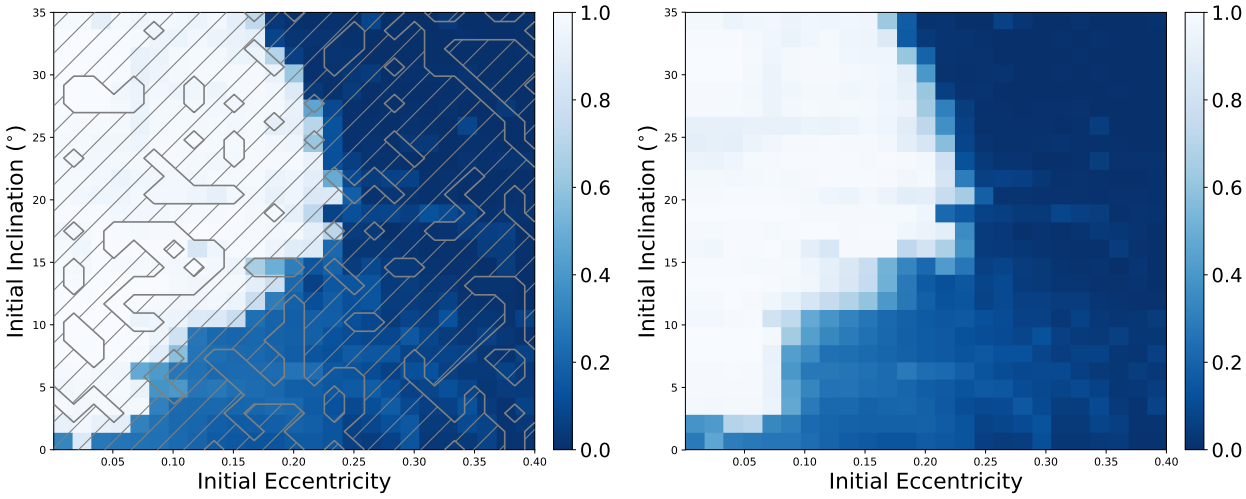

Figure 4.28: Fractional ice coverage area for $P_{rot} = 1$ day and initial obliquity $\psi_0 = 23.5°$, with a stellar constant of $S = 1332.27$ W m^{-2}, as predicted by the machine learning algorithm (random forest regression). On the left, this parameter space was not excluded from the training set—the hatched region represents simulations that went into the training set, where the predictive power is better (99.2%), compared to 93% for the testing set, and the unhatched area is part of the testing set. On the right, this parameter space was excluded from the training set and the model was trained on a similar size set of the remaining data. Compare to the lower right panel in Figure 4.10.

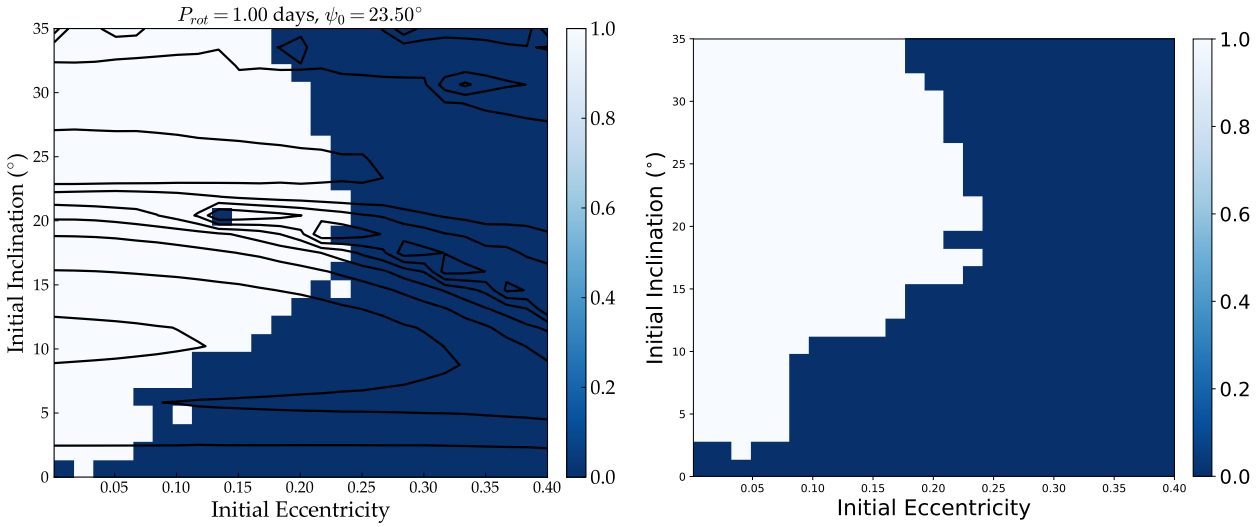

Figure 4.29: Snowball states (δ_{snow}) for $P_{rot} = 1$ day and initial obliquity $\psi_0 = 23.5°$, with a stellar constant of $S = 1332.27$ W m^{-2} from the full orbit/climate simulation (left) and the machine learning algorithm (random forest classification; right). In the machine learning case shown here, this slice of parameter space was excluded from the training set.

obliquity $\psi_0 = 23.5°$ at $S = 1332.27$ W m^{-2}. In the left hand panel, we simply took the ML model, trained on a random 75% of the data, and input this slice of parameter space into the resulting prediction algorithm. Because 75% of the data went into the training set, much of the data shown in a given slice of parameter space (such as this one) belongs to this training set—points belonging to the training set are indicated by the hatched regions. In the right hand panel, we excluded this slice ($P_{rot} = 1$ day, $\psi_0 = 23.5°$, and $S = 1332.27$ W m^{-2}) of parameter space from the training set and retrained the ML model, with a similarly size training set selected from the remaining data, and used the resulting ML model to predict f_{ice}. Obviously, the model does slightly better when a portion of this specific parameter space is in the training set, but it is still remarkable how well the algorithm picks up the various features of the original map (Figure 4.10).

Next, Figure 4.29 shows δ_{snow} for the full orbit+climate simulations on the left, compared to the machine learning algorithm predictions on the right, for this same slice of parameter space. The machine learning algorithm captures the basic shape of the parameter space, though it does miss a few features such as the blue island at $e \approx 0.15$ and $i_0 \approx 20°$. In the case shown, this slice of parameter space ($P_{rot} = 1$ day, $\psi_0 = 23.5°$, and $S = 1332.27$ W m^{-2}) was excluded from the training set.

We see that the machine learning algorithm does very well at predicting the ultimate climate state of this test planet. Though we trained the model on a fixed grid of initial conditions, it should perform equally well or better, and have more predictive power, if it is trained on a random selection. With this type of analysis, we will be able to extend the model beyond what is computational feasible: when it becomes prohibitive to run a desired number of simulations, we may be able to make do with a fraction of that number when we apply machine learning. We will explore this idea more comprehensively in a future work to determine the number of necessary simulations and the optimal sampling techniques.

4.4.5 Importance of obliquity, eccentricity and COPP

With orbital and obliquity cycles as large as our test planet here, the periodicity of the ice is plainly visible. It is interesting, still, to perform periodogram analysis to understand the relative importance of the three insolation parameters: obliquity, eccentricity, and COPP. We calculate periodograms for each of these variables, for the ice sheet heights at 65° north and south, and for the total global ice mass. These are calculated using the periodogram function in the `SciPy` package for Python, with a Bartlett window function to produce a clean power spectrum.

We first perform a periodogram analysis on a static, but eccentric case. Under our "static" conditions, the orbit and obliquity do not change, but we can still allow the spin axis to precess according to Equation (3.15). This results in a sinusoidal variation in COPP. As we shall see, this parameter is typically the weakest of the three insolation parameters, so this example, which has no variation in ψ or e, allows us to see its effect more plainly (Figures 4.30 and 4.31). The ice sheets grow and decay in response to the planet's precession. The total ice volume's strongest peak is at half the period of COPP—this is because the northern and southern ice sheets grow and decay at opposing times.

Figure 4.32 shows the periodograms for two cases with $P_{rot} = 1.62$ day and $\psi_0 = 23.5°$ that are characteristic of the behavior we see over much of this parameter space. The left panel shows a case that is outside the secular resonance (see Figure 4.12) and the right shows a case that is *inside* in the resonance. Outside the resonance, the obliquity and eccentricity have distinct peaks, and both can be seen in the ice sheet growth and decay. In the secular resonance, the obliquity oscillates with almost exactly the same period as the eccentricity (hence, the resonant behavior), and the ice sheets follow this period. Interestingly, in all of the parameter space we explore, the ice mass is dominated by the eccentricity cycle, not the obliquity cycle. The periods associated with COPP cannot even be seen in the ice sheets on a linear scale. The ice sheets are almost entirely driven by the eccentricity and obliquity cycles.

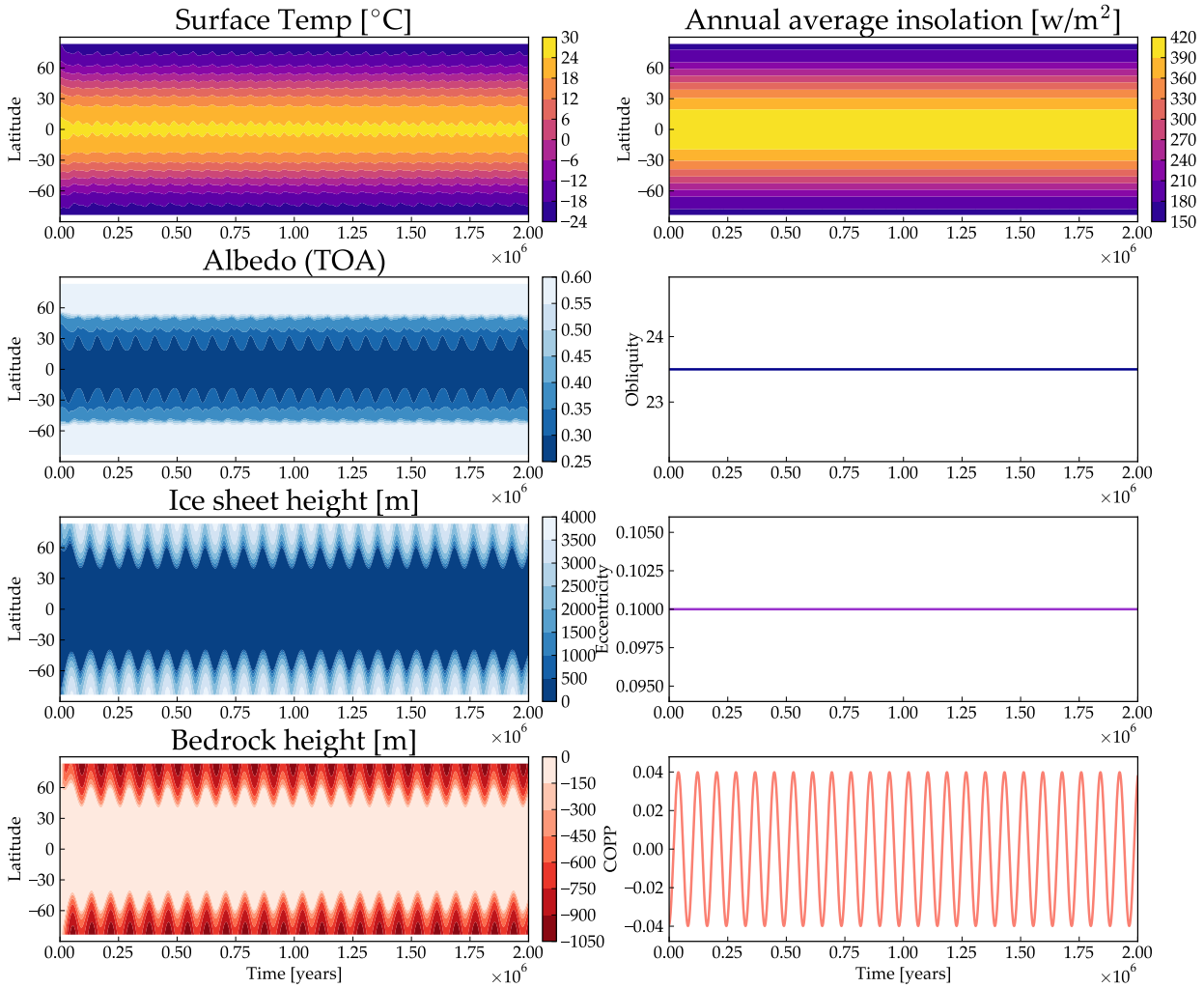

Figure 4.30: Climate evolution for a planet with static eccentricity and obliquity, but with axial precession. See Figure 4.16 for further description of the panels. Here, the ice sheets are forced only by the parameter COPP (through $\varpi + p_A$), which varies sinusoidally.

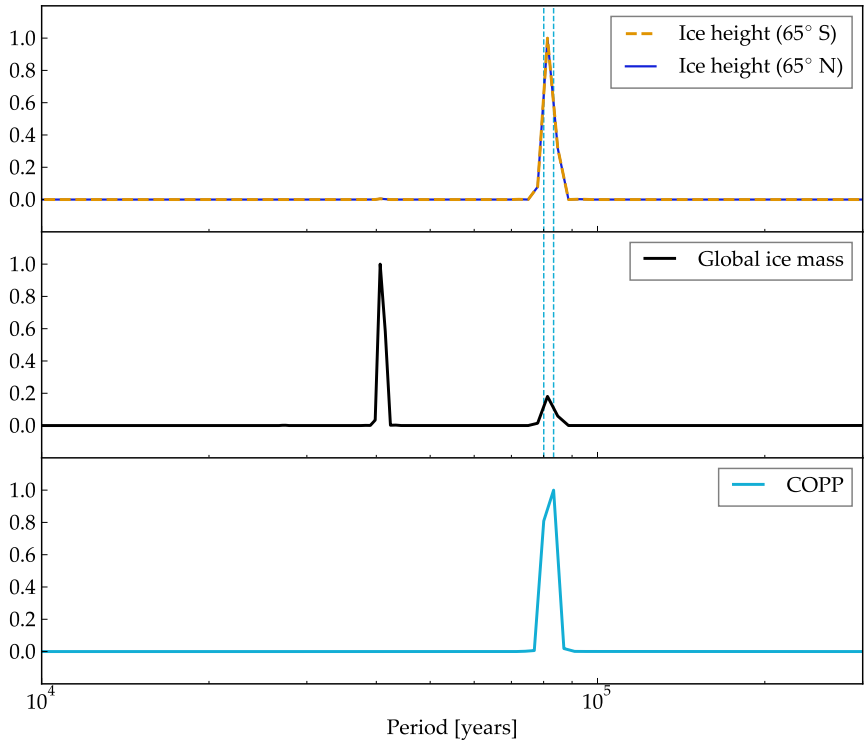

Figure 4.31: Normalized power spectra showing the strength at different periods in the ice height (top panel), global ice volume (middle panel), and the insolation parameter COPP. Vertical dashed lines in the top and middle panel indicate the periods associated with the strongest two periods in COPP. The ice heights in each hemisphere follow the precession period of $\sim 80,000$ years. The global ice mass has its strongest peak at *half* the precession period (see text).

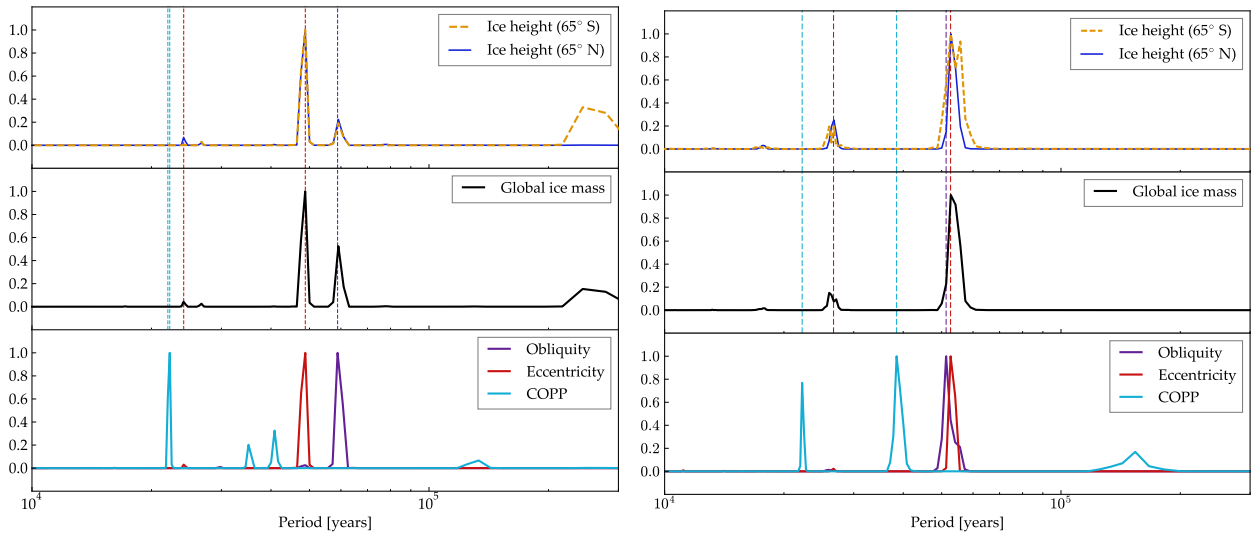

Figure 4.32: Normalized power spectra showing the strength at different periods in the ice height (top panel), global ice volume (middle panel), and the insolation parameters (obliquity, eccentricity, and COPP). Vertical dashed lines in the top two panels indicate peaks in the insolation parameters. The left panel shows a case with $P_{rot} = 1.62$ day, $\psi_0 = 23.5°$, $e_0 = 0.167$, and $i_0 = 11.67°$ and the right shows a case with $P_{rot} = 1.62$ day, $\psi_0 = 23.5°$, $e_0 = 0.25$, and $i_0 = 16.04°$. The ice sheets are strongly coupled to the eccentricity and, to lesser extent, the obliquity. The case on the right lies within the secular spin-orbit resonance, hence the obliquity and eccentricity have the same period of oscillation.

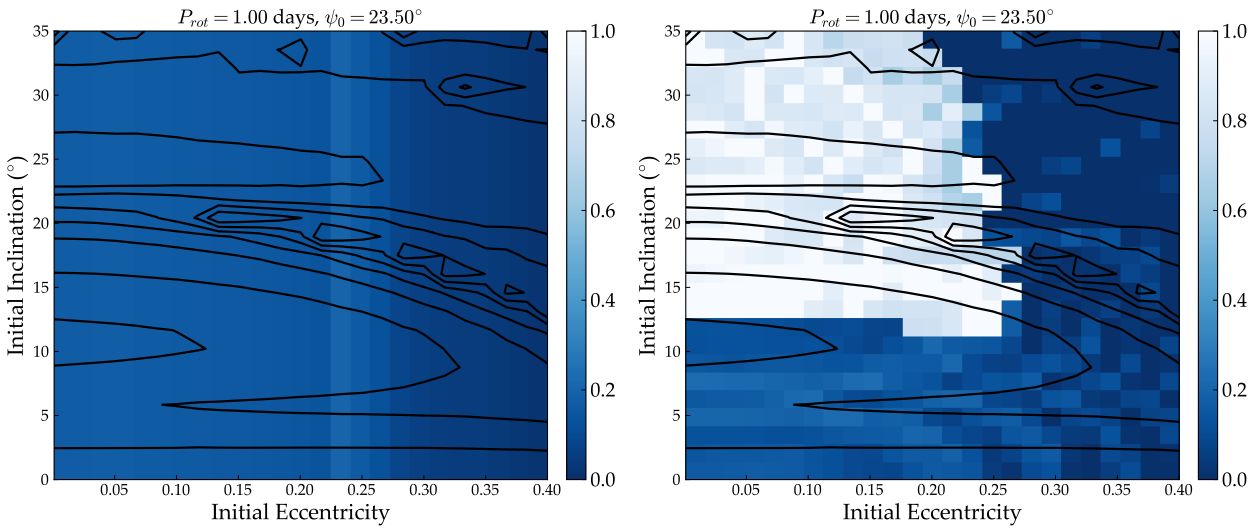

Figure 4.33: Fractional area of ice coverage at $\psi_0 = 23.5°$, $P_{rot} = 1$ day, with ice sheets disabled. On the left are static conditions at the initial values; on the right, dynamic orbit and obliquity. Compare to Figure 4.10. The stellar flux here is lower than in the simulations from Figure 4.10, $S = 1304$ W m^{-2}. The ice coverage is very different from the cases with ice sheets at low inclinations—near the Cassini state, where the obliquity variations are relatively small.

4.4.6 Importance of ice sheets

The inclusion of the ice sheet model in the EBM has important consequences. The snowball instability is triggered more easily (*i.e.*, at higher $S_\star$), because of the extra energy required to melt the ice sheets (compared to the energy required simply to raise the surface temperature above freezing). This means that the climate with ice sheets is generally cooler at the same stellar flux than without. Indeed, without ice sheets, for our test planet at $\psi = 23.5°$, the snowball state is not reached until $S/S_0 \approx 0.95$, compared to $S/S_0 \approx 0.975$ with ice sheets (Figure 4.9).

The response to orbital variations is altered as well. Figure 4.33 shows the fractional area coverage for $\psi_0 = 23.5°$, $P_{rot} = 1$ day, at $S = 1304$ W m^{-2}. Without perturbations, at

this stellar flux, there are no snowball states. At $e \sim 0.25$, the area of ice coverage increases slightly, because of increased apoastron distances and time spent there, but the ice coverage drops to zero at the highest eccentricities. When perturbations are included, the area of ice coverage increases in most regions and snowball states are reached at $i_0 \gtrsim 12°$ and $e_0 \lesssim 0.25$. The change in ice coverage between static and dynamic cases is more pronounced here than in the low obliquity cases with ice sheets (Figure 4.10). Further, the region near the Cassini state (lower left) does not experience snowball states as often as the previous case.

4.5 Discussion

We reiterate our primary conclusions here:

1. In predicting the climate state of a potentially habitable planet, it is not enough to simply run a climate model with the initial conditions (*i.e.* the observed orbit), nor is it sufficient to use the averaged quantities. Variations in the orbit need to be considered, because of the instability brought on by coupled obliquity and eccentricity variations. In particular, we note the instability that occurs when the planet's obliquity reaches $\sim 35°$ during an eccentricity minimum, if a large ice cap is present. At this obliquity, with the climate parameters we use here, there is no stable location for the ice edge; it must either retreat or grow uncontrollably. If the incoming stellar flux is decreased because the eccentricity is low, the ice will grow to the equator. If the eccentricity is sufficiently high at such times, the ice caps will collapse entirely.

2. Coupled orbital and obliquity variations tend to trigger the snowball instability. The eccentricity oscillations cause the global flux to vary and as a result, the planet can go from completely ice free to having large ice caps in a few thousand years. If the obliquity remains low enough, the ice caps remain stable. When the obliquity is oscillating by a large amount, however, the ice latitude can become suddenly unstable. Many times, the ice caps are small enough that they disappear entirely (the small ice cap instability);

other times, the ice caps are large enough to trigger the large ice cap instability and the planet becomes entirely ice covered.

3. For eccentricity variations this large ($\Delta e \sim 0.1 - 0.3$), the ice ages are primarily controlled by the eccentricity, not the obliquity. This is very different from the recent Earth, where the insolation variations are dominated by the obliquity cycle. Obliquity is important mainly in determining the *stability* and *location* of ice sheets.

4. The thermal inertia of ice sheets plays an important role. The inclusion of ice sheets causes snowball states to be triggered at higher incident stellar flux than if a simple temperature dependent albedo is used to mimic ice. Interestingly, the difference between static and dynamic orbital conditions seems to be reduced somewhat by the presence of ice sheets. The model is more susceptible to snowball states in general, but ice sheets somewhat diminish the response of the climate to orbital variations.

Point 1 deserves some further discussion here. We find that, in general, dynamical evolution of the eccentricity and obliquity of a HZ planet tends to make the planet more susceptible to snowball states than when it has static orbital conditions. This is at odds with Armstrong et al. (2014), who found that dynamical variations tended to inhibit glaciation and snowball states. There are two fundamental reasons our results differ from theirs.

The first is related to the parameterization of the OLR. The stability of the EBM is related to the strength of the radiation feedback and the ice-albedo feedback. The radiation feedback is negative: a small positive perturbation to the surface temperature will cause the OLR to increase, generating more cooling and returning the surface to the unperturbed temperature. The process also works in the other direction: a small negative perturbation to the temperature will cause the OLR to decrease, creating additional heating and returning the temperature to its previous value. The ice-albedo feedback is positive: a small negative perturbation to the surface temperature will cause the ice to grow, reflecting more radiation to space and causing the surface to cool further. A positive perturbation will likewise generate

runaway warming, if the ice-albedo is the dominant component of the model. Of course, the real Earth and more sophisticated 3D models have a number of other feedback processes that work to alter the climate stability, but in a 1D EBM like ours and the model in Armstrong et al. (2014), it is simply a competition between the radiation feedback and the ice-albedo feedback.

In this simple formulation, the radiation feedback is contained within the parameter B. A large, positive value of B will create a very stable climate, while a smaller value will create a less stable climate. For Earth, $B \approx 2.09$ W m^{-2} K^{-1}. A Taylor expansion of the OLR parameterization in Spiegel et al. (2009), for example, shows that their model 2 has $B \approx 2.28$ W m^{-2} K^{-1} at a surface temperature of 288 K, and so their model should be more stable against snowball states when using this formulation than with OLR from North & Coakley (1979).

The OLR from Armstrong et al. (2014) is found by combining their Equations (23) and (24) and comparing to the full energy balance equation (our Equation 4.1):

$$I(T) = \frac{\epsilon_s \sigma T_s^4}{1+\tau}, \tag{4.30}$$

where ϵ_s is the emissivity of the atmosphere, σ is the Stefan-Boltzmann constant, and τ is a tunable parameter used to approximate the greenhouse effect that was *not* assumed to be a function of temperature. The authors found that setting $\epsilon_s = 1$ and $\tau = 0.095$ reproduced Earth and so fixed these values for the rest of the study. As stated before, a Taylor expansion of Equation 4.30 with respect to temperature gives the value of B:

$$B = \frac{dI}{dT} = \frac{4\epsilon_s \sigma T_s^3}{1+\tau}. \tag{4.31}$$

Plugging in their constants and a surface temperature of $T_s = 288$ K, one finds $B = 4.95$ W m^{-2} K^{-1}. As far as EBMs go, this model is extremely stable against the snowball instability.

The second reason our model differs from Armstrong et al. (2014) is our inclusion of the horizontal heat transport (however crudely it is represented here). A comparison between our energy balance equation (4.1) and that in Armstrong et al. (2014) shows that $D = 0$ in

the latter. It can be shown that when $D = 0$, the ice-albedo feedback does not affect adjacent latitudes as it should. Conceptually, ice-albedo feedback occurs because, for example, when the albedo (and thus temperature) changes in one model cell, the temperature gradient between adjacent cells is changed. This causes the heat flow between cells to change. The feedback works because cooling (or heating) in one cell alters heat flow to and from adjacent cells, cooling (or heating) those adjacent areas. Without that horizontal heat flow, there is no ice-albedo feedback, and no snowball *instability*—that is, snowball states can still occur, but only when all latitudes in the model *individually* come into radiative equilibrium at below freezing temperatures. That occurs at a much lower stellar flux than that caused by the instability.

In summary, planets undergoing strong orbital forcing are thus prone to the snowball or large ice cap instability, and surface habitability is therefore compromised. It should be noted, however, that Earth potentially went through several snowball states during the Proterozoic Eon ($\sim$ 2.5 to 0.54 billion years ago), and photosynthetic life persisted during these phases (Harland, 1964; Kirschvink, 1992). One explanation is that the surface was not actually completely frozen during such time periods—the Earth was in a "soft" snowball (or "water-belt") state, with some open ocean in the tropics (Chandler & Sohl, 2000). Unfortunately, the EBM does not capture all the necessary physics to distinguish a soft snowball state from a hard snowball state. Therefore, our results are probably pessimistic in regard to surface habitability.

Modeling of this sort is difficult because of the timescales involved. 3D GCMs can take weeks to converge for static orbital conditions and decade long integrations. We have approached the problem with a comparatively simple, computationally efficient EBM—however, such models lack important phenomena and thus must be treated cautiously. As much as possible, we attempt to validate our results against a more sophisticated model. In terms of average yearly behavior, the EBM does a decent job. The greatest discrepancies occur in simulations that reach high obliquity and have relatively high stellar flux. In these cases, the summer irradiation at the poles can be intense enough (locally) to reach runaway

greenhouse temperatures. Undoubtedly, there will also be cloud formation which affects the albedo, as observed in GCM simulations of synchronous rotators (Yang et al., 2013). The difference is that here, the planet is in a very different rotation state, which may inhibit the global scale redistribution of heat.

The carbon-silicate cycle on a planet like Earth is probably too slow to prevent orbitally induced snowball states. Earth's carbon-silicate cycle operates on a ~ 0.5 Myr time-scale (Kasting et al., 1993; Haqq-Misra et al., 2016); the planet in this configuration can evolve from ice-free to completely ice-covered in thousands of years. If a planet has significantly higher outgassing rate and weathering rates than Earth, there may be some hope of preventing the instability through this negative feedback. Even with an Earth-like carbon-silicate cycle, however, the snowball states will eventually be escaped because of the increasing atmospheric carbon-dioxide pressure. The planet may then become extremely warm for an extended period until carbon is weathered out of the atmosphere. And, of course, the obliquity and eccentricity will continue to vary in the same manner as before, perhaps leading to periods of intense polar heating. A long term simulation of exo-Milankovitch cycles with a carbon cycle would certainly be interesting.

4.6 Conclusions

In Chapter 3, we showed that secular spin-orbit resonances are common, even in relatively simple planetary systems, and that they can cause very large obliquity oscillations. In this chapter, we applied a climate model to one of these systems.

We have modeled the climate evolution of a planet with an Earth-like atmosphere in response to extreme orbital forcing. The large changes in eccentricity and obliquity drive the growth and retreat of ice caps, which can extend from the poles to $\sim 30^\circ$ latitude. These exo-Milankovitch cycles often lead to the snowball instability, in which the planet's oceans become completely ice covered, as well as the small ice cap instability, in which the ice completely disappears.

We reiterate that planetary systems are extremely complex, and in cases like that shown

here, the presence of companions can affect an Earth-like planet's habitability. It is particularly important to understand the eccentricity and obliquity evolution in combination, because the stability of ice sheets is intimately coupled to the obliquity and the eccentricity affects the amount of intercepted stellar energy. At a single stellar flux, a planet can be either clement and habitable or completely ice-covered, depending on the orbital parameters and the planet's recent climate history.

This further complicates the concept of a static habitable zone based on the stellar flux. We have shown that orbital and obliquity evolution should be considered when assessing a planet's potential habitability.

4.7 Acknowledgements

Much of the text in Section 4.2.3 was written by co-author David Fleming. This work was supported by the NASA Astrobiology Institute's Virtual Planetary Laboratory under Cooperative Agreement number NNA13AA93A. This work was facilitated though the use of advanced computational, storage, and networking infrastructure provided by the Hyak supercomputer system at the University of Washington. The results reported herein benefited from the authors' affiliation with the NASA's Nexus for Exoplanet System Science (NExSS) research coordination network sponsored by NASA's Science Mission Directorate.

Chapter 5

CONCLUSIONS

"When you come to a fork in the road, take it." [Yogi Berra]

5.1 Thesis Summary

In Chapter 1, I discussed some of the history of exoplanet discovery and the habitable zone, and introduced many of the ideas that are relevant to my research. In Chapter 2, I presented my work on the υ Andromedae system, in which I used stability arguments to predict the unknown inclination and mass of the inner-most planet. More recent observations with high-resolution spectroscopy indicate that the planet is within the region I expected (Piskorz et al., 2017). Though no habitable (or even terrestrial) planet exists in this system, the large orbital variations were the inspiration for the following chapters. Chapter 3 covered the orbital and obliquity evolution of HZ planets in a handful of systems and highlighted the importance of secular spin-orbit resonances and Cassini states for habitability. In Chapter 4, I applied a simple climate model to one of these planets. The planet undergoes severe Milankovitch cycles, in which the ice sheets grow and retreat with the obliquity and eccentricity oscillations. I showed that this behavior often triggers the runaway snowball instability that leaves the surface uninhabitable. In this final chapter, I discuss a number of unresolved issues that my work so far has brought up and several topics I would like to study in the near future.

5.2 Future Work and Outstanding Issues

5.2.1 Ice sheet properties and precipitation

Severa possibilities related to the ice sheet growth, ablation, and flow have not been explored in this work. In all the simulations I discuss in Chapter 4, I assumed a constant

ice deposition rate (precipitation) when the temperature over land was below freezing. A more realistic scheme may be in order—precipitation on Earth varies with temperature, latitude, geography, etc. In fact, one mechanism that may prevent global glaciations (snowball states) is that the descending air at the tropics creates a barrier the ice sheets cannot move beyond—essentially, the rate of evaporation outweighs the rate of precipitation because the air is so dry.

I tuned the rate of ablation to give values consistent with Earth measurements, however, it may be worth exploring the effects of a different tuning and a different functional form. In particular, this could be used to approximate "elevation feedback": the fact that large ice sheets extend to high altitudes, where the air is cooler, gives them a means of self-protection. It is harder to melt a bigger ice sheet, because its surface is colder than a smaller ice sheet. At the same time, once it becomes warm enough to begin melting a large ice sheet, collapse becomes imminent as it begins to lose this self-protection mechanism.

There are a number of properties that affect the ice flow. The temperature and deformability of the ice affect its creep (*i.e.* the motion and deformation of the ice itself)—these are held constant in the model, but vary inside a real glacier. The sediment properties (see Table 4.2) determine how quickly the ice flows at the base. On Earth, a change in the type of sediment or bedrock below the Laurentide ice sheet is our current best explanation for the Mid-Pleistocene transition, at which time the glacial cycles switched from a $\sim 40,000$ year period to a $\sim 100,000$ year period (Clark & Pollard, 1998). Such considerations may be crucial to our understanding of exo-Milankovitch cycles and the susceptibility to snowball states.

Currently, the EBM has no way of dealing with ice sheet behavior at land–ocean boundaries. In reality, at these boundaries, ice flows onto the sea surface to ice shelves, which have very different flow properties and can slow or speed the flow of the sheet (Böhmer & Herterich, 1990; De Angelis & Skvarca, 2003; Joughin et al., 2004; Scambos et al., 2004). Ice sheets are also limited by geography (take Antarctica, for example). A 1D latitudinal model may not be capable of resolving all of these complicated effects, but it may be possible

to tune the flow of ice between land and ocean to replicate the results of more realistic ice dynamics models. Currently, we are probably over-estimating the sensitivity to snowball states because of the lack of land–ocean ice flow and geographic limitations.

In Chapter 4, I tuned the properties of the EBM and ice sheets to reproduce ice ages on Earth—the ice sheets grow and retreat in response to the obliquity and eccentricity cycles in Figure 4.8. However, there is one key characteristic that is missing (also absent in Huybers & Tziperman, 2008): the sawtooth shape seen in the marine cores. Earth seems to have entered its ice ages gradually, the ice sheets slowly growing over ten of thousands of years, then exited rather abruptly, the ice sheets collapsing in thousands of years (Imbrie & Imbrie, 1980; Oerlemans, 1980). Many of the mechanisms discussed in this section and Section 5.2.3 could contribute to this sudden collapse. It would be interesting to explore these to understand which really matter. Further, my model may be overly susceptible to snowball states for exoplanets because the ice sheets do not retreat as quickly as they should, based on Earth history.

5.2.2 The effects of geography

The distribution of land and ocean can have a profound impact on climate, even without the complications of ice sheets. In Chapter 4, I ran the model with a constant fraction of land ($f_L = 0.34$) at all latitudes, to isolate the effects of orbital dynamics. The response of the climate to the dynamics, however, might be very different if large continents cover more of the surface at some latitudes or if some latitudes are totally ocean covered. In particular, large continents in the high latitudes will probably intensify the heating at the poles during high obliquity times because of the lower thermal inertia.

Further, as discussed in the previous section, land–ocean boundaries affect the flow of glaciers. This problem may be difficult to resolve in our EBM, so a first step would be to model the climate response to dynamics without the ice sheet model, under various geographies, and compare to GCMs to ensure that the results are sensible in terms of the temperature distribution, horizontal heat flow, and the OLR.

5.2.3 Carbon cycling

The EBM used in Chapter 4 does not account for the effects of changing CO_2 pressure in the atmosphere. On long time scales ($\gtrsim 0.5$ Myr), the carbon-silicate cycle will provide a stabilizing feedback that extends the habitable zone out to stellar fluxes $\sim 0.34 S_0$, much lower energy than considered here, because weathering rates slow as the atmosphere cools, allowing CO_2 to build up (Kasting et al., 1993; Haqq-Misra et al., 2016). Over the timescales we considered, the decrease in weathering rates is probably not strong enough to prevent the snowball instability. It should, however, provide a means of escape from the fully glaciated state. Consequently, planets with large Milankovitch cycles may enter the snowball state and subsequently recover, resulting in very complicated climate behavior, perhaps similar to the limit cycling noted by Haqq-Misra et al. (2016).

It would be very exciting to explore this idea. Further, it is exactly the type of problem that `VPLANET` (of which my models are a part) was designed to solve. It would, however, require three new components: (1) a robust radiation scheme that accounts for changes in $p\mathrm{CO}_2$; (2) an outgassing model; and (3) a model for weathering rates.

A simple model of both (2) and (3) is used in Haqq-Misra et al. (2016):

$$\frac{d}{dt}(p\mathrm{CO}_2) = V - W - W_{sea}, \tag{5.1}$$

where V is the volcanic outgassing rate, W is the rate of uptake due to continental weathering rate, and W is the rate of update due to sea floor weathering. The outgassing, V, can be assumed to be constant, as those author assumed, or could have a dependence on the internal evolution of the planet. The weathering rates have simple functional forms given in Berner & Kothavala (2001) and Haqq-Misra et al. (2016).

On shorter time scales (tens of kyr), there is another phenomenon related to CO_2 that is intimately connected to Milankovitch cycles: the solubility of CO_2 in water depends on temperature. Cold beer holds onto its carbonation better than warm beer—Earth's oceans do the same (Hartmann, 1994; Kurahashi-Nakamura et al., 2010). This has always been a complicating factor in understanding Earth's ice ages and introduces a kind of chicken–egg

problem: do changes in CO_2 cause the ice ages, or do the ice ages cause changes in CO_2 (Saltzman & Verbitsky, 1994a,b)? Certainly, this phenomenon amplifies the temperature decrease during ice ages, whether or not they are triggered by orbital forcing. In my current best reproduction of Milankovitch cycles (Figure 4.8), the global temperature swing is $\lesssim 1.5°$; the ΔT estimated from marine cores is $\sim 4°$ Hays et al. (1976).

5.2.4 Kepler-62 f and planet in the outer part of the HZ

The radiation scheme that I used in the EBM is tuned to Earth data, which means that it only represents a small slice of the habitable zone—locations where planets can be habitable with a similar level of CO_2. In order to model planets in the outer part of the HZ, where several bars of CO_2 pressure is required, this radiation scheme needs to be adjusted. Williams & Kasting (1997) and Haqq-Misra et al. (2016) provide OLR fits that they use in their EBM to model the CO_2 cycle; however, these have proven to be very unreliable in our model. Essentially, the radiation feedback provided by these OLR models is very weak, which causes the EBM to be unstable. I have thus far not been able to reproduce the results in either paper.

A simpler, first order solution is to fit the coefficients A and B in the linear OLR scheme to a model of a planet with high pCO_2, similar to how this was done for Earth. I am currently working with Prof. Aomawa Shields to do this for simulations of Kepler-62 f, which she found to be in the HZ with $pCO_2 \gtrsim 5$ bars. This should be a very interesting study because of the existence of a secular resonance that can cause the obliquity to oscillate by $\sim 20°$ (see Chapter 3). Because of the lower stellar flux, the ice albedo feedback should be significantly decreased, but the radiation feedback tends to be decreased as well—the 3 bar cases from Shields et al. (2016) have $B \sim 0.9$ W m^{-2} K^{-1}. It isn't clear yet which effect is more important.

One further complication is that the albedo of ice is spectrally dependent. At long wavelengths (infra-red), ice is significantly darker (more absorptive of stellar radiation), so that ice on planets orbiting stars cooler than the sun with absorb more radiation than on

Earth (Shields et al., 2013). At Kepler-62's temperature, a mixture of ice and snow will have an albedo of ~ 0.55 (Shields et al., 2013). The ice-albedo feedback will be further weakened by this effect.

5.2.5 Intense polar heating at high obliquity

As I mentioned briefly in Chapter 4, there are cases, like those in the secular spin-orbit resonance, where the obliquity of a HZ planet can reach $\sim 80°$ while the eccentricity is also high ($e \sim 0.4$). During these times, the poles of the planet can reach temperatures of $> 140°$ C because of the intense summer-time radiation. Extremely high temperatures are also seen at high obliquity in the LMD simulations. For the purposes of the Exo-Milankovitch study, I was primarily focused on the evolution of ice sheets, but this extreme polar heating is worth exploring further, especially in a 3D model. I would like to understand how this changes the albedo and heat transport due to convection. I would expect something similar to the strong Hadley cell seen in simulations of synchronously rotating worlds, however, because the spin state of the planet is very different, the circulation might behave very differently on a rapidly rotating, high obliquity planet.

Horizontal heat transport and increased albedo would most likely prevent the planet from entering a runaway greenhouse. The planet may still have a moist stratosphere, and subsequent water loss, during these times of extreme heating. It would be interesting to determine whether enough water could be lost through this mechanism to endanger the planet's habitability. With a good understanding of the climate behavior from a GCM, we might then be able to model the water loss with `VPLANET`.

5.3 Closing remarks

Throughout my graduate degree, I have been extremely blessed to have the financial and intellectual support of the Virtual Planetary Laboratory. I have also been extremely fortunate to see the number of known planets in the galaxy increase from triple to quadruple digits. The science of astrobiology seems to grow more important by the day. I feel truly honored

to be a part of this emerging field.

Of course, habitability of exoplanets is certainly a complicated puzzle. This thesis almost surely makes the problem sound even more complex that it previously did. Planets, unfortunately for us as scientists trying to understand them, are not stationary objects that can be counted on to stay in one place. Planets move through a high-dimensional parameter space. They evolve in a myriad of ways, only one of which I have tackled in this work. It seems that the more knowledge we gain, the more daunting our task as astrobiologists becomes. I only hope that, rather than obscuring the picture of habitability beyond all recognition, I have helped (in some small way) to guide our knowledge toward greater clarity.

BIBLIOGRAPHY

Aarseth, S. J. 1963, MNRAS, 126, 223

Abe, Y., Abe-Ouchi, A., Sleep, N. H., & Zahnle, K. J. 2011, Astrobiology, 11, 443

Abe-Ouchi, A., Saito, F., Kawamura, K., et al. 2013, Nature, 500, 190

Abramowitz, M., & Stegun, I. A. 1972, Handbook of Mathematical Functions

Adams, F. C., & Laughlin, G. 2006, ApJ, 649, 992

Aksnes, K., & Franklin, F. A. 2001, AJ, 122, 2734

Albanese, D., Filosi, M., Visintainer, R., et al. 2013, Bioinformatics, 29, 407

Applegate, J. H., Douglas, M. R., Gürsel, Y., et al. 1986, in Lecture Notes in Physics, Berlin Springer Verlag, Vol. 267, The Use of Supercomputers in Stellar Dynamics, ed. P. Hut & S. L. W. McMillan, 86

Armstrong, J. C., Barnes, R., Domagal-Goldman, S., et al. 2014, Astrobiology, 14, 277

Armstrong, J. C., Leovy, C. B., & Quinn, T. 2004, Icarus, 171, 255

Atobe, K., Ida, S., & Ito, T. 2004, Icarus, 168, 223

Baines, E. K., McAlister, H. A., ten Brummelaar, T. A., et al. 2008, ApJ, 680, 728

Barkstrom, B. R., Harrison, E. F., & Lee, III, R. B. 1990, EOS Transactions, 71, 279

Barnes, R., & Greenberg, R. 2007a, ApJ, 659, L53

—. 2007b, ApJ, 659, L53

Barnes, R., Greenberg, R., Quinn, T. R., McArthur, B. E., & Benedict, G. F. 2011, ApJ, 726, 71

Barnes, R., Mullins, K., Goldblatt, C., et al. 2013, Astrobiology, 13, 225

Barnes, R., & Quinn, T. 2001, ApJ, 550, 884

—. 2004, ApJ, 611, 494

Barnes, R., & Raymond, S. N. 2004, ApJ, 617, 569

Batalha, N. M., Borucki, W. J., Koch, D. G., et al. 2010, ApJ, 713, L109

Berger, A., & Loutre, M. F. 1991, Quaternary Science Reviews, 10, 297

Berger, A. L. 1978, Journal of Atmospheric Sciences, 35, 2362

Berner, R. A., & Kothavala, Z. 2001, American Journal of Science, 301, 182

Böhmer, W. J., & Herterich, K. 1990, Annals of Glaciology, 14, 17

Bolcar, M. R., Balasubramanian, K., Clampin, M., et al. 2015, in Proc. SPIE, Vol. 9602, Optics for EUV, X-Ray, and Gamma-Ray Astronomy VII, 960209

Bolmont, E., Libert, A.-S., Leconte, J., & Selsis, F. 2016, A&A, 591, A106

Bolmont, E., Raymond, S. N., Leconte, J., Hersant, F., & Correia, A. C. M. 2015, A&A, 583, A116

Boquet, F. 1889, Annales de l'Observatoire de Paris, 19, B.1

Borucki, W. J., Koch, D., Basri, G., et al. 2010, Science, 327, 977

Borucki, W. J., Koch, D. G., Basri, G., et al. 2011, ApJ, 736, 19

Borucki, W. J., Agol, E., Fressin, F., et al. 2013, Science, 340, 587

Braithwaite, R. J., & Zhang, Y. 2000, Journal of Glaciology, 46, 7

Brasser, R., Ida, S., & Kokubo, E. 2014, MNRAS, 440, 3685

Breiman, L. 2001, Machine Learning, 45, 5

Bretagnon, P. 1974, A&A, 30, 141

Brogi, M., Snellen, I. A. G., de Kok, R. J., et al. 2012, Nature, 486, 502

Brouwer, D., & Clemence, G. M. 1961, Methods of celestial mechanics

Brouwer, D., & van Woerkom, A. 1950, Astron. Papers Amer. Ephem., 13, 81

Brown, E. W., & Shook, C. A. 1933, Planetary theory

Budyko, M. I. 1969, Tellus, 21, 611

Burrows, A., Budaj, J., & Hubeny, I. 2008, ApJ, 678, 1436

Butler, R. P., Marcy, G. W., Fischer, D. A., et al. 1999, ApJ, 526, 916

Butler, R. P., Marcy, G. W., Williams, E., Hauser, H., & Shirts, P. 1997, ApJ, 474, L115

Cahalan, R. F., & North, G. R. 1979, Journal of Atmospheric Sciences, 36, 1178

Casertano, S., Lattanzi, M. G., Sozzetti, A., et al. 2008, A&A, 482, 699

Catling, D. C., Krissansen-Totton, J., Kiang, N. Y., et al. 2017, ArXiv e-prints, arXiv:1705.06381

Chambers, J. E. 1999, MNRAS, 304, 793

Chandler, M. A., & Sohl, L. E. 2000, J. Geophys. Res., 105, 20737

Charnay, B., Forget, F., Wordsworth, R., et al. 2013, Journal of Geophysical Research (Atmospheres), 118, 10

Chiang, E. I., Fischer, D., & Thommes, E. 2002, ApJ, 564, L105

Chiang, E. I., & Murray, N. 2002, ApJ, 576, 473

Chiang, E. I., Tabachnik, S., & Tremaine, S. 2001, AJ, 122, 1607

Clark, P. U., & Pollard, D. 1998, Paleoceanography, 13, 1

Clemens, S. C., & Tiedemann, R. 1997, Nature, 385, 801

Colombo, G. 1966, AJ, 71, 891

Cook, A. H. 1980, Interiors of the planets

Copernicus, N. 1543, D revolutionibus orbium coelestium

Cowan, N. B., Fuentes, P. A., & Haggard, H. M. 2013, MNRAS, 434, 2465

Cowan, N. B., Agol, E., Meadows, V. S., et al. 2009, ApJ, 700, 915

Crossfield, I. J. M., Hansen, B. M. S., Harrington, J., et al. 2010, ApJ, 723, 1436

Curiel, S., Cantó, J., Georgiev, L., Chávez, C. E., & Poveda, A. 2011, A&A, 525, A78

Dalcanton, J., Seager, S., Aigrain, S., et al. 2015, ArXiv e-prints, arXiv:1507.04779

Danby, J. M. A. 1988, Fundamentals of celestial mechanics

Darwin, G. H. 1880, Royal Society of London Philosophical Transactions Series I, 171, 713

De Angelis, H., & Skvarca, P. 2003, Science, 299, 1560

Deitrick, R., Barnes, R., McArthur, B., et al. 2015, ApJ, 798, 46

Des Marais, D. J., Nuth, III., J. A., Allamandola, L. J., et al. 2008, Astrobiology, 8, 715

Díaz, R. F., Ségransan, D., Udry, S., et al. 2016, A&A, 585, A134

Dressing, C. D., Spiegel, D. S., Scharf, C. A., Menou, K., & Raymond, S. N. 2010, ApJ, 721, 1295

Duplessy, J. C., Lalou, C., & Vinot, A. C. 1970, Science, 168, 250

Efroimsky, M., & Makarov, V. V. 2013, ApJ, 764, 26

Ellis, K. M., & Murray, C. D. 2000, Icarus, 147, 129

Emiliani, C. 1954, American Journal of Science, 252, 149

Ferraz-Mello, S., Rodríguez, A., & Hussmann, H. 2008, Celestial Mechanics and Dynamical Astronomy, 101, 171

Ferreira, D., Marshall, J., O'Gorman, P. A., & Seager, S. 2014, Icarus, 243, 236

Fischer, D. A., Marcy, G. W., & Spronck, J. F. P. 2014, ApJS, 210, 5

Fischer, D. A., Marcy, G. W., Butler, R. P., et al. 2003, ApJ, 586, 1394

Ford, E. B., Havlickova, M., & Rasio, F. A. 2001, Icarus, 150, 303

Ford, E. B., Lystad, V., & Rasio, F. A. 2005, Nature, 434, 873

Ford, E. B., & Rasio, F. A. 2008, ApJ, 686, 621

Forgan, D. 2016, MNRAS, 463, 2768

François, P., Briot, D., Spite, F., & Schneider, J. 1999, A&A, 349, 220

Fujii, Y., & Kawahara, H. 2012, ApJ, 755, 101

Fujii, Y., Angerhausen, D., Deitrick, R., et al. 2017, ArXiv e-prints, arXiv:1705.07098

Galilei, G. 1610, Sidereus nuncius magna, longeque admirabilia spectacula pandens lunae facie, fixis innumeris, lacteo circulo, stellis nebulosis, ... Galileo Galileo : nuper a se reperti beneficio sunt observata in apprime vero in quatuor planetis circa Iovis stellam disparibus

intervallis, atque periodis, celeritate mirabili circumvolutis ... atque Medicea sidera nuncupandos decrevit, doi:10.3931/e-rara-695

—. 1632, Dialogo DI Galileo Galilei Linceo matematico spraordinario dello stvdio DI Pisa.

—. 1710, Dialogo sopra i due Massimi Sistemi del Mondo Tolemaico E Copernicano

Gardner, J. P., Mather, J. C., Clampin, M., et al. 2006, Space Sci. Rev., 123, 485

Goldblatt, C., Robinson, T. D., Zahnle, K. J., & Crisp, D. 2013, Nature Geoscience, 6, 661

Goldreich, P., & Soter, S. 1966, Icarus, 5, 375

Goździewski, K., Bois, E., Maciejewski, A. J., & Kiseleva-Eggleton, L. 2001, A&A, 378, 569

Grimm, S. L., & Stadel, J. G. 2014, ApJ, 796, 23

Hamilton, D. P., & Ward, W. R. 2004, AJ, 128, 2510

Haqq-Misra, J., Kopparapu, R. K., Batalha, N. E., Harman, C. E., & Kasting, J. F. 2016, ApJ, 827, 120

Harland, W. B. 1964, Geologische Rundschau, 54, 45

Harrington, J., Hansen, B. M., Luszcz, S. H., et al. 2006, Science, 314, 623

Hart, M. H. 1979, Icarus, 37, 351

Hartman, J. D., Bakos, G. Á., Torres, G., et al. 2011, ApJ, 742, 59

Hartmann, D. L. 1994, Global physical climatology, International geophysics series ; v. 56 (San Diego: Academic Press)

Hays, J. D., Imbrie, J., & Shackleton, N. J. 1976, Science, 194, 1121

Heller, R., Leconte, J., & Barnes, R. 2011, A&A, 528, A27

Holmberg, E. 1941, ApJ, 94, 385

Hourdin, F., Musat, I., Bony, S., et al. 2006, Climate Dynamics, 27, 787

Huang, S. 1959, American Scientist, 47, 397

Hunt, B. G. 1982, Journal of the Meteorological Society of Japan. Ser. II, 60, 309

Huybers, P., & Tziperman, E. 2008, Paleoceanography, 23, PA1208

Ibgui, L., & Burrows, A. 2009, ApJ, 700, 1921

Imbrie, J., & Imbrie, J. Z. 1980, Science, 207, 943

Ito, T., & Miyama, S. M. 2001, ApJ, 552, 372

Jenkins, G. S. 2000, J. Geophys. Res., 105, 7357

Jenson, J. W., Macayeal, D. R., Clark, P. U., Ho, C. L., & Vela, J. C. 1996, J. Geophys. Res., 101, 8717

Jiang, I.-G., & Ip, W.-H. 2001, A&A, 367, 943

Joughin, I., Abdalati, W., & Fahnestock, M. 2004, Nature, 432, 608

Kaib, N. A., Raymond, S. N., & Duncan, M. 2013, Nature, 493, 381

Kasting, J. F., Whitmire, D. P., & Reynolds, R. T. 1993, Icarus, 101, 108

Kepler, J. 1609, Astronomia nova ..., seu physica coelestis, tradita commentariis de motibus stellae martis, doi:10.3931/e-rara-558

—. 1619, Ioannis Keppleri harmonices mundi libri V : quorum primus harmonicus ... quartus metaphysicus, psychologicus et astrologicus geometricus ... secundus architectonicus ... tertius proprie ... quintus astronomicus metaphysicus ... : appendix habet comparationem huius operis cum harmonices Cl. Ptolemaei libro III cumque Roberti de Fluctibus

... speculationibus harmonicis, operi de macrocosmo microcosmo insertis, doi:10.3931/e-rara-8723

Kinoshita, H. 1975, SAO Special Report, 364

—. 1977, Celestial Mechanics, 15, 277

Kirschvink, J. L. 1992, in The Proterozoic biosphere; a multidisciplinary study (Cambridge: Cambridge Univ. Press), 51–52

Kopparapu, R. K., Ramirez, R. M., SchottelKotte, J., et al. 2014, ApJ, 787, L29

Kopparapu, R. k., Wolf, E. T., Haqq-Misra, J., et al. 2016, ApJ, 819, 84

Kopparapu, R. K., Ramirez, R., Kasting, J. F., et al. 2013, ApJ, 765, 131

Kurahashi-Nakamura, T., Abe-Ouchi, A., & Yamanaka, Y. 2010, Climate Dynamics, 35, 713

Lagrange, J. L. 1811, Mécanique Analytique

Laplace, P. S., Bowditch, N., & Bowditch, N. I. 1829, Mécanique céleste

Laskar, J. 1985, A&A, 144, 133

—. 1986, A&A, 157, 59

—. 1990, Icarus, 88, 266

Laskar, J., Correia, A. C. M., Gastineau, M., et al. 2004, Icarus, 170, 343

Laskar, J., Joutel, F., & Boudin, F. 1993a, A&A, 270, 522

Laskar, J., Joutel, F., & Robutel, P. 1993b, Nature, 361, 615

Laughlin, G., & Adams, F. C. 1999, ApJ, 526, 881

Le Verrier, U.-J. 1855, Annales de l'Observatoire de Paris, 1, 258

Leconte, J., Forget, F., Charnay, B., Wordsworth, R., & Pottier, A. 2013, Nature, 504, 268

Lefebre, F., Gallée, H., van Ypersele, J.-P., & Huybrechts, P. 2002, Annals of Glaciology, 35, 391

Li, G., & Batygin, K. 2014, ApJ, 790, 69

Libert, A.-S., & Henrard, J. 2007, A&A, 461, 759

Libert, A.-S., & Tsiganis, K. 2011, MNRAS, 412, 2353

Lisiecki, L. E. 2010, Nature Geoscience, 3, 349

Lisiecki, L. E., & Raymo, M. E. 2005, Paleoceanography, 20, PA1003

—. 2007, Quaternary Science Reviews, 26, 56

Lissauer, J. J. 1999, Nature, 398, 659

Lissauer, J. J., Barnes, J. W., & Chambers, J. E. 2012, Icarus, 217, 77

Lissauer, J. J., & Rivera, E. J. 2001, ApJ, 554, 1141

Lovett, E. O. 1895, AJ, 15, 113

Malbet, F., Léger, A., Shao, M., et al. 2012, Experimental Astronomy, 34, 385

Malhotra, R. 2002, ApJ, 575, L33

Maslin, M. 2016, Nature, 540, 208

Mayor, M., & Queloz, D. 1995, Nature, 378, 355

Mazeh, T., Zucker, S., dalla Torre, A., & van Leeuwen, F. 1999, ApJ, 522, L149

McArthur, B. E., Benedict, G. F., Barnes, R., et al. 2010, ApJ, 715, 1203

McArthur, B. E., Benedict, G. F., Henry, G. W., et al. 2014, ApJ, 795, 41

Meadows, V. S. 2017, Astrobiology, 17, 1022

Meadows, V. S., Reinhard, C. T., Arney, G. N., et al. 2017, ArXiv e-prints, arXiv:1705.07560

Michtchenko, T. A., Ferraz-Mello, S., & Beaugé, C. 2006, Icarus, 181, 555

Michtchenko, T. A., & Malhotra, R. 2004, Icarus, 168, 237

Migaszewski, C., & Goździewski, K. 2009, MNRAS, 392, 2

Miguel, Y., & Brunini, A. 2010, MNRAS, 406, 1935

Miller, N., Fortney, J. J., & Jackson, B. 2009, ApJ, 702, 1413

Murray, C. D., & Dermott, S. F. 1999, Solar system dynamics

Naef, D., Mayor, M., Beuzit, J. L., et al. 2004, A&A, 414, 351

Nagasawa, M., & Lin, D. N. C. 2005, ApJ, 632, 1140

Nagasawa, M., Lin, D. N. C., & Ida, S. 2003, ApJ, 586, 1374

Namouni, F. 2005, AJ, 130, 280

Newcomb, S. 1895, [United States. Nautical Almanac Office. Astronomical paper ; v.5, pt. 1 (1895)], [Washington : U.S. Nautical Almanac Office, 1895], p. 1-48 ; 30 X 23 cm., 5, 1

Newton, I. 1687, Philosophiae Naturalis Principia Mathematica. Auctore Js. Newton, doi:10.3931/e-rara-440

North, G. R. 1975, Journal of Atmospheric Sciences, 32, 2033

North, G. R., & Coakley, Jr., J. A. 1979, Journal of Atmospheric Sciences, 36, 1189

Oerlemans, J. 1980, Nature, 287, 430

Ogilvie, G. I., & Lin, D. N. C. 2004, ApJ, 610, 477

Oglesby, R., & Ogg, J. 2000, in Illumina Conference Papers Index - unstructured

Paterson, W. S. B. 1994, The physics of glaciers

Peale, S. J. 1969, AJ, 74, 483

Pedregosa, F., Varoquaux, G., Gramfort, A., et al. 2011, Journal of Machine Learning Research, 12, 2825

Piskorz, D., Benneke, B., Crockett, N. R., et al. 2017, AJ, 154, 78

Pourbaix, D. 2001, A&A, 369, L22

Quinn, T. R., Tremaine, S., & Duncan, M. 1991, AJ, 101, 2287

Quirrenbach, A. 2010, in Exoplanets, ed. S. Seager (The University of Arizona Press)

Rauch, K. P., & Hamilton, D. P. 2002, in Bulletin of the American Astronomical Society, Vol. 34, AAS/Division of Dynamical Astronomy Meeting #33, 938

Raymo, M. E. 1997, Paleoceanography, 12, 577

Raymond, S. N., Armitage, P. J., & Gorelick, N. 2009, ApJ, 699, L88

Reffert, S., & Quirrenbach, A. 2011, A&A, 527, A140

Reshef, D. N., Reshef, Y. A., Finucane, H. K., et al. 2011, Science, 334, 1518

Rivera, E., & Haghighipour, N. 2007, MNRAS, 374, 599

Rivera, E. J., & Lissauer, J. J. 2000, ApJ, 530, 454

Rodler, F., Lopez-Morales, M., & Ribas, I. 2012, ApJ, 753, L25

Roe, G. 2006, Geophys. Res. Lett., 33, L24703

Rose, B. E. J., Cronin, T. W., & Bitz, C. M. 2017, ApJ, 846, 28

Saltzman, B., & Verbitsky, M. 1994a, Nature, 367, 419

—. 1994b, Paleoceanography, 9, 767

Scambos, T. A., Bohlander, J. A., Shuman, C. A., & Skvarca, P. 2004, Geophys. Res. Lett., 31, L18402

Schwartz, J. C., Sekowski, C., Haggard, H. M., Pallé, E., & Cowan, N. B. 2016, MNRAS, 457, 926

Schwieterman, E. W., Kiang, N. Y., Parenteau, M. N., et al. 2017, ArXiv e-prints, arXiv:1705.05791

Sellers, W. D. 1969, Journal of Applied Meteorology, 8, 392

Selsis, F., Kasting, J. F., Levrard, B., et al. 2007, A&A, 476, 1373

Shackleton, N. J., & Opdyke, N. D. 1973, Quaternary Research, 3, 39

Sharaf, S., & Boudnikova, N. 1967, Trudy Institute Theoreticheskol Astronomn. Leningrad, 11, 231

Shields, A. L., Barnes, R., Agol, E., et al. 2016, Astrobiology, 16, 443

Shields, A. L., Meadows, V. S., Bitz, C. M., et al. 2013, Astrobiology, 13, 715

Short, D. A., Mengel, J. G., Crowley, T. J., Hyde, W. T., & North, G. R. 1991, Quaternary Research, 35, 157

Simpson, E. K., Baliunas, S. L., Henry, G. W., & Watson, C. A. 2010, MNRAS, 408, 1666

Spiegel, D. S., Menou, K., & Scharf, C. A. 2008, ApJ, 681, 1609

—. 2009, ApJ, 691, 596

Spiegel, D. S., Raymond, S. N., Dressing, C. D., Scharf, C. A., & Mitchell, J. L. 2010, ApJ, 721, 1308

Stepinski, T. F., Malhotra, R., & Black, D. C. 2000, ApJ, 545, 1044

Takeda, G., Ford, E. B., Sills, A., et al. 2007, ApJS, 168, 297

Tamayo, D., Silburt, A., Valencia, D., et al. 2016, ApJ, 832, L22

Triaud, A. H. M. J., Collier Cameron, A., Queloz, D., et al. 2010, A&A, 524, A25

Tuomi, M., Pinfield, D., & Jones, H. R. A. 2011, A&A, 532, A116

Tziperman, E., Raymo, M. E., Huybers, P., & Wunsch, C. 2006, Paleoceanography, 21, PA4206

Valenti, J. A., & Fischer, D. A. 2005, ApJS, 159, 141

Van de Kamp, P. 1967, Principles of Astrometry (W. H. Freeman and Company)

Veras, D., & Armitage, P. J. 2007, ApJ, 661, 1311

von Hoerner, S. 1960, ZAp, 50

Walker, J. C. G., Hays, P. B., & Kasting, J. F. 1981, J. Geophys. Res., 86, 9776

Ward, W. R. 1974, J. Geophys. Res., 79, 3375

—. 1982, Icarus, 50, 444

—. 1992, Long-term orbital and spin dynamics of Mars, ed. H. H. Kieffer, B. M. Jakosky, C. W. Snyder, & M. S. Matthews, 298–320

Ward, W. R., & Hamilton, D. P. 2004, AJ, 128, 2501

Way, M. J., & Georgakarakos, N. 2017, ApJ, 835, L1

Williams, D. M., & Kasting, J. F. 1997, Icarus, 129, 254

Williams, D. M., & Pollard, D. 2002, International Journal of Astrobiology, 1, 61

—. 2003, International Journal of Astrobiology, 2, 1

Williams, G. P. 1988, Climate Dynamics, 3, 45

Wisdom, J., & Holman, M. 1991, AJ, 102, 1528

Wolf, E. T., & Toon, O. B. 2014, Geophys. Res. Lett., 41, 167

Wordsworth, R. D., Forget, F., Selsis, F., et al. 2011, ApJ, 733, L48

Wright, J. T., Upadhyay, S., Marcy, G. W., et al. 2009, ApJ, 693, 1084

Wunsch, C. 2004, Quaternary Science Reviews, 23, 1001

Yang, J., Boué, G., Fabrycky, D. C., & Abbot, D. S. 2014, ApJ, 787, L2

Yang, J., Cowan, N. B., & Abbot, D. S. 2013, ApJ, 771, L45

Yoder, C. F. 1995, Icarus, 117, 250

Yoder, C. F., & Peale, S. J. 1981, Icarus, 47, 1

VITA

Russell Deitrick was born in Mount Shasta, California, in 1982, and has lived next to mountains his entire life. He graduated from Rocky Mountain High School in Fort Collins, CO, in 2001, and spent the next few years at Front Range Community College trying to figure out what he wanted to be when he grew up. He then transferred to University of Colorado Denver, where he finished his BS in Physics in 2010. The next year, he started working on his PhD in Astronomy and Astrobiology at the University of Washington in Seattle, where he has been since. He will begin his first post-doctoral position at Universität Bern in Switzerland in 2018.

List of publications

1. **Deitrick, R.**, Barnes, R., Quinn, T.R., Armstrong, J.C., Charnay, B. & Wilhelm, C. 2018. Exo-Milankovitch Cycles I: Orbits and Rotation States. *Astronomical Journal*, in review.

2. Fujii, Y., Angerhausen, D., **Deitrick, R.**, Domagal-Goldman, S., Grenfell, J.L., Hori, Y., Palle, E., Siegler, N., Stapelfeldt, K., Rauer, H. 2018. Exoplanet Biosignatures: Observational Prospects. *Astrobiology*, in review.

3. Meadows, V.S., Reinhard, C.T., Arney, G.N., Parenteau, M.N., Schwieterman, E.W., Domagal-Goldman, S.D., Lincowski, A.P., Stapelfeldt, K.R., Rauer, H., DasSarma, S., Hegde, S., Narita, N., **Deitrick, R.**, Lyons, T.W., Siegler, N., Lustig-Yaeger, J. 2018. Exoplanet Biosignatures: Understanding Oxygen as a Biosignature in the Context of Its Enviroment. *Astrobiology*, in review.

4. Meadows, V.S., Arney, G.N., Schwieterman, E.W., Lustig-Yaeger, J., Lincowski, A.P., Domagol-Goldman, S.D., Barnes, R.K., Fleming, D.P., **Deitrick, R.**, Luger, R., Driscoll, P.E., Quinn, T.R., & Crisp, D. 2018. The Habitability of Proxima Centauri b: Environmental States and Observational Discriminants. *Astrobiology*, accepted.

5. Luger, R., Lustig-Yaeger, J., Fleming, D.P., Tilley, M.A., Agol, E., Meadows, V.S., **Deitrick, R.**, & Barnes, R. 2017. The Pale Green Dot: A Method to Characterize Proxima Centauri b using Exo-Aurorae. *Astrophysical Journal*, 837, 1.

6. Barnes, R., **Deitrick, R.**, Greenberg, R., Quinn, T.R., & Raymond, S.N. 2015. Long-lived Chaotic Orbital Evolution of Exoplanets in Mean Motion Resonances with Mutual Inclinations. *Astrophysical Journal*, 801:101.

7. **Deitrick, R.**, Barnes, R., McArthur, B., Quinn, T.R., Luger, R., Antonsen, A., &

Benedict, G.F., 2015. The Three-dimensional Architecture of the υ Andromedae Planetary System. *Astrophysical Journal*, 798:46.

8. Hawley, S.L., Davenport, J.R.A., Kowalski, A.F., Wisniewski, J.P., Hebb, L., **Deitrick, R.**, & Hilton, E.J. 2014. Kepler Flares I. Active and Inactive M Dwarfs. *Astrophysical Journal*, 797:121.

9. Abdo, A. A. *et al.* (including **Deitrick, R.**) 2010. The Spectral Energy Distribution of Fermi Bright Blazars. *Astrophysical Journal*, 716, 30-70.